

VITALY PETROV

Analysis and Enhancement of Directional Millimeter Wave and Terahertz Band Systems

VITALY PETROV

Analysis and Enhancement
of Directional Millimeter Wave
and Terahertz Band Systems

ACADEMIC DISSERTATION

To be presented, with the permission of
the Faculty of Information Technology and Communication Sciences
of Tampere University,
for public discussion at Tampere University
on 10 August 2020, at 16 o'clock.

ACADEMIC DISSERTATION

Tampere University, Faculty of Information Technology and Communication Sciences
Finland

<i>Responsible supervisor and Custos</i>	Professor Yevgeni Koucheryavy Tampere University Finland	
<i>Supervisors</i>	Assoc. Professor Sergey Andreev Tampere University Finland	Dr. Dmitri Moltchanov Tampere University Finland
<i>Pre-examiners</i>	Professor Tapani Ristaniemi University of Jyväskylä Finland	Professor Angeliki Alexiou University of Piraeus Greece
<i>Opponent</i>	Professor Tommaso Melodia Northeastern University USA	

The originality of this thesis has been checked using the Turnitin OriginalityCheck service.

Copyright ©2020 author

Cover design: Roihu Inc.

ISBN 978-952-03-1612-9 (print)
ISBN 978-952-03-1613-6 (pdf)
ISSN 2489-9860 (print)
ISSN 2490-0028 (pdf)
<http://urn.fi/URN:ISBN:978-952-03-1613-6>

PunaMusta Oy – Yliopistopaino
Tampere 2020

From a dialog between two researchers:

— Dear colleague, do you understand this effect?

— Yes, sure, I can explain it to you...

— No doubt. I can explain it as well. But do you actually understand it?!

Dedicated to my parents, my teachers, and my mentors, who encouraged me to always understand the things myself before teaching others.

PREFACE

The research work described herein has been conducted in the Unit of Electrical Engineering, Tampere University (former Department of Electronics and Communications Engineering, Tampere University of Technology) over the years 2016–2020.

This research has been primarily supported by the 4-years Tampere University of Technology President’s Scholarship. The work was also partially covered by the Academy of Finland FiDiPro program, projects PRISMA and RADIANT, as well as the collaboration between Tampere University and Intel Labs, USA, on millimeter wave networking. A notable part of the research was performed within a WiFiUS project MILLI co-financed by the Academy of Finland and the National Science Foundation, USA. A special appreciation goes to Nokia Foundation, HPY Research Foundation, and DELTA Network for facilitating the needed research mobility.

Many personalities played their roles in the present work. First and foremost, I would like to express my deepest gratitude to my advisor, Prof. Yevgeni Koucheryavy, for giving me the life-changing opportunity to work under his guidance, the freedom in selecting my research directions, as well as for his support and encouragement throughout my entire studies. I am very grateful to my co-advisors, Assoc. Prof. Sergey Andreev and Dr. Dmitri Moltchanov. Since joining the team, I have obtained substantial guidance from Sergey, who showed me that success is not a matter of luck, but persistence. I am incredibly indebted to Dmitri for strengthening my mathematical background and inculcating a habit to read books before “reinventing a wheel”. I am also thankful to Prof. Ian F. Akyildiz and Dr. Sasitharan Balasubramaniam, for extending horizons of my mind far beyond the state-of-the-art networking.

Substantial credit should be given to my collaborators from outside Tampere. My foremost gratitude goes to Assoc. Prof. Josep Miquel Jornet (Northeastern University, USA), who, among many other aspects, taught me “the art of doing one thing at a time”. I am thankful to Dr. Joonas Kokkonen, Dr. Janne Lehtomäki, Asst. Prof. Konstantin Mikhaylov, and Prof. Markku Juntti (University of Oulu, Fin-

land), as well as to Johannes Eckhardt and Prof. Thomas Kürner (TU Braunschweig, Germany) for their help in driving away my fear of wireless equipment. I acknowledge Dr. Maria A. Lema and Prof. Mischa Dohler (King's College London, UK). Their example showed me that impactful things could be done even under a desperate shortage of time. A special appreciation goes to Prof. Robert W. Heath Jr. (UT Austin, USA) for bringing my research to a whole new level. Finally, I thank our industrial partners – Dr. Gabor Fodor (Ericsson Research and KTH, Sweden), Johan Torsner (Ericsson Research, Finland), and Dr. Nageen Himayat (Intel Labs, USA) – for always questioning the feasibility of crazy ideas and concepts that I developed.

My deepest appreciation goes to SUAI University, where I started my research career. This includes, but not limited to Prof. Evgenii Krouk, who inspired my interest in science when I was a 16-years-old kid; my first mentor, Dr. Evgeny Linksy, who showed me that “a journey of a thousand miles begins with a single step”; Prof. Andrey Turlikov and Prof. Sergey Bezzateev, who convinced me that the appropriate methodology gives the key to every problem; Dr. Gregori Evseev and my thesis advisor, Alexandra Afanasyeva, who taught me to be precise in all the derivations.

During recent years, I was fortunate to work in a fantastic research environment created within Tampere University. I would like to particularly mention Prof. Mikko Valkama, who consistently managed our Unit and continuously worked to improve its visibility. I am extremely thankful to my fellow colleagues, co-authors, and friends for their support and understanding, as well as for the memorable moments together. This includes (in alphabetic order) Dr. Olga Galinina, Dr. Mikhail Gerasimenko, Roman Kovalchukov, Dr. Alexander Ometov, Dr. Rustam Pirmagomedov, Anton Podkletnov, Aleksei Ponomarenko-Timofeev, Dr. Alexander Pyattaev, Yekaterina Sadovaya, Andrey Samuylov, Dr. Dmitrii Solomitckii, Nikita Tafintsev, and Jani Urama. I would love to express my extensive gratitude to each of you individually, but this preface must be kept under two pages (for environmental reasons, as I guess).

I cannot find the words to acknowledge my family for their encouragement and love. Last but not least, I would like to thank Margarita Gapeyenko. Your support during the thesis writing was invaluable. Thank you for always backing me in work and life, as well as making this long adventure even more exciting.

VITALY PETROV

May 25, 2020, Tampere, Finland

ABSTRACT

The emergence of directional millimeter wave (mmWave) and terahertz (THz) communication systems is one of the major innovations introduced by the telecommunication industry in recent decades. First, the broad bands available in the mmWave and THz spectrums promise an order of magnitude improvement in the data rates. Second, highly-directional transmissions offer better spatial diversity that facilitates the performance and security of next-generation communication systems. As a result, the directional communications over the mmWave and THz bands may effectively support novel applications and services, ranging from augmented reality to collective driving by the fleets of autonomous vehicles.

Together with many advantages, mmWave and THz communications bring new challenges that require *revisiting the conventional approaches* to design and analyze wireless networks. The unique features of mmWave and THz signal propagation combined with the directionality of the links form a unique set of open research problems that were not as pressing at lower frequencies. In response, novel approaches, methods, and tools are needed to carefully model and evaluate the emerging mmWave and THz wireless systems.

This thesis is targeted at developing *a comprehensive set of mathematical frameworks and simulation tools* capable of accounting for the essential features of directional mmWave and THz wireless systems. The formulated models are then applied for constructing the *first-order performance estimations* of mmWave and THz communications operation in prospective usage scenarios. Later, on top of analyzing the state-of-the-art approaches for building mmWave and THz systems, the new technological enhancements to the advanced wireless networks operating in these bands are evaluated. The contributed frameworks and tools can be extended to model and assess the further developments in mmWave and THz communications.

CONTENTS

1	Introduction	1
1.1	General Background	1
1.2	Thesis Motivation	3
1.3	Thesis Structure and Main Contributions	4
2	Performance Evaluation of Directional Communications in mmWave and THz Bands	7
2.1	Research Motivation	7
2.2	Important Features of mmWave and THz Communications	8
2.2.1	Directionality	8
2.2.2	Molecular absorption	10
2.2.3	Blockage	11
2.3	Interference in Directional mmWave and THz Communications	13
2.3.1	Interference in the presence of directional communications	13
2.3.2	Modeling directional interference	13
2.3.3	Impact of interference on directional communications	15
2.4	Mobility Constraints in Directional Communications	17
2.4.1	Macro- and micro-scale mobility	17
2.4.2	Modeling THz communications with UE micro-mobility	17
2.4.3	Performance of THz link in presence of micro-mobility	20
2.4.4	Effect of directionality on performance of mmWave and THz band communications	21
3	Understanding Effects of Directional Communications on Emerging Wireless Networks	23

3.1	Research Motivation	23
3.2	Directional Communications in Wireless Access Networks	24
3.2.1	Utilizing multi-connectivity for reliable data exchange	24
3.2.2	Challenges with MC-enhanced networks	25
3.2.3	Modeling MC-enhanced directional communications	27
3.2.4	Network performance with different MC strategies	29
3.3	Directional Vehicular Communications	32
3.3.1	High-rate vehicular networking for emerging applications	32
3.3.2	Modeling vehicles assistance in mmWave communications	33
3.3.3	Quantifying gains of mmWave vehicular relaying	35
3.4	Directional UAV Communications	37
3.4.1	UAV assistance in mmWave networks	37
3.4.2	Evaluating opportunistic mmWave UAV relaying	39
3.4.3	Modeling mmWave communications with UAV-based APs	40
3.4.4	Comparing deployment options for UAV-based APs	42
4	Application-specific Aspects of Directional Communications	45
4.1	Research Motivation	45
4.2	Interference Mitigation in Vehicular Networks	46
4.2.1	Impact of interference in vehicular networks	46
4.2.2	Mitigating deafness in directional vehicular communications	47
4.2.3	Performance improvements with coordinated transmissions	49
4.3	Improving Security with Directional Transmissions	51
4.3.1	Physical-layer security with directional communications	51
4.3.2	Enhancing security levels with multi-path transmissions	52
4.3.3	Analyzing trade-offs between capacity and security	53
5	Conclusions and Future Work	57
5.1	Summary	57
5.2	Future Work	58

References	61
Publication I	77
Publication II	97
Publication III	107
Publication IV	127
Publication V	135
Publication VI	147
Publication VII	155
Publication VIII	165

List of Figures

2.1 Cone-shaped approximation for the antenna radiation pattern.	10
2.2 Total path loss at the frequencies above 100 GHz.	11
2.3 Considered scenario for interference modeling.	14
2.4 Mean interference and SINR vs. antenna radiation pattern angle [77].	16
2.5 Scenario for micro-mobility modeling.	18
2.6 SE of the THz link in the presence of micro-mobility [80].	20
3.1 Link management with multi-connectivity in mmWave networks. . .	25
3.2 Proposed methodology for modeling an MC-enhanced directional communication systems.	28
3.3 Deployment for directional communications divided into <i>zones</i>	28
3.4 Effect of MC strategies on directional mmWave communications [83].	31
3.5 Considered urban street deployment for mmWave vehicular relaying.	34
3.6 Effect of fraction of COW vehicles involved in relaying [79].	37
3.7 Opportunistic relaying of mmWave links by flying UAVs.	40

3.8	Comparing airborne and landed deployment options for UAV-based mmWave APs.	42
3.9	Key trade-offs for “Airborne vs. Landed” deployment of UAV-based mmWave APs [74].	43
4.1	Signal reflections from vehicle body in directional V2V communications.	48
4.2	Coordinated channel access in vehicular networks.	48
4.3	SE of mmWave V2V system with Directional CSMA [73].	50
4.4	Secure directional communications in urban deployments.	53
4.5	“Security vs. capacity” trade-off brought by multi-path THz communications [81].	55

ABBREVIATIONS

2D	two-dimensional
3D	three-dimensional
3GPP	3rd Generation Partnership Project
AP	access point
AR	augmented reality
COW	Cell on Wheels
CPS	Cone-plus-sphere
CSMA	carrier sense multiple access
CSMA/CA	carrier sense multiple access with collision avoidance
DCF	distributed coordination function
eMBB	enhanced mobile broadband
FAA	Federal Aviation Administration
FCC	Federal Communications Commission
HITRAN	high-resolution transmission molecular absorption database
IEEE	Institute of Electrical and Electronics Engineers
LIDAR	light detection and ranging device
LoS	line-of-sight
LTE	Long Term Evolution
MAC	medium access control
MC	multi-connectivity
MCS	modulation and coding scheme

mmWave	millimeter wave
nLoS	non-line-of-sight
NR	New Radio
pdf	probability density function
PHY	physical
PPP	Poisson point process
RV	random variable
Rx	receiver
SE	spectral efficiency
SINR	signal-to-interference-plus-noise ratio
SNR	signal-to-noise ratio
TCP	Transmission Control Protocol
TDMA	time-division multiple access
THz	terahertz
THz-AP	THz access point
THz-UE	THz user equipment
Tx	transmitter
UAV	unmanned aerial vehicle
UE	user equipment
V2V	vehicle-to-vehicle
V2X	vehicle-to-everything
VR	virtual reality
WLAN	wireless local area network

ORIGINAL PUBLICATIONS

- Publication I V. Petrov, M. Komarov, D. Moltchanov, J. M. Jornet and Y. Koucheryavy. Interference and SINR in Millimeter Wave and Terahertz Communication Systems With Blocking and Directional Antennas. *IEEE Transactions on Wireless Communications* 16.3 (Mar. 2017), 1791–1808.
- Publication II V. Petrov, J. Kokkonen, D. Moltchanov, J. Lehtomaki, Y. Koucheryavy and M. Juntti. Last Meter Indoor Terahertz Wireless Access: Performance Insights and Implementation Roadmap. *IEEE Communications Magazine* 56.6 (June 2018), 158–165.
- Publication III V. Petrov, D. Solomitckii, A. Samuylov, M. A. Lema, M. Gapeyenko, D. Moltchanov, S. Andreev, V. Naumov, K. Samouylov, M. Dohler and Y. Koucheryavy. Dynamic Multi-Connectivity Performance in Ultra-Dense Urban mmWave Deployments. *IEEE Journal on Selected Areas in Communications* 35.9 (Sept. 2017), 2038–2055.
- Publication IV V. Petrov, D. Moltchanov, S. Andreev and R. W. Heath. Analysis of Intelligent Vehicular Relaying in Urban 5G+ Millimeter-Wave Cellular Deployments. *Proc. of IEEE Global Communications Conference (IEEE GLOBECOM)*. Dec. 2019, 1–6.
- Publication V M. Gapeyenko, V. Petrov, D. Moltchanov, S. Andreev, N. Himayat and Y. Koucheryavy. Flexible and Reliable UAV-Assisted Backhaul Operation in 5G mmWave Cellular Networks. *IEEE Journal on Selected Areas in Communications* 36.11 (Nov. 2018), 2486–2496.

- Publication VI V. Petrov, M. Gapeyenko, D. Moltchanov, S. Andreev and R. W. Heath. Comparison of Airborne and Landed Deployments for On-Demand UAV-based mmWave Access Points. *IEEE Wireless Communications Letters* (Mar. 2020). Submitted publication, 1–5.
- Publication VII V. Petrov, G. Fodor, J. Kokkonniemi, D. Moltchanov, J. Lehtomaki, S. Andreev, Y. Koucheryavy, M. Juntti and M. Valkama. On Unified Vehicular Communications and Radar Sensing in Millimeter-Wave and Low Terahertz Bands. *IEEE Wireless Communications* 26.3 (June 2019), 146–153.
- Publication VIII V. Petrov, D. Moltchanov, J. M. Jornet and Y. Koucheryavy. Exploiting Multipath Terahertz Communications for Physical Layer Security in Beyond 5G Networks. *Proc. of IEEE Conference on Computer Communications Workshops (IEEE INFOCOM WKSHPS)*. Apr. 2019, 1–8.

Author's contribution

All the works presented in this thesis have been produced by the author when staying with the Faculty of Information Technology and Communication Sciences (ITC), Tampere University, former Faculty of Computing and Electrical Engineering, Tampere University of Technology, Tampere, Finland.

- Publication I **“Interference and SINR in Millimeter Wave and Terahertz Communication Systems With Blocking and Directional Antennas”**. The problem was identified together by the author, his supervisors, and Assoc. Prof. Josep M. Jornet. The author developed the methodology and obtained the numerical results following the guidance by his co-supervisor, Dr. Dmitri Moltchanov. The author also wrote the paper. Other authors contributed to editing the article structure and writing. The article writing was finalized during the author’s research visit to Prof. Jornet’s research lab, University at Buffalo, The State University of New York, NY, USA.

- Publication II **“Last Meter Indoor Terahertz Wireless Access: Performance Insights and Implementation Roadmap”**. The author proposed the problem formulation and the core idea of the article. The propagation measurements were conducted together with Dr. Joonas Kokkonen and Dr. Janne Lehtomaki during the author’s research visit to Prof. Markku Juntti’s research team, University of Oulu, Finland. The author developed the ray-based modeler and produced the simulation results, as well as wrote the paper. Other authors contributed to editing the article structure and writing.
- Publication III **“Dynamic Multi-Connectivity Performance in Ultra-Dense Urban mmWave Deployments”**. This article is a result of extensive cooperation between the research teams from Tampere University, Finland; King’s College London, UK; and RUDN University, Russia. The author proposed the problem statement and wrote the paper. The author’s main contribution is the compound multi-stage evaluation methodology that integrates (i) the ray-based modeler developed by Dr. Dmitrii Solomitskii; (ii) the system-level simulation tool developed by Dr. Maria A. Lema; and (iii) the mathematical framework developed by Andrey Samuylov, Margarita Gapeyenko, Dr. Dmitri Moltchanov, and Prof. Valeriy Naumov. Assoc. Prof. Sergey Andreev has notably contributed to planning the paper structure and content. All the authors contributed to editing the article structure and writing.
- Publication IV **“Analysis of Intelligent Vehicular Relaying in Urban 5G+ Millimeter-Wave Cellular Deployments”**. The problem formulation was proposed jointly by the author and Prof. R.W. Heath during the author’s research visit to Prof. Heath’s research lab, The University of Texas at Austin, TX, USA. The author identified the target scenario, developed the evaluation methodology, obtained and analyzed the numerical results. The author also wrote the paper. All the authors contributed to editing the article structure and writing.

- Publication V **“Flexible and Reliable UAV-Assisted Backhaul Operation in 5G mmWave Cellular Networks”**. The author contributed to identifying the problem statement and writing the paper. The author developed the simulation-based tool to model directional mmWave communications between the ground units and the airborne UAV nodes. The author obtained the simulation results and contributed to outlining the major conclusions of the performed numerical study. This publication is planned to be also included in the PhD thesis by Margarita Gapeyenko, the first author of the article.
- Publication VI **“Comparison of Airborne and Landed Deployments for On-Demand UAV-based mmWave Access Points”**. The author proposed the problem statement and the conceptual approach of utilizing landed UAVs for mmWave communications thus increasing the drone battery lifetime. The mathematical framework was developed by the author together with Margarita Gapeyenko and Dr. Dmitri Moltchanov. The author also obtained the simulation results and wrote the final version of the article. Assoc. Prof. Sergey Andreev and Prof. R. W. Heath have notably contributed to editing the paper structure and writing.
- Publication VII **“On Unified Vehicular Communications and Radar Sensing in Millimeter-Wave and Low Terahertz Bands”**. The author proposed the problem statement and the conceptual approach to coordinate vehicular communications and radar sensing using the signal reflections. The measurements were carried by the author together with Dr. Joonas Kokkonen and Dr. Janne Lehtomaki. The author also performed computer simulations and wrote the paper. Assoc. Prof. Sergey Andreev, Dr. Dmitri Moltchanov, and Dr. Gabor Fodor from Ericsson Research, Sweden contributed significantly to the paper structure and content. Prof. Yevgeni Koucheryavy, Prof. Markku Juntti, and Prof. Mikko Valkama supervised the work and contributed to editing the paper.

Publication VIII **“Exploiting Multipath Terahertz Communications for Physical Layer Security in Beyond 5G Networks”**. The author proposed the problem statement and the conceptual approach of secure multi-path communications in the THz band. The mathematical framework was developed by the author together with Dr. Dmitri Moltchanov. The author identified the key metrics of interest, obtained the numerical results, and also wrote the paper. Assoc. Prof. Josep M. Jornet and Prof. Yevgeni Koucheryavy contributed to editing the paper.

1 INTRODUCTION

1.1 General Background

The continuous growth in the users demands for the data rates in wireless systems calls for the corresponding growth in the amount of radio resources the networks should offer per a connected device. As the densification of wireless networks and the enhancements for the physical (PHY) layer have technological and economical limitations [60, 22], this demand is primarily satisfied by the further increase of the total bandwidth allocated for the wireless communications. An illustrative example here is the evolution of the 802.11-family of technologies by the Institute of Electrical and Electronics Engineers (IEEE), which is a de-facto standard for wireless local area networks (WLANs). Starting from 20 MHz in IEEE 802.11a over two decades ago, the technology expanded to 160 MHz-wide channels in modern IEEE 802.11ax. The 3rd Generation Partnership Project (3GPP) followed a similar path with its cellular technologies, such as the Long Term Evolution (LTE).

The technologies mentioned above operate at the frequencies of up to 6 GHz, as well as feature compact and cost-efficient wireless equipment. However, this part of the spectrum is extremely congested, serving not only numerous consumer wireless technologies, but also military communications, solutions for satellite connectivity, positioning, radar sensing, and more. Although the Federal Communications Commission (FCC) in the U.S. has recently authorized the commercial use of an additional band at 3.5 GHz, the predicted user demands already started exceeding the capabilities offered by the sub-6 GHz networks [12]. The latter trend motivates the telecommunication sector to start harnessing higher frequencies.

The exploration of millimeter wave (mmWave, 30 GHz–300 GHz) and terahertz (THz, 300 GHz–3 THz) bands for the consumer networking is one of the major technology innovations over the recent decades. Communications over these frequencies offer orders of magnitude greater bandwidth than the microwave systems

can provide. The use of GHz-wide channels, consequently, leads to massive improvements in the network capacity and the data rates available for the connected users. Hence, a larger number of devices can potentially be supported at higher rate, hence facilitating the appearance of new bandwidth-oriented services. Even the applications that are futuristic today, such as ubiquitous penetration of high-definition augmented reality (AR) and virtual reality (VR) systems, holographic communications, tactile Internet, and fleets of autonomous robots, may soon become a reality with emerging wireless networks exploiting mmWave and THz bands [17, 20, 32].

Together with these tempting opportunities, mmWave and THz band wireless systems present new engineering features. One of the significant novelties here is the use of highly-directional antenna radiation patterns to expand the communication range. The directional antenna systems capable to point in a given direction bring an additional level of diversity – *spatial diversity* – to mmWave and THz networks. The intelligent management of the joint frequency-time-space resources, in its turn, leads to further improvements in the performance characteristics [10].

The development of directional mmWave and THz communication systems for high-rate data exchange between the users is currently an active field of research and engineering. Several practical solutions have been presented to date in this area. First, the 3GPP has adopted outdoor mmWave communications as a part of their New Radio (NR) technology. The 3GPP mmWave solutions target enhanced mobile broadband (eMBB) as one of the primary use cases aiming to provide high-rate wireless access at the frequencies above 6 GHz to groups of emerging handheld and wearable devices in dense deployments [88].

The second group of activities has been carried by the IEEE aiming to design an operational mmWave networking system for the next-generation indoor WLANs. Some recent deliverables by the IEEE in this field include two amendments to Wi-Fi – IEEE 802.11ad and IEEE 802.11ay – enabling the mmWave communications at 60 GHz [45, 102]. Finally, the initial effort to harness the low THz spectrum for extremely high-rate wireless systems has been made by the IEEE in 802.15.3d-2017, where the directional communications at 300 GHz with up to 69 GHz of bandwidth are applied for kiosk download, data center, and fronthaul/backhaul scenarios [47].

In parallel with developing the wireless access networks to operate in the mmWave and THz bands, other activities were carried out aiming to enable directional communications with new types of connected devices: smart cars and unmanned aerial

vehicles (UAVs) [109, 119]. The prospective connected vehicles and UAVs are expected to enable novel applications, such as collective autonomous driving and ubiquitous video surveillance. In addition, the emerging connected vehicles and drones are considered to assist the prospective mmWave and THz band wireless access networks in handling the steadily increasing volume of user traffic [121]. However, the successful design of all these emerging high-rate communication systems requires a better understanding of the performance that directional mmWave and THz communication systems may achieve in target scenarios.

1.2 Thesis Motivation

Wireless communications in mmWave and THz frequency bands are impacted by several effects, less profound or even not manifesting at lower frequencies. In addition to directionality, mmWave and THz communication systems feature an additional propagation loss component caused by molecular absorption [59], as well as blockage of mmWave and THz radiation when propagating through obstacles [40]. As a result, the appropriate models for mmWave and THz band communications appear to be considerably different from those available for lower frequencies. Hence, the presence of new features naturally calls for novel methods and tools to evaluate the performance of mmWave and THz band systems.

In its turn, the spatial diversity introduced with highly-directional communications enables the design of complex network topologies connecting handheld devices, wearable electronics, smart vehicles, and UAVs into multi-hop networks [8]. Such dynamic and flexible systems, not widespread at lower frequencies, also demand new solutions for their modeling and evaluation [58]. Finally, additional novel techniques are employed in mmWave and THz systems to maintain reliable connectivity in the presence of blockage. Therefore, the corresponding modeling approaches should become even more sophisticated to also account for the major effects caused by the mmWave- and THz-specific connectivity enhancements.

Summarizing, the combination of (i) features brought by directional communications in the mmWave and THz bands; (ii) novel techniques for mmWave and THz networking; and (iii) specific properties of directional data exchange with new categories of connected devices, such as vehicles and UAVs; calls for a *thorough rethinking* of the approaches to design and evaluate wireless networks. This unique set of

challenges and open research problems related to the analysis and enhancement of directional mmWave and THz communication systems serves as the motivation for the present research work, as outlined in the following section.

1.3 Thesis Structure and Main Contributions

The *main contribution* of this thesis is a collection of mathematical frameworks and simulation tools to characterize the impact of directional mmWave and THz communications on the performance of future wireless networks. With the use of the developed methodologies, additional concepts are proposed and evaluated aiming to improve the emerging directional mmWave and THz communication systems.

The thesis consists of an introductory part comprising *five* chapters appended by *eight* publications. The scope of this work is also closely related to several other publications by the author referred to in the bibliography for this text.

The thesis is structured as follows. Chapter 1 introduces the general background to the topic and the research motivation, the main contribution of this work, as well as the thesis structure.

Chapter 2 is dedicated to the performance evaluation of directional mmWave and THz communication systems. Particularly, a novel mathematical framework is contributed in Section 2.3 to model the interference in directional communications at the mmWave and THz frequencies. Then, another mathematical framework is contributed in Section 2.4 to study the implications of node micro-mobility on the performance of directional links. With the use of these frameworks, important numerical observations are made on the trade-offs enabled by narrow and wide mmWave/THz beams.

Chapter 3 extends the material presented in Chapter 2 by exploring the impact of directional communications on the emerging wireless networks. For this purpose, a compound analytical-simulation methodology is introduced in Section 3.2 to evaluate the performance of a mmWave access network in realistic urban deployments. Then, a mathematical framework is contributed in Section 3.3 capable to analyze the performance improvements brought by mmWave vehicular relaying. Finally, a simulation tool and a mathematical framework are delivered in Section 3.4 to evaluate the gains of UAV assistance in mmWave networking. With the contributed frameworks and tools, first-order predictions are made on the performance of directional

mmWave communication systems in typical urban scenarios.

We continue our study on directional mmWave and THz communications in Chapter 4, where application-specific enhancements are explored. Particularly, an approach for interference mitigation in directional vehicular communication systems is presented and analyzed in Section 4.2. Then, another approach is proposed and evaluated in Section 4.3, aiming to enhance the security of data exchange in THz networks by exploiting the multi-path directional communications. With the performed studies, we observe that directional communications in the mmWave and THz bands bring not only challenges but also new system design opportunities, not feasible with omnidirectional communications at lower frequencies.

Chapter 5 concludes the thesis and outlines possible future research directions.

2 PERFORMANCE EVALUATION OF DIRECTIONAL COMMUNICATIONS IN MMWAVE AND THZ BANDS

2.1 Research Motivation

The emergence of highly-directional mmWave and THz communications requires major modifications of modern consumer wireless networks that, as of today, primarily operate with much less directional systems in the microwave band. Foreseeing these changes, the research community has been actively exploring the key features and trade-offs introduced by the data exchange over directional links [65]. Several important observations have already been made to date. The mmWave and THz band-specific channel models appear to be substantially different from those developed for lower frequencies [4, 39]. It was particularly observed that the impact of multi-path propagation changes significantly in the presence of directional communications: instead of transmitting the signal over all the available paths, the node can select *some* of the paths by pointing its beam in one direction or another.

On the link level, directional communications call for novel methods to maintain the beam alignment between the transmitter (Tx) and the receiver (Rx) antenna systems [44, 15]. The approaches to model the link-level performance characteristics, such as the link capacity and the communication range, also need to be revisited accordingly. On the system level, directional transmissions affect connectivity and interference models. Additional challenges arise in the design and evaluation of the wireless system performing directional communications with mobile nodes. Here, the mobility of the node brings both engineering difficulties (e.g., making the directional beams to follow the mobile entity) and evaluation-related issues, as the effect must be properly accounted for in the analysis.

In addition to the directionality, communications in the mmWave and THz bands are also featured by several effects that are less pronounced at lower frequencies. First of all, the *molecular absorption* causes additional losses when the signal propagates through the environment at particular frequencies [59]. Then, the mmWave and THz band signals become severely attenuated when penetrating through almost any object in the environment, ranging from a large building and up to a single human body [40, 98]. This effect, often termed as *blockage*, should also be considered when modeling mmWave and THz communications as well as must be addressed in the design of future wireless systems.

Due to the highlighted difference, the accurate performance evaluation of the directional communications in the mmWave and THz bands requires novel analytical methods and simulation tools. In this chapter, we aim to facilitate the research in this area by proposing two novel mathematical frameworks tailored to the specifics of mmWave and THz communications. Our frameworks are then applied to explore the key trade-offs of using narrow and wide beams in the directional communications over these frequencies. The rest of the chapter is structured as follows. In Section 2.2, we detail the key features of mmWave and THz band communications, such as directionality, molecular absorption, and blockage. Then, in Section 2.3, the interference model for the random deployment of mmWave/THz band nodes is contributed that accounts for the listed specifics. Finally, the impact of device small-scale mobility on the performance of a directional link is explored in Section 2.4 with the use of the developed mathematical framework.

2.2 Important Features of mmWave and THz Communications

2.2.1 Directionality

One of the advantages of mmWave and THz communications is the availability of the significant parts of the spectrum: from a few GHz in the mmWave band [45] up to several tens or even hundreds of GHz in the THz band [5, 47]. Hence, the bandwidth of these systems can be at least one order of magnitude higher than of those offered by existing microwave solutions [4]. Simultaneously, it is more difficult to

achieve a long communication range of mmWave and THz band systems due to several reasons. First, assuming constant transmit power, equal for a microwave and a mmWave/THz system, the wider bandwidth of the latter naturally leads to a reduction of the power spectral density. Thereby, due to less energy received per 1 Hz, the reliable reception of the mmWave/THz signal is more affected by the thermal noise. Second, assuming isotropic antennas at both Tx and Rx, the smaller wavelength of mmWave/THz signal leads to the lower effective area of the Rx antenna, and consequently the greater free-space path loss.

The negative impact of the above-mentioned effects can be partially compensated by utilizing directional antennas at the Tx node, the Rx node, or, preferably, on both sides. With directional antennas on both Tx and Rx nodes, the higher fraction of the transmit power is concentrated in the direction towards the Rx, as well as the greater portion of the transmitted energy is captured by the Rx antenna. There are different approaches available to design a directional antenna for the mmWave and THz frequencies, including a horn antenna, a parabolic antenna, and others [42, 49]. In this work, we primarily concentrate on the two-dimensional (2D) phased arrays, where the highest fraction of the transmit power can be electronically steered to point in different directions without moving the antenna itself.

While an isotropic antenna radiates the same power in all directions, a directional antenna is characterized by a nontrivial *antenna radiation pattern* defining the variation of the power radiated by an antenna as a function of the specific direction. The radiation pattern of a real directional antenna typically has a complex shape with a strong *main lobe* pointing towards the direction where the highest fraction of power is transmitted and several weaker *side lobes* [90]. Simpler models are often used to approximate the real pattern and, thus, facilitate the link-level and, especially, the system-level analysis of directional mmWave and THz band communications.

In this thesis, we primarily utilize the *cone-shape* approximation for the directional antenna radiation pattern assuming that all the transmitted energy is concentrated inside a single cone-shaped beam of a width α (see Fig. 2.1). It has been shown in [77] that, assuming the 100% efficiency, the antenna gain for a cone model, G , can be derived from the antenna radiation pattern angle, α , as $G = 2/(1 - \cos(\alpha/2))$. Hence, a smaller α leads to a narrower beam and greater antenna gains.

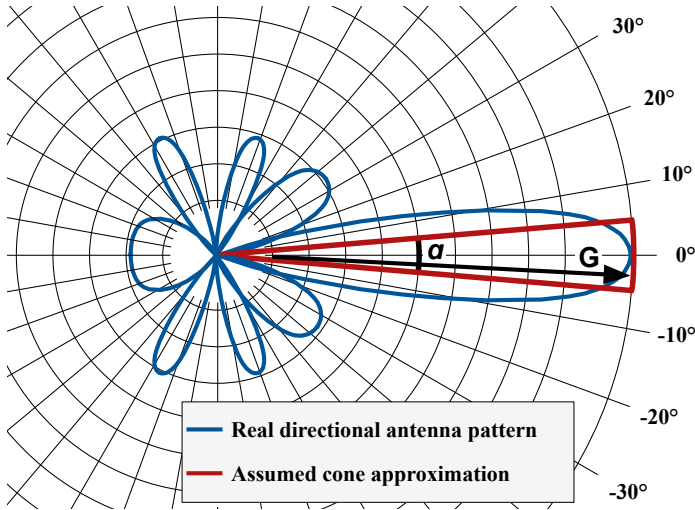


Figure 2.1. Cone-shaped approximation for the antenna radiation pattern.

2.2.2 Molecular absorption

On top of the spatial loss, the wave propagation at mmWave and THz frequencies is notably affected by an additional source of energy losses termed as *molecular absorption*. Molecular absorption is an effect where a certain part of the electromagnetic wave energy is converted into kinetic energy of the molecules present in the environment [59]. This effect does not damage the molecular structure, but induces internal vibrations in the molecules. The fraction of the wave energy absorbed by the environment depends on the wave frequency and the environment composition [5].

In this thesis, we primarily rely on the molecular absorption model given in [48]. Following this model, the absorption loss, $L_A(f, d)$, where the wave of a frequency f propagates over a distance d , is calculated as

$$L_A(f, d) = \frac{1}{\tau(f, d)} = e^{K(f)d}, \quad (2.1)$$

where $\tau(f, d)$ is the transmittance of the medium following the Beer-Lambert law, while $K(f)$ is the overall absorption coefficient of the medium. These absorption coefficients are taken from the high-resolution transmission molecular absorption database (HITRAN) [41] compiled by the research teams from Harvard University, California Institute of Technology, University College London, and others [33].

Fig. 2.2 illustrates the total path loss at the frequencies above 100 GHz (conventional free-space loss plus the molecular absorption loss following (2.1) as a function of the frequency. Following this figure, the molecular loss in mmWave and THz bands is frequency-selective as the average loss may differ dramatically in the neighboring sub-bands. We also observe that the frequencies below 300 GHz feature relatively low levels of absorption loss. Hence, the aggregate effect of the molecular absorption on mmWave communications is noticeable only over longer links with the range of at least several tens or hundred meters. e.g., a wireless backhaul link [99]. In contrast, the absorption losses at higher frequencies may also impact the short-range links of only a few meters or even less. Therefore, an intelligent selection of the sub-bands that are the least affected by the molecular absorption – sometimes termed as *transparency windows* [16, 50] – becomes crucial for the wireless communications above 300 GHz.

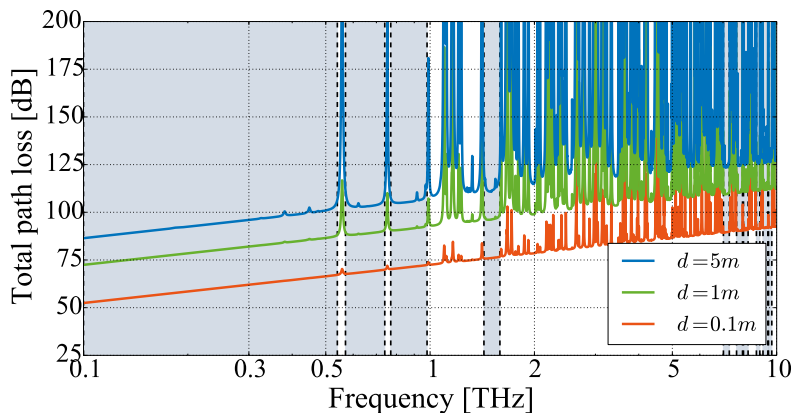


Figure 2.2. Total path loss at the frequencies above 100 GHz.

2.2.3 Blockage

Another important feature of directional communications in the mmWave and THz frequency bands is their vulnerability to the signal path blockage by various obstacles, ranging from buildings and individual walls up to vehicles, road signs, and human bodies [98]. The existing measurement studies show that a single human-body blocker may decrease the received power by non-negligible 20–35 dB depending on the signal frequency and the actual deployment [40]. Such drastic and often unex-

pected losses may easily lead to an outage.

Depending on the level of detail, the events of the signal path occlusion by obstacles are modeled differently. For a first-order analysis, only the blockage of the line-of-sight (LoS) path is considered, as the characteristics of this path have the strongest implications on the link quality. Here, at least two popular approaches can be used. With the first approach, only the blockages by large obstacles, such as buildings, are considered. Here, 3GPP provides different path loss equations for the conditions where the LoS path of the outdoor mmWave link is blocked or not blocked by a building [1]. The latter event leads to so-called *LoS conditions*, while the former one leads to *non-line-of-sight (nLoS) conditions*.

Following the second approach, the modeling can be detailed by accounting for the blockage caused by smaller obstacles, such as human bodies. Here, the LoS conditions is divided into two subcategories (e.g., as in [25]): (i) *LoS blocked* – where the LoS path is not occluded by a building but is still blocked by a small-scale obstacle (e.g., a human body) and (ii) *LoS non-blocked* where the LoS path is neither occluded by a building nor by any smaller object. It is important to note that the nLoS state is not divided into any subcategories as the impact of small obstacles is considered negligible in the presence of the LoS path occlusion by a building.

Finally, for fine-graded studies, the multi-path propagation of mmWave and THz band signal can be modeled explicitly [1, 26, 28]. Here, not only the blockage of the LoS path but also the states of all other available paths (e.g., reflected paths) are studied separately. As detailed in [28], this approach allows improving the accuracy of the performance evaluation at the cost of the considerably increased complexity of the resulting model.

The impact of human-body blockage on mmWave and THz communications becomes especially harmful in dense deployments, which are the target scenarios for bandwidth-hungry data exchange [13]. Here, the LoS path between the handheld or wearable mmWave/THz band user equipment (UE) and the access point (AP) is often occluded by the moving crowd surrounding the UE. As has been shown in [27], the average duration of the LoS path blockage event in a dense crowd scenario can exceed 200 ms, while the average fraction of time when the link is blocked may reach 70%. Therefore, the blockage effect must be incorporated in the design and evaluation of the wireless systems operating in the mmWave and THz frequencies.

2.3 Interference in Directional mmWave and THz Communications

2.3.1 Interference in the presence of directional communications

Accounting for directional antenna radiation patterns in mmWave and THz communications brings additional challenges when it comes to interference modeling. In many microwave systems featured by wide antenna radiation patterns the dominant factor determining the received power from the interfering node is the separation distance between the interfering node and the target receiver. In contrast, in directional mmWave/THz communications, the impact of a particular interfering node depends not only on its separation distance from the target receiver but also on the mutual orientation of the antenna radiation patterns at these two nodes. Also, the effect of signal blockage by various obstacles (buildings, walls, vehicles, and human bodies) is much more profound in directional communications over the mmWave and THz frequencies.

To facilitate the performance assessment for prospective mmWave/THz wireless systems, a new interference model is needed, accounting for the key features of directional mmWave/THz band communications. For this purpose, a novel interference model was developed in [77] by explicitly capturing three phenomena inherent at these frequencies: (i) high directivity of the transmit and receive antenna radiation patterns; (ii) molecular absorption; and (iii) blockage of high-frequency radiation. While there were several approaches for interference modeling in mmWave/THz communications [97, 105, 110, 111, 112], to the best of the author's knowledge, the work [77] was one of the first ones to investigate the interplay between the three above-mentioned effects and their collective impact on the interference in mmWave/THz systems.

2.3.2 Modeling directional interference

As the exact locations of communicating entities vary significantly depending on the scenario, a random deployment of nodes in \mathfrak{R}^2 is typically considered for the first-order analysis of interference in wireless networks [37, 35]. The same approach

was followed in [77] resulting in the deployment illustrated in Fig. 2.3. Particularly, the field of interfering nodes is modeled as a Poisson point process (PPP) with the intensity of λ_I . Each of the interferers also acts as a blocker with the radius r_B . An arbitrary node is selected as a target Rx. The Tx is located at a fixed distance of r_0 from the Rx. We finally utilize the THz-specific propagation model from [48] to calculate the radius of the zone, R , where the nodes produce non-negligible interference.

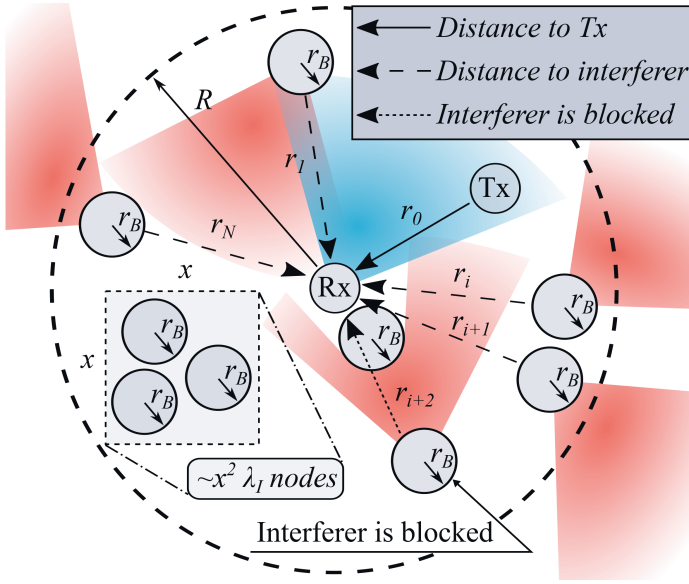


Figure 2.3. Considered scenario for interference modeling.

Two models were considered to approximate the antenna radiation pattern in our study:

- *Cone model.* The antenna radiation pattern is modeled with a single cone-shaped beam, as discussed in the previous section. No side lobes are modeled. This model represents an idealistic directional antenna.
- *Cone-plus-sphere (CPS) model.* This model takes into account the presence of side lobes that are modeled as a sphere around the main beam. This model represents a more realistic antenna with non-negligible side lobes.

The introduced approximations for complex mmWave and THz antenna radiation patterns allow to analytically derive the crucial characteristics, such as the mean interference at the Rx node.

For this purpose, we consider the cone model first and assume that the interferer located at a distance r is not blocked. For such a configuration, the contribution of the selected interferer to the total interference power at Rx is $A r^{-2} e^{-K r}$, where K is the molecular absorption coefficient [48]. In its turn, A can be derived from the Tx power, P_{Tx} , antenna gains, G_{Tx} and G_{Rx} , speed of light in the environment, c , and the frequency, f , as $A = P_{Tx} G_{Tx} G_{Rx} \frac{c^2}{16\pi^2 f^2}$.

Hence, the mean interference when the cone models are used for the interfering nodes, $E[I]$, can be derived with the following equation:

$$E[I] = \int_{r_B}^R A r^{-2} e^{-K r} e^{-\lambda_I(x-r_B)r_B} \frac{\alpha}{2\pi} 2\lambda_I \pi r dr = A \alpha \lambda_I \Theta(R, r_B, \lambda_I, K), \quad (2.2)$$

where $\Theta(R, r_B, \lambda_I, K)$ is given by

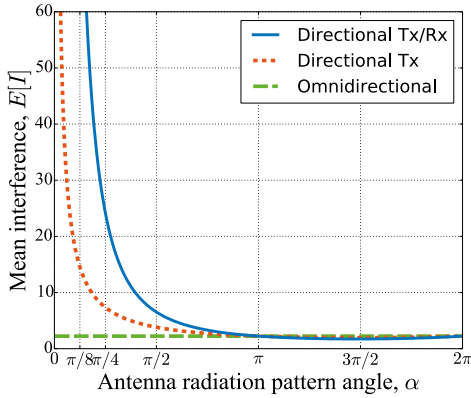
$$\Theta = e^{-\lambda_I r_B^2} \text{Ei}(-R[K + \lambda_I r_B]) - \text{Ei}(-r_B^2[K + r_B \lambda_I]), \quad (2.3)$$

and $Ei(\cdot)$ is the exponential integral function.

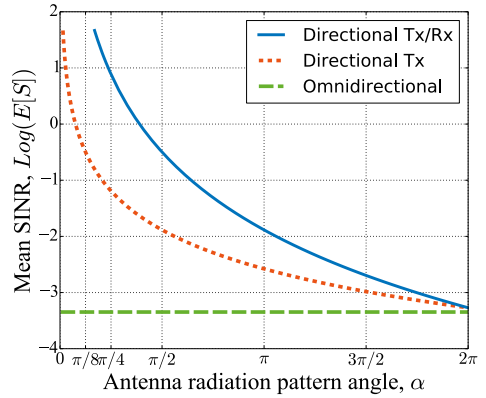
The mean interference power for the cone antenna model at the Rx and the CPS antenna model at all the interferers are obtained similarly, thus concluding the first stage of our analysis. At the second stage, the mean signal-to-interference-plus-noise ratio (SINR) at the Rx node in the presence of interference is calculated numerically using Taylor expansion as detailed in [77].

2.3.3 Impact of interference on directional communications

In addition to the quantitative results summarized in [77], several important qualitative observations have been made in our numerical study. First, as illustrated in Fig. 2.4a, the mean interference power increases with the reduced angle of the antenna radiation pattern, α . The main reason is that all the nodes are considered to be placed on the same 2D plane, and all the modeled beams are horizontal in space. In such a case, directional antenna radiation patterns concentrate most of the interference power from the three-dimensional (3D) area to the 2D plane, where the nodes are. Hence, the more directional the considered pattern becomes (smaller α), the greater part of the energy is concentrated in the considered 2D plane (and, consequently, around the Rx node).



(a) Mean interference



(b) Mean SINR

Figure 2.4. Mean interference and SINR vs. antenna radiation pattern angle [77].

From the first read, the above-mentioned observation is counterintuitive, as it was stated in [11, 95] that directional communications are primarily noise-limited, not interference-limited. At the same time, a transition from noise- to interference-limited regimes is determined not by the absolute level of interference, but rather by the impact of the interference characterized by e.g., the SINR [64, 100]. Therefore, it is essential to recall that the received power of the target communication link (Tx-Rx) also grows with the directionality. Moreover, the received power grows faster with directionality than the interference power. Hence, the smaller values of α result in more favorable conditions for mmWave and THz band communications from the interference perspective, as illustrated in Fig. 2.4b.

Summarizing, our proposed model shows that the interference plays an essential role in mmWave and THz band communications, especially in dense environments featured by many strong interferers surrounding the target Rx. The probability of being affected by the interference coming from a neighboring node decreases notably with the use of directional antennas. However, our model shows that this effect is partially compensated by the considerably increased power of the interfering signal in cases the Rx and the interferer antennas are aligned. Nevertheless, the use of narrow beams reduces the impact of interference on mmWave and THz band communication systems. Ultimately, the purely noise-limited regime can be achieved with extremely-directional “razor-sharp” beams.

2.4 Mobility Constraints in Directional Communications

2.4.1 Macro- and micro-scale mobility

Highly-directional antenna radiation patterns at both Tx and Rx sides extend the range of mmWave and THz communications and, as illustrated in the previous section, reduce the impact of interference from the surrounding nodes. At the same time, the use of narrow Tx and Rx beams simultaneously imposes additional difficulties when the communicating nodes are mobile. Specifically, narrow radiation patterns in mobile mmWave and THz communications challenge the accuracy and speed of the employed beam steering procedures to follow the mobility of the nodes.

In addition to conventional macro-mobility (e.g., a walking human user or a driving connected vehicle), much less predictable effects related to micro-mobility (rotations and shakes) are to be considered when it comes to the prospective handheld and wearable devices [44, 84]. Here, fast and unexpected displacements of the mobile UE may lead to beam misalignments. The frequent misalignments of the highly-directional beams, in their turn, lead to degradation of the average link capacity and possible outages [68]. Hence, narrowing the beam simultaneously results in: (i) improved link signal-to-noise ratio (SNR) when the Tx and Rx beams are aligned (positive); and (ii) increased frequency of the beam misalignment events (negative). Therefore, the effects imposed by micro-mobility on mmWave and THz band communication systems must be carefully studied.

2.4.2 Modeling THz communications with UE micro-mobility

While the performance of mmWave and THz communications in the presence of macro-mobility has already been explored in several works [89, 106, 115], there were only a few attempts to account for micro-mobility effects in the performance evaluation of mobile communication systems operating over these frequencies [38, 124]. Understanding the gap, in this subsection, we present a mathematical framework to evaluate the performance of a wireless link between a THz access point (THz-AP) and a THz user equipment (THz-UE) with different levels of micro-mobility. The framework has been originally contributed in [80] and can also be applied to mmWave systems.

Particularly, a directional link between a stationary THz-AP and a handheld THz-UE is considered (see Fig. 2.5). The micro-mobility of the THz-UE is modeled as a combination of random mobility processes along the axes OX, OY, and OZ, as well as the random rotation processes over these axes. Both THz-AP and THz-UE are considered to be equipped with 2D antenna arrays of $N_A \times N_A$ and $N_U \times N_U$ ($N_A \gg N_U$) elements. We apply the THz-specific model from [48] to estimate the signal attenuation as it propagates between the nodes.

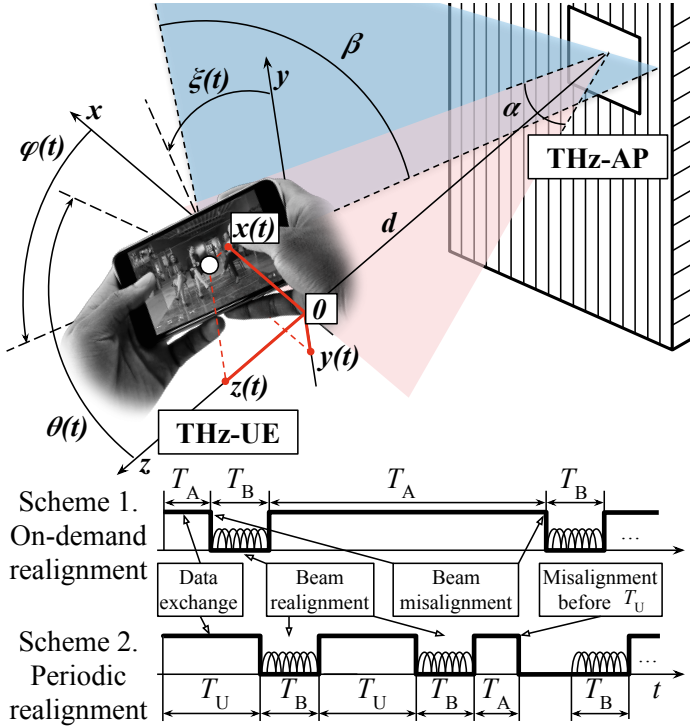


Figure 2.5. Scenario for micro-mobility modeling.

To compare and contrast possible solutions for the beam alignment procedures, two different schemes were studied. With the first scheme, *Scheme 1*, the beam alignment is performed on-demand, so the procedure runs immediately after an outage caused by the mobility of the THz-UE. With the second scheme, *Scheme 2*, the beam alignment is performed periodically with the parameter T_U .

Our mathematical framework to evaluate this scenario can be divided into two stages. At the first stage, we characterize a random variable (RV) representing the time period from the end of the previous beam alignment procedure to the next

beam misalignment caused by the micro-mobility of the THz-UE, T_A . Here, an important result from [80] is a tractable approximation for the probability density function (pdf) of this RV, $f_{T_A}(t)$:

$$f_{T_A}(t) = \frac{\frac{e^{-\frac{(\log(t)-\mu_x)^2}{2\sigma_x^2}}}{\sigma_x} \left[2 - \operatorname{erfc}\left(\frac{\mu_y - \log(t)}{\sqrt{2}\sigma_y}\right) \right] + \frac{e^{-\frac{(\log(t)-\mu_y)^2}{2\sigma_y^2}}}{\sigma_y} \left[2 - \operatorname{erfc}\left(\frac{\mu_x - \log(t)}{\sqrt{2}\sigma_x}\right) \right]}{2\sqrt{2\pi}t \left[1 - \frac{1}{2}\operatorname{erfc}\left(\frac{\mu_\phi - \log(t)}{\sqrt{2}\sigma_\phi}\right) + \frac{1}{2}\operatorname{erfc}\left(\frac{\mu_\theta - \log(t)}{\sqrt{2}\sigma_\theta}\right) \right]^{-1}} + \frac{\frac{e^{-\frac{(\log(t)-\mu_\phi)^2}{2\sigma_\phi^2}}}{\sigma_\phi} \left[2 - \operatorname{erfc}\left(\frac{\mu_\theta - \log(t)}{\sqrt{2}\sigma_\theta}\right) \right] + \frac{e^{-\frac{(\log(t)-\mu_\theta)^2}{2\sigma_\theta^2}}}{\sigma_\theta} \left[2 - \operatorname{erfc}\left(\frac{\mu_\phi - \log(t)}{\sqrt{2}\sigma_\phi}\right) \right]}{2\sqrt{2\pi}t \left[1 - \frac{1}{2}\operatorname{erfc}\left(\frac{\mu_x - \log(t)}{\sqrt{2}\sigma_x}\right) + \frac{1}{2}\operatorname{erfc}\left(\frac{\mu_y - \log(t)}{\sqrt{2}\sigma_y}\right) \right]^{-1}}, \quad (2.4)$$

where parameters $\mu_x, \mu_y, \sigma_x, \sigma_y, \mu_\phi, \mu_\theta, \sigma_\phi$, and σ_θ are derived from the characteristics of the THz-UE micro-mobility processes $x(t), y(t), \phi(t)$, and $\theta(t)$, as well as the number of elements in the employed 2D antenna arrays, N_A and N_U .

At the second stage of our evaluation framework, the characterized random time to the next beam misalignment, T_A , is applied to deriving the communication-centric metrics: the fraction of time that THz-UE remains in an outage and the link spectral efficiency (SE). For this purpose, we utilize the properties of renewal processes, as the time moments immediately after the beam alignment can be considered as regeneration points. Following this understanding, the selected performance indicators can be obtained via direct integration of the corresponding equations over time.

Particularly, the fraction of time in outage for *Scheme 1*, $p_{O,1}$, is derived directly from the definition $p_{O,1} = E[T_B/(T_A + T_B)]$ as

$$p_{O,1} = \int_0^\infty \frac{T_B}{t + T_B} f_{T_A}(t) dt, \quad (2.5)$$

where T_B stands for the duration of the beam alignment procedure.

Other metrics for both *Scheme 1* and *Scheme 2* are obtained similarly, thus allowing to evaluate the performance of the THz link with micro-mobility of one communicating node. The contributed framework can also be directly extended by a proper adjustment of (2.4) to account for the micro-mobility of the second communicating entity as well as incorporate different models for macro-scale mobility

of the THz-UE. In addition, the framework can be elaborated to model mmWave communications by modifying the employed path loss model.

2.4.3 Performance of THz link in presence of micro-mobility

To numerically characterize the effects of the THz-UE micro-mobility on the performance of the THz link, the methodology developed in the previous subsection is applied. Following the first IEEE standard for low THz band communications, IEEE 802.15.3d-2017 [47], we model a wireless link at 300 GHz with 50 GHz of bandwidth. The representative characteristics of the THz-UE micro-mobility are taken from the measurement campaign summarized in [84].

The key numerical results are illustrated in Fig. 2.6. Here, Fig. 2.6a presents the dependency between the size of the employed antenna array at the THz-AP and the THz link SE. The SE first grows with N_A until a certain point and then starts degrading, as a slightly improved SE during the beam alignment cannot anymore compensate for the notably increased frequency of beam misalignment events. Similar observations are made for the SE as a function of N_U . The results presented in Fig. 2.6a also directly imply the need to account for the expected levels of the THz-UE micro-mobility when determining the sizes of the employed THz antenna arrays, N_A and N_U and, consequently, the angles of the antenna radiation patterns.

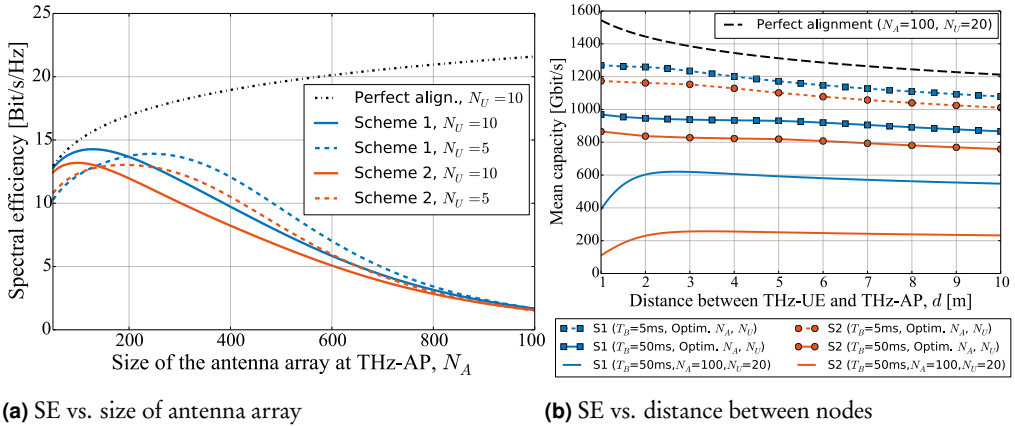


Figure 2.6. SE of the THz link in the presence of micro-mobility [80].

We proceed with Fig. 2.6b that presents the mean SE of the THz link versus the separation distance, d , for both schemes and different durations of the employed

beam alignment procedure, T_B . Particularly, we compare two options for selecting the sizes of the employed antenna arrays, N_A and N_U . With the first approach, these values are set constant. With the second approach, the values for N_A and N_U are calculated using our framework to maximize the mean SE. Following Fig. 2.6b, accounting for the expected levels of micro-mobility using the developed framework results in up to 50% improvement in the mean SE of the THz link.

Summarizing, the following important observation is made in our study:

“The average capacity of a THz link in the presence of THz-UE micro-mobility is a non-monotonic function of the antenna radiation pattern angles on THz-AP and THz-UE sides. Specifically, there are certain threshold levels of antenna radiation pattern angles. For the angles, smaller than the threshold value, the negative effects of frequent beam misalignments start dominating the positive effects of improved SNR when the beams are aligned.”

2.4.4 Effect of directionality on performance of mmWave and THz band communications

The performed study illustrates that the angle of the employed antenna radiation patterns is one of the crucial characteristics determining the performance of directional mmWave and THz band communications. Multiple ongoing projects are aiming to design directional antenna arrays with thousands of elements and thus potentially enable the extremely-directional antenna radiation patterns that are less than 1° wide [6]. However, as illustrated above, extremely-directional patterns are not always the best solution; instead, the better performance may be achieved with less directional transmissions. Hence, the antenna radiation pattern angles are to be selected carefully in future wireless solutions for the mmWave and THz bands.

At the technology design phase, the expected levels of node mobility (at both macro- and micro-scales) must be accounted for together with the target performance levels, communication range, carrier frequency, and bandwidth, as well as the transceiver characteristics. With all these parameters defined, one may apply the contributed frameworks to optimize the angles of the employed antenna radiation patterns when considering several important factors. These factors include: (i) the positive effects of higher directivity on the SNR and, consequently, SE, when the beams are aligned; (ii) the positive impact of higher directivity brought by the reduc-

tion of interference on other nodes; and (iii) the harmful effects of higher directivity on the performance caused by the expected levels of node mobility.

The mathematical frameworks and tools developed in this chapter can be further extended to model more sophisticated scenarios, such as the 3D deployment of interferers, e.g., for UAVs as in [55], different scenario geometries (e.g., highway vehicular communications setups as in [75]), as well as dual mobility of communicating nodes (e.g., to model device-to-device data exchange). The obtained analytical approximation for the beam misalignment time pdf in (2.4) can also be replaced with another distribution without any significant modifications of the framework. Hence, the analysis presented in this chapter may be further elaborated to model other practical scenarios for directional communications in the mmWave and THz bands, including prospective vehicular and UAV-centric networks.

3 UNDERSTANDING EFFECTS OF DIRECTIONAL COMMUNICATIONS ON EMERGING WIRELESS NETWORKS

3.1 Research Motivation

As illustrated in the previous chapter, the use of directional communications in the mmWave and THz bands requires novel methods and tools for performance evaluation. Complementing other proposals already available in the literature, the new approaches have been contributed in Chapter 2 to model the performance of mmWave and THz band communications in the presence of directional interference and micro-mobility. In this chapter, we proceed with studying the implications of directional transmissions on emerging wireless systems, tailored to particular use cases, scenarios, and target deployments.

Understanding the effects of directional mmWave and THz communications on the network characteristics in different practical scenarios is ongoing work with many important contributions already presented to date. Particularly, the scenario-specific channel models for directional mmWave links have been proposed by the 3GPP in [1]. Today, these approximate models are heavily utilized to simplify the analysis of mmWave systems. Then, several simulation-based tools to model the performance of mmWave networks were presented in [92], [62], and, recently, in [51], among others. An interference model for mmWave device-to-device communications was introduced in [21], while the initial performance predictions for indoor directional communications in the THz band were presented in [76].

In this chapter, we advance the research on this topic by exploring the implications of directional communications over the mmWave and higher frequencies in several practical scenarios. For this purpose, novel mathematical frameworks and

simulation tools, as well as extensive numerical studies, are contributed. Particularly, the effects of directional communications on wireless access networks are studied in Section 3.2. In that section, the novel evaluation methodology capable to model the mmWave network operation with abrupt link blockage and session rerouting is contributed [83].

The approach proposing to relay the mmWave UE transmissions via directional vehicular communications is presented and analyzed in Section 3.3. A detailed mathematical framework is contributed to estimate the performance gains enabled by mmWave vehicular relays in an urban street scenario [79].

Finally, the performance improvements to mmWave networks when exploiting UAV nodes are discussed in Section 3.4. For this purpose, both a mathematical framework [74] and a simulation-based tool are contributed [26] in that section. Our developed performance evaluation frameworks and the accompanying conclusions may be helpful for the design choices regarding the emerging mmWave and THz band communication systems.

3.2 Directional Communications in Wireless Access Networks

3.2.1 Utilizing multi-connectivity for reliable data exchange

The emerging wireless access networks operating in the mmWave and THz bands enable data exchange with the rates considerably higher than those offered by existing microwave solutions [10]. At the same time, as detailed in the previous chapter, mmWave and THz band communications employ directional narrow-beam transmissions that are vulnerable to blockages. Thereby, in real deployments, frequent blockages caused by buildings, vehicles, and human bodies, challenge the reliability of data exchange at these frequencies [51, 113]. It is also important to note that such blockage events (e.g., by a walking human near the UE) may occur unexpectedly and often result in an outage, as the SNR degrades drastically and rapidly when the signal path becomes occluded [98].

The prospective mmWave and THz band access networks are envisioned to support attractive latency-constrained applications and services, ranging from augmented

and virtual reality and up to holographic communications [7, 14, 93]. However, as estimated in [27], interruptions caused by a blockage may notably exceed the latencies that are tolerable for the above-mentioned use cases. Therefore, to maintain reliable data exchange in the mmWave and THz bands, additional mechanisms are needed. Specifically, both the UE-side and the network-side equipment should have specific procedures to follow in the case when a directional link currently used for the data transmission becomes interrupted.

One of the possible solutions for this problem proposed to date is to introduce additional redundancy in mmWave and THz band wireless networks. The envisioned deployment densities for the mmWave and THz APs suggest that the UEs have multiple APs in proximity. Hence, instead of connecting to a single AP, the UE can maintain multiple simultaneous links with different APs in range using e.g., *multi-connectivity (MC)* capabilities [31]. Following this approach, the UE becomes able to perform fast fallback to one of the “backup” links in the case when the active link becomes interrupted (see Fig. 3.1). With MC, the spatial diversity of directional links decreases the chances that all of them are blocked at the same time.

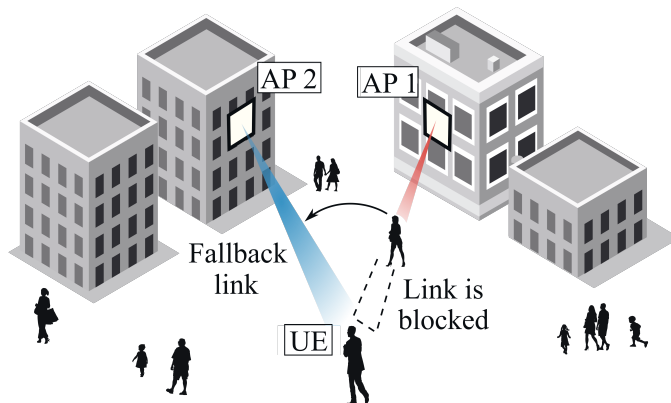


Figure 3.1. Link management with multi-connectivity in mmWave networks.

3.2.2 Challenges with MC-enhanced networks

Together with the expected performance and reliability gains, the use of MC for directional communications brings associated design- and engineering-related difficulties. First, as briefly discussed in the previous chapter, maintaining a single directional link is already challenging in the presence of UE large-scale and small-scale

mobility. Second, instant fallbacks to a “backup” wireless link towards another AP during an active data transmission demand a tight synchronization between the UEs, the APs, and the network equipment. For the downlink, such a fallback requires the network to reroute all the data fragments from one AP to another, including those already delivered to the original AP. For the uplink, the network must also have a mechanism to maintain the integrity and order of the data fragments transmitted by the UE, so that the higher-level UE session, e.g., an active Transmission Control Protocol (TCP) session, is not interrupted. Finally, continuously maintaining several mmWave connections by each of the UEs brings additional overheads to the connected devices and networking protocols as well as challenges the energy budget of battery-powered UE nodes.

The use of MC in directional mmWave and THz band communications does not only bring engineering difficulties but also calls for novel methods and tools to model the network performance. Selected prior works in this direction are summarized below. First, the protocol-related enhancements for MC mechanisms were described and analyzed in [31]. Then, a simulation-based methodology to model fast handover between mmWave APs was contributed in [85]. Later, mathematical frameworks to capture the main features of MC-enhanced wireless networks were delivered in [25] and [29], among others.

The existing approaches to model mmWave networks with MC can be classified into two large categories. The works from the first category contribute tractable and easy-to-use mathematical models (e.g., as in [25]). However, for the sake of analytical tractability, certain simplifying assumptions are often introduced, such as PPP deployment of nodes in R^2 , random locations of various obstacles, etc. Hence, the contributed frameworks can hardly be applied to study a particular detailed scenario (e.g., a street or a city square of a non-trivial shape). However, as argued in multiple works [34, 57], the characteristics of directional communications in the mmWave and, especially, THz bands heavily depend on the deployment. Even minor modifications of the scenario geometry may considerably affect the network performance that leaves room for the second group of modeling approaches.

The second category of modeling approaches is simulation-based, hence they feature all the needed flexibility to tailor the modeling tool to a specific detailed scenario (e.g., as in [85]). In addition, the approaches from the second category model the underlying mechanisms at a greater level of detail, thus, give more accurate predictions

for the performance and reliability levels. However, the complexity of the developed simulation tools is considerably higher, thus challenging the applicability of the obtained results to a wider variety of possible deployments. Summarizing, there is room for new approaches to model directional communications with MC that are simultaneously scalable, accurate, and efficient. Addressing this gap, we deliver a detailed yet scalable performance evaluation framework for directional mmWave communications [83]. The key aspects of this framework are outlined in the following section.

3.2.3 Modeling MC-enhanced directional communications

Aiming to better understand the implications of multi-connectivity on mmWave networks, we propose a novel compound simulation-analytical framework for the performance evaluation of MC-enhanced mmWave communications in realistic deployments. The framework was initially contributed in [83] and takes into account: (i) peculiarities of mmWave radio propagation in realistic urban deployments; (ii) dynamic mmWave link blockage caused by moving human crowd; and (iii) different MC strategies applied to preserve session continuity. The presented framework is designed flexible so it can be tailored to a given deployment and carefully model the characteristics of mmWave links in a particular scenario. Simultaneously, the framework offers a tolerable level of computational complexity, as it avoids modeling individual blockage events and data sessions reroutings with MC.

The contributed framework consists of several integral parts, as illustrated in Fig. 3.2. The first part of our framework is dedicated to characterizing the mmWave propagation in the target deployment. At the first stage, a precise 3D map of the deployment area is constructed with all the relevant objects (e.g., buildings and smaller architectural forms, mmWave APs, etc.). This is important as even minor differences in the deployment scenario may notably affect the performance of mmWave communications due to e.g., additional strong reflection component. In the second stage, a detailed coverage map is built by simulating the deployment with our in-house ray-based modeler described in [101]. Independent simulations are run for each of the deployed mmWave APs.

Then, the results of our ray-based modeling are converted into the scaling coefficients in Hz/bits/s that correspond to the appropriate modulation and coding

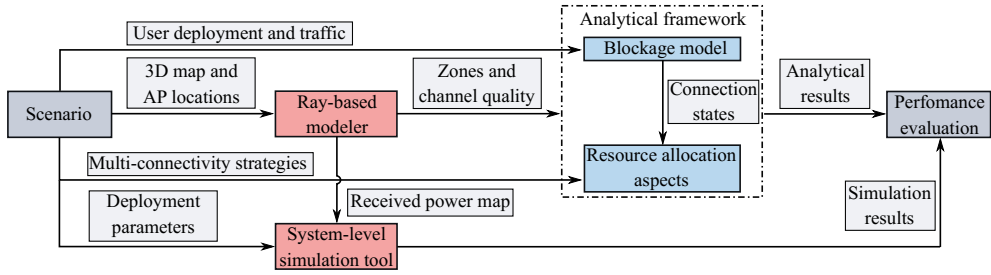


Figure 3.2. Proposed methodology for modeling an MC-enhanced directional communication systems.

scheme (MCS) the UE will use for the calculated channel conditions. Later, the calculated scaling coefficients are utilized as a criterion when dividing the entire area of interest into a certain number of clusters, named *zones* (see Fig. 3.3). The characteristics of the formed zones, together with the UE- and network-related parameters serve as the input to the second part of our framework.

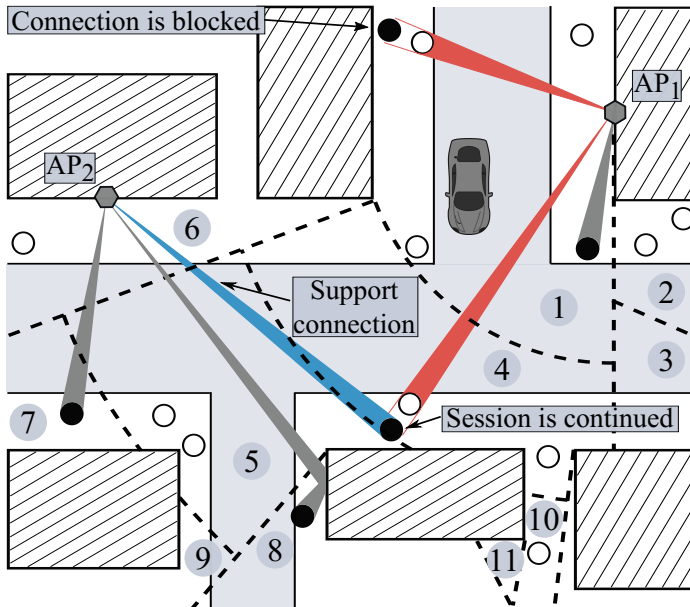


Figure 3.3. Deployment for directional communications divided into *zones*.

The second part of our framework, in its turn, comprises of two main components. The first component is the stochastic model we use to characterize the blockage of directional mmWave links by the moving crowd surrounding the UEs [27]. The primary role of this model is to predict the state of the individual mmWave

connections at a specific moment of time. The second component of this part is a novel queuing system based formulation that is used to calculate both the user-centric and the network-centric characteristics of our mmWave network. The formulation incorporates (i) the results of the ray-based modeling, (ii) the characteristics of the blockage process, (iii) the session-level attributes of the user traffic, and converts them into the target output characteristics. Particularly, the denial of service probability, the session drop probability, and the mean number of active sessions have been identified as illustrative metrics for modeling the mmWave network at the session level.

The accuracy of the constructed compound framework is ensured by calibrating the ray-based modeling in a reference 3GPP scenario for urban cities [1] as well as cross-verifying the results obtained with our framework against those produced by a system-level simulator. As detailed in [83], a close match is observed between the results. At the same time, the computation complexity of our framework is considerably lower, allowing to study more scenarios of interest with given time and performance constraints.

The framework contributed in [83] thus provides a powerful and efficient tool to model directional links in prospective wireless access networks enhanced with MC capabilities. The framework can be extended to account for other system design options, such as multi-radio MC schemes where the data session can also be rerouted to other wireless access technologies (e.g., microwave NR, LTE, or Wi-Fi [78]).

3.2.4 Network performance with different MC strategies

Enabling MC-enhanced directional communications raises new research questions related to the systems design choices. Some of these questions have already been studied in the literature. Specifically, the authors in [25], discovered the minimum number of simultaneous links – termed as *the degree of MC* – that are sufficient to maintain the target levels of reliability and performance in mmWave networks. For this purpose, a mathematical framework to study the implications of different degrees of MC in typical outdoor setups has been proposed. Following [25], the MC of degree 4 is sufficient for outdoor deployments, while any greater number of mmWave links leads to only incremental gains. These conclusions have been later confirmed via computer simulations in [91].

Operating with multiple simultaneous directional links causes additional overheads at both the UE and the network side. As the rerouting of an active session from one link to the other takes a non-negligible time, the authors in [29] studied the possible negative implications brought by high degrees of MC. Their mathematical framework accounts for different densities of mmWave APs and mmWave UEs, as well as the switching times associated with the session rerouting. The study in [29] shows that in many cases the MC of degree 2 results in the best trade-off between the connection reliability gains and the associated overheads. Hence, the use of 2, 3, or 4 mmWave links is envisioned for emerging MC-enhanced mmWave networks.

Not only the degree of MC but also the algorithm to select a fallback link impacts the network characteristics. To investigate this matter, the methodology developed in [83] was applied. Several practical link management algorithms, termed as *MC strategies*, were assessed. It is important to note that the directional link between the UE and the AP may be interrupted unexpectedly. Therefore, in certain conditions, the network will not be able to immediately deliver a rerouting command to the UE. Accordingly, in our study, we primarily focus on the UE-centric algorithms to select the best fallback links out of those currently available.

Particularly, we modeled a reality-inspired scenario representing Times Square in New York City, USA [66]. Several mmWave APs were placed on the walls of the buildings surrounding the area. The target mmWave UEs were uniformly deployed in the area with a certain density and surrounded by a moving human crowd to model random blockages of directional links. Five different UE-centric MC strategies have been considered and compared in our study. We present them below in the order of increasing implementation complexity:

1. *No reconnection (Baseline, NORECON)*. The reference strategy with a single mmWave link assuming no MC.
2. *Dual-connectivity (DCON)*. UE reroutes the active session to the link associated with the lowest probability of blockage.
3. *Multi-connectivity, blockage (MCON, bkg)*. An enhancement of the previous strategy. The UE reroutes the active session to the randomly-chosen mmWave AP in range. The probability of selecting a particular AP is inversely proportional to the blockage probability of the corresponding UE-AP link.
4. *Multi-connectivity, throughput (MCON, tpt)*. This strategy develops the previ-

ous one by suggesting the average throughput to be used as a metric instead of the link blockage probability.

5. *Multi-connectivity, both blockage and throughput (MCON, bkg+tpt)*. This strategy assumes that the UE knows the conditions of all the available mmWave links when rerouting the session. UE always selects the link offering the highest instantaneous throughput.

The performance and reliability of the mmWave communications with each of the selected MC strategies have been evaluated. As illustrated in Fig. 3.4, the trade-offs between the strategies are non-trivial, as each of them is beneficial in certain conditions. Nevertheless, several higher-level observations have been made in [83] regarding the impact of MC strategies on directional mmWave communications. First, even the basic MC strategy – DCON – already offers significant gains: up to 7 times lower denial of service probability and up to 25% greater number of supported sessions. Second, more intelligent MC strategies also bring non-negligible improvements on top of the DCON (e.g., up to 3 times lower session drop probability). Finally, it has been explored that the impact of complex MC strategies is the most profound in overloaded setups featured by many simultaneous data sessions.

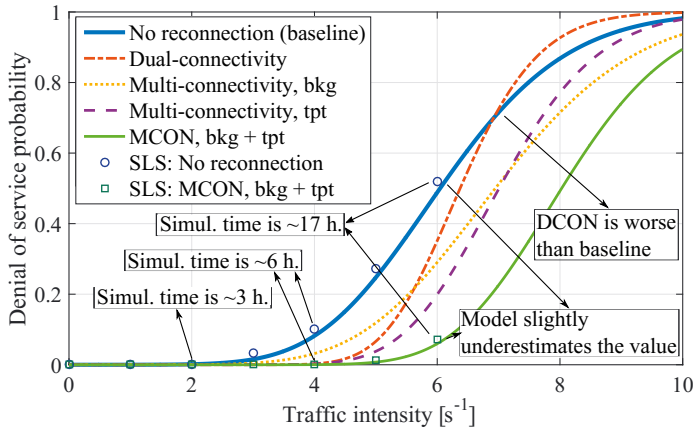


Figure 3.4. Effect of MC strategies on directional mmWave communications [83].

Our numerical study complements prior knowledge in the field and can be used as a reference when identifying the MC strategies that are the most appropriate for the prospective deployments.

3.3 Directional Vehicular Communications

3.3.1 High-rate vehicular networking for emerging applications

In the previous section, we made important observations regarding the effects of directional communications on emerging wireless access networks. In this section, we continue our study by focusing on the problems and opportunities brought by directional transmissions to vehicular networks.

Over the last decade, the research on data exchange with vehicles made a fundamental transformation. The earlier proposals were primarily focused on low-rate connectivity at the microwave frequencies (supported by e.g., IEEE 802.11p and LTE Release 14). In contrast, the recent developments in the field explore a broader range of vehicle-to-everything (V2X) communication scenarios, ranging from platooning to remote driving [23]. Many of these emerging use cases require high data rates and reliability levels as well as demand extremely low latencies, especially when aiming to support coordinated (semi-)autonomous driving by groups of vehicles [72].

As projected in [18], prospective autonomous cars featured by radars, light detection and ranging devices (LIDARs), and high-resolution cameras, will generate up to *one terabyte of sensor data per vehicle per hour*. A considerable part of this data (either raw or processed) should be distributed among the nearby vehicles to coordinate their actions on the road. In addition, with a greater level of vehicle autonomy, the lower fraction of driver's and passengers' attention will be paid to driving. Therefore, future vehicles are about to become "moving offices" and "moving theatres" thus demanding additional radio resources to deliver the content (e.g., remote desktop, high-resolution video streaming, or online gaming). All these stringent requirements demand a new wave of the V2X communication research focused on high-rate vehicular networking in the bands between 30 GHz and 300 GHz [104].

The prospective directional vehicular communications in the mmWave and low THz bands are envisioned not only to support the driving and entertainment use cases but also to enable new applications and services, such as e.g., vehicular crowd-sensing and vehicle-based video surveillance [70, 109]. At the same time, the adaptation of directional mmWave and THz band communications to the moving vehicles calls for a better understanding of the performance of directional communications in vehicular setups. Particularly, as illustrated in [71], the exact signal attenuation by a

vehicle-body blockage heavily depends on the height of the beam when penetrating through the vehicle. The connectivity and interference models also notably differ from those available for the wireless access [69, 75]. In addition, the implications of vehicular mobility on short-range mmWave and THz band communications must be carefully studied. Hence, several attractive applications, on one side, and a variety of open research problems, on the other, make directional vehicular communications at the mmWave and THz frequencies an attractive research field.

Among many open questions related to high-rate vehicular transmissions, the researchers have recently started to explore the densification of stationary mmWave networks with moving vehicle-mounted mmWave relays. The emerging vehicles are expected to be equipped with mmWave connectivity options at a certain point in time. Therefore, at relatively low costs, these moving devices may be used to extend the coverage of a static mmWave network and support the UEs currently experiencing poor connectivity conditions. While the MC mechanisms analyzed in the previous section are tailored to several static mmWave APs in the UE's proximity, vehicular relaying extends this approach by adding alternative connections to the same static mmWave AP via available relay links.

It has been particularly noted in [8] that assistance from connected vehicles may reduce the outage probability for wearable UEs by almost two times. However, further investigations in this research direction require novel approaches to quantify the gains brought by mmWave vehicular relays in different setups. While the trade-offs related to deploying static mmWave relays are already explored [86], modeling mmWave vehicular relaying is a work-in-progress. Here, enhanced tools are needed to simultaneously account for: (i) characteristics of directional communications at the mmWave and higher frequencies; and (ii) peculiarities of vehicular deployments. Understanding this need, a novel mathematical framework to model mmWave vehicular relaying was contributed in [79], as detailed in the following subsection.

3.3.2 Modeling vehicles assistance in mmWave communications

Our study in [79] considers an urban street scenario, as illustrated in Fig. 3.5. To model the diversity of city traffic, two different types of vehicles are deployed in the streets: (i) smaller regular vehicles termed as *cars*, and (ii) larger vehicles termed as *buses*. All the nodes are randomly placed in their areas. It is important to note that

the random distances between the pedestrians and between the vehicles are characterized by general distributions. Hence, an additional level of flexibility is delivered, as the framework can be tailored to a particular deployment with e.g., Poisson, uniform, or other distances between the nodes.

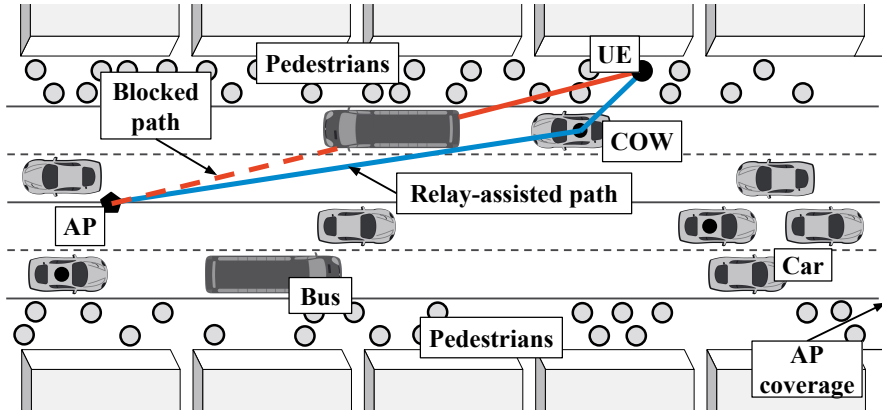


Figure 3.5. Considered urban street deployment for mmWave vehicular relaying.

A fraction of regular cars are equipped with mmWave radio and may relay the traffic between human users in its coverage range and stationary mmWave APs. These smart vehicles are termed as *Cell on Wheels (COW)*. The COWs primarily assist the UEs that have their direct link to the nearest mmWave AP occluded by a large vehicle or a human body. When there is at least one COW vehicle in range, the UE selects either the direct link to the AP or the relay link to the AP via the COW node, whichever currently provides the higher SNR level. The 3GPP-aligned approaches have been used to model directional mmWave communications [1].

In order to analyze the performance of data exchange between the UE and the AP both with and without mmWave vehicular relaying, the characteristics of individual UE-AP, UE-COW, and COW-AP links were first derived. Important contributions here are the equations to calculate the blockage probabilities for the UE-AP link, p_B , the UE-COW link, p_B^* , and the COW-AP link, p_B^* , in the presence of both

human-body and vehicle-body blockers:

$$p_B = \begin{cases} F_L(z) + \frac{1-F_L(z)}{E[L]} \left(2z - \int_0^{2z} F_L(x) dx \right), & h_T < h_T^* \cap \omega_S \leq 2r_P + \frac{(b_P - b_U)(8w_L + 3w_S)}{2(b_A - b_U)}, \\ F_L(z), & h_T < h_T^* \cap \omega_S > 2r_P + \frac{(b_P - b_U)(8w_L + 3w_S)}{2(b_A - b_U)}, \\ 1 - \frac{(\ell_C - p_T \ell_C + E[D])(1 - F_L(z) - \frac{1-F_L(z)}{E[L]}(2z - \int_0^{2z} F_L(x) dx))}{p_T \ell_T + (1 - p_T) \ell_C + E[D]}, & h_T \geq h_T^* \cap \omega_S \leq 2r_P + \frac{(b_P - b_U)(8w_L + 3w_S)}{2(b_A - b_U)}, \\ 1 - \frac{(\ell_C - p_T \ell_C + E[D])(1 - F_L(z))}{p_T \ell_T + (1 - p_T) \ell_C + E[D]}, & h_T \geq h_T^* \cap \omega_S > 2r_P + \frac{(b_P - b_U)(8w_L + 3w_S)}{2(b_A - b_U)}, \end{cases} \quad (3.1)$$

$$p_B^* = F_L(z_1) + \frac{1 - F_L(z_1)}{E[L]} \left(2z_1 - \int_0^{2z_1} F_L(x) dx \right), \quad (3.2)$$

$$p_B^* = \begin{cases} F_{D_B}(\ell_{B,C} - \frac{\ell_C}{2}), & h_T < h_T^*, \\ 1 - \left(1 - \frac{p_T \ell_T}{p_T \ell_T + (1 - p_T) \ell_C + E[D]} \right) (1 - F_{D_B}(\ell_{B,C} - \frac{\ell_C}{2})), & h_T \geq h_T^*, \end{cases} \quad (3.3)$$

where h_T^* and h_T^* are the minimum heights of a bus resulting in a possibility for the vehicle-body blockage of UE-AP and COW-AP links, respectively, while other parameters are detailed in Fig. 3.5 and in [79].

These equations derived with the use of stochastic geometry and probability theory are later applied to calculate the mean SE and the mean capacity of directional mmWave communications in the present setup. The contributed framework can be further extended to model more sophisticated scenarios, involving multi-hop vehicular communications and vehicular mesh networks with directional transmissions [9].

3.3.3 Quantifying gains of mmWave vehicular relaying

The successful implementation of mmWave vehicular relaying requires efforts from the community and also brings additional overheads to the communication protocols. Therefore, before progressing with the implementation, it is essential to understand if mmWave vehicular relaying provides non-negligible gains in realistic deployments. These gains would allow the better estimation of the trade-off between the potential performance improvements brought by mmWave vehicular relaying, on one side, and the associated difficulties and costs, on the other.

To facilitate this task, the framework developed in [79] is applied to numerically characterize the performance gains of mmWave vehicular relaying in an urban street

deployment. Particularly, the following three connectivity strategies for a handheld UE on a sidewalk are analyzed and compared:

1. *Baseline*. UEs always utilize the infrastructure mmWave link to the nearest stationary mmWave AP.
2. *Conservative Relay*. COWs assist UEs in their coverage. The radio resources allocated for UE-COW link *do not overlap* with the ones allocated for other active links in the mmWave cell.
3. *Aggressive Relay*. COWs assist UEs in their coverage. The radio resources allocated for UE-COW link *may overlap* with the ones allocated for other active links in the mmWave cell. This strategy exploits the substantial reduction in interference brought by the directional mmWave transmissions.

Several important observations are made in our numerical study. First, as detailed in [79], the developed framework appears to be extremely accurate when modeling directional mmWave communications in the target setup: the analytical results are tightly in line with those obtained via computer simulations.

Second, the UE performance with mmWave vehicular relaying is a non-monotonic function of the density of vehicles on the street. The reason is that the higher density of vehicles has both positive and negative effects on the SE of the target mmWave connection. Particularly, the higher density increases the chances to have at least one relay vehicle in the UE's proximity, but at the same time increases the blockage probability for the directional mmWave transmissions. For the considered deployment, it has been noted that the highest gains of vehicular relaying are observed for moderate densities of the vehicular traffic: 3–5 cars per 100 m of the lane.

Finally, as illustrated in Fig. 3.6, the relative gain in the SE with Aggressive Relay strategy reaches 100% when approximately 30% of the vehicles are involved in relaying. The gain grows much slower after this point. Therefore, we conclude that mmWave vehicular relaying using directional transmissions can effectively mitigate the blockage of mmWave links in street deployments. Moreover, mmWave vehicular relaying can bring decisive performance improvements at relatively low involvement levels. Therefore, the considered approach may assist the stationary mmWave infrastructure already at the early stages of the technology roll-outs.

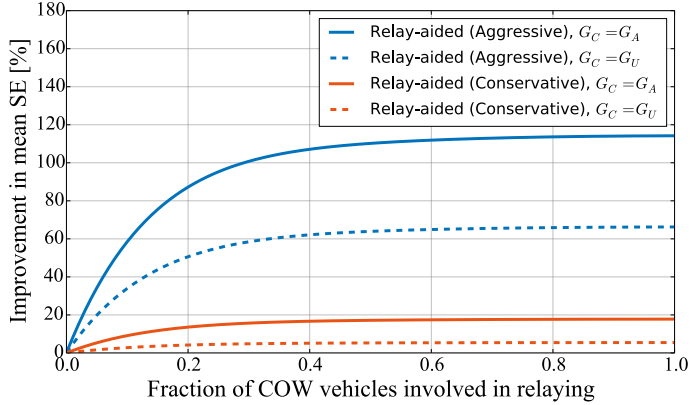


Figure 3.6. Effect of fraction of COW vehicles involved in relaying [79].

3.4 Directional UAV Communications

3.4.1 UAV assistance in mmWave networks

As discussed in the previous section, assistance from driving vehicles may considerably improve the performance of directional user communications. Clearly, smart vehicles equipped with mmWave capabilities are not the only category of nodes, whose assistance to wireless networks is being investigated. Particularly, the research community has recently shifted its focus towards utilizing the devices moving not next to the human crowds but rather above them – namely, UAVs or *drones*.

Recent developments in the UAV industry are approaching their pinnacle. According to the Federal Aviation Administration (FAA), the numbers of UAVs will soon reach 450,000 items in the US alone [67]. The unconstrained mobility of UAVs will open the door to advancements in transportation, medicine, surveillance, and many other sectors [94]. In addition, the ability of UAV nodes to easily adjust their positions and heights allows them to be visible simultaneously from many different locations, even in a city scenario [2]. Such an unprecedented level of flexibility decreases the chances for the link occlusion between e.g., the UAV and the stationary mmWave AP on the wall or the UAV and the handheld/wearable mmWave UE on the ground. Therefore, the UAVs are naturally explored as an additional connectivity option for the UEs when performing directional communications at the mmWave and higher frequencies.

At the same time, utilizing UAV-based mmWave transceivers to assist ground users brings additional design, technological, and regulatory challenges [36]. The limiting factors here are the cost and weight of radio equipment for high-rate directional data transmissions. Further, intelligent procedures for automated or semi-automated control of flying UAVs need to be implemented and approved by the appropriate regulatory bodies. Finally, the battery lifetime concerns as well as safety- and noise-related restrictions have to be addressed. Hence, utilizing UAV nodes in future mmWave wireless networks may bring not only attractive improvements but also potentially high capital and operational expenses. Therefore, the performance gains of possible UAV assistance must be first carefully studied.

Accounting for peculiarities of airborne nodes in the performance evaluation of directional communication systems requires certain modifications in the existing modeling tools. First, the elevation and mobility of UAVs impact the blockage modeling of narrow-beam mmWave links. Second, the relatively high altitude of UAVs challenges their ability to backhaul the user traffic. Therefore, new methods are needed to jointly account for the characteristics of UAV access and UAV backhaul links. Finally, the limited flight time on batteries should also be considered, as the discharged battery may lead to the temporal discontinuities in the UAV assistance.

Directional mmWave UAV communications is an actively-growing research area. Here, several important contributions have already been made to date. First, an iterative algorithm was delivered in [30] to select the trajectory of a dual-band UAV node that maximizes the performance of the mmWave UAV communications with ground users. The importance of optimizing the UAV height has been further discussed in [24]. Later, an in-depth survey on UAV-assisted mmWave networks was presented in [122]. Recently, a simulation framework to jointly optimize the performance of mmWave UAV access and backhaul links was contributed in [103].

We aim to facilitate the ongoing work on quantifying the performance gains brought by UAVs to directional mmWave communications. For this purpose, our novel frameworks and extensive numerical studies are contributed. We particularly analyze two possible deployment options for UAV operations. First, in subsection 3.4.2, we explore opportunistic relaying of mmWave transmissions via flying third-party UAVs. Later, in subsection 3.4.3 and subsection 3.4.4 we evaluate the performance levels achievable with the fleet of operator-controlled UAV-based mmWave APs.

3.4.2 Evaluating opportunistic mmWave UAV relaying

Opportunistic UAV relaying may be used to temporarily boost the performance of mmWave networks in dense urban deployments. The approach is considered especially beneficial in overloaded scenarios, where the static mmWave infrastructure, even when additionally densified with vehicle-mounted COWs, cannot provide adequate performance for the target UEs. To study such an extreme scenario, a comprehensive simulation tool has been developed in [26].

Particularly, a dense deployment of UEs and COWs in a large pedestrian plaza is considered to mimic e.g., a St. Peter's Square in Vatican City or any other large city square (see Fig. 3.7). UAV nodes randomly pass through the square at certain speeds and heights. The static mmWave infrastructure is represented by a single mmWave AP at the side of the square. For such a scenario, a single mmWave AP is sufficient to handle infrequent data transmissions from the pedestrians in regular operation but is completely inadequate during the peak hours related e.g., to the Pope elections or similar events. In our setup, the passing UAVs assist the mmWave network by relaying the backhaul traffic from COW vehicles to the stationary mmWave AP. The tool can be further extended to analyze other scenarios of opportunistic mmWave UAV relaying, e.g., focused on the UAV assisting in the mmWave access.

The contributed framework models the mmWave-specific physical layer by following the corresponding 3GPP guidelines. We particularly employed the detailed multi-path channel model for directional mmWave communications presented by 3GPP in [1]. Our simulation tool has been primarily implemented in Python and models the network operation at the session level. Hence, all the essential aspects have been considered, such as (i) session arrival and departure processes, (ii) mobility of flying UAVs, and (iii) complex process of the moving crowd temporarily blocking the 3D link between a static COW vehicle and a flying UAV.

The developed tool is applied to quantify the gains brought by UAV-based mmWave relays in the target scenario. Several observations important for future studies on the topic have been made in [26]. Particularly, we note that when assistance from the UAV-based mmWave relays is entirely opportunistic, visible performance gains are observed only for high densities of drones in the area: at least *five* drones appearing every minute. However, such densities of mmWave-capable UAVs will not appear at the early stages of the mmWave technology development.

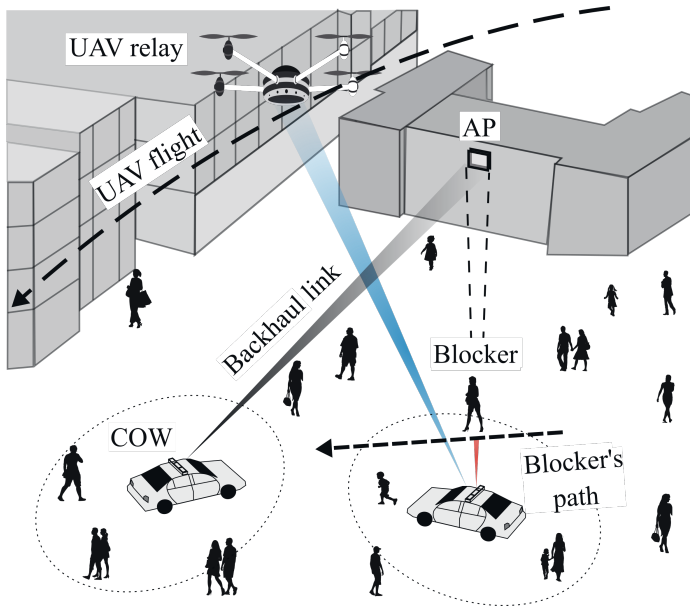


Figure 3.7. Opportunistic relaying of mmWave links by flying UAVs.

In contrast, the achievable gains become considerably higher with a certain level of operator’s involvement. Particularly, when the network operator is able to enforce certain heights and cruising speeds for the drones flying over the service area, the average duration of an outage experienced by a COW vehicle decreases by almost two times, while the SE of the backhaul mmWave link increases by over 40%. Hence, we conclude our study by advocating that opportunistic UAV relaying in mmWave communications is beneficial only with a certain level of operator’s involvement in determining the trajectories of the assisting drones.

3.4.3 Modeling mmWave communications with UAV-based APs

While limited flight time on batteries is a secondary problem for the network operators when dealing with opportunistic relaying, the battery constraints become crucial when the operator starts managing its fleet of UAV-based APs. Correspondingly, there is a need to consider the battery factor in the performance evaluation frameworks. Several approaches have been proposed to date aiming to account for UAV batteries running low in *microwave* UAV networks, including [43], [63], and [108], among others. We complement these activities in [74] by contributing a novel math-

emtical framework to analyze the performance of *mm Wave* UAV communications. Particularly, we explore the network performance achievable with a fleet of several operator-controlled UAV-based mmWave APs.

The contributed framework is built using the tools from stochastic geometry, probability theory, and the analysis of renewal processes. A service area with a uniform deployment of mmWave UEs is modeled at a given distance from the drone charging station. Each of the UAVs follows an operation cycle with three main stages: (i) serving the target UEs in the service area; (ii) charging the battery at the charging station; and (iii) flying between these two locations.

Our framework consists of two parts. The first part is focused on studying the characteristics of the mmWave wireless links between the UEs and their nearest UAV-based APs in the service area. Here, the 3D distance between the UAV and the selected UE determines the characteristics of the mmWave link. The altitude of the UAV operation also impacts the performance, as the altitude not only contributes to the said 3D distance but also determines the probability of the directional mmWave link to be occluded by the human crowd surrounding the UE.

The second part of the analysis is used to characterize the battery consumption process by a UAV-based mmWave AP. Initially, the fraction of time that the drone can serve UEs is calculated. Then, the number of UAV-based mmWave APs that can simultaneously be present in the service area is determined from the said fraction and the total size of the drone fleet. Finally, we combine the two parts of our analysis to derive the UE-centric and network-centric performance characteristics, such as the mean UE SE and the mean capacity of the constructed mmWave UAV network.

As one of the results, the mean capacity of the network formed by N airborne mmWave APs, \bar{C}_A , is characterized with the following equation:

$$\bar{C}_A = B \lfloor N \rho_A \rfloor \int_0^R \left(p_B(x) \log_2 \left(1 + P_B(x) / (N_0 N_F) \right) + [1 - p_B(x)] \log_2 \left(1 + P_N(x) / (N_0 N_F) \right) \right) f_{X_A}(x) dx, \quad (3.4)$$

where B , N_0 , and N_F stand for the system bandwidth and the noise levels, respectively, $p_B(x)$ represents the blockage probability of the directional link between the UE and its nearest UAV-based AP, $P_B(x)$ and $P_N(x)$ characterize the received power of the mmWave signal in blocked and non-blocked conditions of the directional link, while R is the radius of the service area.

The contributed framework can be elaborated to model other deployment scenarios (e.g., with multiple service areas) and directional communications over the THz frequencies. Our framework can also be further extended to account for different considerations regarding the UAV backhaul, as well as a possible presence of terrestrial mmWave APs.

3.4.4 Comparing deployment options for UAV-based APs

The current state-of-the-art in battery technology and, consequently, the short UAV flight time on batteries, are the limiting factors for the development of mmWave drone cells [108]. In addition, the flying UAV-based mmWave APs raise concerns related to safety and noise pollution when hovering over people's heads. To partially address these issues, an alternative deployment option may be considered suggesting the UAV-based mmWave APs to land on the buildings and other objects (e.g., lamp-posts) surrounding the service area. Following this approach, the UAVs may switch off their motors during the entire AP service time and use them exclusively for the flights between the service area and the charging station. Today, the motors are the primary source of UAV energy consumption. Therefore, the landed deployment option may result in considerable improvements of the drone battery lifetime.

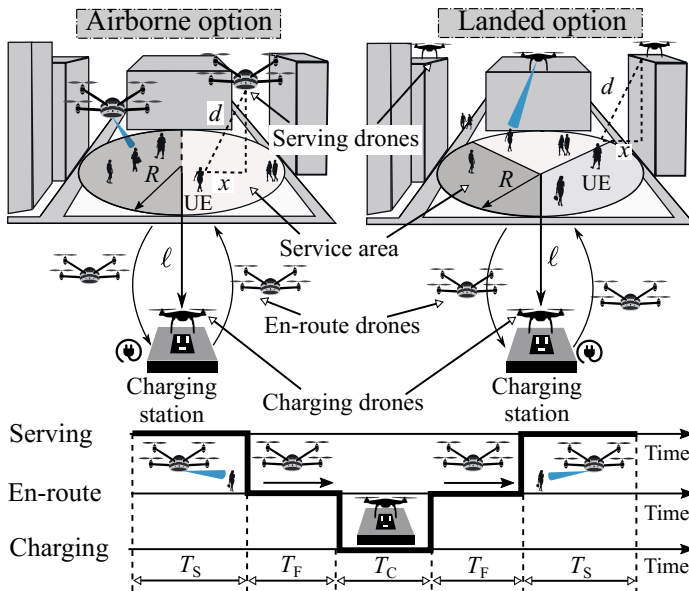


Figure 3.8. Comparing airborne and landed deployment options for UAV-based mmWave APs.

Motivated by the listed advantages, we apply our mathematical framework developed in [74], to compare the performance levels achievable with UAV-based mmWave APs when following either airborne or landed deployment options (see Fig. 3.8). Accounting for the landed deployment option requires minor modifications to be introduced in our mathematical framework. Particularly, the deployment of landed UAVs around the service area affects the separation distances between the UEs and their nearest drones. Therefore, the evaluation of the directional mmWave link is modified accordingly. We also introduce the changes to the second part of our framework that enables accounting for the UAV engines off when serving the UEs.

Several key observations are made in the numerical comparison of the performance brought by UAV-based mmWave APs with either airborne or landed deployments [74]. First, our study highlights a clear trade-off between the options. The airborne deployment features better characteristics of the mmWave channel, as the hovering UAVs can locate closer to the target users. In contrast, the landed option leads to a considerably higher UAV lifetime on batteries. Therefore, with the same size of the drone fleet, a higher number of UAVs can continuously be present in the service area.

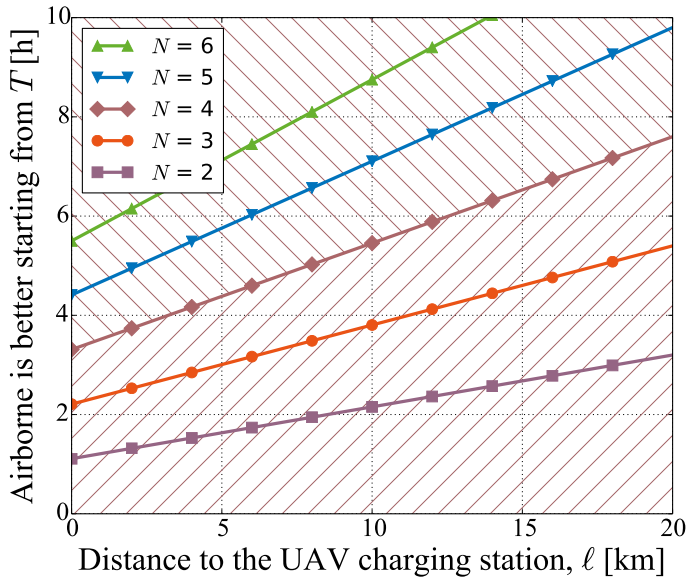


Figure 3.9. Key trade-offs for “Airborne vs. Landed” deployment of UAV-based mmWave APs [74].

Our numerical study in [74] also reveals that the key factors determining the

preferable deployment options (airborne or landed) are: (i) the distance to the UAV charging station; (ii) the UAV flight time on batteries; and (iii) the size of the drone fleet. The interplay between these parameters is presented in Fig. 3.9, where any setup above the target line should be served with airborne UAVs, while the configurations below the line will achieve higher network capacity with the landed option.

Continuing with Fig. 3.9, the airborne option appears to be more attractive in easy scenarios: small sizes of the drone fleet, short distance between the service area and the drone charging station, together with a high UAV flight time on batteries. In contrast, more challenging setups (e.g., with a distant service area or only a few drones available) call for the landed option. Our contributed framework and results can be used to determine the system design choices when utilizing the drone-cells in emerging mmWave networks.

4 APPLICATION-SPECIFIC ASPECTS OF DIRECTIONAL COMMUNICATIONS

4.1 Research Motivation

The studies presented in the previous two chapters illustrated that the use of directional communications calls for novel methods and tools to evaluate the network characteristics in both general and use case-specific scenarios. However, the peculiarities of directional links should also be accounted for when developing practical solutions for the PHY, medium access control (MAC), and higher layers of emerging wireless networks.

To date, there have been multiple studies highlighting different research problems in this area. Particularly, directional communications with mobile nodes call for advanced beam tracking techniques [44, 69]. Node discovery and initial network entry also become considerably more challenging when operating exclusively over directional links [114]. To address these problems, a novel solution has been proposed in [118] suggesting to utilize the side lobes of the directional antenna radiation pattern for the node discovery. Substantial resources have been invested by the 3GPP and the IEEE towards the construction of directional MAC for their NR and IEEE 802.11ad/ay technologies. Recently, the negative effects of directional communications on the TCP performance were explored in [123], among others.

In the present chapter, we aim to complement the research in this field. For this purpose, we propose and evaluate two approaches exploiting the properties of directional communications in the design of future wireless systems. Particularly, in Section 4.2, we target the mitigation of interference in mmWave and THz band vehicular networks. Later, in Section 4.3, we describe and analyze solutions to maintain the security of directional communications already at the physical layer.

4.2 Interference Mitigation in Vehicular Networks

4.2.1 Impact of interference in vehicular networks

As discussed in Chapter 2, the use of directional communications can reduce the impact of interference in emerging wireless networks. However, interference from other nodes is still non-negligible in many practical scenarios, thus challenging the reliability and performance of the wireless systems [95, 100]. According to our analysis in [75], mmWave and THz band *vehicular* communications appear to be particularly vulnerable to the interference, as the uncoordinated transmissions coming from the vehicles in neighboring lanes drastically reduce the network performance. To mitigate this inter-lane interference, a certain level of coordination between the connected cars is needed.

There are two major approaches to coordinate the transmissions in a vehicular network. The first approach relies on a centralized control via e.g., a cellular interface. An illustrative example here is the development of the 3GPP *sidelink* technology for their NR Release 15 and beyond [3, 23]. With the use of this technology, certain radio resources are allocated for direct vehicle-to-vehicle (V2V) interactions. The cellular-controlled communications feature high reliability and performance levels in the presence of sufficiently dense cellular infrastructure [107, 120]. On the other side, the cellular-assisted data exchange becomes unreliable under intermittent cellular connectivity, thus limiting the scope of possible use cases.

The second approach is focused on building a distributed coordination function (DCF) among the vehicles and can thus work without any centralized control. An illustrative example here is the adaptation of the IEEE 802.11 to vehicular communications termed as the IEEE 802.11p [46]. This amendment supports data exchange between the vehicles in the wireless channel at 5.9 GHz. Unfortunately, the solution cannot be directly exploited for directional communications in the mmWave and THz bands. The key problem here is that the 802.11-driven MAC is based on the carrier sense multiple access with collision avoidance (CSMA/CA): the node about to transmit first senses the channel to ensure there is no active transmission in range to collide with.

With directional communications, the use of a conventional CSMA/CA technique has certain limitations. Particularly, the node about to transmit (Tx 1) may

miss an ongoing transmission from another Tx nearby (Tx 2), e.g., when the Tx 1 is located outside the Tx 2 beam. Hence, when located outside of each other's beams, Tx 1 and Tx 2 may initiate transmissions to the same Rx node and thus collide if their transmissions overlap in time. The described effect is often referred to as *directional deafness* or *the deafness problem*.

The deafness problem is one of the crucial challenges in the design of directional MAC solutions. According to prior studies (e.g., in [19] and [96], among others), deafness problem considerably reduces the performance achievable in the wireless networks with directional communications. At the same time, vehicular deployments have specific differences from the open environments with point Tx and Rx nodes typically considered in the deafness-related studies. In this section, we propose and evaluate an approach to exploit the properties of the vehicle-centric deployments and thus partially mitigate the deafness problem in directional vehicular communications.

4.2.2 Mitigating deafness in directional vehicular communications

Vehicle-centric communication scenarios have several features that are different from the general wireless access networks focused primarily on handheld and wearable devices. First, vehicle mobility is more predictable than that of a handheld device. Particularly, during regular operation, the vehicle is unlikely to experience unexpected 3D rotations that would change the orientation of the directional antenna system. Second, as measured in [71] and other works, the power of the signals at mmWave and THz frequencies substantially degrade when penetrating through the vehicle body at the engine and doors height. Hence, the vehicle body is a potent blocker of the mmWave and THz band radiation.

Finally, a considerable part of the signal power blocked by the vehicle body is reflected [71, 75]. Particularly, if the directional antenna arrays are mounted on the front and rear bumpers of the vehicles (e.g., to facilitate direct V2V communications), a part of the signal transmitted forward from the front antenna of the Tx 1 car in Fig. 4.1 will reflect from the rear of the Rx vehicle. The same applies to the transmissions from the rear antenna directed backward – a part of the energy is reflected from the front of the car behind.

Our conceptual approach suggests utilizing these reflected signals to perform the

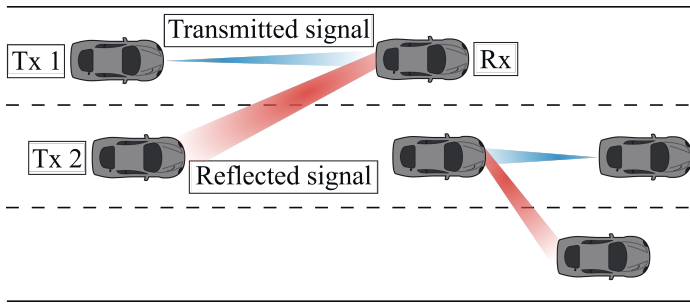


Figure 4.1. Signal reflections from vehicle body in directional V2V communications.

channel sensing and, consequently, enable the distributed coordination of the vehicular transmissions. It is important to note that before reaching Tx 2 in Fig. 4.1, the signal transmitted from Tx 1 is attenuated not only by the reflection losses but also by additional propagation losses. Hence, the received power and SNR at Tx 2 are considerably lower than those at the target Rx. Therefore, conventional mechanisms from 802.11-family standards (such as those based on the energy detection or frame header decoding) are not sufficiently robust to detect such transmissions.

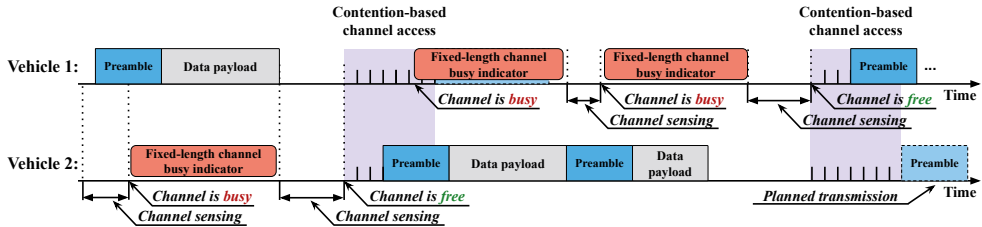


Figure 4.2. Coordinated channel access in vehicular networks.

We propose to address this challenge by using additional preambles injected into the transmitted frame with a fixed periodicity, termed as *inter-preamble interval*, as illustrated in Fig. 4.2. Our motivation here is that preamble-based detection is considerably more reliable than conventional frame header decoding and thus allows operating even in the regimes having extremely low SNR levels [56]. By following this approach, Tx 2 can perform the channel sensing as follows: if Tx 2 about to transmit detects at least one preamble during the inter-preamble interval, the channel is considered busy and the transmission is postponed. Whenever Tx 2 about to transmit does not detect any preambles during the inter-preamble interval, the channel is considered idle, and Tx 2 starts its transmission.

The proposed conceptual approach allows to partially address the deafness problem in directional vehicular communications, as the vehicle *can* now detect an ongoing transmission even when located outside of the neighbor's Tx beam. Hence, the number of collided transmissions is envisioned to reduce. It is also worthwhile to note that the implementation of the proposed approach does not require any substantial modifications in the existing radio technology signaling. However, the introduction of additional preambles into the transmitted frames brings overheads, thus challenging the system performance. Therefore, an evaluation study is needed to quantify both the advantages and the issues brought by our approach. We present a first-order analysis of our proposal, termed as *Directional carrier sense multiple access (CSMA)*, in the following subsection.

4.2.3 Performance improvements with coordinated transmissions

The conceptual approach presented in the previous subsection aims to reduce the number of collisions in directional vehicular communications. However, the proposed approach introduces additional overheads to the underlying channel access protocol. Therefore, a careful study is needed to explore if the brought improvements dominate the shortcomings caused by the additional signaling. For this purpose, we evaluate the proposed access scheme with a compound measurement-simulation methodology contributed in [73].

Particularly, a wide city avenue is considered with three lanes in each of the directions and a randomized deployment of vehicles. We model a directional communication link at 300 GHz between the two neighboring vehicles in the middle lane. The link is thus vulnerable to the directional interference coming from both the left and the right lanes (see Fig. 4.1). Our evaluation study is divided into two stages. At the first stage, a measurement campaign is conducted to characterize the reflection properties of the typical materials present in vehicular scenarios, such as aluminum, glass, and plastic.

At the second stage of our framework, the data measured during the first stage serve as the input when modeling the signal propagation in the considered vehicular environment using our in-house ray-based modeler introduced in [76]. Later, the propagation data obtained with the ray-based modeler are used to characterize vehicular communications at the PHY layer. The obtained PHY-layer characteris-

tics are finally exploited when performing system-level computer simulations of the described scenario.

With the use of our evaluation framework, the performance of the proposed approach is compared with the performance of other possible solutions for the channel access in directional vehicular communications, such as:

- *Idealistic*. Theoretical upper bound. Perfect time-division multiple access (TDMA) with an oracle.
- *Uncoordinated*. ALOHA-based uncoordinated random access.
- *Adaptive access*. Modification of the previous solution, where vehicles perform binary exponential backoff in the case of a collision.

Fig. 4.3 illustrates the SE of the directional V2V link as a function of the distance between the interacting vehicles. As observed in this figure, the proposed *Directional CSMA* approach results in an SE higher than those offered by *Uncoordinated* and *Adaptive* schemes. In addition, our approach considerably extends the communication range between the vehicles as the distance where the SINR drops below 10 dB is around 30% greater than the one offered by the *Uncoordinated* scheme.

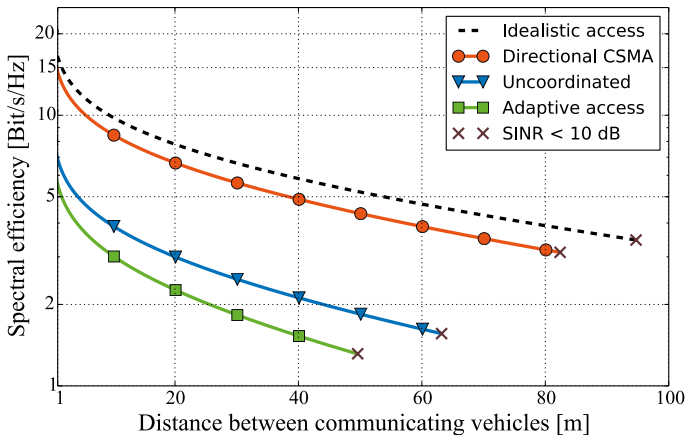


Figure 4.3. SE of mmWave V2V system with Directional CSMA [73].

Finally, we observe that a gap is insignificant between the results reported for our Directional CSMA and those for the idealistic access. Hence, the proposed conceptual approach demonstrates the performance close to the estimated theoretical upper bound. At the same time, as detailed in [73], the performance of our proposal heavily depends on the robustness of the introduced preambles. Particularly, the SINR at

the receiver decreases by almost 30% when the preamble detection probability drops from 99% down to 80%. Therefore, the design of robust preamble sequences to accommodate the described concept is an important research problem to be resolved in the future studies.

Summarizing, as illustrated in this section, the deafness problem can be partially addressed in directional vehicular communications by exploiting the reflections of mmWave or THz band signal from the vehicle bodies. It is important to note that there are multiple research questions to be addressed before the proposed conceptual design can be converted into a concrete engineering solution. These are the design of robust preamble sequences and optimization of the inter-preamble interval, among others. The presented evaluation framework should be further extended to model more sophisticated scenarios, involving e.g., street intersections, traffic lights, pedestrians, etc. Nevertheless, the study performed in this section outlines one of the possible research directions for future vehicular networks. Hence, the presented approach and the contributed evaluation framework serve as building blocks towards the design of reliable and efficient vehicular communication systems.

4.3 Improving Security with Directional Transmissions

4.3.1 Physical-layer security with directional communications

Directional communications bring not only novel challenges but also new opportunities for the design of future wireless systems. Particularly, the use of narrow beams propagating in a specified direction improves the confidentiality of data exchange. As illustrated in [87], specific encoding techniques can be successfully applied to guarantee the *secrecy* of the transmission whenever the difference in the SNR levels at the target Rx node and the attacking node is non-negligible.

Therefore, in most of the cases, the attacking node (or *Attacker*) must be physically located either inside the transmit beam or close to the Rx node to successfully eavesdrop the message. In contrast, omnidirectional transmissions can be eavesdropped by an Attacker located far away from both the Tx and Rx nodes [125]. Hence, directional communications provide additional protection for the transmitted data already at the PHY layer.

At the same time, as noted in [61], even the extremely-directional transmissions

in the THz band can still suffer from the eavesdropping when only a single propagation path is used for communications. In response to the vulnerability highlighted in [61], in this section, we describe and evaluate the concept of enhanced physical-layer security for directional communications. Particularly, multi-beam transmissions at the mmWave and THz frequencies are exploited in our approach, as further detailed in the subsection below.

4.3.2 Enhancing security levels with multi-path transmissions

The principal idea behind our *multi-path* security scheme introduced in [81] is based on the fact that there might be more than one available path for directional communications in typical environments. Besides the LoS path, the objects surrounding the communicating entities (building walls, etc.) can be used to enable other propagation paths e.g., via one or more reflections. These reflected paths are expected to be featured by more significant path loss and, consequently, lower SNR, in comparison to the LoS path. At the same time, as illustrated in prior studies [52, 53, 54], both mmWave and THz band communications can still be performed over a reflected path with lower performance levels.

In the presence of M communication paths currently available, our approach, termed as a *multi-path* scheme, suggests splitting the message into M shares (see Fig. 4.4). Each of the shares is to be transmitted over a different communication path. An additional security-oriented encoding is applied before the transmission so that the Rx node can decode the message only if all its shares are successfully received [116]. By following this approach, the Rx node located in the intersection of *all* the communication paths towards this node is capable to decode the message as long as all the transmissions are successful. In contrast, any Attacker located near the Rx node can decode only *some* of the message shares and thus is not able to decode the entire message.

The solution described above is envisioned to further improve the security of directional communications, as eavesdropping all the message shares becomes more difficult. At the same time, the implementation of the presented approach increases the complexity of the underlying communication algorithms and protocols. In addition, the link capacity is also about to decrease with the multi-path scheme, as the data transmission is performed not via the best available path, but rather split be-

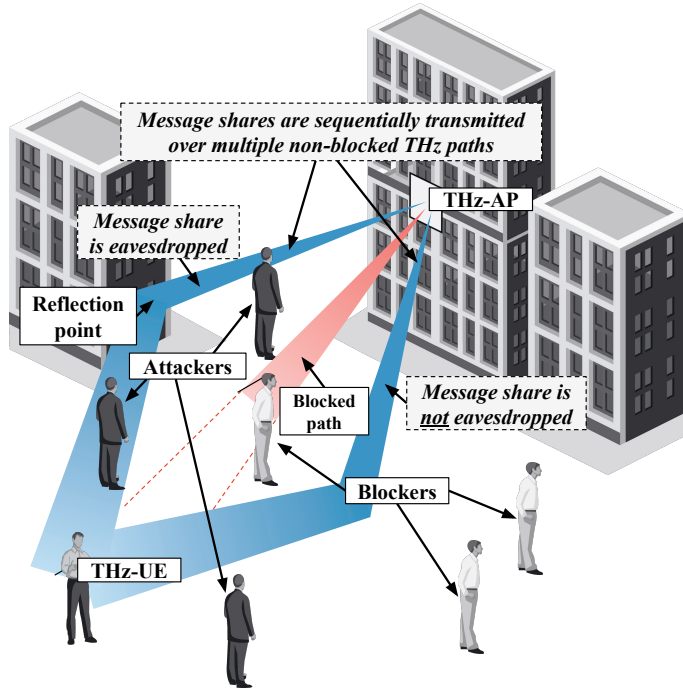


Figure 4.4. Secure directional communications in urban deployments.

tween multiple paths with worse characteristics. Therefore, an in-depth analysis is needed to investigate the trade-offs between the introduced security improvements and the associated capacity reductions. A first-order analysis of the dependencies between the security-centric and the capacity-centric metrics brought by the multi-path strategy is presented in the following subsection.

4.3.3 Analyzing trade-offs between capacity and security

To study the introduced trade-offs between the security and performance of directional communications brought by the *multi-path* scheme, a mathematical framework has been developed in [81]. The framework utilizes the tools from stochastic geometry and probability theory to characterize a directional link between a stationary AP and a stationary UE in an urban environment. The target UE is surrounded by a human crowd, so the link also is interrupted by dynamic blockage. Both the baseline *single-path* scheme (the data is transmitted via the best available link) and the presented *multi-path* schemes are analyzed.

For illustration, we assume wireless communications between the AP and the UE to be performed in the THz band, thus utilizing extremely-directional beams. Accordingly, multi-path propagation of the THz signal is modeled assuming a cone antenna radiation pattern at the AP. We particularly focus on the downlink in our study, while the analysis for the uplink can be performed by a direct extension of the contributed methodology. Similar to [1], the UE has multiple alternative signal paths to interact with the AP (see Fig. 4.4). We approximate the spatial and performance-related characteristics of these links using the model proposed in [28]

For the security analysis, a random field of Attackers is deployed with a certain density around the target UE. Any Attacker can eavesdrop all the data traffic from the AP to the UE, whenever the Attacker is located within the AP beam. We particularly focus on the most challenging scenario, where all the Attackers cooperate: the data eavesdropped by one of the Attackers become available to all the Attackers.

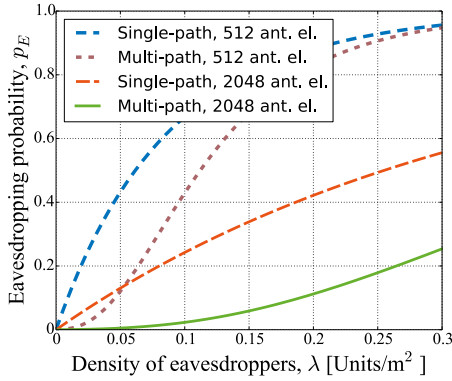
For the considered setup, both the security-centric and the performance-centric metrics of interest are derived with the use of our mathematical framework. Particularly, the capacity with the multi-path scheme, $C(x)$, in the presence of M signal paths is approximated by the following equation:

$$C(x) = \frac{1 - p_B^M}{M} \sum_{i=1}^M C_i(x), \quad (4.1)$$

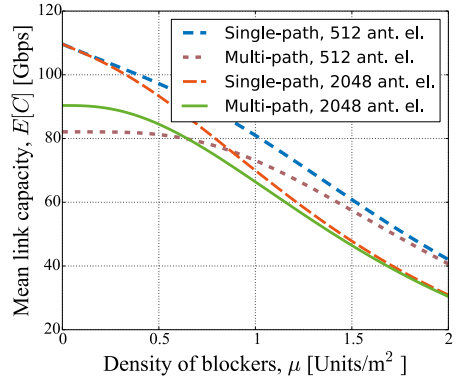
where x is the 2D separation distance between the UE and the AP, p_B represents the blockage probability of the signal path, while $C_i(x)$ stands for the capacities of the THz links over individual paths. In contrast, other key metrics are characterized by more complex expressions, as detailed in [81].

The revealed trade-offs between the eavesdropping probability and the link capacity are illustrated in Fig. 4.5. It is observed that the use of the multi-path scheme decreases the eavesdropping probability *by up to 10 times*. Simultaneously, the capacity of the THz link decreases by not more than 25%. Assuming that the underline solutions for advanced beam tracking bring relatively low overheads, the multi-path scheme is thus considered beneficial for emerging THz communications, especially when an additional level of security is demanded.

At the same time, the performance of the THz communications decreases non-negligibly with the presented security enhancement and is envisioned to decrease even further when the beam tracking and protocol overheads are taken into account.



(a) Eavesdropping probability



(b) Capacity of THz communications

Figure 4.5. “Security vs. capacity” trade-off brought by multi-path THz communications [81].

Therefore, we propose utilizing the multi-path scheme selectively, e.g., to improve the security of sensitive data. Another possible use of the described solution is to additionally secure the exchange of the session encryption keys, while the baseline single-path scheme featured by a higher performance can then be used for all the further interactions.

The wireless communications are involved more and more in everyday life, so maintaining secure delivery of sensitive data becomes one of the critical targets for the system design. As illustrated in this section, directional communications can assist by providing an additional level of security already at the PHY layer. Within this research direction, the presented multi-path scheme, as well as the contributed evaluation framework, may facilitate the design of prospective mmWave and THz band systems deeply integrated into future wireless networks.

5 CONCLUSIONS AND FUTURE WORK

5.1 Summary

In this thesis, a set of mathematical frameworks and simulation tools has been developed to characterize the performance of directional wireless communications in the mmWave and THz frequency bands. The introduced solutions were applied to evaluate the characteristics of mmWave and THz systems in different prospective usage scenarios. Finally, certain technological enhancements for mmWave and THz communication networks have been presented and analyzed with the contributed evaluation frameworks.

The study performed in this thesis has led to the following main conclusions:

1. The informed selection of the beamwidth in directional communications in the mmWave and THz bands is essential. It was observed that the use of narrow beams challenges the link reliability in mobile environments, while wide beams cause substantial levels of interference on neighboring nodes.
2. The performance of mmWave wireless access networks can be considerably improved with the assistance from vehicle-based and UAV-based mmWave relays. The theoretical performance gains reach 100% and more.
3. The drone battery is one of the most important limitations in mmWave UAV networking. Particularly, when the fleet of UAV-based mmWave APs is utilized to temporarily boost the network capacity in a certain area, the landed deployment option surpasses the airborne layout in the majority of possible configurations.
4. Directional communications in the mmWave and THz bands can bring advantages to the applications and services running over these communications. As an example, an enhanced level of confidentiality can be provided to the data

exchange with an intelligent combining of multiple highly-directional transmissions in the THz band.

5.2 Future Work

The performed study has also identified several directions in which the research on mmWave and THz communication systems will continue progressing:

Dynamic 3D mm Wave networks. Active exploitation of the link spatial diversity may lead to the emergence of complex highly-dynamic 3D network topologies with multi-hop directional communications between heterogeneous entities, including handheld devices, wearable, and, later, implantable electronics, smart vehicles, and connected UAVs. Accordingly, a notable extension of the modeling tools will be needed, where the frameworks presented in Chapter 3 can serve as individual building blocks.

Focus on energy-efficiency. As the initial phase of the mmWave networks development is completed, the energy limitations at both the user devices (e.g., handheld and wearable) and the network equipment become a critical research problem to address. Massive deployments of mmWave small cells and ubiquitous penetration of mmWave UEs are infeasible without considerable improvements in power consumption. As a part of this work, the corresponding modeling tools (e.g., those described in Chapter 3) should be enhanced to account for the energy constraints together with the conventional coverage- and capacity-centric characteristics.

Mobile THz networks. Going higher in frequency, the further development of high-rate wireless communications in the THz band is envisioned. The first-generation THz systems primarily target the use cases with no or limited node mobility (e.g., backhaul links and kiosk download, as in [47]). On top of these, new solutions offering THz connectivity with mobile devices will appear. In response to this trend, the performance evaluation frameworks for THz communications, including those provided in Chapter 2, should be further extended to carefully model the combined macro- and micro-mobility of the connected devices.

Novel usage scenarios for mm Wave and THz communications. A continuation of research on this topic is also envisioned to result in revisiting the existing methods to build a wireless network. For instance, the limited range of THz small cells can still be exploited by strategically deploying THz data showers to deliver the

cached traffic instead of targeting a continuous THz connectivity [82]. Expensive phased arrays for mmWave and THz communication systems can also be utilized for high-resolution radar sensing, e.g., in vehicular scenarios [56]. New beam tracking solutions to follow mobile nodes not only increase the complexity of the radio equipment but also enable determining the 3D location and orientation of the connected devices without assistance from the satellites [117]. Hence, the emergence of mmWave and THz communications will lead to further innovations in wireless systems.

REFERENCES

- [1] 3GPP. *Study on channel model for frequencies from 0.5 to 100 GHz (Release 16)*. 3GPP TR 38.901 V16.1.0. Jan. 2020.
- [2] 3GPP. *Study on enhanced LTE support for aerial vehicles (Release 15)*. TR 36.777 V15.0.0. Jan. 2018.
- [3] 3GPP. *Vehicle to Vehicle (V2V) services based on LTE sidelink; User Equipment (UE) radio transmission and reception*. 3GPP TR 36.785 V14.0.0. Oct. 2016.
- [4] M. R. Akdeniz, Y. Liu, M. K. Samimi, S. Sun, S. Rangan, T. S. Rappaport and E. Erkip. Millimeter wave channel modeling and cellular capacity evaluation. *IEEE Journal on Selected Areas in Communications* 32.6 (2014), 1164–1179.
- [5] I. F. Akyildiz, J. M. Jornet and C. Han. TeraNets: Ultra-broadband communication networks in the terahertz band. *IEEE Wireless Communications* 21.4 (2014), 130–135.
- [6] I. F. Akyildiz and J. M. Jornet. Realizing ultra-massive MIMO (1024x1024) communication in the (0.06–10) terahertz band. *Nano Communication Networks* 8 (2016), 46–54.
- [7] I. F. Akyildiz, J. M. Jornet and C. Han. Terahertz band: Next frontier for wireless communications. *Physical Communication* 12 (2014), 16–32.
- [8] S. Andreev, V. Petrov, M. Dohler and H. Yanikomeroglu. Future of ultra-dense networks beyond 5G: Harnessing heterogeneous moving cells. *IEEE Communications Magazine* 57.6 (2019), 86–92.
- [9] S. Andreev, V. Petrov, K. Huang, M. A. Lema and M. Dohler. Dense moving fog for intelligent IoT: Key challenges and opportunities. *IEEE Communications Magazine* 57.5 (2019), 34–41.

- [10] J. G. Andrews, T. Bai, M. N. Kulkarni, A. Alkhateeb, A. K. Gupta and R. W. Heath. Modeling and analyzing millimeter wave cellular systems. *IEEE Transactions on Communications* 65.1 (2017), 403–430.
- [11] J. G. Andrews, S. Buzzi, W. Choi, S. V. Hanly, A. Lozano, A. C. K. Soong and J. C. Zhang. What will 5G be?: *IEEE Journal on Selected Areas in Communications* 32.6 (2014), 1065–1082.
- [12] *Annual Internet Report (2018–2023) White paper*. 2020. URL: <https://www.cisco.com/c/en/us/solutions/collateral/executive-perspectives/annual-internet-report/white-paper-c11-741490.pdf> (visited on 04/05/2020).
- [13] T. Bai and R. W. Heath. Coverage in dense millimeter wave cellular networks. *Proc. of Asilomar Conference on Signals, Systems and Computers*. 2013, 2062–2066.
- [14] F. Boccardi, R. W. Heath, A. Lozano, T. L. Marzetta and P. Popovski. Five disruptive technology directions for 5G. *IEEE Communications Magazine* 52.2 (2014), 74–80.
- [15] R. Bonjour, M. Singleton, S. A. Gebrewold, Y. Salamin, F. C. Abrecht, B. Baeuerle, A. Josten, P. Leuchtman, C. Hafner and J. Leuthold. Ultra-fast millimeter wave beam steering. *IEEE Journal of Quantum Electronics* 52.1 (2016), 1–8.
- [16] P. Boronin, V. Petrov, D. Moltchanov, Y. Koucheryavy and J. M. Jornet. Capacity and throughput analysis of nanoscale machine communication through transparency windows in the terahertz band. *Nano Communication Networks* 5.3 (2014), 72–82.
- [17] A. A. Boulogeorgos, A. Alexiou, T. Merkle, C. Schubert, R. Elschner, A. Katsiotis, P. Stavrianos, D. Kritharidis, P. Chartsias, J. Kokkonniemi, M. Juntti, J. Lehtomaki, A. Teixeira and F. Rodrigues. Terahertz technologies to deliver optical network quality of experience in wireless systems beyond 5G. *IEEE Communications Magazine* 56.6 (2018), 144–151.
- [18] J. Choi, V. Va, N. Gonzalez-Prelcic, R. Daniels, C. R. Bhat and R. W. Heath. Millimeter-wave vehicular communication to support massive automotive sensing. *IEEE Communications Magazine* 54.12 (2016), 160–167.

- [19] O. Chukhno, N. Chukhno, O. Galinina, Y. Gaidamaka, S. Andreev and K. Samouylov. Analysis of 3D deafness effects in highly directional mmWave communications. *Proc. of IEEE Global Communications Conference (IEEE GLOBECOM)*. 2019, 1–6.
- [20] K. David and H. Berndt. 6G vision and requirements: Is there any need for Beyond 5G?: *IEEE Vehicular Technology Magazine* 13.3 (2018), 72–80.
- [21] N. Deng, M. Haenggi and Y. Sun. Millimeter-wave device-to-device networks with heterogeneous antenna arrays. *IEEE Transactions on Communications* 66.9 (2018), 4271–4285.
- [22] M. Dohler, R. W. Heath, A. Lozano, C. B. Papadias and R. A. Valenzuela. Is the PHY layer dead?: *IEEE Communications Magazine* 49.4 (2011), 159–165.
- [23] G. Fodor, H. Do, S. A. Ashraf, R. Blasco, W. Sun, M. Belleschi and L. Hu. Supporting enhanced vehicle-to-everything services by LTE Release 15 systems. *IEEE Communications Standards Magazine* 3.1 (2019), 26–33.
- [24] M. Gapeyenko, I. Bor-Yaliniz, S. Andreev, H. Yanikomeroglu and Y. Koucheryavy. Effects of blockage in deploying mmWave drone base stations for 5G networks and beyond. *Proc. of IEEE International Conference on Communications Workshops (IEEE ICC Workshops)*. 2018, 1–6.
- [25] M. Gapeyenko, V. Petrov, D. Moltchanov, M. R. Akdeniz, S. Andreev, N. Himayat and Y. Koucheryavy. On the degree of multi-connectivity in 5G millimeter-wave cellular urban deployments. *IEEE Transactions on Vehicular Technology* 68.2 (2019), 1973–1978.
- [26] M. Gapeyenko, V. Petrov, D. Moltchanov, S. Andreev, N. Himayat and Y. Koucheryavy. Flexible and Reliable UAV-Assisted Backhaul Operation in 5G mmWave Cellular Networks. *IEEE Journal on Selected Areas in Communications* 36.11 (Nov. 2018), 2486–2496.
- [27] M. Gapeyenko, A. Samouylov, M. Gerasimenko, D. Moltchanov, S. Singh, M. R. Akdeniz, E. Aryafar, N. Himayat, S. Andreev and Y. Koucheryavy. On the temporal effects of mobile blockers in urban millimeter-wave cellular scenarios. *IEEE Transactions on Vehicular Technology* 66.11 (2017), 10124–10138.

- [28] M. Gapeyenko, V. Petrov, D. Moltchanov, S. Andreev, Y. Koucheryavy, M. Valkama, M. R. Akdeniz and N. Himayat. An analytical representation of the 3GPP 3D channel model parameters for mmWave bands. *Proc. of the 2nd ACM Workshop on Millimeter Wave Networks and Sensing Systems (mmNets)*. 2018, 33–38.
- [29] M. Gerasimenko, D. Moltchanov, M. Gapeyenko, S. Andreev and Y. Koucheryavy. Capacity of multiconnectivity mmWave systems with dynamic blockage and directional antennas. *IEEE Transactions on Vehicular Technology* 68.4 (2019), 3534–3549.
- [30] H. Ghazzai, M. Ben Ghorbel, A. Kessler and M. J. Hossain. Trajectory optimization for cooperative dual-band UAV swarms. *Proc. of IEEE Global Communications Conference (IEEE GLOBECOM)*. 2018, 1–7.
- [31] M. Giordani, M. Mezzavilla, S. Rangan and M. Zorzi. Multi-connectivity in 5G mmWave cellular networks. *Proc. of Mediterranean Ad Hoc Networking Workshop (Med-Hoc-Net)*. 2016, 1–7.
- [32] M. Giordani, M. Polese, M. Mezzavilla, S. Rangan and M. Zorzi. Toward 6G networks: Use cases and technologies. *IEEE Communications Magazine* 58.3 (2020), 55–61.
- [33] I. Gordon et al. The HITRAN2016 molecular spectroscopic database. *Journal of Quantitative Spectroscopy and Radiative Transfer* 203 (2017), 3–69.
- [34] K. Guan, B. Ai, M. Liso Nicolas, R. Geise, A. Moller, Z. Zhong and T. Kurner. On the influence of scattering from traffic signs in Vehicle-to-X communications. *IEEE Transactions on Vehicular Technology* 65.8 (2016), 5835–5849.
- [35] A. K. Gupta, X. Zhang and J. G. Andrews. SINR and throughput scaling in ultradense urban cellular networks. *IEEE Wireless Communications Letters* 4.6 (2015), 605–608.
- [36] L. Gupta, R. Jain and G. Vaszkun. Survey of important issues in UAV communication networks. *IEEE Communications Surveys and Tutorials* 18.2 (2016), 1123–1152.
- [37] M. Haenggi. Mean interference in hard-core wireless networks. *IEEE Communications Letters* 15.8 (2011), 792–794.

- [38] M. K. Haider and E. W. Knightly. Mobility resilience and overhead constrained adaptation in directional 60 GHz WLANs: Protocol design and system implementation. *Proc. of the 17th ACM International Symposium on Mobile Ad Hoc Networking and Computing (MobiHoc)*. 2016, 61–70.
- [39] C. Han, A. O. Bicen and I. F. Akyildiz. Multi-ray channel modeling and wideband characterization for wireless communications in the terahertz band. *IEEE Transactions on Wireless Communications* 14.5 (2015), 2402–2412.
- [40] K. Haneda, J. Zhang, L. Tan, G. Liu, Y. Zheng, H. Asplund, J. Li, Y. Wang, D. Steer, C. Li, T. Balercia, S. Lee, Y. Kim, A. Ghosh, T. Thomas, T. Nakamura, Y. Kakishima, T. Imai, H. Papadopoulos, T. S. Rappaport, G. R. MacCartney, M. K. Samimi, S. Sun, O. Koymen, S. Hur, J. Park, C. Zhang, E. Mellios, A. F. Molisch, S. S. Ghassamzadeh and A. Ghosh. 5G 3GPP-like channel models for outdoor urban microcellular and macrocellular environments. *Proc. of IEEE 83rd Vehicular Technology Conference (IEEE VTC-Spring)*. 2016, 1–7.
- [41] *High-resolution transmission molecular absorption database*. URL: <https://hitran.org/> (visited on 04/05/2020).
- [42] W. Hong, K. Baek and S. Ko. Millimeter-wave 5G antennas for smartphones: Overview and experimental demonstration. *IEEE Transactions on Antennas and Propagation* 65.12 (2017), 6250–6261.
- [43] H. Huang and A. V. Savkin. A method for optimized deployment of unmanned aerial vehicles for maximum coverage and minimum interference in cellular networks. *IEEE Transactions on Industrial Informatics* 15.5 (2019), 2638–2647.
- [44] S. Hur, T. Kim, D. J. Love, J. V. Krogmeier, T. A. Thomas and A. Ghosh. Millimeter wave beamforming for wireless backhaul and access in small cell networks. *IEEE Transactions on Communications* 61.10 (2013), 4391–4403.
- [45] *IEEE 802.11ad-2012: IEEE Standard for information technology-Telecommunications and information exchange between systems-Local and metropolitan area networks-Specific requirements-Part 11: Wireless LAN Medium Access Control (MAC) and Physical Layer (PHY) Specifications Amendment 3: Enhancements for Very High Throughput in the 60 GHz Band*. Standard. Institute of Electrical and Electronics Engineers, 2012.

- [46] 802.11p-2010 - IEEE Standard for Information technology– Local and metropolitan area networks– Specific requirements– Part 11: Wireless LAN Medium Access Control (MAC) and Physical Layer (PHY) Specifications Amendment 6: Wireless Access in Vehicular Environments. Standard. Institute of Electrical and Electronics Engineers, 2010.
- [47] IEEE 802.15.3d-2017: IEEE standard for high data rate wireless multi-media networks Amendment 2: 100 Gb/s wireless switched point-to-point physical layer. Standard. Institute of Electrical and Electronics Engineers, 2017.
- [48] J. M. Jornet and I. F. Akyildiz. Channel modeling and capacity analysis for electromagnetic wireless nanonetworks in the terahertz band. *IEEE Transactions on Wireless Communications* 10.10 (2011), 3211–3221.
- [49] J. M. Jornet and I. F. Akyildiz. Graphene-based plasmonic nano-antenna for terahertz band communication in nanonetworks. *IEEE Journal on Selected Areas in Communications* 31.12 (2013), 685–694.
- [50] J. M. Jornet. Fundamentals of electromagnetic nanonetworks in the terahertz band. PhD thesis. Georgia Institute of Technology, 2013.
- [51] S. Ju, O. Kanhere, Y. Xing and T. S. Rappaport. A millimeter-wave channel simulator NYUSIM with spatial consistency and human blockage. *Proc. of IEEE Global Communications Conference (IEEE GLOBECOM)*. 2019, 1–6.
- [52] N. Khalid and O. B. Akan. Wideband THz communication channel measurements for 5G indoor wireless networks. *Proc. of IEEE International Conference on Communications (IEEE ICC)*. 2016, 1–6.
- [53] J. Ko, Y. Cho, S. Hur, T. Kim, J. Park, A. F. Molisch, K. Haneda, M. Peter, D. Park and D. Cho. Millimeter-wave channel measurements and analysis for statistical spatial channel model in in-building and urban environments at 28 GHz. *IEEE Transactions on Wireless Communications* 16.9 (2017), 5853–5868.
- [54] J. Kokkonen, V. Petrov, D. Moltchanov, J. Lehtomaki, Y. Koucheryavy and M. Juntti. Wideband terahertz band reflection and diffuse scattering measurements for beyond 5G indoor wireless networks. *Proc. of the 22th European Wireless Conference*. 2016, 1–6.

- [55] R. Kovalchukov, D. Moltchanov, A. Samuylov, A. Ometov, S. Andreev, Y. Koucheryavy and K. Samouylov. Analyzing effects of directionality and random heights in drone-based mmWave communication. *IEEE Transactions on Vehicular Technology* 67.10 (2018), 10064–10069.
- [56] P. Kumari, J. Choi, N. Gonzalez-Prelcic and R. W. Heath. IEEE 802.11ad-based radar: An approach to joint vehicular communication-radar system. *IEEE Transactions on Vehicular Technology* 67.4 (2018), 3012–3027.
- [57] J. Lee, J. Lee and S. Kim. Improving the accuracy of millimeter-wave ray-tracing simulations by modeling roadside trees. *IEEE Antennas and Wireless Propagation Letters* 18.1 (2019), 162–166.
- [58] X. Lin and J. G. Andrews. Connectivity of millimeter wave networks with multi-hop relaying. *IEEE Wireless Communications Letters* 4.2 (2015), 209–212.
- [59] I. Llatser, A. Mestres, S. Abadal, E. Alarcon, H. Lee and A. Cabellos-Aparicio. Time- and frequency-domain analysis of molecular absorption in short-range terahertz communications. *IEEE Antennas and Wireless Propagation Letters* 14 (2015), 350–353.
- [60] D. Lopez-Perez, M. Ding, H. Claussen and A. H. Jafari. Towards 1 Gbps/UE in cellular systems: Understanding ultra-dense small cell deployments. *IEEE Communications Surveys Tutorials* 17.4 (2015), 2078–2101.
- [61] J. Ma, R. Shrestha, J. Adelberg, C.-Y. Yeh, Z. Hossain, E. Knightly, J. M. Jornet and D. M. Mittleman. Security and eavesdropping in terahertz wireless links. *Nature* 563.7729 (2018), 89–93.
- [62] M. Mezzavilla, M. Zhang, M. Polese, R. Ford, S. Dutta, S. Rangan and M. Zorzi. End-to-end simulation of 5G mmWave networks. *IEEE Communications Surveys and Tutorials* 20.3 (2018), 2237–2263.
- [63] M. Mozaffari, W. Saad, M. Bennis and M. Debbah. Wireless communication using unmanned aerial vehicles (UAVs): Optimal transport theory for hover time optimization. *IEEE Transactions on Wireless Communications* 16.12 (2017), 8052–8066.
- [64] S. Niknam and B. Natarajan. On the regimes in millimeter wave networks: Noise-limited or interference-limited?: *Proc. of IEEE International Conference on Communications Workshops (IEEE ICC Workshops)*. 2018, 1–6.

- [65] Y. Niu, Y. Li, D. Jin, L. Su and A. V. Vasilakos. A survey of millimeter wave communications (mmWave) for 5G: Opportunities and challenges. *Wireless Networks* 21.8 (Nov. 2015), 2657–2676.
- [66] Nokia et al. *5G channel model for bands up to 100 GHz*. 5GCM white paper available at: <http://www.5gworkshops.com>. Oct. 2016.
- [67] *Official website of Federal Aviation Administration*. 2020. URL: <https://www.faa.gov/> (visited on 04/05/2020).
- [68] B. Peng and T. Kurner. Three-dimensional Angle of Arrival estimation in dynamic indoor terahertz channels using a forward-backward algorithm. *IEEE Transactions on Vehicular Technology* 66.5 (2017), 3798–3811.
- [69] C. Perfecto, J. Del Ser and M. Bennis. Millimeter-wave V2V communications: Distributed association and beam alignment. *IEEE Journal on Selected Areas in Communications* 35.9 (2017), 2148–2162.
- [70] V. Petrov, S. Andreev, M. Gerla and Y. Koucheryavy. Breaking the limits in urban video monitoring: Massive crowd sourced surveillance over vehicles. *IEEE Wireless Communications* 25.5 (2018), 104–112.
- [71] V. Petrov, J. Eckhardt, D. Moltchanov, Y. Koucheryavy and T. Kuerner. Measurements of reflection and penetration losses in low terahertz band vehicular communications. *Proc. of the 14th European Conference on Antennas and Propagation (EUCAP)*. 2020, 1–5.
- [72] V. Petrov, G. Fodor, S. Andreev, H. Do and H. Sahlin. V2X connectivity: From LTE to joint millimeter wave vehicular communications and radar sensing. *Proc. of 53rd Asilomar Conference on Signals, Systems, and Computers*. 2019, 1120–1124.
- [73] V. Petrov, G. Fodor, J. Kokkonen, D. Moltchanov, J. Lehtomaki, S. Andreev, Y. Koucheryavy, M. Juntti and M. Valkama. On Unified Vehicular Communications and Radar Sensing in Millimeter-Wave and Low Terahertz Bands. *IEEE Wireless Communications* 26.3 (June 2019), 146–153.
- [74] V. Petrov, M. Gapeyenko, D. Moltchanov, S. Andreev and R. W. Heath. Comparison of Airborne and Landed Deployments for On-Demand UAV-based mmWave Access Points. *IEEE Wireless Communications Letters* (Mar. 2020). Submitted publication, 1–5.

- [75] V. Petrov, J. Kokkonen, D. Moltchanov, J. Lehtomaki, M. Juntti and Y. Koucheryavy. The impact of interference from the side lanes on mmWave/THz band V2V communication systems with directional antennas. *IEEE Transactions on Vehicular Technology* 67.6 (2018), 5028–5041.
- [76] V. Petrov, J. Kokkonen, D. Moltchanov, J. Lehtomaki, Y. Koucheryavy and M. Juntti. Last Meter Indoor Terahertz Wireless Access: Performance Insights and Implementation Roadmap. *IEEE Communications Magazine* 56.6 (June 2018), 158–165.
- [77] V. Petrov, M. Komarov, D. Moltchanov, J. M. Jornet and Y. Koucheryavy. Interference and SINR in Millimeter Wave and Terahertz Communication Systems With Blocking and Directional Antennas. *IEEE Transactions on Wireless Communications* 16.3 (Mar. 2017), 1791–1808.
- [78] V. Petrov, M. A. Lema, M. Gapeyenko, K. Antonakoglou, D. Moltchanov, F. Sardis, A. Samuylov, S. Andreev, Y. Koucheryavy and M. Dohler. Achieving end-to-end reliability of mission-critical traffic in softwarized 5G networks. *IEEE Journal on Selected Areas in Communications* 36.3 (2018), 485–501.
- [79] V. Petrov, D. Moltchanov, S. Andreev and R. W. Heath. Analysis of Intelligent Vehicular Relaying in Urban 5G+ Millimeter-Wave Cellular Deployments. *Proc. of IEEE Global Communications Conference (IEEE GLOBECOM)*. Dec. 2019, 1–6.
- [80] V. Petrov, D. Moltchanov, J. M. Jornet and Y. Koucheryavy. Capacity and Outage of Terahertz Communications with User Micro-mobility and Beam Misalignment. *accepted to IEEE Transactions on Vehicular Technology (Early Access)* (2020), 1–5.
- [81] V. Petrov, D. Moltchanov, J. M. Jornet and Y. Koucheryavy. Exploiting Multipath Terahertz Communications for Physical Layer Security in Beyond 5G Networks. *Proc. of IEEE Conference on Computer Communications Workshops (IEEE INFOCOM WKSHPs)*. Apr. 2019, 1–8.
- [82] V. Petrov, D. Moltchanov and Y. Koucheryavy. Applicability assessment of terahertz information showers for next-generation wireless networks. *Proc. of IEEE International Conference on Communications (IEEE ICC)*. 2016, 1–7.

- [83] V. Petrov, D. Solomitckii, A. Samuylov, M. A. Lema, M. Gapeyenko, D. Moltchanov, S. Andreev, V. Naumov, K. Samouylov, M. Dohler and Y. Koucheryavy. Dynamic Multi-Connectivity Performance in Ultra-Dense Urban mmWave Deployments. *IEEE Journal on Selected Areas in Communications* 35.9 (Sept. 2017), 2038–2055.
- [84] V. Petrov, D. Moltchanov, Y. Koucheryavy and J. M. Jornet. The effect of small-scale mobility on terahertz band communications. *Proc. of the 5th ACM International Conference on Nanoscale Computing and Communication (NANOCOM)*. 2018.
- [85] M. Polese, M. Giordani, M. Mezzavilla, S. Rangan and M. Zorzi. Improved handover through dual connectivity in 5G mmWave mobile networks. *IEEE Journal on Selected Areas in Communications* 35.9 (2017), 2069–2084.
- [86] M. Polese, M. Giordani, T. Zugno, A. Roy, S. Goyal, D. Castor and M. Zorzi. Integrated access and backhaul in 5G mmWave networks: Potential and challenges. *IEEE Communications Magazine* 58.3 (2020), 62–68.
- [87] H. V. Poor and R. F. Schaefer. Wireless physical layer security. *Proceedings of the National Academy of Sciences* 114.1 (2017), 19–26.
- [88] P. Popovski, K. F. Trillingsgaard, O. Simeone and G. Durisi. 5G wireless network slicing for eMBB, URLLC, and mMTC: A communication-theoretic view. *IEEE Access* 6 (2018), 55765–55779.
- [89] S. Priebe, M. Jacob and T. Kurner. Affection of THz indoor communication links by antenna misalignment. *Proc. of 6th European Conference on Antennas and Propagation (EUCAP)*. 2012, 483–487.
- [90] M. Rebato, L. Resteghini, C. Mazzucco and M. Zorzi. Study of realistic antenna patterns in 5G mmWave cellular scenarios. *Proc. of IEEE International Conference on Communications (IEEE ICC)*. 2018, 1–6.
- [91] P. Roy. Performance evaluation of 5G mmWave communications with multi-connectivity. MA thesis. Tampere University, 2020.
- [92] H. Rutagemwa, K. E. Baddour, C. Brown and S. Raut. Evaluation metrics and simulation tools for 5G millimeter-wave networks. *IEEE Wireless Communications* 25.4 (2018), 52–57.

- [93] K. Sakaguchi, T. Haustein, S. Barbarossa, E. C. Strinati, A. Clemente, G. Destino, A. Pärssinen, I.-G. Kim, H.-S. Chung, J. Kim, W. Keusgen, R. J. Weiler, K. Takinami, E. Ceci, A. Sadri, L. Xian, A. Maltsev, G. K. Tran, H. Ogawa, K. Mahler and R. W. Heath. Where, when, and how mmWave is used in 5G and beyond. *IEICE Transactions 100-C* (2017), 790–808.
- [94] H. Shakhathreh, A. H. Sawalmeh, A. Al-Fuqaha, Z. Dou, E. Almaita, I. Khalil, N. S. Othman, A. Khreishah and M. Guizani. Unmanned aerial vehicles (UAVs): A survey on civil applications and key research challenges. *IEEE Access* 7 (2019), 48572–48634.
- [95] H. Shokri-Ghadikolaei and C. Fischione. Millimeter wave ad hoc networks: Noise-limited or interference-limited?: *Proc. of IEEE Globecom Workshops (IEEE GC Wkshps)*. 2015, 1–7.
- [96] G. H. Sim, T. Nitsche and J. C. Widmer. Addressing MAC layer inefficiency and deafness of IEEE802.11ad millimeter wave networks using a multi-band approach. *Proc. of IEEE 27th Annual International Symposium on Personal, Indoor, and Mobile Radio Communications (IEEE PIMRC)*. 2016, 1–6.
- [97] S. Singh, M. N. Kulkarni, A. Ghosh and J. G. Andrews. Tractable model for rate in self-backhauled millimeter wave cellular networks. *IEEE Journal on Selected Areas in Communications* 33.10 (2015), 2196–2211.
- [98] C. Slezak, V. Semkin, S. Andreev, Y. Koucheryavy and S. Rangan. Empirical effects of dynamic human-body blockage in 60 GHz communications. *IEEE Communications Magazine* 56.12 (2018), 60–66.
- [99] E. K. Smith. Centimeter and millimeter wave attenuation and brightness temperature due to atmospheric oxygen and water vapor. *Radio Science* 17.06 (1982), 1455–1464.
- [100] D. Solomitckii, V. Petrov, H. Nikopour, M. Akdeniz, O. Orhan, N. Himayat, S. Talwar, S. Andreev and Y. Koucheryavy. Detailed interference analysis in dense mmWave systems employing dual-polarized antennas. *Proc. of IEEE Globecom Workshops (IEEE GC Wkshps)*. 2017, 1–7.
- [101] D. Solomitckii. Evaluation of mmWave 5G performance by advanced ray tracing techniques. PhD thesis. Tampere University, 2019.

- [102] *Status of project IEEE 802.11ay: Enhanced throughput for operation in license-exempt bands above 45 GHz*. 2020. URL: http://www.ieee802.org/11/Reports/tgay_update.htm (visited on 04/05/2020).
- [103] N. Tafintsev, D. Moltchanov, M. Gerasimenko, M. Gapeyenko, J. Zhu, S. Yeh, N. Himayat, S. Andreev, Y. Koucheryavy and M. Valkama. Aerial access and backhaul in mmWave B5G systems: Performance dynamics and optimization. *IEEE Communications Magazine* 58.2 (2020), 93–99.
- [104] A. Tassi, M. Egan, R. J. Piechocki and A. Nix. Modeling and design of millimeter-wave networks for highway vehicular communication. *IEEE Transactions on Vehicular Technology* 66.12 (2017), 10676–10691.
- [105] A. Thornburg, T. Bai and R. W. Heath. Interference statistics in a random mmWave ad hoc network. *Proc. of IEEE International Conference on Acoustics, Speech and Signal Processing (IEEE ICASSP)*. 2015, 2904–2908.
- [106] A. Thornburg and R. W. Heath. Ergodic capacity in mmWave ad hoc network with imperfect beam alignment. *Proc. of IEEE Military Communications Conference (IEEE MILCOM)*. 2015, 1479–1484.
- [107] B. Toghi, M. Saifuddin, H. N. Mahjoub, M. O. Mughal, Y. P. Fallah, J. Rao and S. Das. Multiple Access in cellular V2X: Performance analysis in highly congested vehicular networks. *Proc. of IEEE Vehicular Networking Conference (IEEE VNC)*. 2018, 1–8.
- [108] A. Trotta, M. D. Felice, F. Montori, K. R. Chowdhury and L. Bononi. Joint coverage, connectivity, and charging strategies for distributed UAV networks. *IEEE Transactions on Robotics* 34.4 (2018), 883–900.
- [109] V. Va, T. Shimizu, G. Bansal and R. W. Heath Jr. *Millimeter wave vehicular communications: A survey*. 2016.
- [110] K. Venugopal and R. W. Heath. Location based performance model for indoor mmWave wearable communication. *Proc. of IEEE International Conference on Communications (IEEE ICC)*. 2016, 1–6.
- [111] K. Venugopal and R. W. Heath. Millimeter wave networked wearables in dense indoor environments. *IEEE Access* 4 (2016), 1205–1221.

- [112] K. Venugopal, M. C. Valenti and R. W. Heath. Interference in finite-sized highly dense millimeter wave networks. *Proc. of Information Theory and Applications Workshop (ITA)*. 2015, 175–180.
- [113] X. Wang, L. Kong, F. Kong, F. Qiu, M. Xia, S. Arnon and G. Chen. Millimeter wave communication: A comprehensive survey. *IEEE Communications Surveys and Tutorials* 20.3 (2018), 1616–1653.
- [114] Y. Wang, S. Mao and T. S. Rappaport. On directional neighbor discovery in mmWave networks. *Proc. of IEEE 37th International Conference on Distributed Computing Systems (IEEE ICDCS)*. 2017, 1704–1713.
- [115] J. Wildman, P. H. J. Nardelli, M. Latva-aho and S. Weber. On the joint impact of beamwidth and orientation error on throughput in directional wireless poisson networks. *IEEE Transactions on Wireless Communications* 13.12 (2014), 7072–7085.
- [116] Y. Wu, A. Khisti, C. Xiao, G. Caire, K. Wong and X. Gao. A survey of physical layer security techniques for 5G wireless networks and challenges ahead. *IEEE Journal on Selected Areas in Communications* 36.4 (2018), 679–695.
- [117] H. Wymeersch, G. Seco-Granados, G. Destino, D. Dardari and F. Tufvesson. 5G mmWave positioning for vehicular networks. *IEEE Wireless Communications* 24.6 (2017), 80–86.
- [118] Q. Xia and J. M. Jornet. Expedited neighbor discovery in directional terahertz communication networks enhanced by antenna side-lobe information. *IEEE Transactions on Vehicular Technology* 68.8 (2019), 7804–7814.
- [119] Z. Xiao, P. Xia and X. Xia. Enabling UAV cellular with millimeter-wave communication: Potentials and approaches. *IEEE Communications Magazine* 54.5 (2016), 66–73.
- [120] X. Xu, Y. Zeng, Y. L. Guan and Y. Li. Cellular-V2X Communications with Weighted-Power-Based Mode Selection. *IEEE Open Journal of the Communications Society* (2020), 1–1.
- [121] L. Zhang, H. Zhao, S. Hou, Z. Zhao, H. Xu, X. Wu, Q. Wu and R. Zhang. A survey on 5G millimeter wave communications for UAV-assisted wireless networks. *IEEE Access* 7 (2019), 117460–117504.

- [122] L. Zhang, H. Zhao, S. Hou, Z. Zhao, H. Xu, X. Wu, Q. Wu and R. Zhang. A survey on 5G millimeter wave communications for UAV-assisted wireless networks. *IEEE Access* 7 (2019), 117460–117504.
- [123] M. Zhang, M. Polese, M. Mezzavilla, J. Zhu, S. Rangan, S. Panwar and M. Zorzi. Will TCP work in mmWave 5G cellular networks?: *IEEE Communications Magazine* 57.1 (2019), 65–71.
- [124] A. Zhou, L. Wu, S. Xu, H. Ma, T. Wei and X. Zhang. Following the shadow: Agile 3-D beam-steering for 60 GHz wireless networks. *Proc. of IEEE Conference on Computer Communications (IEEE INFOCOM)*. 2018, 2375–2383.
- [125] Y. Zou, J. Zhu, X. Wang and L. Hanzo. A survey on wireless security: Technical challenges, recent advances, and future trends. *Proceedings of the IEEE* 104.9 (2016), 1727–1765.

PUBLICATIONS

PUBLICATION

I

Interference and SINR in Millimeter Wave and Terahertz Communication Systems With Blocking and Directional Antennas

V. Petrov, M. Komarov, D. Moltchanov, J. M. Jornet and Y. Koucheryavy

IEEE Transactions on Wireless Communications 16.3 (2017), 1791–1808

Publication reprinted with the permission of the copyright holders

Interference and SINR in Millimeter Wave and Terahertz Communication Systems with Blocking and Directional Antennas

V. Petrov, *Student Member, IEEE*, M. Komarov, *Member, IEEE*, D. Moltchanov, J. M. Jornet, *Member, IEEE*, and Y. Koucheryavy, *Senior Member, IEEE*

Abstract—The fifth generation wireless systems are expected to rely on a large number of small cells to massively offload traffic from the cellular and even from the wireless local area networks. To enable this functionality, mm-wave (EHF) and Terahertz (THF) bands are being actively explored. These bands are characterized by unique propagation properties compared to microwave systems. As a result, the interference structure in these systems could be principally different to what we observed so far at lower frequencies. In this paper, using the tools of stochastic geometry, we study the systems operating in the EHF/THF bands by explicitly capturing three phenomena inherent for these frequencies: (i) high directivity of the transmit and receive antennas, (ii) molecular absorption, and (iii) blocking of high-frequency radiation. We also define and compare two different antenna radiation pattern models. The metrics of interest are the mean interference and the signal-to-interference-plus-noise (SINR) ratio at the receiver. Our results reveal that (i) for the same total emitted energy by a Poisson field of interferers, both the interference and SINR significantly increase when simultaneously both transmit and receive antennas are directive, (ii) blocking has a profound impact on the interference and SINR creating much more favorable conditions for communications compared to no blocking case.

Index Terms—Interference, Millimeter Waves, Terahertz Band, Directional Antennas, Blocking, 5G Systems

I. INTRODUCTION

To keep up with constantly increasing traffic demands and quality of service requirements [2], industry is preparing for a 1000x increase in mobile data [3]. Despite the significant steps forward, current 4G cellular technologies will soon be insufficient to satisfy the constantly growing device base and customer traffic demands.

Among the possible solutions, future generation of wireless systems are expected to rely on high-capacity small cells to offload heavy traffic from the cellular and even local area networks. To enable this, millimeter wave systems operating in

V. Petrov, M. Komarov, D. Moltchanov and Y. Koucheryavy are with the Department of Electronics and Communications Engineering, Tampere University of Technology, Tampere, Finland (e-mail: {vitaly.petrov,dmitri.moltchanov}@tut.fi, yk@cs.tut.fi).

J. M. Jornet is with the Department of Electrical Engineering, University at Buffalo, The State University of New York, NY 14260, USA (e-mail: jmjornet@buffalo.edu).

This work was supported by Academy of Finland FiDiPro program "Nanocommunication Networks", 2012 – 2016. Dr. J. M. Jornet acknowledges the support of AFRL, under AFRL Grant No. FA8750-15-1-0050. V. Petrov acknowledges the support by Nokia Foundation.

A preliminary version of this work appeared in the Proc. of IEEE Globecom'16 [1].

the EHF band (30–300GHz) have been heavily investigated in the recent years [4]. Furthermore, several groups are already exploring the use of even higher frequency windows available in the Terahertz band (THF, 0.3–3THz), e.g., 300GHz, 640GHz, or even the entire THz window [5]–[10].

There are a number of critical factors that affect the propagation of waves in the EHF and THF bands, which will shape the interference in 5G systems. First of all, electromagnetic (EM) waves at these frequencies are affected by inherently very high pathloss [11] as the much smaller size of EHF/THF antennas results in a large spreading loss. Molecular absorption further hampers the signal propagation. This phenomenon reflects the process by which a part of the EM energy of the propagating signal is converted into kinetic energy in internally vibrating molecules. In the EHF band, oxygen, which is abundant in the atmosphere, affects the path loss [12]. For the THF band, water vapor serves the role of primary absorbent [13], [14]. Irrespective of the type of absorbent, the result is a more complex expression for the received power at a distance from the transmitter, which now includes not only the power law function but an exponent as well.

Given the transmission power constraints, highly directional antennas are needed at the transmitter (Tx) and/or receiver (Rx) to overcome the severe propagation losses. The belief is that high directivity of Tx/Rx antennas will eventually lead to a noise-limited regime of communications systems [15]. However, razor-sharp-beam interference-free communications are not on the immediate horizon. The reasons range from the complexity of high directivity beamforming antennas to the synchronization challenges that they introduce. In addition, it has been experimentally shown that interference may still play a substantial role in specific environments [4]. The increasing network densification [16], the use of advanced networking mechanisms such as pico/femto cells [17], client-relays [18], and direct device-to-device communications [19] may still cause interference even when directional antennas are used.

Another effect to take into account is line-of-sight (LoS) blockage. This phenomenon has been addressed in a number of papers in the context of microwave communication systems [20], [21], where buildings block the path between Tx and Rx. Millimeter-wave and THz systems are expected to operate over much shorter distances than microwave cellular systems and, thus, buildings are not expectedly a major problem in outdoor deployments [12]. However, at these frequencies, users themselves may block the LoS path between

Tx and Rx, as almost any object whose volume is larger than several wavelengths (millimeters in the bands of interest) is effectively an obstacle. Recent measurements and simulations report that up to 60~80% of energy available at the Rx comes from the LoS component and dictates the channel quality [12], [22]–[24]. Therefore, the process of LoS possible blockage by users has also to be taken into account in performance modeling of EHF and THF communications systems.

Despite the many existing works in the broad field of multi-user interference modeling, which we summarize in Sec. II, to the best of our knowledge, there is no study that simultaneously captures all these effects. In this paper, using the tools of stochastic geometry, we develop an analytical model of interference and SINR for systems operating in the EHF and THF bands that explicitly captures the following three effects inherent for these frequencies: (i) directivity of the Tx and Rx antennas, (ii) additional path loss component caused by molecular absorption, and (iii) blocking of high frequency radiation. Two radiation pattern models of directional antennas are considered, namely, the *cone* model representing an ideal directional antenna, and the *cone-plus-sphere* model capturing specifics of a non-ideal directional antenna with side lobes. The metrics of interest are the mean interference and the SINR at the receiver.

Using the developed model, we numerically investigate the multi-user interference in different scenarios. Our results show that the mean interference increases when the Tx or the Rx or both are equipped with directional antennas. However, the associated increase in the useful signal strength effectively compensates this effect and the SINR drastically improves showing that EHF/THF communication systems can indeed be designed to be noise-limited in the most cases. The effect of blocking further improves the performance in terms of SINR while the molecular absorption substantially degrades it.

The rest of the paper is organized as follows. In Sec. II, we provide a brief account of previous studies on interference estimation for directional antennas and blocking. In Sec. III, we review the propagation characteristics of EHF and THF bands and introduce the antenna and network models for our study. The mathematical models of interference and mean value of SINR are derived in Sec. IV and Sec. V, respectively. Numerical results are reported and discussed in Sec. VI. The conclusions are drawn in Sec. VII.

II. RELATED WORK

Many stochastic models of interference have been developed to date. An extensive review of the existing models can be found in [25]–[27]. Typically, these models assume a random isotropic and homogenous deployments in \mathbb{R}^2 , such as Poisson Point Process [20], [28] or, rarely, Mattern hardcore process [29]. In most studies, the antenna radiation pattern is assumed to be omnidirectional and the path loss is a power law function of the distance [30], even the exponent value may be different for different communication ranges [31].

The models reported in the literature do not simultaneously capture all the effects of the EHF/THF bands. Recently, the studies addressing interference modeling in presence of direc-

tional antennas [32], [33] and signal blockage by human bodies [34], [35] in EHF band started to appear. The propagation model used in [32]–[35] neglects the exponential attenuation term caused by molecular absorption loss, while the model in [35] also assumes interferers located on the fixed positions, which is not realistic for dynamic environments. The interference and SIR analysis in presence of the absorption losses has been provided in [36]. However, the presented model neglects the effects of blocking. The study in [37] relies on a simple model of absorption presuming a constant attenuation coefficient and also neglects the effect of blocking. In addition, several simulation-based studies estimating the interference in mm-wave systems have been recently presented [38], [39]. However, their applicability to the wide range of frequencies, nodes densities, and antenna radiation patterns, is limited.

In [40], a stochastic interference model for pulse-based THz communications was developed by taking into account the impact of molecular absorption. The work has targeted nanoscale communication networks and, thus, the impact of directivity or blockage was not captured. In [41], a model for continuous-wave THz communications was developed to compute also the SINR under similar assumptions. In both cases, the results show that for an omnidirectional antenna pattern the interference has similar structure to what is observed at lower frequencies. At the same time, specifics of THz waves propagation, namely, molecular absorption (see Section III-A) has a notable quantitative effect on the mean interference level and SINR values. Therefore, the effect of molecular absorption should not be avoided in interference modeling for more sophisticated scenarios.

The impact of multi-user interference at the link layer has been addressed in several recent studies. In [42], the authors study the collision probability in mm-wave networks. The analysis takes into account the antenna directivity and molecular absorption, but does not incorporate blockage and is performed exclusively for the selected channel access method. In [43], the authors develop a collision-aware scheduling scheme for mm-waves, ignoring the blockage and molecular absorption effects. There have been many other directional MAC protocols, including [44], [45] and our recent work in [46], but none of these works either estimate the interference level in a random deployment or incorporate other important propagation effects.

III. PROPAGATION, ANTENNA RADIATION PATTERN, AND NETWORK MODELS

In this section, we introduce the system model. Our notation is summarized in Table I.

A. Propagation in EHF/THF Bands

The distinguishing feature of the EHF/THF channels is the presence of molecular absorption [13], [47], albeit much stronger in the THF band. In the former, especially, in the unlicensed 60GHz band, absorption is dominated by O_2 molecules; in the latter, absorption is mainly caused by H_2O vapor [14]. These losses make the wireless channel highly

TABLE I
NOTATION USED IN THE PAPER.

Parameter	Definition
System parameters	
P_{Tx_0}	Emitted power at the tagged transmitter
P_{Rx_0}	Received power at the tagged receiver
r_0	The distance between Rx_0 and Tx_0
r_i	The distances between interferers/blockers and Rx_0
r_B	Radius of interferer/blocker
r^*	Radius for side lobe approximation
R	The interference zone around the tagged receiver
λ_I	The intensity of interferers/blockers in the area
Propagation model parameters	
K	Absorption coefficient, $K \in (0, 1)$
$S_{Rx}(f, r)$	Received signal psd
$L_P(f, r)$	Propagation losses
$L_A(f, r)$	Absorption losses
$S_M(f, r)$	Molecular noise psd
$S_{JN}(f)$	Johnson-Nyquist thermal noise psd
$S_T(f, r)$	Total noise psd
k_B	Boltzmann constant
T	Temperature in Kelvin
h	Planck constant
$\tau(f, r)$	Transmittance of the medium
f	Operational frequency
Antenna model parameters	
G, G_1, G_2	Antenna gains
k	Coefficient of losses to the side lobes, $k \in (0, 1)$
α	Antenna directivity angle
H	Tx power + frequency-dependant loss coefficient (introduced in (15) to simplify derivations)
A, A_1, A_2	Tx power + frequency-dependant loss + gains coefficient (introduced in (15) to simplify derivations)
Blocking model parameters	
L_A	Length of an arc of the circumference
λ_P	Intensity of projections of blockers
L	Distance from the receiver to a blocker
W	Blocked interval created by a single blocker
v_i	Renewal points associated with blocking process
V	Length of a single blocked/unblocked interval
$p_B(x), p_A(x)$	Probability that a random point in blocked/unblocked
Interference and SINR models parameters	
I	Aggregate interference
$Ei(\cdot)$	Exponential integral function
$E[\cdot]$	Mean value
S	Signal-to-interference-plus-noise ratio
p_C	Probability that interferer affects Rx_0
Λ	Intensity of the unblocked interferers
r_*	Radius of side lobe's effect
N	Number of interferers in the circle of radius R
N_0	The mean number of interferers affecting Rx_0
$W(\cdot)$	Lambert W function
$\Gamma(\cdot, \cdot)$	The incomplete Gamma function
C	Normalization constant
G	Interference from a single node
λ_E	Intensity of the thinned process

frequency selective. The received power spectral density (psd) in the EHF/THF band can be written as

$$S_{Rx}(f, r) = \frac{S_{Tx}(f)G_{Tx}(f)G_{Rx}(f)}{L_A(f, r)L_P(f, r)}, \quad (1)$$

where f is the operating frequency, r is the separation distance between the transmitter and the receiver, $S_{Tx}(f)$ stands for the transmitted signal psd, $L_A(f, r)$ represents the absorption loss, $L_P(f, r)$ is the spreading loss, and $G_{Tx}(f)$ and $G_{Rx}(f)$ refer to the antenna gains in transmission and reception, respectively, which we consider to be constant within the

specific transmission window (and, thus, we remove their dependence on f from now on).

Following [13], the absorption loss is defined as

$$L_A(f, r) = \frac{1}{\tau(f, r)}, \quad (2)$$

where $\tau(f, r)$ is the transmittance of the medium following the Beer-Lambert law, $\tau(f, r) \approx e^{-K(f)r}$, $K(f)$ is the overall absorption coefficient of the medium available from the HITRAN database [14]. The propagation loss is obtained under the assumption of spherical propagation in free space, i.e., $L_P(f, r) = (4\pi r f/c)^2$, where c refers to the speed of the EM wave.

In addition to the path loss, we have to specify the noise in THz band. First, the EM radiation absorbed by the molecules in the medium is re-radiated out-of-phase at approximately the same frequencies it has been absorbed. This is known as the medium emissivity [48] and, from the communication perspective, it is considered as a noise source [13]. Following [13], [49], the molecular absorption noise psd is

$$S_M(f, r) = \frac{S_{Tx}(f)G_{Tx}G_{Rx}}{L_P(f, r)}[1 - \tau(f, r)]. \quad (3)$$

As of now, there is still no definite conclusion whether this noise is high enough to affect the reception (we refer the readers to [50] for detailed discussion on molecular noise). However, as we will see in what follows, the presence/absence of this noise affects SINR analysis. In this paper we address both cases.

The second contributor to the noise is the Johnson-Nyquist noise generated by thermal agitation of electrons in conductors. The form of this noise changes when entering the EHF/THF frequencies. Its power stays flat up until 0.1THz as $P_{JN} = k_B T = -174\text{dBm/Hz}$, where k_B is the Boltzmann constant and T is the temperature in Kelvin, and then it declines non-linearly up until approximately 6THz [51]. Thus, the Johnson-Nyquist noise is a function of the operating frequency and we approximate its psd using [51]

$$S_{JN}(f) = \frac{hf}{\exp(hf/k_B T) - 1}, \quad (4)$$

where h is Planck's constant.

Summarizing, the total noise psd at the receiver is

$$S_T(f, d) = \frac{hf}{\exp(hf/k_B T) - 1} + \frac{S_{Tx}(f)G_{Tx}G_{Rx}[1 - \tau(f, r)]}{L_P(f, r)}. \quad (5)$$

B. Antenna Radiation Pattern Models

We consider two antenna radiation pattern models (see Fig. 1), namely, the cone model and the cone-plus-sphere model. In the first model, Fig. 1(a), the antenna radiation pattern is modeled with a single cone-shaped beam, whose width determines the antenna directivity. The second model, Fig. 1(b), takes into account the presence of side-lobes around the single main lobe, which are modeled as a sphere around the antenna. Whereas the first antenna radiation diagram

corresponds to a rather ideal directional antenna, the second model can be understood as a simplified model for a more realistic antenna.

To parameterize the cone model, we need to provide the antenna gain G for the single lobe with directivity angle α . For the second model, G_1 and G_2 , corresponding to the gains for the main and side lobes, respectively, have to be provided. The gains G , G_1 , and G_2 will be used to amplify the signal with respect to the direction it goes to or comes from.

1) *Cone Model*: For this antenna radiation pattern, the psd \mathcal{P}_{R_x} at a distance r is

$$\mathcal{P}_{R_x} = \frac{P_{T_x}}{S_A} = \frac{P_{T_x}}{2\pi r h}, \quad (6)$$

where S_A is the surface area of the wavefront, given by the surface area of the spherical cap, with $h = r[1 - \cos(\alpha/2)]$, and α is the antenna directivity angle.

Alternatively, according to free-space propagation model, the psd \mathcal{P}_{R_x} at the wavefront is

$$\mathcal{P}_{R_x} = \frac{P_{T_x}}{S_A} = P_{T_x} \frac{G}{4\pi r^2}, \quad (7)$$

which implies that the antenna gain G for the main lobe in the cone model is given by

$$G = \frac{2}{1 - \cos(\alpha/2)}. \quad (8)$$

Note that for $\alpha = 2\pi$, i.e., an ideal omnidirectional antenna, the gain $G = 1$ and $S_A = 4\pi r^2$ as in omnidirectional spherical spreading.

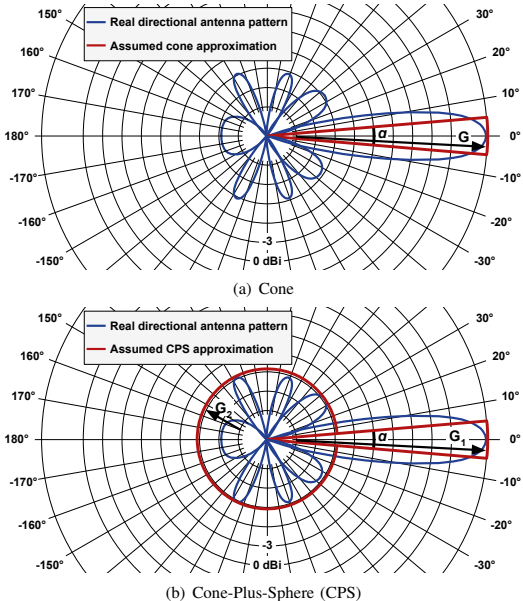


Fig. 1. Illustration of the considered antenna radiation pattern models.

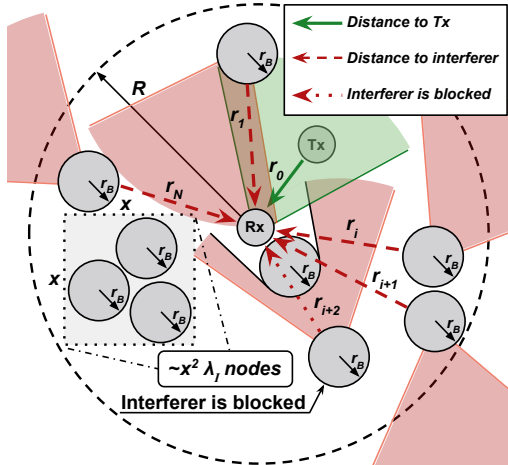


Fig. 2. An illustration of the considered network deployment.

2) *Cone-Plus-Sphere Model*: To parameterize this model we need to provide G_1 and G_2 . Denoting the fraction of energy concentrated along the main lobe by k_1 and the one lost to side lobes by k_2 , and following the same reasoning as for the cone model, we get the set of equations

$$\begin{cases} \mathcal{P}_{R_x1} 2\pi r^2 [1 - \cos(\alpha/2)] = k_1 P_{T_x} \\ \mathcal{P}_{R_x2} 2\pi r^2 [1 + \cos(\alpha/2)] = k_2 P_{T_x} \\ k_1 + k_2 = 1 \end{cases}, \quad (9)$$

where, according to the free space propagation model,

$$\begin{cases} \mathcal{P}_{R_x1} = G_1 P_{T_x} / 4\pi r^2 \\ \mathcal{P}_{R_x2} = G_2 P_{T_x} / 4\pi r^2 \end{cases}. \quad (10)$$

Thus, we have the following relation between G_1 and G_2

$$G_1 [1 - \cos(\alpha/2)] + G_2 [1 + \cos(\alpha/2)] = 2. \quad (11)$$

There are multiple solutions for (G_1, G_2) . Setting $G_2 = 0$ reduces the model to cone antenna. Introducing $k = k_1/k_2$, $k \in (0, 1)$ we see that $G_2 = kG_1$ and G_1, G_2 are given by

$$\begin{cases} G_1 = 2[(1 - \cos(\alpha/2)) + k(1 + \cos(\alpha/2))]^{-1} \\ G_2 = kG_1 \end{cases}. \quad (12)$$

We now have the relations to specify G , G_1 , and G_2 as functions of α and k in such a way that total transmit power does not change with the antenna directivity. This allows us to further compare the interference levels in fair conditions.

C. Network Model

As the major emphasis of this study is to assess the interference and SINR in the EHF/THF bands communications, we consider a random nodes deployment in \mathbb{R}^2 , see Fig. 2. We model the field of interferers by a Poisson point process with intensity λ_I . We tag an arbitrary one and assign it as a Rx of interest, R_{x0} . The associated Tx, denoted as T_{x0} , is

chosen to be at the distance r_0 from the Rx_0 . The rest of the nodes are considered as interferers. To model the respective receivers we assume that the orientation of the bisects of all coverage zones of transmitters are uniformly distributed in $(0, 2\pi)$. The radius of the zone where the nodes provide non-negligible interferences, R , can be computed using the propagation model. The transmissions of the nodes that are further than R is considered as noise. In our study, we consider interferers acting as blockers as well, i.e., a certain interferer residing along the path between another interferer and Rx_0 blocks the LoS path. Thus, depending on the context, the terms blocker and interferer are used interchangeably. The blockers are assumed to be of circular shape with radius r_B , see Fig. 2. The considered scenario corresponds to the case on “uncontrolled” direct communications in a random deployment providing the upper bound on the interference experienced by nodes.

D. Metrics of Interest

For the described scenario, the SINR is given by

$$S(\vec{r}, \vec{P}_T, f) = \frac{P_{Rx_0}(r_0, P_{Tx_0}, f)}{I(\vec{P}_{Tx}, \vec{r}, f) + S_N(\vec{P}_T, \vec{r}, f)}, \quad (13)$$

where $P_{Rx_0}(r_0, P_{Tx_0}, f)$ is the received signal power at a distance r_0 , $I(\vec{P}_{Tx}, \vec{r}, f)$ is the aggregate power of the interferers at Rx_0 , $S_N(\vec{P}_T, \vec{r}, f)$ is the total noise at Rx_0 , \vec{r} is the vector of distances between interferers and Rx_0 , f is the frequency and N is the number of interfering nodes in the area of radius R . In this study, we consider no power control and assign $P_{Tx_i} = P_{Tx_j} = P_{Tx_0}$, $i, j = 0, 1, \dots, N$. In what follows, for SINR, interference and noise we drop arguments that are often silently assumed, i.e., f , P_{Tx} and r_i .

The useful received power is given by

$$P_{Rx_0} = Ar_0^{-2}e^{-Kr_0}, \quad (14)$$

where we abstract the effect of transmission power, antenna gains, and path loss as

$$A = P_{Tx}G_{Tx}G_{Rx} \frac{c^2}{16\pi^2 f^2} = HG_{Tx}G_{Rx}, \quad (15)$$

where $H = P_{Tx}c^2/(16\pi^2 f^2)$ to simplify further derivations. The values for antenna gains at Tx and Rx sides, G_{Tx} and G_{Rx} , can be obtained as described in Section III-B.

The aggregate interference is then

$$I = A \sum_{i=1}^N r_i^{-2} e^{-Kr_i}. \quad (16)$$

where N is a random variable (RV) denoting the number of interferers and, for clarity, the cone radiation pattern is assumed (we provide elaborated equations for the cone-plus-sphere antenna radiation pattern in the following section).

The expression in the denominator of SINR depends on whether we take into account the effect of molecular noise or not. When molecular noise is present, the aggregated noise is written as

$$S_N = S_{JN} + A \sum_{i=0}^N r_i^{-2} (1 - e^{-Kr_i}). \quad (17)$$

Since $Ar_i^{-2}(1 - e^{-Kr_i}) + Ar_i^{-2}e^{-Kr_i} = Ar_i^{-2}$, the denominator of (13) can be written as

$$S_{JN} + I = S_{JN} + A \sum_{i=1}^N r_i^{-2}. \quad (18)$$

Substituting (17) and (18) into (13) gives the following expression for the SINR

$$S = \frac{Ar_0^{-2}e^{-Kr_0}}{S_{JN} + A \sum_{i=1}^N r_i^{-2}}. \quad (19)$$

The expression (19) is a generic one with all the phenomena taken into account. Depending on 1) the type of technology used for receiver design, 2) the frequency band and 3) the assumption about the molecular noise, we can distinguish between a number of special cases. For conventional transceiver technology such as silicon germanium and frequencies below 6THz there is always the thermal noise introduced by the receiver S_{JN} . If the principal parts of the transceivers are made of superconductive materials, such as graphene, and/or the frequency of interest is higher than 6THz the thermal noise is negligible [51], [52].

When molecular noise is ignored, (19) reduces to

$$S = \frac{Ar_0^{-2}e^{-Kr_0}}{S_{JN} + A \sum_{i=1}^N r_i^{-2}e^{-Kr_i}}. \quad (20)$$

Below, we first characterize interference according to (20) assuming that the effect of molecular noise is negligible. We then extend the analysis to the case of molecular noise. In Sec. V we characterize mean SINR for both (19) and (20).

IV. CHARACTERIZATION OF MEAN INTERFERENCE

A. Blocking Model

In a Poisson field of interferers, the nodes themselves act as blockers for interference LoS paths. We assume that if the interference LoS path between a certain interferer and the Rx_0 is blocked by another interferer, the interference at the Rx_0 is zero. Let us fix a distance from the interferer to Rx_0 , x . In Appendix A, we show that the blocking probability is given by

$$p_B(x) = 1 - e^{-\lambda_I(x-r_B)r_B}, \quad (21)$$

where r_B is the blocker radius.

Note that in addition to interferers, other humans currently not participating in the communications may also block the interference LoS paths. Modeling this process as an Poisson process with intensity λ_B we can still apply (21) with intensity $(\lambda_I + \lambda_B)$.

Using (21), the blocking probability as a function of the distance, x , for different values of λ_I and r_B is plotted in Fig. 3. As one may observe, the blocking probability tends to one exponentially fast when $x \rightarrow \infty$. Also, the higher the intensity λ_I , the higher the blocking probability. The radius of blockers, r_B , also affects the value of p_B . Expectedly, for larger radii the blocking probability is higher.

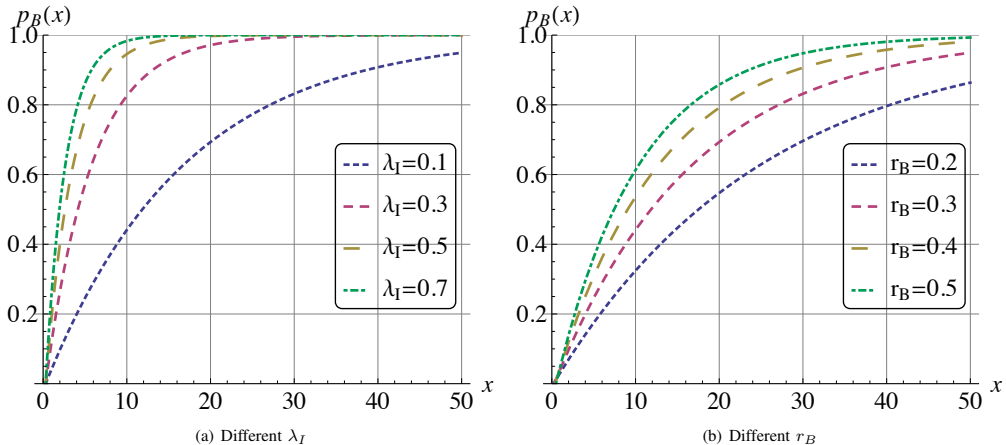


Fig. 3. The probability of blocking as a function of the separation distance x .

B. Cone Antenna Model

Consider the case of directional antenna at either Tx or Rx first. There are two cases when an interferer located at distance x does not contribute to the interference at the Rx₀: (i) its contribution is blocked by other interferers, and (ii) the Rx₀ is not in coverage of the interferer. The former happens with probability p_B , derived previously. The probability that Rx₀ is not in coverage of the interferer is independent of the distance x and given by

$$p_C = \frac{\alpha x}{2\pi x} = \frac{\alpha}{2\pi}. \quad (22)$$

Consider the infinitesimal radial increment dr . Since the process of blockers/interferers is Poisson, multiple events are not allowed to happen within dr and the probability that the interferer is located at distance r is proportional to the increment of the area dr . The area increment is

$$\pi(r + dr)^2 - \pi r^2 = 2\pi r dr + O(1), \quad (23)$$

implying that the probability that interferer is in $(r, r + dr)$ is $2\lambda_I \pi r dr$.

When the interferer located at the distance r is not blocked and the Rx₀ is in its coverage area, the contribution to the interference is $A r^{-2} e^{-Kr}$. Thus, the mean interference is

$$E[I] = \int_{r_B}^R A r^{-2} e^{-Kr} p_C [1 - p_B(r)] 2\lambda_I \pi r dr. \quad (24)$$

Substituting (21) and (22) into (24) we get

$$\begin{aligned} E[I] &= \int_{r_B}^R A r^{-2} e^{-Kr} e^{-\lambda_I(x-r_B)r_B} \frac{\alpha}{2\pi} 2\lambda_I \pi r dr \\ &= A\alpha\lambda_I \Theta(R, r_B, \lambda_I, K), \end{aligned} \quad (25)$$

where $\Theta(R, r_B, \lambda_I, K)$ is given by

$$\begin{aligned} \Theta &= e^{-\lambda_I r_B^2} Ei(-R[K + \lambda_I r_B]) \\ &\quad - Ei(-r_B^2[K + r_B \lambda_I]), \end{aligned} \quad (26)$$

and $Ei(\cdot)$ is the exponential integral function.

When blocking is not taken into account, we get

$$E[I] = A\alpha\lambda_I \int_{r_B}^R \frac{1}{r} e^{-Kr} dr = A\alpha\lambda_I \Theta_1(R, r_B, K), \quad (27)$$

where $\Theta_1(R, r_B, K) = Ei(-KR) - Ei(-Kr_B)$.

When the antenna is omnidirectional, we arrive at

$$E[I] = 2\pi\lambda_I A \Theta(R, r_B, \lambda_I, K), \quad (28)$$

Similarly, for omnidirectional antennas and no blocking we have

$$E[I] = 2\pi\lambda_I A \Theta_1(R, r_B, K). \quad (29)$$

Finally, when directivity at both sides is assumed we have

$$\begin{aligned} \text{Blocking: } E[I] &= \frac{A\alpha^2\lambda_I}{2\pi} \Theta(R, r_B, \lambda_I, K), \\ \text{No blocking: } E[I] &= \frac{A\alpha^2\lambda_I}{2\pi} \Theta_1(R, r_B, \lambda_I, K). \end{aligned} \quad (30)$$

C. Cone-Plus-Sphere Antenna Model

For the cone-plus-sphere antenna, we have to distinguish between three cases for an individual interferer: (i) interferer's LoS path is blocked, (ii) interferer's LoS path is not blocked and points to the Rx₀ with its main lobe, and (iii) interferer's LoS path is not blocked and points to the Rx₀ with its side/back lobes. The probability of the first event is p_B and the contribution of the interferer to the total interference is 0. The probability of the second event is $p_c(1 - p_B)$ and the contribution can be expressed via (25) with A_1 gain replacing A . The third event happens with the probability $(1 - p_c)(1 - p_B)$ and the contribution can be estimated by

extending the result from (25) with A_2 replacing A . The mean interference for cone-plus-sphere antenna model is

$$E[I] = \int_{r_B}^R A_1 r^{-2} e^{-Kr} p_C p_A 2\lambda_I \pi r dr + \int_{r_B}^R A_2 r^{-2} e^{-Kr} (1 - p_C) p_A 2\lambda_I \pi r dr. \quad (31)$$

Evaluating the integrals in (31) we arrive at

$$E[I] = A_1 \alpha \lambda_I \Theta(R, r_B, \lambda_I, K) + A_2 [2\pi - \alpha] \lambda_I \Theta_1(R, r_B, \lambda_I, K). \quad (32)$$

When blocking is not taken into account we have

$$E[I] = A_1 \alpha \lambda_I \Theta_1(R, r_B, K) + A_2 [2\pi - \alpha] \lambda_I \Theta_1(R, r_B, K). \quad (33)$$

For directive antennas at both Tx and Rx, we obtain

$$\begin{aligned} \text{Blocking: } E[I] &= \frac{A_1 \alpha^2 \lambda_I}{2\pi} \Theta(R, r_B, \lambda_I, K) \\ &\quad + \frac{A_2 [2\pi - \alpha^2] \lambda_I}{2\pi} \Theta(R, r_B, \lambda_I, K), \\ \text{No blocking: } E[I] &= \frac{A_1 \alpha^2 \lambda_I}{2\pi} \Theta_1(R, r_B, K) \\ &\quad + \frac{A_2 [2\pi - \alpha^2] \lambda_I}{2\pi} \Theta_1(R, r_B, K). \end{aligned} \quad (34)$$

Note that different directivity at Rx and Tx can also be modeled.

D. Interference in Presence of Molecular Noise

When molecular noise is taken into account, the mean interference for the cone model is

$$E[I] = \int_{r_B}^R A r^{-2} e^{-\lambda_I(x-r_B)r_B} \frac{\alpha}{2\pi} 2\lambda_I \pi r dr = A \alpha \lambda_I \Theta_1^*(R, r_B, \lambda_I), \quad (35)$$

where the term $\Theta_1^*(R, r_B, \lambda_I)$ is

$$\Theta_1^*(R, r_B, \lambda_I) = e^{-\lambda_I r_B} E(-\lambda_I r_B R) - E(-\lambda_I r_B^2). \quad (36)$$

The difference compared to the absence of molecular noise is that the interfering power at the receiver from a single node is now $A r^{-2}$ instead of $A r^{-2} e^{-Kr}$ due to additional contribution of molecular noise, $A r_0^{-2} (1 - e^{-K r_0})$.

Similarly, for cone-plus-sphere model we have

$$E[I] = A_1 \alpha \lambda_I \Theta_1^*(R, r_B, \lambda_I) + A_2 [2\pi - \alpha] \lambda_I \Theta_1^*(R, r_B, \lambda_I). \quad (37)$$

For directive antennas at both Tx and Rx we have

$$\begin{aligned} \text{Cone: } E[I] &= \frac{A \alpha^2 \lambda_I}{2\pi} \Theta_1^*(R, r_B, \lambda_I) \\ \text{CPS: } E[I] &= \frac{A_1 \alpha^2 \lambda_I}{2\pi} \Theta_1^*(R, r_B, \lambda_I, K) \\ &\quad + \frac{A_2 [2\pi - \alpha^2] \lambda_I}{2\pi} \Theta_1^*(R, r_B, \lambda_I, K). \end{aligned} \quad (38)$$

V. SIR AND SINR FUNCTIONS

As discussed in Sec. III, SIR and SINR are the functions of the interference. According to the conventional approach, to determine these metrics one has to first obtain the distribution of interference and then transform this distribution to the metrics of interest. The distribution of interference is obtained by finding the distribution of each component $A r_i^{-2} e^{-K r_i}$ and then either switching to the transform domain to obtain the sum of RVs $\sum_{i=1}^N A r_i^{-2} e^{-K r_i}$, where N is a RV denoting the number of non-blocked interferers and r is the distance from the Rx₀ to an interferer or by directly approximating it with a certain distribution [41], [53].

Working with EHF/THF propagation with blocking effect, we face fundamental difficulties applying the abovementioned approach. First of all, the density of interferers is non-uniform over the circle as the blocking probability $p_B(x)$ depends on the distance to the potential interferer. Secondly, switching to the transform domain is infeasible for the propagation model in hand as there is no closed form for Laplace transform of the interference from a single node, $A e^{-K r} r^{-2}$. On top of this, even if it would have been feasible (e.g., in case of power-law propagation and no blocking), the inversion of the resulting transform back to the RV domain is also infeasible in most cases implying that we are limited to first few moments of the metric of interest.

To obtain approximations for the mean and variance of SIR and SINR functions we propose to use the Taylor expansion technique outlined in Appendix B. Particularly, for the mean value of a RV $Y = g(X)$, where X is a RV with mean and variance μ_0 and $\sigma^2[X]$ we have

$$E[Y] = g(\mu_0) + \frac{g''(\mu_0)}{2} \sigma^2[X], \quad (39)$$

while for variance of $Y = g(X)$ we have

$$\sigma^2[Y] = [g'(\mu_0)]^2 \sigma^2[X] - \frac{1}{4} [f''(\mu_0) \sigma^2[X]]^2. \quad (40)$$

The SIR and SINR functions are given by

$$g_1(x) = \frac{C}{x}, \quad g_2(x) = \frac{C}{S_{JN} + x}, \quad (41)$$

where $C = A r_0^{-2} e^{-K r_0}$, S_{JN} is the Johnson-Nyquist noise.

The first and second derivatives of (41) are

$$\begin{aligned} g_1'(x) &= -\frac{C}{x^2}, & g_2'(x) &= -\frac{C}{(S_{JN} + x)^2}, \\ g_1''(x) &= \frac{2C}{x^3}, & g_2''(x) &= \frac{2C}{(S_{JN} + x)^3}. \end{aligned} \quad (42)$$

The mean interference has been found in the previous section. To find mean and variance of the metrics of interest we need variance of interference provided in Appendix C. Now, for the mean SINR for directive antennas at one side only we arrive at (43) for blocking and no blocking cases, respectively, where r_0 is the separation distance between Tx and Rx, the functions $\Phi(R, r_B, \lambda_I, K)$ and $\Phi_1(R, r_B, K)$ are defined in Appendix C.

For the mean SINR for directive antennas at both Tx and Rx we have (44) for blocking and no blocking cases, respectively, where the functions $\Phi(R, r_B, \lambda_I, K)$ and $\Phi_1(R, r_B, K)$ are

$$\text{Directional Tx or Rx} \left\{ \begin{array}{l} \text{Blocking: } E[S] = \frac{Ae^{-Kr_0}r_0^{-2}}{S_{JN} + A\alpha\lambda_I\Theta(R,r_B,\lambda_I,K)} + \frac{A^3e^{-Kr_0}r_0^{-2}[\alpha\lambda_I\Phi(R,r_B,\lambda_I,K) - (\alpha\lambda_I\Theta(R,r_B,\lambda_I,K))^2]}{[S_{JN} + A\alpha\lambda_I\Theta(R,r_B,\lambda_I,K)]^3}, \\ \text{No blocking: } E[S] = \frac{Ae^{-Kr_0}r_0^{-2}}{S_{JN} + A\alpha\lambda_I\Theta_1(R,r_B,K)} + \frac{A^3e^{-Kr_0}r_0^{-2}[\alpha\lambda_I\Phi_1(R,r_B,K) - (\alpha\lambda_I\Theta_1(R,r_B,K))^2]}{[S_{JN} + A\alpha\lambda_I\Theta_1(R,r_B,K)]^3}, \end{array} \right. \quad (43)$$

$$\text{Directional Tx and Rx} \left\{ \begin{array}{l} \text{Blocking: } E[S] = \frac{Ae^{-Kr_0}r_0^{-2}}{S_{JN} + \frac{A\alpha^2\lambda_I}{2\pi}\Theta(R,r_B,\lambda_I,K)} + \frac{A^3e^{-Kr_0}r_0^{-2}[\frac{\alpha\lambda_I}{2\pi}\Phi(R,r_B,\lambda_I,K) - (\frac{\alpha^2\lambda_I}{2\pi}\Theta(R,r_B,\lambda_I,K))^2]}{[S_{JN} + \frac{A\alpha^2\lambda_I}{2\pi}\Theta(R,r_B,\lambda_I,K)]^3}, \\ \text{No blocking: } E[S] = \frac{Ae^{-Kr_0}r_0^{-2}}{S_{JN} + \frac{A\alpha^2\lambda_I}{2\pi}\Theta_1(R,r_B,\lambda_I,K)} + \frac{A^3e^{-Kr_0}r_0^{-2}[\frac{\alpha\lambda_I}{2\pi}\Phi_1(R,r_B,K) - (\frac{\alpha^2\lambda_I}{2\pi}\Theta_1(R,r_B,\lambda_I,K))^2]}{[S_{JN} + \frac{A\alpha^2\lambda_I}{2\pi}\Theta_1(R,r_B,\lambda_I,K)]^3}, \end{array} \right. \quad (44)$$

defined in Appendix C. The mean SINR in presence of molecular noise as well as the mean SIR for all considered cases can be obtained similarly. Note that getting higher moments of interference, e.g., skewness, excess, allows to increase the accuracy of approximations in (62), (66).

VI. NUMERICAL RESULTS

In this section, we assess the effects of the radiation pattern model, antenna directivity, blocking, absorption loss and molecular noise on the mean interference and the mean SINR. For comparison purposes, throughout this section, we present the results assuming that interference coming from the nodes more than R from the receiver is zero, while the coefficient A , introduced in (15), equals to 1 for omnidirectional antenna ($H = 1$). The results for other models are relative to the omnidirectional one. In addition to A , (15) includes the frequency-dependent component of the path loss, related to the Rx antenna aperture. In the rest of this section, to qualitatively illustrate the dependencies of the metrics of interest on the continuum of values of the absorption coefficient K without referring to particular frequencies, we assume that this component is constant. Also, throughout this section the radius of the interference zone, R , around Rx_0 is set to 10.

A. Interference Assessment

1) *The Effect of Directivity*: In the first two subfigures in Fig. 4 the mean interference for scenarios with omnidirectional antennas is illustrated and compared to the simulation data when blocking is not taken into account. The *same emitted power* at all the nodes was assumed, absorption coefficient was set to $K = 0.01$ and blocking was not taken into account.

The simulation results have been obtained using an in-house-made simulator emulating the deployment scenarios. Simulated data points are indicated with markers of the same color in Fig. 4. As one may notice observing illustrations in Fig. 4, the analytical data closely resemble those of simulations confirming the accuracy of the proposed analysis. For this reason, in what follows, we illustrate the mean interference using analytical results only.

Analyzing Fig. 4(a) computed using (27), (29) and (30), we first note that all the models converge to the same value

for $\alpha = 2\pi$ confirming our derivations. We see that using a directional antenna at Tx (or Rx) only results in much larger interference compared to omnidirectional case in the interval of most interest $(0, \pi)$. This is due to the fact that for small values of α both cone and cone-plus-sphere antenna radiation patterns concentrate the majority of the emitted power in the plane, all the interferers and target receiver are in. So, the probability to hit the receiver with the beam decreases slower than the average impact of a single hit, which leads to the greater interference. Furthermore, the less the directivity angle α the more interference is observed. The reason is that highly directional antennas concentrate the emitted power in a single beam and although only few may affect the receiver, their effect on average is higher compared to omnidirectional antennas. Enabling directivity at both Tx and Rx increases the interference even further. The effect of the density of interferers is linear when blocking is not taken into account as shown in Fig. 4(b), computed using (27), (29) and (30). The larger the value of λ_I the larger the gap between systems with directional and omnidirectional antennas. The highest interference is observed when both Tx and Rx are equipped with directional antennas.

This destructive effect of interference is mitigated by: (i) higher received signal strength compared to omnidirectional antennas, (ii) reduction in transmission power and (iii) blocking of EHF/THF radiation by the interferers themselves. The latter is a natural phenomenon of EHF/THF band that may inherently improve performance of communications.

2) *The Effect of Blocking*: The last two figures in Fig. 4, computed using (25), (28) and (30), show the mean interference for scenarios with omnidirectional and directional antennas, when blocking is taken into account and cone directional antenna model is used. Comparing Fig. 4(c) to Fig. 4(a), we see that the blocking drastically decreases the interference for all considered cases. Still the system with directional Tx and Rx is characterized by the highest interference.

The effect of blocking on the mean interference as a function of the interference intensity, λ_I , shown in Fig. 4(d) and computed using (25), (28) and (30), illustrates that the structure of interference principally changes when blocking is taken into account. Instead of the linear increase in response to the increase in λ_I inherent for systems without blocking, see Fig. 4(b), the increase is sublinear. Furthermore, the aggregate interference in presence of blocking does not tend to infinity as

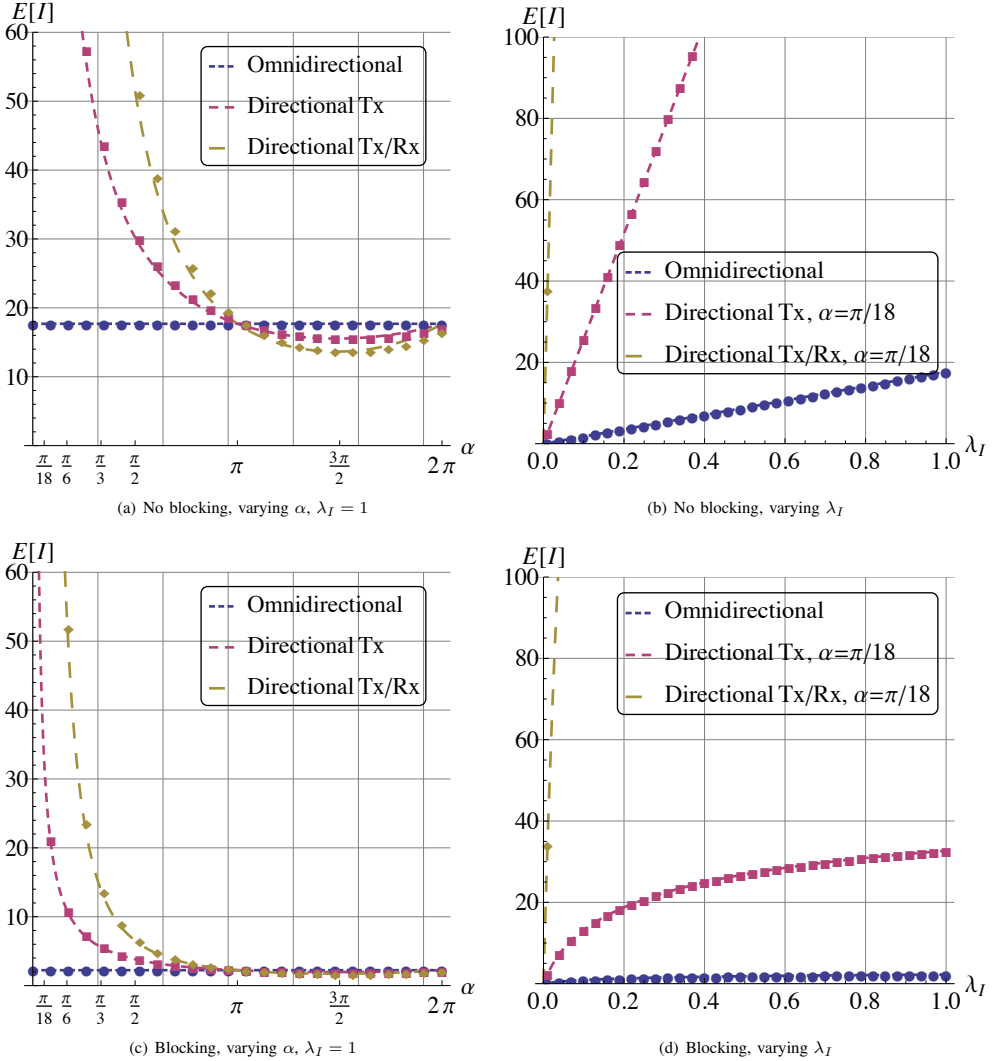


Fig. 4. Comparison of interference for scenarios with omnidirectional and directional cone antenna radiation pattern models.

$\lambda_I \rightarrow \infty$. The reason is that, in presence of blocking, there is always a certain radius around the Rx_0 such that the interferers located outside do not contribute to the interference at Rx as their interference LoS paths are blocked.

3) *The Effect of Absorption*: Let us now illustrate the effect of absorption coefficient. Fig. 5, computed using (30), highlights dependence of the mean interference on the absorption coefficient K for cone directional antenna model with blocking taken into account. Fixing the density of interferers, λ_I , we observe the expected dependency on K , i.e., the interference is smaller for higher values of K , see Fig. 5(a). In general, when K increases, the interference naturally decreases due

to less radiation reaching the receiver. It is important to note that this feature of EHF/THF bands is often claimed to have negative effect. Here, we see that the proper choice of the emitted power and the operational frequency may, in fact, allow for point-to-point links creating only little interference to concurrent transmissions. Fig. 5(a) and Fig. 5(c), computed using (30), show that the effect of absorption is similar for different directivity angles.

4) *The Effect of the Antenna Model*: Consider the effect of different antenna radiation pattern model. Recall that according to cone model no radiation is lost to the side lobes. The cone-plus-sphere model takes into account losses to side

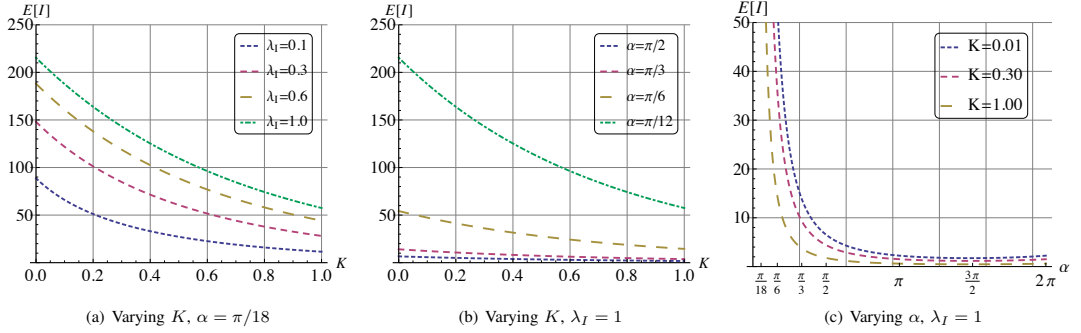


Fig. 5. Dependence of the mean interference on the absorption coefficient K for cone directional antenna model.

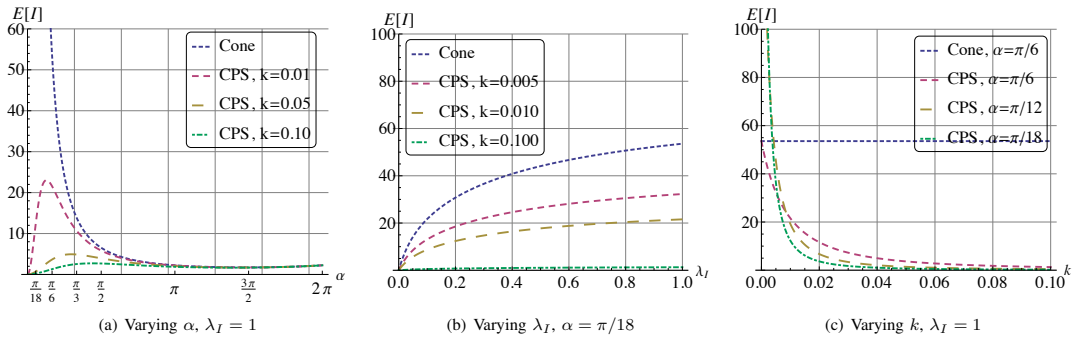


Fig. 6. The comparison of mean interference between cone and cone-plus-sphere antenna models.

lobes via coefficient k . The question is whether the gap between these models is large to warrant additional modeling complexity.

The mean interference as a function of the antenna directivity α for different values of loss coefficient k is shown in Fig. 6(a), computed using (30) and (34). As one may observe the behavior of the cone-plus-sphere model is more complicated compared to the cone one. When losses to side lobes are rather low, it, expectedly, resembles on the properties of the cone model. However, when k increases, the mean interference no longer tends to linear function characterizing the omnidirectional case. The dependence on λ_I is illustrated in Fig. 6(b), computed using (30) and (34). As one may observe, when losses to side lobes increases the interference decreases, i.e., the cone model greatly overestimates the actual interference. Fig. 6(c) illustrates this effect for a wide range of k and different α . Since realistic antennas are non-perfect, characterized by k in the range $0.1 \sim 0.2$ [54], no accurate approximation can be provided by the simple cone model.

5) *The Effect of Molecular Noise*: Let us analyze the effect of molecular noise. Recall that the presence of molecular noise simplifies the interference to $\sum_{i=1}^N A d_i^{-\gamma}$ as noise terms $(1 - e^{-K d_i})$ now contribute to the interference at the Rx_0 . Fig. 7, computed using (38), provides the comparison between scenarios where the effect of molecular noise is taken into

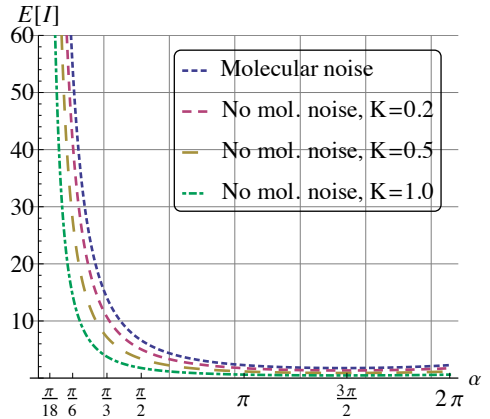


Fig. 7. The effect of molecular noise for cone antenna model.

account and neglected for cone antenna model and several values of absorption coefficient K . Expectedly, the scenario, where the molecular noise is considered leads to higher interference. When K increases from 0.2 to 0.5 to 1.0 the interference decreases.

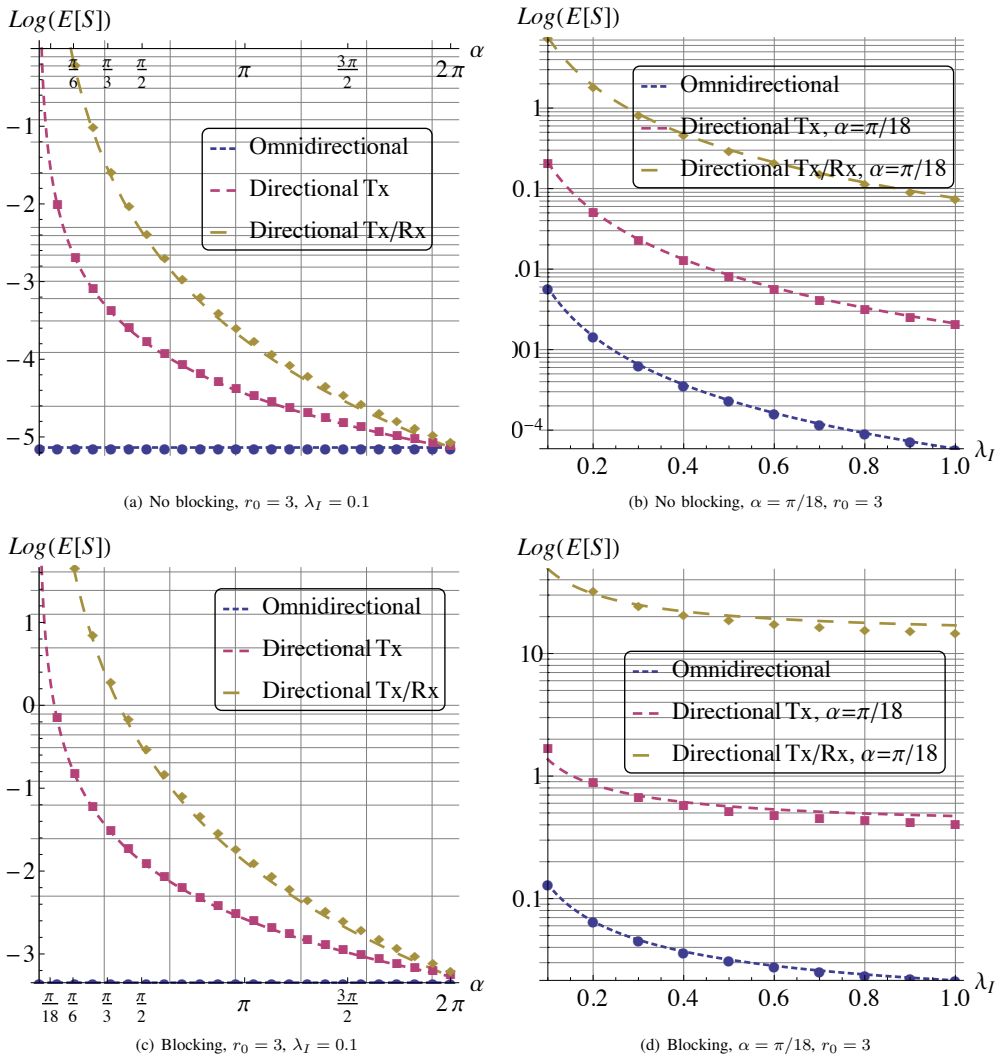


Fig. 8. Comparison of SINR for scenarios with omnidirectional and directional (cone) models.

B. SINR Assessment

The interference alone does not allow to make final conclusions about the performance of EHF/THF systems. The reason is that antenna directivity not only affects the interference but the useful received signal strength too. Below, we assess performance of the considered scenarios using mean SINR as a metric of interest concentrating on the cone antenna model.

1) *The Effect of Directivity*: The effect antenna directivity on the SINR, illustrated using (43) and (44), is demonstrated in Fig. 8(a) and Fig. 8(b) for $r_0 = 3$, when blocking is not taken into account. Fig. 8 also shows the results obtained by simulation of the considered scenarios. The model provides

accurate SINR approximations for a wide range of input parameters. For this reason, from now on, we use the analytical model only.

As one may observe from Fig. 8(a), the system with directional antennas shows better SINR performance compared to the one with omnidirectional antennas. When directivity is enabled at both sides the SINR improves even further. The SINR increases exponentially fast when the directivity of antennas increases. Recall, that the aggregated interference in this case also increases. However, it is compensated by the increase in the useful received power. We note that all the models converge to the same value for $\alpha = 2\pi$ further

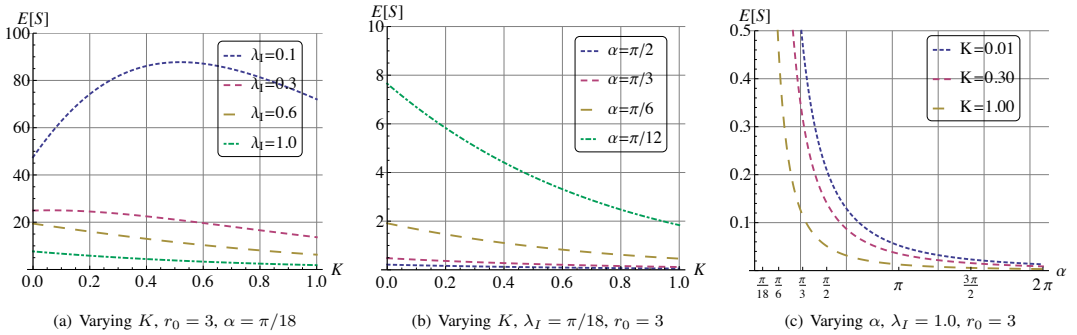


Fig. 9. Dependence of the SINR on the absorption coefficient K for cone antenna model.

confirming our derivations. We also note that the substantial increase in SINR when $\alpha \rightarrow 0$ may not be achieved in real systems due to the risk of antennas misalignment between transmitter and receiver.

Fig. 8(b) highlights that the increase in the density of interferers leads to the corresponding exponential decrease of SINR. The system with directional Tx and Rx greatly outperforms the system with directional Tx or Rx while the worst performance is observed for omnidirectional antennas. The effect of the distance between Tx and Rx, r_0 , on SINR has an expected behavior, that is, the SINR decreases with the increase of r_0 for all considered models, and for this reason is not shown here. The system with directional antennas at both Tx and Rx outperforms the one with omnidirectional one by approximately two orders of magnitude for all distances r_0 .

2) *The Effect of Blocking*: Consider now the effect of blocking on SINR. Fig. 8(c), computed using (43) and (44), shows the comparison between systems when blocking is taken into account. Comparing it to the results in Fig. 8(a) for no blocking case, one may observe, that even for rather small value of interferers density, $\lambda_I = 0.1$, the blocking effect drastically increases the resulting SINR. This conclusion is valid not only for directional antennas but for omnidirectional ones as well. Note that the behavior of the mean SINR curves is qualitatively similar to those shown in Fig. 8(a). In other words, the effect of blocking affects SINR numerically only.

Fig. 8(d) shows the effect of varying interferers intensity, λ_I , on the mean SINR. Similarly to the no blocking case the mean SINR decreases as the value of λ_I increases. However, as opposed to the no blocking case, SINR does not tend to zero as $\lambda_I \rightarrow 0$. Instead, it approaches a plateau for any given antennas directivity angle α . This behavior is explained by the fact, that for any chosen values of λ_I there is always a separation distance from the Rx such that all the interferers located outside are blocked. Note that in practice, the interference from such nodes may still reach the Rx via reflections and or diffuse scattering phenomena. However, according to the recent measurements, the contributions of these components are expected to be rather weak and may not drastically change the mean SINR structure [55].

3) *The Effect of Absorption Loss*: The effect of absorption loss on the mean SINR for directional antennas at both Tx

and Rx when blocking is taken into account is illustrated in Fig. 9, computed using (44). Observing the dependence on K in Fig. 9(a) we notice that the small values of λ_I always lead to higher SINR. However, the dependence is not linear and changes with λ_I . For small values of the intensity of interferers the mean SINR first increases approaching the maximum point and then decreases. On the other hand, for larger values of λ_I the mean SINR is a monotonously decreasing function of K . The underlying reason for this behavior is the effect of blocking and the presence of the molecular loss coefficient in both numerator and denominator of the SINR. Thus, when K and λ_I are both small, the numerator is not greatly affected by the absorption losses while blocking effectively conceal the interference in the denominator. Further, when K becomes greater than a certain value the numerator is heavily affected and the SINR decreases. For larger values of λ_I the effect of blocking cannot conceal the aggregated effect of interference even for small values of K .

Fig. 9(b), computed using (44), shows the effect of K on the mean SINR for different values of the antenna directivity angle α for directive antennas at both Tx and Rx and with blocking taken into account. Observe that for a given value of antenna directivity angle α the mean SINR decreases with the increase of K . This is explained by the effect of the denominator of the SINR. The detailed structure of the mean SINR as a function of α is further illustrated in Fig. 9(c), computed using (44). As one may observe, the mean SINR decreases as the antenna directivity increases. It is important that the gap between the environment with low and high absorption losses is high.

4) *The Effect of Molecular Noise*: Finally, Fig. 10 demonstrates the effect of molecular noise for a system with directional antennas at both Tx and Rx and with blocking taken into account. Recall, that according to (19), in presence of the molecular noise the exponential term disappears in the denominator of SINR making the aggregated interference stronger and still remains in numerator attenuating the useful received signal. Thus, expectedly, the mean SINR for $K = 1.0$ is lower compared to absence of molecular noise and $K = 1.0$ for the entire range of α . This conclusion is preserved for all intensities of interferers.

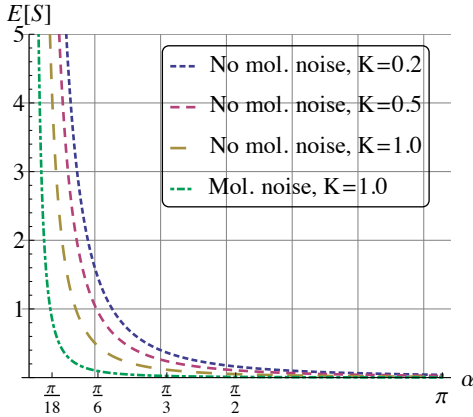


Fig. 10. The effect of molecular noise on SINR, $\lambda_I = 1$.

VII. CONCLUSIONS

In this paper, we have developed an analytical model for the mean interference and the SINR in mm-wave and THz communication networks. By utilizing the model, we have characterized the impact of the type of the antenna directivity and radiation pattern, the molecular absorption and blocking on aggregate interference and SINR in random Poisson deployment.

Our results show that for the same emitted power, the mean interference in a system with directional antennas drastically increases when directivity angle decreases. At the same time, the impact of the smaller directivity angle on the mean SINR is positive, as the received signal strength increases faster than the interference. The inherent property of EHF/THF bands of self-blocking of radiation by interferers leads to drastic performance improvements in terms of aggregate interference and SINR metrics compared to microwave systems. On the contrast, molecular absorption leads to the lower values of SINR. While molecular absorption loss further decreases the interference exponentially, it decreases the received signal strength too, and the effect on the latter is stronger. Finally, the effect of the molecular noise on SINR is also negative. The reason is that the useful received signal is still exponentially attenuated while the aggregated interference increases.

In our study, we have assumed that interferers completely blocks the EHF/THF radiation. In practice, reflections as well as diffuse scattering of EM waves inherent for these frequencies may still contribute to the aggregate interference at the Rx even when LoS is blocked, requiring advanced analysis.

APPENDIX A BLOCKING MODEL

Here, we derive the probability of blocking using the elements of the stochastic geometry and renewal theory. The idea is to find the mean length of the blocked and open intervals at the circumference of the circle of radius x and then

determine the probability of blocking of a random interferer located at x as a ratio of means of these intervals.

Consider the projection of blockers' along the radial lines as shown in Fig. 11(a). It forms a homogeneous Poisson process. Indeed, it is easy to prove that the process (i) has marginal Poisson distribution, (ii) is independent at all arc intervals, and (iii) is homogeneous. To demonstrate (i), we observe that the number of points projected at any arc of a fixed length equals to the number of points in the corresponding sector of a circle. Recalling that the number of points of a Poisson process falling into a certain area follows Poisson distribution we see that (i) holds true. The second property (ii) stems from the non-overlapping nature of sectors. Finally, (iii) is a direct consequence the homogeneity of the original Poisson process in \mathbb{R}^2 .

Let us determine the intensity of the blocker's projections on the circumference of the circle of radius x , $\lambda_P(x)$. This is accomplished by finding the mean number of points contained in the subsector of a circle defined by radii x and r_B , $S(r_B, x)$, where r_B is radius of a blocker. Recalling that the angle of the sector, α , is related to the chosen arc l_A as $\alpha = l_A/x$, while the area of the sector is related to the angle as $r^2\alpha/2$, we have

$$S(r_B, x) = \frac{l_A r_B^2}{2x}, \quad (45)$$

Expressing the area of the sector with radius x as $S(x) = l_A x/2$, the intensity $\lambda_P(x)$ is

$$\begin{aligned} \lambda_P(x) &= [S(x) - S(r_B, x)] \frac{1}{l_A} \lambda_I \\ &= \left(\frac{l_A x}{2} - \frac{l_A r_B^2}{2x} \right) \frac{\lambda_I}{l_A} = \frac{\lambda_I (x^2 - r_B^2)}{2x}. \end{aligned} \quad (46)$$

where $S(r_B, x) = l_A r_B^2/2x$ is the area of the difference between sectors of radius x and r_B , l_A is the length of the arc, r_B is the radius of the blocker.

So far we have dealt with a point process of centers of blockers. Consider now the RV W denoting the length of a "shadow" created by an individual blocker at circumference, in Fig. 11(b). Observe that it depends on the distance from Tx to the blocker. For $r \gg 2r_B$, where r is the distance from the base of Tx to Rx, we could replace the arc ARxB by a chord AB. Since the points of the Poisson process are uniformly distributed in a circle, the probability density function (pdf) of the distance to a randomly selected blocker is

$$f_L(r; x) = \frac{2r}{x^2 - r_B^2}, \quad r_B < r < x. \quad (47)$$

Observing Fig. 11(b), by simple geometry we see that

$$W = \frac{2xr_B}{L}, \quad (48)$$

where the distance to the blocker, L , is the only RV involved.

The density of W can be obtained using the RV transformation technique [56]. Although the inverse function $\psi(y) = 1/x$ has a discontinuity as $x \rightarrow 0$ over the domain of L , it is continuous. The modulo of the derivative of $\psi(y)$ is $1/y^2$.

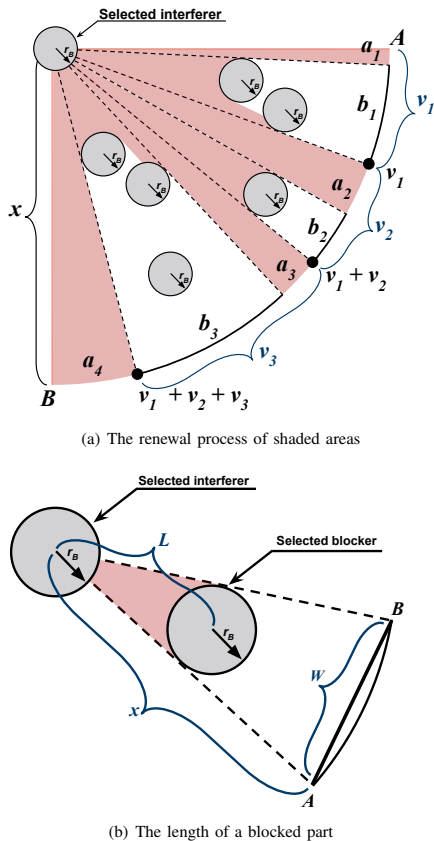


Fig. 11. Graphical illustrations of the blocking process.

Applying non-linear transformation in the form $2r_Bx/L$ the pdf of W can be written as

$$f_W(y; x) = f(\psi(y))|\phi'(y)| = \frac{8x^2r_B^2}{(x^2 - r_B^2)y^3}, \quad (49)$$

The mean of the shadow on the circumference is then

$$E[W(x)] = \int_{2r_B}^{2x} \frac{8x^2r_B^2}{(x^2 - r_B^2)y^3} dy = \frac{4r_Bx}{x + r_B}. \quad (50)$$

Consider now the projections of blockers onto the circumference of radius x , as shown in Fig. 11(a). The lengths of the projections of individual blockers are independent with density $f_W(x)$ and mean $E[W]$. It is easy to see that similarly to the centers of blockers, the left hand points and right hand points of individual blockers organize Poisson processes with the same intensity λ_P . The superposed process of all projections forms a renewal process with interchanging blocked and unblocked parts. An arbitrary point on the line is considered blocked if it belongs to one of the blocked interval. We find the probability of blocking as the ratio of the means of blocked interval to the sum of the means of blocked and unblocked intervals.

Let $a_i, b_i, i = 1, 2, \dots$, denote the lengths of unblocked and blocked intervals respectively, and define $v_i = a_i + b_i$. Points $0, v_1, v_1 + v_2, \dots, \sum_{j=1}^N v_j, \dots$, are the renewal moments that form the renewal process. The density of this process is [57]

$$f(x) = \lambda_P F_W(x) \exp\left(-\lambda_P \int_0^x [1 - F_W(y)] dy\right). \quad (51)$$

Let $f_V(t)$ be the pdf of $v_i, i = 1, 2, \dots$. The functions $f_V(x)$ and $f(x)$ are related to each other via the renewal equation as [57]

$$f(x) = f_V(x) + \int_0^x f_V(x-y)f(y)dy. \quad (52)$$

The length of the unblocked part a_j follows an exponential distribution with parameter λ_P [57]. This can be verified observing that the left-hand sides of individual shadows follow Poisson process with intensity λ_P . Thus, the distance from the end of the blocked part, considered as an arbitrary point, to the starting point of the next blocked interval is exponentially distributed.

Let $F_B(x)$ and $F_V(x)$ be the CDFs of the length of blocked intervals b_i , and joint blocked/unblocked intervals, V_i , respectively, with means $E[B]$ and $E[V]$. Let further $F_B^*(s)$ and $F_V^*(s)$ be the corresponding Laplace-Stieltjes (LT) transforms. For the joint interval V_i we have

$$F_V^*(s) = F_B^*(s)F_A^*(s) = \lambda_P \frac{F_B^*(s)}{\lambda_P + s}, \quad (53)$$

which can be solved for $F_B(x)$ in the RV domain as

$$F_B(x) = F_V(x) + \frac{f_V(x)}{\lambda_P}. \quad (54)$$

When $l \rightarrow \infty$ the renewal density approaches $1/E[V]$. From (51), it also equals to $f(x) = \lambda_P \exp(-\lambda_P E[W])$. Thus,

$$E[V] = \frac{1}{\lambda_P} \exp(\lambda_P E[W]). \quad (55)$$

Consequently, $E[B]$ can now be found as

$$\begin{aligned} E[B] &= \int_0^\infty \left(1 - F_V(x) - \frac{f_V(x)}{\lambda_P}\right) dx \\ &= E[V] - \frac{1}{\mu} = \frac{1}{\lambda_P} [\exp(\lambda_P E[W]) - 1]. \end{aligned} \quad (56)$$

The probability of blocking is thus

$$p_B(x) = \frac{E[B]}{E[A] + E[B]} = 1 - e^{-\lambda_P(x-r_B)r_B}, \quad (57)$$

where we substituted the mean of W from (50).

APPENDIX B TAYLOR EXPANSION APPROXIMATION

Here, we introduce the Taylor expansion approximation, used to derive the mean SIR and SINR in Section V. Let X and Y be RVs and let $Y = g(X)$, where $y = g(x)$ is some function. According to the conventional technique, to find the

TABLE II
 $E[I^2]$ FOR CONE ANTENNA PATTERN MODEL.

Model	No molecular noise	Molecular noise
No blocking, omnidirectional	$2\pi A^2 \lambda_I \Phi_1(R, r_B, K)$	$2\pi A^2 \lambda_I \Phi_1^*(R, r_B)$
Blocking, omnidirectional	$2\pi A^2 \lambda_I \Phi(R, r_B, \lambda_I, K)$	$2\pi A^2 \lambda_I \Phi^*(R, r_B, \lambda_I)$
No blocking, directional Tx or Rx	$A^2 \alpha \lambda_I \Phi_1(R, r_B, K)$	$A^2 \alpha \lambda_I \Phi_1^*(R, r_B)$
Blocking, directional Tx or Rx	$A^2 \alpha \lambda_I \Phi(R, r_B, \lambda_I, K)$	$A^2 \alpha \lambda_I \Phi^*(R, r_B, \lambda_I)$
No blocking, directional Tx + Rx	$\frac{A^2 \alpha \lambda_I}{2\pi} \Phi_1(R, r_B, K)$	$\frac{A^2 \alpha \lambda_I}{2\pi} \Phi_1^*(R, r_B)$
Blocking, directional Tx and Rx	$\frac{A^2 \alpha \lambda_I}{2\pi} \Phi(R, r_B, \lambda_I, K)$	$\frac{A^2 \alpha \lambda_I}{2\pi} \Phi^*(R, r_B, \lambda_I)$

pdf of Y , we need pdf of X . Also, when pdf of X is known the raw moments of Y can be found directly as

$$E[Y^v] = \int_{-\infty}^{\infty} [g(x)]^v f_X(x) dx. \quad (58)$$

In our case the pdf of interference is not known and only moments can be obtained. Thus, the task is to determine moments of Y based on the moments of X given a certain $y = g(x)$. Note that knowing the moments of SIR and SINR one may also obtain bounds in the form $Pr\{Y \leq y\}$ applying Markov or Chebyshev inequalities.

Let $g(x)$ be infinitely differentiable function. Let also μ_i and β_i , $i = 0, 1, \dots$, be the raw and central moments of X , respectively, i.e., $\mu_i = E[X^i]$, $\beta_i = E[(X - \mu_0)^i]$. Consider the Taylor series expansion of $g(x)$ around μ , that is,

$$g(x) = \sum_{i=0}^{\infty} \frac{g^{(i)}(\mu_0)}{i!} (x - \mu_0)^i. \quad (59)$$

Taking expectations from both sides of (59) we get

$$E[g(x)] = \sum_{i=0}^{\infty} \frac{g^{(i)}(\mu_0)}{i!} E[(x - \mu_0)^i]. \quad (60)$$

where $g^{(i)}(x)$ denotes i th derivative of $g(x)$.

Noting that $\beta_i = E[(x - \mu_0)^i]$, $E[g(x)] = E[Y]$ we it as

$$E[Y] = \sum_{i=0}^{\infty} \frac{g^{(i)}(\mu_0)}{i!} \beta_i. \quad (61)$$

Knowing the central moments of X and leaving a certain amount of terms in (61) we could approximate the mean of Y with any given accuracy. For practical applications two or three terms often suffice. Analyzing (61) one may observe that the first term $\beta_1 = E[X - \mu_0]$ is always zero. Thus, in what follows, we use

$$E[Y] = g(\mu_0) + \frac{g''(\mu_0)}{2} \sigma^2[X], \quad (62)$$

where $\sigma^2[X]$ is the variance of X .

Let $a_i = g^{(i)}/i!$ and consider the variance of Y . Using $\sigma^2[Y] = E[Y^2] - (E[Y])^2$ we can show

$$\begin{aligned} (E[Y])^2 &= \sum_{i=0}^{\infty} a_i^2 \beta_i^2 + \sum_{i=0}^{\infty} a_i \beta_i \sum_{j=i+1}^{\infty} a_j \beta_j \\ &= a_0^2 + 2a_0 \sum_{i=2}^{\infty} a_i \beta_i + \left(\sum_{i=2}^{\infty} a_i \beta_i \right)^2, \end{aligned} \quad (63)$$

where we separated quadratic and linear terms.

Using the Taylor series expansion around μ , squaring it and taking expectations we arrive at

$$E[Y^2] = \sum_{i=0}^{\infty} b_i \beta_i, \quad (64)$$

where the sequence b_i is given by

$$b_i = \begin{cases} a_{i/2}^2 + 2 \sum_{k=0}^{i/2-1} a_k a_{i-k}, & i \text{ is even} \\ 2 \sum_{k=0}^{\lfloor n/2 \rfloor} a_k a_{i-k}, & i \text{ is odd} \end{cases}, \quad (65)$$

and $\lfloor \cdot \rfloor$ denotes the floor function.

Leaving linear terms in (63) and (64) and simplifying

$$\sigma^2[Y] = \sum_{i=2}^{\infty} c_i \beta_i + \left(\sum_{i=2}^{\infty} a_i \beta_i \right)^2, \quad (66)$$

where the sequence c_i is

$$c_i = \begin{cases} a_{i/2}^2 + 2 \sum_{k=1}^{i/2-1} a_k a_{i-k}, & i \text{ is even} \\ 2 \sum_{k=1}^{\lfloor n/2 \rfloor} a_k a_{i-k}, & i \text{ is odd} \end{cases}. \quad (67)$$

The approximation for variance is now given by

$$\sigma^2[Y] = [g'(\mu_0)]^2 \sigma^2[X] - \frac{1}{4} [f''(\mu_0) \sigma^2[X]]^2, \quad (68)$$

where we also included the quadratic correction term.

APPENDIX C VARIANCE OF INTERFERENCE

There are two ways to find variance of interference. According to the first approach we (i) determine the distribution of distance to a randomly chosen interferer that is not blocked, (ii) estimate the moments of the interference from this nodes, (iii) observe that the number of non-blocked interferers follows Poisson distribution with reduced intensity and, finally, (iv) obtain the variance of aggregated interference as a variance of a random sum of RVs, see, e.g., [56]. Note that this approach can also be used to find mean interference (via Wild's identity) and it is feasible due to finite mean and variance of interference from a single node.

$$\Phi = \frac{4R^2(K + \lambda_I r_B)^2 e^{2R(K + \lambda_I r_B)} Ei(2R(r_B \lambda_I + K)) + 2KR + 2\lambda_I R r_B - 1}{2R^2 e^{-2\lambda_I r_B(r_B - R)} - 2KR} \Bigg|_{r_B}^R \quad (70)$$

$$\Phi_1(R, r_B, K) = \left(2K^2 Ei(-2KR) + e^{-2KR} \left(\frac{K}{R} - \frac{1}{2R^2} \right) \right) \Bigg|_{r_B}^R,$$

$$\Phi_1^*(R, r_B) = \frac{1}{2r_B^2} - \frac{1}{2R^2}, \quad \Phi^*(R, r_B, \lambda_I) = \frac{\lambda_I^2 R^2 r_B^2 e^{\lambda_I R r_B} Ei(-R r_B \lambda_I) + \lambda_I R r_B - 1}{2R^2 e^{-\lambda_I r_B(r_B - R)}} \Bigg|_{r_B}^R, \quad (71)$$

In what follows, we rely on the approach similar to that we used for finding mean interference in Sec. IV. Particularly, representing the variance of interference as $\sigma^2[I] = E[I^2] - (E[I])^2$ we will be looking for $E[I^2]$. Owing to the independence of the RVs representing the number of points of a Poisson process in non-overlapping areas we use integral expressions to get $E[I^2]$. Since the derivation is similar for all considered cases, we demonstrate the approach it for cone antenna model with blocking and Tx (or Rx) directivity.

Taking into account Tx (or Rx) directivity and blocking we write

$$\begin{aligned} E[I^2] &= \int_{r_B}^R (Ar^{-2} e^{-Kr})^2 e^{-\lambda_I(x-r_B)r_B} \frac{\alpha}{2\pi} 2\lambda_I \pi r dr \\ &= \frac{A^2 \alpha^2 \lambda_I}{2\pi} \Phi(R, r_B, \lambda_I, K), \end{aligned} \quad (69)$$

where $\Phi(R, r_B, \lambda_I, K)$ is given in (70). The second raw moment for cone antenna model without blocking and/or directivity is found similarly to (69). Also, one can use this approach to obtain $E[I^2]$ for cone-plus-sphere model. The resulting expressions for cone antenna models are shown in Table II, where $\Phi_1(R, r_B, K)$, $\Phi_1^*(R, r_B)$, and $\Phi^*(R, r_B, \lambda_I)$ are given in (71).

REFERENCES

- [1] V. Petrov, M. Komarov, D. Moltchanov, J. M. Jornet, and Y. Koucheryav, "Interference analysis of EHF/THF communications systems with blocking and directional antennas," in *Proc. of IEEE Global Communications Conference (GLOBECOM)*, December 2016.
- [2] Cisco, "Cisco visual networking index: Global mobile data traffic forecast update, 2014-2019," 2015.
- [3] Qualcomm, "The 1000x mobile data challenge," Tech. Rep., 2013.
- [4] Y. Niu, Y. Li, D. Jin, L. Su, and A. V. Vasilakos, "A survey of millimeter wave communications (mmwave) for 5G: Opportunities and challenges," *Wireless Networks*, vol. 21, no. 8, pp. 2657-2676, April 2015.
- [5] S. Rey, "TERAPAN: Ultra-high data rate transmission with steerable antennas at 300 GHz," IEEE 802.15-15-0167-02-0thz, March 2015.
- [6] J. Boyd, "Fujitsu makes a THz receiver small enough for a smartphone," <http://www.spectrum.ieee.org/tech-talk/telecom/wireless/fujitsu-makes-a-terahertz-receiver-small-enough-for-a-smartphone>, October 2015.
- [7] V. Petrov, D. Moltchanov, and Y. Koucheryav, "Applicability assessment of terahertz information showers for next-generation wireless networks," in *Proc. of IEEE International Conference on Communications (ICC)*, May 2016.
- [8] I. F. Akyildiz, J. M. Jornet, and C. Han, "TeraNets: Ultra-broadband communication networks in the terahertz band," *IEEE Wireless Communications Magazine*, vol. 21, no. 4, pp. 130-135, August 2014.
- [9] S. Kim, W. T. Khan, A. Zajic, and J. Papapolymerou, "D-band channel measurements and characterization for indoor applications," *IEEE Transactions on Antennas and Propagation*, vol. 63, no. 7, pp. 3198-3207, July 2015.
- [10] V. Petrov, A. Pyattaev, D. Moltchanov, and Y. Koucheryav, "Terahertz band communications: Applications, research challenges, and standardization activities," in *Proc. of International Congress on Ultra Modern Telecommunications and Control Systems (ICUMT)*, October 2016.
- [11] S. Kim and A. G. Zajic, "Statistical characterization of 300-GHz propagation on a desktop," *IEEE Transactions on Vehicular Technology*, vol. 64, no. 8, pp. 3330-3338, August 2015.
- [12] M. Akdeniz, Y. Liu, M. Samimi, S. Sun, S. Rangan, T. S. Rappaport, and E. Erkip, "Millimeter wave channel modeling and cellular capacity evaluation," *IEEE Journal on Selected Areas in Communications*, vol. 32, no. 6, pp. 1164-1179, June 2014.
- [13] J. M. Jornet and I. F. Akyildiz, "Channel modeling and capacity analysis for electromagnetic wireless nanonetworks in the terahertz band," *IEEE Transactions on Wireless Communications*, vol. 10, no. 10, pp. 3211-3221, October 2011.
- [14] L. S. Rothman *et al.*, "HITRAN: High-resolution transmission molecular absorption database," Harvard-Smithsonian Center for Astrophysics, www.cfa.harvard.edu, 2014.
- [15] J. G. Andrews, S. Buzzi, W. Choi, S. Hanly, A. Lozano, A. Soong, and J. Zhang, "What will 5G be?" *IEEE Journal on Selected Areas in Communications*, vol. 32, no. 6, pp. 1065-1082, June 2014.
- [16] N. Bhushan, J. Li, D. Malladi, R. Gilmore, D. Brenner, A. Damnjanovic, R. Sukhvasi, C. Patel, and S. Geirhofer, "Network densification: The dominant theme for wireless evolution into 5G," *IEEE Communications Magazine*, vol. 52, no. 2, pp. 82-89, 2014.
- [17] J. G. Andrews, H. Claussen, M. Dohler, and S. Rangan, "Femtocells: Past, present, and future," *IEEE Journal on Selected Areas in Communications*, vol. 30, no. 3, pp. 497-508, April 2012.
- [18] J. Lee, H. Wang, J. G. Andrews, and D. Hong, "Outage probability of cognitive relay networks with interference constraints," *IEEE Transactions on Wireless Communications*, vol. 10, no. 2, pp. 390-395, February 2011.
- [19] G. Fodor, S. Parkvall, S. Sorrentino, P. Wallentin, Q. Lu, and N. Brahm, "Device-to-device communications for national security and public safety," *IEEE Access*, vol. 2, no. 1, pp. 1510-1520, April 2014.
- [20] T. Bai, R. Vaze, and R. W. Heath Jr., "Using random shape theory to model blockage in random cellular networks," in *Proc. of International Conference on Signal Processing and Communications (SPCOM)*, July 2012.
- [21] —, "Analysis of blockage effects on urban cellular networks," *IEEE Transactions on Wireless Communications*, vol. 13, no. 9, pp. 5070-5083, September 2014.
- [22] J. Kokkonen, V. Petrov, D. Moltchanov, J. Lehtomaki, Y. Koucheryav, and M. Juntti, "Wideband terahertz band reflection and diffuse scattering measurements for beyond 5G indoor wireless networks," in *Prof. of European Wireless Conference*, May 2016.
- [23] S. Kim and A. Zajic, "Statistical modeling and simulation of short-range device-to-device communication channels at sub-THz frequencies," *IEEE Transactions on Wireless Communications*, vol. 15, no. 9, pp. 6423-6433, September 2016.
- [24] M. Gapeyenko *et al.*, "Analysis of human body blockage in millimeter-wave wireless communications systems," in *Proc. of IEEE International Conference on Communications (ICC)*, May 2016.
- [25] J. G. Andrews, R. K. Ganti, M. Haenggi, N. Jindal, and S. Weber, "A primer on spatial modeling and analysis in wireless networks," *IEEE Communications Magazine*, vol. 48, no. 11, pp. 156-163, November 2010.

- [26] P. Cardieri, "Modeling interference in wireless ad hoc networks," *IEEE Communications Surveys and Tutorials*, vol. 12, no. 4, pp. 551–572, Fourth Quarter 2010.
- [27] M. Win, P. Pinto, and L. Shepp, "A mathematical theory of network interference and its applications," *Proceedings of the IEEE*, vol. 97, no. 2, pp. 205–230, February 2009.
- [28] M. Haenggi, J. G. Andrews, F. Baccelli, O. Dousse, and M. Franceschetti, "Stochastic geometry and random graphs for the analysis and design of wireless networks," *IEEE Journal on Selected Areas in Communications*, vol. 27, no. 7, pp. 1029–1046, September 2009.
- [29] M. Haenggi, "Mean interference in hard-core wireless networks," *IEEE Communications Letters*, vol. 15, no. 8, pp. 792–794, August 2011.
- [30] H. ElSawy and E. Hossain, "On stochastic geometry modeling of cellular uplink transmission with truncated channel inversion power control," *IEEE Transactions on Wireless Communications*, vol. 13, no. 8, pp. 4454–4469, August 2014.
- [31] A. K. Gupta, X. Zhang, and J. G. Andrews, "SINR and throughput scaling in ultradense urban cellular networks," *IEEE Wireless Communications Letters*, vol. 4, no. 6, pp. 605–608, December 2015.
- [32] K. Venugopal and R. W. Heath Jr., "Millimeter wave networked wearables in dense indoor environments," *IEEE Access*, vol. 4, pp. 1205–1221, March 2016.
- [33] A. Thornburg, T. Bai, and R. W. Heath Jr., "Interference statistics in a random mmwave ad hoc network," in *Proc. of IEEE International Conference on Acoustics, Speech and Signal Processing (ICASSP)*, April 2015.
- [34] K. Venugopal and R. W. Heath Jr., "Location based performance model for indoor mmwave wearable communication," in *Proc. of IEEE International Conference on Communications (ICC)*, May 2016.
- [35] K. Venugopal, M. C. Valenti, and R. W. Heath Jr., "Interference in finite-sized highly dense millimeter wave networks," in *Proc. of Information Theory and Applications Workshop (ITA)*, February 2015.
- [36] M. Di Renzo, "Stochastic geometry modeling and analysis of multi-tier millimeter wave cellular networks," *IEEE Transactions on Wireless Communications*, vol. 14, no. 9, pp. 5038–5057, September 2015.
- [37] S. Singh, M. N. Kulkarni, A. Ghosh, and J. G. Andrews, "Tractable model for rate in self-backhauled millimeter wave cellular networks," *IEEE Journal on Selected Areas in Communications*, vol. 33, no. 10, pp. 2196–2211, May 2015.
- [38] M. Rebato, M. Mezzavilla, S. Rangan, F. Boccardi, and M. Zorzi, "Understanding noise and interference regimes in 5G millimeter-wave cellular networks," *CoRR*, vol. abs/1604.05622, 2016. [Online]. Available: <http://arxiv.org/abs/1604.05622>
- [39] M. Rebato, "Simulation analysis of algorithms for interference management in 5G cellular networks using spatial spectrum sharing," Ph.D. dissertation, University of Padova, 2015.
- [40] J. M. Jornet and I. F. Akyildiz, "Low-weight channel coding for interference mitigation in electromagnetic nanonetworks in the terahertz band," in *Proc. of IEEE International Conference on Communications (ICC)*, June 2011.
- [41] V. Petrov, D. Moltchanov, and Y. Koucheryavy, "Interference and SINR in dense terahertz networks," in *Proc. of IEEE Vehicular Technology Conference (VTC-Fall)*, September 2015.
- [42] S. Singh, R. Mudumbai, and U. Madhow, "Interference analysis for highly directional 60-GHz mesh networks: The case for rethinking medium access control," *IEEE/ACM Transactions on Networking*, vol. 19, no. 5, pp. 1513–1527, October 2011.
- [43] L. X. Cai, L. Cai, X. Shen, and J. W. Mark, "REX: A randomized EXclusive region based scheduling scheme for mmWave WPANs with directional antenna," *IEEE Transactions on Wireless Communications*, vol. 9, no. 1, pp. 113–121, January 2010.
- [44] M. X. Gong, R. Stacey, D. Akhmetov, and S. Mao, "A directional CSMA/CA protocol for mmWave wireless PANs," in *Proc. of IEEE Wireless Communication and Networking Conference (WCNC)*, April 2010.
- [45] E. Shihab, L. Cai, and J. Pan, "A distributed asynchronous directional-to-directional mac protocol for wireless ad hoc networks," *IEEE Transactions on Vehicular Technology*, vol. 58, no. 9, pp. 5124–5134, November 2009.
- [46] Q. Xia, Z. Hossain, M. Medley, and J. M. Jornet, "A link-layer synchronization and medium access control protocol for terahertz-band communication networks," in *Proc. of IEEE Global Communications Conference (GLOBECOM)*, December 2015.
- [47] J. M. Jornet and I. F. Akyildiz, "Femtosecond-long pulse-based modulation for terahertz band communication in nanonetworks," *IEEE Transactions on Communications*, vol. 62, no. 5, pp. 1742–1754, May 2014.
- [48] S. Chandrasekhar, *Radiative Transfer*. Dover Publications, 1960.
- [49] P. Boronin, V. Petrov, D. Moltchanov, Y. Koucheryavy, and J. M. Jornet, "Capacity and throughput analysis of nanoscale machine communication through transparency windows in the terahertz band," *Elsevier Nano Communication Networks*, vol. 5, no. 3, pp. 72–82, September 2014.
- [50] J. Kokkonen, J. Lehtomaki, and M. Juntti, "A discussion on molecular absorption noise in the terahertz band," *Elsevier Nano Communication Networks*, vol. 8, pp. 35–45, June 2016.
- [51] L. Kish, "Stealth communication: Zero-power classical communication, zero-quantum quantum communication and environmental-noise communication," *Applied Physics Letters*, vol. 87, no. 23, December 2005.
- [52] N. Atindra and A. Ghosh, "Ultralow noise field-effect transistor from multilayer graphene," *Applied Physics Letters*, vol. 95, no. 8, August 2009.
- [53] V. Petrov, D. Moltchanov, and Y. Koucheryavy, "On the efficiency of spatial channel reuse in ultra-dense thz networks," in *Proc. of IEEE Global Communications Conference (GLOBECOM)*, December 2015.
- [54] T. S. Rappaport, *Wireless Communications: Principles and Practice*. Prentice Hall, 2002.
- [55] M. R. Akdeniz, Y. Liu, M. K. Samimi, S. Sun, S. Rangan, T. S. Rappaport, and E. Erkip, "Millimeter wave channel modeling and cellular capacity evaluation," *IEEE Journal on Selected Areas in Communications*, vol. 32, no. 6, pp. 1164–1179, June 2014.
- [56] S. Ross, *Introduction to probability models*. Academic Press, 2010.
- [57] D. R. Cox, *Renewal theory*. Methuen and Co Ltd., 1970.

PUBLICATION

II

Last Meter Indoor Terahertz Wireless Access: Performance Insights and Implementation Roadmap

V. Petrov, J. Kokkonen, D. Moltchanov, J. Lehtomaki, Y. Koucheryavy and
M. Juntti

IEEE Communications Magazine 56.6 (2018), 158–165

Publication reprinted with the permission of the copyright holders

Last Meter Indoor Terahertz Wireless Access: Performance Insights and Implementation Roadmap

Vitaly Petrov[†], Joonas Kokkonen, Dmitri Moltchanov, Janne Lehtomäki, Yevgeni Koucheryavy, Markku Juntti

Abstract—The terahertz (THz) band, 0.1–10 THz, has sufficient resources not only to satisfy the 5G requirements of 10 Gbit/s peak data rate but to enable a number of tempting rate-greedy applications. However, the THz band brings novel challenges, never addressed at lower frequencies. Among others, the scattering of THz waves from any object, including walls and furniture, and ultra-wideband highly-directional links lead to fundamentally new propagation and interference structures. In this article, we review the recent progress in THz propagation modeling, antenna and testbed designs, and propose a step-by-step roadmap for wireless THz Ethernet extension for indoor environments. As a side effect, the described concept provides a second life to the currently underutilized Ethernet infrastructure by using it as a universally available backbone. By applying real THz band propagation, reflection, and scattering measurements as well as ray-tracing simulations of a typical office, we analyze two representative scenarios at 300 GHz and 1.25 THz frequencies illustrating that extremely high rates can be achieved with realistic system parameters at room scales.

Index Terms—Terahertz band communications, beyond-5G networks, massive data offloading, last-meter connectivity, ray-based modeling, THz band propagation measurements.

I. INTRODUCTION

The ever-increasing wireless data demands place extreme requirements on the future communications systems. In addition to physical layer improvements including advanced coding, massive multiple-input and multiple-output (massive MIMO), and cognitive radio systems, researchers currently investigate a number of architectural solutions. Since most of the traffic is generated indoors, the future systems are expected to rely on a significant number of indoor small cells to *massively offload heavy traffic* from cellular networks. To enable this, the millimeter wave (mmWave) frequencies such as 28 GHz, 60 GHz have been recently investigated. However, the use of mmWaves still leads to certain limitations as the shared throughput indoors will only approach a few Gbit/s.

Several wireless communication actors are already investigating the use of even higher frequencies available in the terahertz (THz), 0.1–10 THz, frequency band, e.g. 120 GHz

V. Petrov, D. Moltchanov, and Y. Koucheryavy are with the Laboratory of Electronics and Communications Engineering, Tampere University of Technology, Tampere, Finland.

J. Kokkonen, J. Lehtomäki, and M. Juntti are with the Centre for Wireless Communications, University of Oulu, Oulu, Finland.

The work of V. Petrov, D. Moltchanov, and Y. Koucheryavy was supported by Academy of Finland. The work of J. Kokkonen, J. Lehtomäki, and M. Juntti was supported by Horizon 2020, European Union's Framework Programme for Research and Innovation, under grant agreement No. 761794 (TERRANOVA project). V. Petrov also acknowledges the support by Nokia Foundation and HPY Research Foundation funded by Elisa.

Manuscript submitted March 2016; revised January 2017, October 2017, and January 2018; accepted February 2018.

[†]V. Petrov is the contact author: vitaly.petrov@tut.fi

and 300 GHz and even the entire THz band [1]. With extreme antenna gains, a number of testbeds operating in the lower THz band have already demonstrated data rates on the order of tens of Gbit/s over hundreds of meters as in [2]. In indoor environments with mobility of users, realistically, the THz band is the most suitable for short link distances such as few meters. The achievable capacity at such distances could be extremely high, approaching hundreds of Gbit/s [1], [3].

The potential of THz band has been recently recognized by IEEE, which formed an IEEE 802.15.3d Task Group identifying THz band communications as a feasible wireless technology for extremely high access rates of up to 100 Gbit/s. If properly integrated into the existing infrastructure, a wireless communications solution operating in the THz band could become a technology enabler for massive data offloading, satisfying 10 Gbit/s peak data rate requirement of 5G systems, as well being the first competitor to wired Internet access potentially providing comparable data rates and latency.

Together with the exceptional promises, THz communications bring novel unique challenges requiring to rethink the classic communications mechanisms. The ultra-wideband extremely directional nature of the communications links leads to the fundamentally new propagation and interference structures in a system with multiple reflected, diffracted and scattered beams causing complex received signal waveform. Medium access protocols have to operate with narrowly focused beams, fast handover procedures have to include the time required for localization and tracking functionalities. This combination of challenges is unique to the THz systems and has never been observed at lower frequencies. Finally, the question of enabling an ultra-high speed wireless access is related to finding cost-effective solutions for connecting it to the Internet. This is foreseen as a hidden bottleneck of wireless systems that may strike in the near future.

In this article, we present the roadmap towards an indoor THz communications technology well integrated into the existing infrastructure. Specifying the steps needed to achieve the goals and related challenges allows to unify the efforts of the community to build a solid way towards networking in the THz band. We also perform an extensive joint measurement-simulation campaign to report the capacity and signal-to-noise ratio (SNR) in typical indoor scenarios for the existing level of electronics and transceivers.

The attractive values of estimated capacity and data rates confirm the claim that the successful implementation of THz wireless access will provide the bearer technology not only for conventional Internet access and massive data offloading but to a number of emerging applications requiring exceptionally high data rates in indoor scenarios, such as augmented reality,

mobile-edge computing, and holographic communications.

The article is organized as follows. In the next section, we describe the state-of-the-art in THz communications highlighting the lessons learned over the last two decades. Later on, we introduce the vision of the last-meter THz access and assess its potential for realistic indoor scenarios is performed next. The roadmap towards fully integrated THz systems is then outlined. Conclusions are drawn in the last section.

II. THz COMMUNICATIONS: THE LESSONS LEARNED

A. THz Emitters

One of the reasons for slow take-off of THz communications technologies has been the unique technical challenge, known as the *THz gap* [4]. The THz frequency range is too high for the regular oscillators and too low for the optical photon emitters to let any of them be used as a THz signal generator. Thereby, THz waves are often generated by either a combination of lower frequency oscillator and frequency multiplier or an optical signal source (e.g., laser) and frequency divider. Both approaches have the overall efficiency several orders of magnitude lower than that of direct signal generator.

The applicability of both Si and SiGe technologies is limited to $\sim 200\text{--}300\text{ GHz}$. This intrinsic device speed limitation is set by the transit time of the carriers through the material. Materials beyond the conventional Si and SiGe for THz applications include GaN, InP, and metamorphic technologies. These materials exhibit high electron mobility and large material breakdown voltage. InP-based and GaN HEMTs have been reported with a cut-off frequency greater than 600 GHz and maximum oscillation frequency higher than 1.2 THz. Resonant tunneling diodes (RTDs) are also actively studied for building THz semiconductor oscillators.

Current efforts to increase the output power at THz include the iBROW project targeting transmits more than 1mW with RTD on a III-V with Si platform. Optoelectronic RTD could enable mmWave or THz femtocells connected to high-speed optical networks. Portable devices are pursued with all-electronic RTD¹. The DARPA THzE program target is 10 mW at 1.03 THz [5]. Finally, nanoplasmonic technologies, manipulating electromagnetic radiation at the scales smaller than the wavelength of light, and, thus, overcoming the diffraction limit, have recently attracted special attention [6].

B. THz Wave Propagation

The abovementioned efforts promise to soon close the THz gap allowing for compact yet powerful THz transceivers. However, even if the THz signal can be generated and received, a challenge that still questions the applicability of the THz band for communications is the attenuation of the THz signal with distance. The frequency dependency of the free space path loss comes from the frequency dependent antenna aperture of the receiver. The effective antenna aperture is *million times* lower at 1 THz than at 1 GHz, resulting in 60 dB higher attenuation. The transmit power at THz will likely also be lower. As a

¹H2020 project “Innovative ultra-BROadband ubiquitous Wireless communications through terahertz transceivers (iBROW)”: <http://ibrow-project.eu/> [Accessed 10-02-2017]

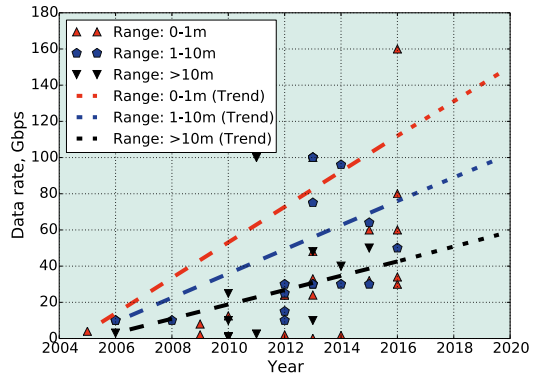


Fig. 1. Advances in THz communications prototypes.

result, for reliable connectivity over a few meters, high gain antennas on both Tx and Rx are needed. This is feasible as high gain antennas are easier to construct at higher frequencies.

Molecules absorb electromagnetic energy at their resonance frequencies. Notable already for mmWaves, molecular absorption becomes much more harmful in the THz band. Following the Beer-Lambert law, the absorption loss is *exponential* in the distance. To overcome this issue, the use of the sub-bands less affected by molecular absorption, so-called “transparency windows” (e.g. 0.1–0.54 THz), have been recently proposed [3].

The absorption of energy by the environment results in the so-called *molecular noise* as the absorbed energy is released back to the environment. This noise has been studied over the last few years as its presence may complicate link and system level analyses [9]. There is yet no definite conclusion about its effect as this theoretically predicted phenomenon has never been observed in real experiments [10]. However, the majority of the models predict its level to be proportional to the received power level, and, thus, rapidly decreasing with distance.

C. THz Communication Prototyping

Several testbeds have already been demonstrated, especially, in the lower end of the THz band. In [4], quadrature phase shift keying (QPSK) modulator and demodulator have been demonstrated at 0.3 THz. A miniature 15 dBi gain antenna with maximum dimension of 5mm with easy to connect to package has also been reported [4]. By integrating antenna and other components, a compact THz module can be developed. Communication at 0.385 THz has been demonstrated in [11] using photonics based emitter and electronic receiver using oscilloscope, 32 Gbit/s data rate at link distances of 0.4 m was achieved with QPSK. Recently, a 0.3 THz prototype receiver small enough to fit in a mobile phone was presented by Fujitsu [12]. Communication distance is currently limited to about 1 meter only and data rates are in the order of 20 Gbit/s. At the same time, this data rate is an order of magnitude larger than what could be achieved with lower bands.

Broadening the summary, Fig. 1 illustrates the evolution of the THz communications test benches. Based on the com-

TABLE I
THE PROSPECTIVE APPLICATIONS OF THZ WIRELESS COMMUNICATIONS.
SUMMARY OF IEEE 802.15.3D VISION (BASED ON [7], [8], AND INDIVIDUAL CONTRIBUTIONS)

Application	Topology	Antennas directivity	Beam steering	Range, m	Data rates, Gbit/s	Target BER
Wireless backhaul	Point-to-point	Extremely directive (>50dBi each side)	Not required	500	10–100	10^{-12}
Wireless fronthaul	Ad hoc	Highly directive (Base station: >20dBi)	Mandatory	200	10–100	10^{-12}
Data centers	Point-to-point	Highly directive (>20dBi each side)	Not required	100	1/10/40/100	10^{-12}
Kiosk downloading	Point-to-point	Directive (>10dBi kiosk side)	Optional	0.1	1–100	10^{-6}
Intra-chip networks	Ad hoc	Deployment specific	Optional	0.03	1–100	10^{-12}

munication range, we group them into three categories and supplement each group with the “averaged” line, highlighting the trend. The data are partially reproduced from [13] and supplemented with the recently published materials. Analyzing these data, we stress the following three main points. First, the achieved data rate is constantly growing for all demonstrated categories. Then, the growth rate is, expectedly, inverse proportional to the communication range. That is, the shorter communication range is, the faster the achieved data rate is. Finally, as one may observe, the growth of the middle line (“Range: 1–10 m” that we concentrate on in this paper) allows us to expect the 100 Gbit/s solutions to appear by 2020.

These practical testbeds and the progress with RTDs illustrate the progress in THz technology and the possibility to soon convert the testbeds into an operational networking solution.

D. IEEE THz Standardization Activity

The process of standardizing THz communications technology started back in 2008, when a Terahertz Interest Group (IGthz) has been established under the IEEE 802.15 family. During 2008–2013 this group led by TUBS, NICT, Intel, NTT, and AT&T studied the fundamental limitations and capabilities of THz band. In 2014, it has been reformed to an IEEE 802.13.3d Task Group on “100G wireless” (TG100G) aiming to develop a PHY-MAC layer solution for wireless communications in the lower THz band, 252–325 GHz, [8].

The IEEE vision on prospective applications for the THz communications and associated technical requirements are summarized in Table I. The scenarios range from wired links replacement in future electronics (e.g., intra-chip communications) and data centers to backhaul and fronthaul links for beyond 5G mobile systems. The range of applicable communications distances is from 3 cm to 500 m. Surprisingly, the list of the applications, envisioned by IEEE 802.15.3d group, has a gap in the range 0.1–100 m. However, based on the trends in THz technology development and constantly increasing demands for higher rates at the air interface, we believe that indoor wireless access via the THz band in the range 0.1–10 m has to be also addressed as one of the potential applications. In the following section, we describe the roadmap towards the last-meter terabit-per-second wireless access and highlight the associated research and engineering challenges.

III. THE LAST METER THz WIRELESS ACCESS VISION

A. The THz Plug Concept

Motivated by the recent progress in THz transceiver design, in this section, we introduce a high data rate “last-meter”

indoor THz communications system reusing the existing Ethernet infrastructure for Internet connectivity and massive traffic offloading from wireless local area and cellular networks. The presented concept is well integrated into the network infrastructure and represents a disruptive shift from the current access systems leading to rapid performance improvements.

The envisioned *THz plug*, see Fig. 2, is a low-cost THz hotspot that is inserted into an Ethernet socket connected to standard Ethernet infrastructure and, if copper wire medium is used, powered via Power-over-Ethernet (PoE) technology. If a THz plug is placed next to the office desk, a user can reliably connect a laptop or tablet to a *multi-gigabit-a-second* wireless link on any location on the table or few meters around.

The Ethernet infrastructure is already deployed in the offices and some other venues, leading to efficient and cost-effective data offloading to/from the high data rate THz interface. Currently, the Ethernet infrastructure is severely under-utilized due to the popularity of WLAN technologies. The envisioned system helps users to avoid convenience/performance trade-off by combining advantages of both wired and wireless networks and to fully benefit from the extraordinary rates offered by the THz frequency band. In conjunction with the modern Ethernet backbone, it enables truly broadband wireless indoor access.

Indoor locations comprise difficult propagation environment for the radio waves. The architectural solutions vary significantly from building to building and even from room to room. Potentially, a large number of furniture combined with walls and moving objects, such as doors and even humans, cause significant shadowing, thus, large spatial variations in the signal quality. The conventional indoor communication systems, such as WLANs, cope with these problems with sufficient penetration properties provided by the microwave band. Moving to the THz band, the objects become opaque and even small structures, e.g., a mug on a table may prevent the line-of-sight (LoS) communications, the lifeline of the THz communications. To assess the potential of the proposed concept we need to understand the principal benefits and limitation of THz propagation in indoor environment.

Owing to the complexity of the indoor propagation environment, we apply a two-stage measurement-simulation campaign to assess the performance of the proposed system:

- A) *Field Measurement Campaign*. In the first stage, we measure THz waves propagation (0.3–3 THz) in typical indoor environment focusing on waves reflection and scattering from such materials as concrete, plastic, hardwood, etc. To the best of authors’ knowledge, the exact values for above 1 THz are reported for the first time.
- B) *Ray-Tracing Assessment*. In the second stage, we utilize the measured data to parameterize our ray-tracing simu-



Fig. 2. A vision of immersive THz indoor wireless access environment.

lation tool. We then simulate the typical office scenarios characterizing the performance of THz wireless access using capacity and SNR as metrics of interest.

B. Field Measurement Campaign

We utilized TeraView Mini Pulse², capable on THz band transmission/reception from 60 GHz to 4 THz, with time resolution of 8.3 fs and frequency resolution 5.9 GHz. Focus was on scattering properties of typical materials in office rooms including glass, plastic, hardwood, concrete and aluminium. To obtain these data, two test benches have been developed. The main one is illustrated in Fig. 3A and is used to measure the amount of the received energy reflected/scattered from a given sample subject to an angle of incidence and a 3D angle of reflection/scattering. The second test bench presents a LoS transmission of the same signal over the equal distance but without any obstacle on the way. Finally, the measured values of received energy coming from the first test bench are normalized with the data obtained with the second one to eliminate the propagation effects. As the result, the virgin data on the materials reflection and scattering properties are obtained and reported in Fig. 3.

As one may observe from Fig. 3, the smoother the material is, the higher is the peak response around the reflection path. The surface roughness decreases the reflected path energy by distributing the energy on the diffuse scattering field. The measurement results in Fig. 3 show that the reflected path has the most energy, but also confirm that rough surfaces such as concrete have quite a flat response over the Rx angles. It can be seen that aluminium is the best reflector among the considered materials. However, glass, plastic, and hardboard are not much worse. One of the reasons is that THz signals do not penetrate aluminium, whereas plastic for example does allow a part of the THz signal to go through. On the other hand, concrete has significantly different properties than the other materials. We can see from Fig. 3F that only at relatively low frequencies does concrete have a significant reflected component. This represents a challenge on THz modeling,

both strongly reflecting and strongly diffusing materials must be considered. *We would like stress that even at extremely high frequencies such as 3THz there is still a strong reflected component out of typical office materials.* This implies that nLoS communications through the first reflection might be feasible even at the THz frequencies.

C. Ray-Tracing Assessment

To assess performance of the prospective THz plugs in indoor environment, we designed ray-tracing simulation framework, based on the surface tessellation to miniature segments. The size of each segment is comparable to the wavelength, thus, the segments can be considered as point transceivers, receiving some energy from Tx and reflecting a part of it to Rx or to another point transceiver on a different surface.

We study a typical $6 \times 4 \times 3$ meters office room with walls, window, desks, ceiling and floor built from different materials as illustrated in Fig. 4A. We consider two scenarios as shown in Fig. 4D. The first one reflects the IEEE standardization efforts and takes into account the current state of THz electronics. With the second scenario, we take a look in the future, assessing performance of THz indoor communications by taking into account the potential progress in THz devices. Both LoS and nLoS communications are of interest. The nLoS setup presents an ideal case, where the path having the lowest losses is always selected.

We consider both laptop and mobile device connectivity cases. In the former case, the device is located at the wooden desk 10cm below and 50cm apart from the THz plug. In mobile connectivity case, a device might be located at any point within the room at a height of 1 m. The metrics of interest are capacity and SNR coverage of a room as well as power delay profile (PDP) of surfaces contributing to the received signal at a fixed point in a room.

PDP for involved surfaces in laptop connectivity case at 0.3 THz is shown in Fig. 4B. As we observe, the LoS component is dominating and the reflections from the closest two surfaces (wooden desk and window) are ~ 20 dB weaker. The reflected rays from the concrete walls scatter a lot and are from 75 to 120 dB lower than the LoS component, making

²TeraView, “TeraPulse 4000 – THz Pulsed Imaging and Spectroscopy”, <http://www.teraview.com/products/TeraPulse%204000/index.html> [Accessed 10-02-2017]

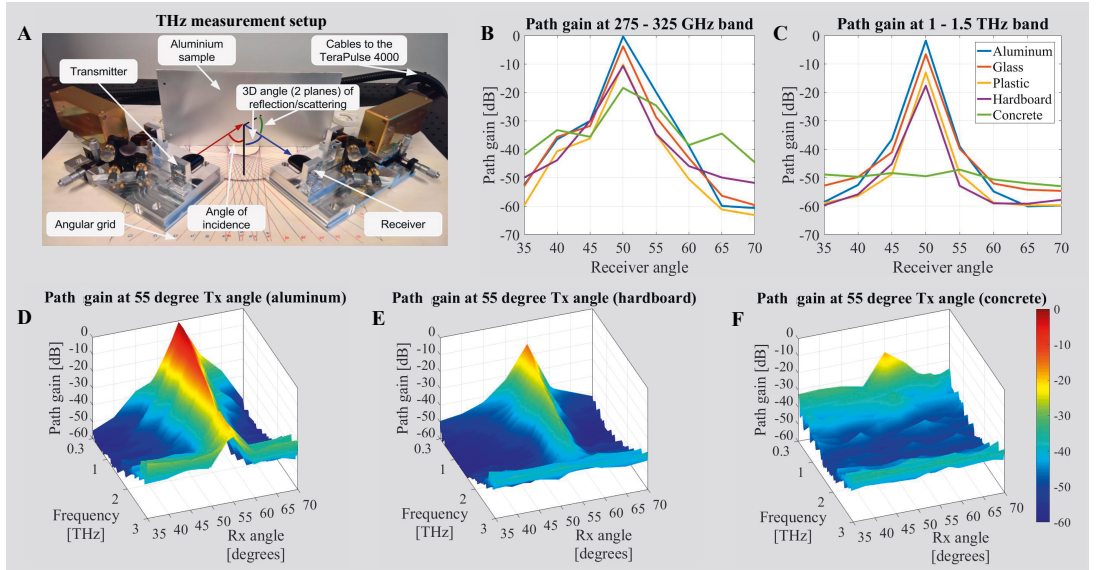


Fig. 3. Measured scattering properties of aluminum, glass, plastic, hardboard, and concrete in 0.1–3 THz band.

their impact negligible. Notice that the level of scattering significantly affects the PDP structure from a selected surface.

The aggregated PDP is presented in Fig. 4C. It is important that the same qualitative picture is observed for all the chosen frequencies, irrespective of whether they belong to transparency window (0.3 THz) or not (1 THz and 3 THz). As expected, the LoS is dominating the PDP. Then, there are clearly five peaks in the received signal (first reflections from the surfaces) each with its own tail of scattered waves, potentially enabling nLoS communication.

We show the average capacity for “IEEE” scenario between a THz plug and a mobile node located inside the room for LoS, Fig. 4E, and nLoS, Fig. 4F, cases. For nLoS we assume an obstacle close to the mobile node blocking the LoS, e.g. head, hand, etc. As one may observe, it is possible to ensure a reliable connectivity even in the absence of the LoS by capturing the power of the the best direct reflection: the minimal SNR is around 0dB within 1–3 meters from a THz plug (Fig. 4F). This result assumes that the reflected component from the window is not blocked. The approach requires precise tracking of the node location and ability to dynamically adjust the transmit and receive antenna patterns on a THz plug, which is a critical research problem. At the same time we maintain a sufficiently high data rate, as the theoretical Shannon channel capacity is above 100 Gbit/s. Assuming pessimistic 10% of modulation and MAC efficiency, this would lead to expected throughput of around 10 Gbit/s.

Finally, we present the results for the “THz” scenario assuming efficient directional antennas at both THz plug and mobile node. Observing Fig. 4G and Fig. 4H, the level of SNR is much higher for both LoS and nLoS even for ten times wider bandwidth and higher propagation loss. Although the concept of utilizing razor sharp beams might sound futuristic today, it illustrates the potential of the research in this field,

as the theoretical link capacity achieves *terabits-per-second*.

IV. IMPLEMENTATION ROADMAP

The proposed last-meter THz system allows for incremental development and can be specified in four phases with increasing complexity, usability and impact:

- *Phase I. Connectivity.* The Ethernet wireless extension system for point-to-multipoint connectivity with semi-stationary devices will be developed.
- *Phase II. Handover.* In-room nodes mobility and multiple THz plugs are included to the system. The emphasis is on enabling THz beamsteering at the air interface and associated mechanisms for handover support.
- *Phase III. Interference mitigation.* The support for multiple transmitters and receivers in the same environment is incorporated. Particularly, interference problems due to concurrent transmissions are to be addressed.
- *Phase IV. Integration.* THz wireless access is integrated as one of the radio access technologies into the Heterogeneous Network (HetNet) concept under the umbrella of beyond 5G systems.

A. Phase I: Reliable THz Connectivity

In the first phase, directional antennas, beam learning/tracking, modulation, coding, and plug and play operation are addressed. Directional antennas (implemented e.g., with a phased array) are needed to increase the receiver’s effective antenna aperture. The transmitter also needs to use directional antennas to compensate for the low transmit power. At millimeter waves, miniature phased arrays have already been implemented, but the achieved progress in THz is still limited and more work needs to be done. Going in this direction, the small wavelengths in the THz band enable packing tens of

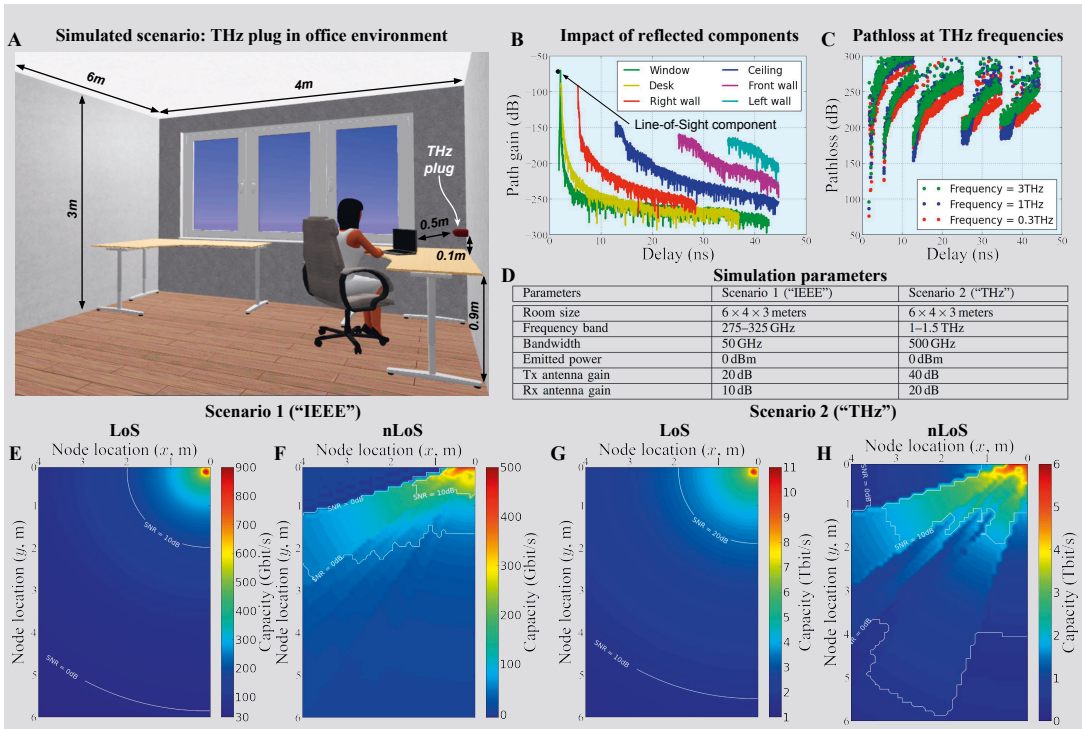


Fig. 4. Specifics of THz room propagation for the two considered scenarios.

thousands of upcoming plasmonic nanoantenna elements in a small area [6]. This is to be sufficient to support meters-distance links.

It may well be worth it to include several antenna arrays in *THz plug* and mobile THz modules to reduce the chances for blocking and to support finding a good propagation path. With directional antennas, finding good beam pointing becomes critical. To support user mobility, fast and accurate beam tracking is required, especially in nLoS conditions [14]. Although mechanically steerable antennas for 0.3 THz have been demonstrated [15], faster electronic beam steering is required for practical use.

For plug and play functionality the THz plug has to be seen by the network as a regular switch. Thus, the envisioned device is assumed to be IP-free with all the data forwarding performed on the link layer. A special question of interest is the possibility of preserving the Ethernet frame structure for seamless service extension to the air interface. The latter is highly desirable to avoid the continuous transcoding of both uplink and downlink traffic.

B. Phase II: Handover in THz Networks

At the second stage, the user macro mobility has to be taken into account and supported with handover functionality. In particular, at this stage an SDN-like network controller, collecting data and managing all the THz plugs in a dedicated area, has to be introduced. The role of this device is to

constantly monitor the user location and pre-select the new THz plug to catch the user, when it is close to leaving the current connection.

This type of feedback can be implemented by estimating user trajectories through beam configurations and received power level. Since the majority of the time the link is expected to be in LoS, and the THz plug is stationary with known location, the calculation is feasible. When a user is reaching the last available antenna configuration on its trajectory, the handover procedure has to be performed by directing the receiving beam from the next THz plug. Forwarding of unsent data from the current THz plug to the next one via the Ethernet interface has to be performed.

C. Phase III: THz Interference Management

Although the high directivity of beams may lead to noise-limited communications in the outdoor scenarios, the interference still plays a substantial role in the indoor environment. For instance, a massive interference might occur when two mobile Rx are in close proximity.

The experience accumulated standardizing IEEE 802.11ad highlights that completely new multiple access mechanisms will be required for systems with directional antennas. This is one of the fundamentally “grey” areas in the telecommunications research with no comprehensive solution proposed yet. On top of this, reflected/diffracted/scattered waves from one link may interfere with another, which is even more difficult

to predict. Due to the presence of these effects in combination with nodes mobility, the total interference structure is completely new, in comparison to lower frequencies, with unpredicted reductions of received signal quality.

Therefore, an in-depth and accurate interference modeling for highly-directional THz antennas is required to understand and specify interference mitigation techniques for the multi-user THz wireless access. As candidates both conventional mitigation techniques such as power control and frequency division, as well as novel techniques, specific to the high-density wireless networks and THz wireless access, need to be considered.

D. Phase IV: THz Integration into Beyond-5G

Following the HetNet concept, currently envisioned as a collection of access networks with centralized control over the "always-on" macro base station interface, the proposed system can be integrated into the modern wireless world. Furthermore, the THz wireless access may become a network-controlled technology enabler for the recently introduced concept of Tactile Internet. Similarly to other access networks, the integration will require an in-building network control entity to interface with mobile operators infrastructure. The data plane will operate at high-speed last-meter connectivity whenever a user is in the proximity of a THz plug or being switched to a slower technology when a user leaves the coverage.

V. CONCLUSIONS

In this article, we introduced the concept of THz plug, a device operating in the terahertz frequency band, directly attached to an Ethernet socket. Combining gigabit Ethernet and the prospective THz wireless interfaces would enable massive wireless data transfers. A step-by-step roadmap towards the implementation of the proposed multi-gigabit last-meter indoor wireless access in the THz band is presented and major research challenges are highlighted.

We demonstrate the potential of the first step of the proposed roadmap for both IEEE 802.15.3d scenario (50 GHz bandwidth with 300 GHz center frequency) and the true THz case with massive 500 GHz bandwidth in the 1–1.5 THz band. Despite the desirable capacity and data rate values, high level of THz signal attenuation and scattering is limiting the communication range and has to be mitigated in both LoS and nLoS cases by using sufficiently directive antennas with dynamic beamforming. Design of such antennas, associated transceivers, as well as efficient beam tracking algorithms is the key challenge to fully benefit from extraordinary capacity provided by the THz frequency band.

REFERENCES

- [1] J. M. Jornet and I. F. Akyildiz, "Channel modeling and capacity analysis for electromagnetic wireless nanonetworks in the terahertz band," *IEEE Transactions on Wireless Communications*, vol. 10, pp. 3211–3221, October 2011.
- [2] I. Kallfass, F. Boes, T. Messinger, J. Antes, U. Inam, A. Lewark, and R. Tessman, A. Henneberger, "64 Gbit/s transmission over 850 m fixed wireless link at 240 GHz carrier frequency," *Journal of Infrared, Millimeter, and Terahertz Waves*, vol. 36, pp. 221–233, January 2015.
- [3] P. Boronin, V. Petrov, D. Moltchanov, Y. Koucheryavy, and J. Jornet, "Capacity and throughput analysis of nanoscale machine communication through transparency windows in the terahertz band," *Elsevier Nano Communication Networks*, vol. 5, pp. 72–82, September 2014.
- [4] H.-J. Song, J.-Y. Kim, K. Ajito, N. Kukutsu, and M. Yaita, "50-Gb/s direct conversion QPSK modulator and demodulator MMICs for terahertz communications at 300GHz," *IEEE Transactions on Microwave Theory and Techniques*, vol. 62, pp. 600–609, March 2014.
- [5] J. D. Albrecht, M. J. Rosker, H. B. Wallace, et al., "THz electronics projects at DARPA: Transistors, TMICs, and amplifiers," in *Proc. IEEE MTT-S International Microwave Symposium*, pp. 1118–1121, May 2010.
- [6] J. M. Jornet and I. F. Akyildiz, "Graphene-based plasmonic nano-antenna for terahertz band communication in nanonetworks," *IEEE Journal on Selected Areas in Communications*, vol. 31, pp. 685–694, December 2013.
- [7] *IEEE 802.15.3d, "Application Requirements Document"*, IEEE 802.15-14/0304r16, May 2015.
- [8] *IEEE 802.15.3d, "Technical Requirements Document"*, IEEE 802.15-14/0309r20, March 2016.
- [9] V. Petrov, M. Komarov, D. Moltchanov, J. M. Jornet, and Y. Koucheryavy, "Interference and SINR in millimeter wave and terahertz communication systems with blocking and directional antennas," *IEEE Transactions on Wireless Communications*, vol. 16, pp. 1791–1808, March 2017.
- [10] J. Kokkonen, J. Lehtomäki, and M. Juntti, "A discussion on molecular absorption noise in the terahertz band," *Nano Communication Networks*, vol. 8, pp. 35–45, June 2016.
- [11] G. Ducournau, K. Engenhardt, P. Szriftgiser, D. Bacquet, M. Zaknoute, R. Kassi, E. Lecomte, and J.-F. Lampin, "32 Gbit/s QPSK transmission at 385 GHz using coherent fibre-optic technologies and THz double heterodyne detection," *Elect. Letters*, vol. 51, pp. 915–917, June 2015.
- [12] J. Boyd, "Fujitsu makes a THz receiver small enough for a smartphone." <http://www.spectrum.ieee.org/tech-talk/telecom/wireless/fujitsu-makes-a-terahertz-receiver-small-enough-for-a-smartphone>, October 2015. [Accessed 10-02-2017].
- [13] G. Ducournau, P. Szriftgiser, A. Beck, D. Bacquet, F. Pavanello, E. Peytavit, M. Zaknoute, T. Akalin, and J. F. Lampin, "Ultrawide-bandwidth single-channel 0.4-THz wireless link combining broadband quasi-optic photomixer and coherent detection," *IEEE Transactions on Terahertz Science and Technology*, vol. 4, pp. 328–337, May 2014.
- [14] R. Bonjour, M. Singleton, S. A. Gebrewold, Y. Salamin, F. C. Abrecht, B. Baeuerle, A. Josten, P. Leuchtman, C. Hafner, and J. Leuthold, "Ultra-fast millimeter wave beam steering," *IEEE Journal of Quantum Electronics*, vol. 52, pp. 1–8, January 2016.
- [15] S. Rey, "TERAPAN: Ultra-high data rate transmission with steerable antennas at 300 GHz," IEEE 802.15-15-0167-02-0thz, March 2015.

AUTHORS' BIOGRAPHIES

Vitaly Petrov (vitaly.petrov@tut.fi) is a PhD candidate at the Laboratory of Electronics and Communications Engineering at Tampere University of Technology (TUT), Finland. He received the Specialist degree (2011) from SUAI University, St. Petersburg, Russia, as well as the M.Sc. degree (2014) from TUT. He was a Visiting Scholar with Georgia Institute of Technology, Atlanta, USA, in 2014. Vitaly (co-)authored more than 30 published research works on terahertz band communications, Internet-of-Things, nanonetworks, cryptology, and network security.

Joonas Kokkonen (joonas.kokkonen@oulu.fi) is a Postdoctoral Research Fellow with the Centre for Wireless Communications, University of Oulu. He received the B.Sc. (2011), M.Sc. (2012), and Dr.Sc. (2017) degrees from University of Oulu, Oulu, Finland. He was a Visiting Researcher with Tokyo University of Agriculture and Technology, Japan (2013) and a Visiting Researcher with State University of New York at Buffalo, USA (2017). Joonas's research interests include THz band and mmWave channel modeling and communication systems.

Dmitri Moltchanov (dmitri.moltchanov@tut.fi) is a Senior Research Scientist at the Laboratory of Electronics and Communications Engineering, Tampere University of Technology. He received his M.Sc. (2000) and Cand. Sc. (2002) degrees from Saint Petersburg State University of Telecommunications, as well as the Ph.D. (2006) degree from Tampere University of Technology. His research interests include performance evaluation and optimization issues in wired and

wireless IP networks, Internet traffic dynamics, and traffic localization in P2P networks.

Janne Lehtomäki (janne.lehtomaki@oulu.fi) is an Adjunct Professor with the Centre for Wireless Communications, University of Oulu. He received the M.Sc. (1999) and the Ph.D. (2005) in telecommunications from University of Oulu. His research interests are in terahertz wireless communication, channel modeling, IoT, and spectrum sharing. Janne co-authored the winner of the Best Paper Award at IEEE WCNC 2012. He is an Editorial Board Member of Elsevier Physical Communication.

Yevgeni Koucheryavy (evgeni.koucheryavy@tut.fi) is a Full Professor at the Laboratory of Electronics and Communications Engineering of Tampere University of Technology (TUT), Finland. He received his Ph.D. degree (2004) from TUT. His current research interests include various aspects in heterogeneous wireless communication networks and systems, the Internet of Things and its standardization, as well as nanocommunications. He is Associate Technical Editor of IEEE Communications Magazine and Editor of

IEEE Communications Surveys and Tutorials.

Markku Juntti (markku.juntti@oulu.fi) received his Dr.Sc. (EE) degree from University of Oulu, Oulu, Finland in 1997. Dr. Juntti was with University of Oulu in 1992–98. In academic year 1994–95, he was a Visiting Scholar at Rice University, Houston, Texas. In 1999–2000, he was a Senior Specialist with Nokia Networks. Dr. Juntti has been a professor of communications engineering since 2000 at University of Oulu, Centre for Wireless Communications (CWC), where he leads the Communications Signal Processing (CSP) Research Group. He also serves as Head of CWC – Radio Technologies (RT) Research Unit. His research interests include signal processing for wireless networks as well as communication and information theory. Dr. Juntti is also an Adjunct Professor at Department of Electrical and Computer Engineering, Rice University, Houston, Texas, USA. Dr. Juntti is an Editor of IEEE TRANSACTIONS ON COMMUNICATIONS

PUBLICATION

III

Dynamic Multi-Connectivity Performance in Ultra-Dense Urban mmWave Deployments

V. Petrov, D. Solomitckii, A. Samuylov, M. A. Lema, M. Gapeyenko,
D. Moltchanov, S. Andreev, V. Naumov, K. Samouylov, M. Dohler and
Y. Koucheryavy

IEEE Journal on Selected Areas in Communications 35.9 (2017), 2038–2055

Publication reprinted with the permission of the copyright holders

Dynamic Multi-Connectivity Performance in Ultra-Dense Urban mmWave Deployments

Vitaly Petrov, Dmitrii Solomitckii, Andrey Samuylov, Maria A. Lema, Margarita Gapeyenko, Dmitri Moltchanov, Sergey Andreev, Valeriy Naumov, Konstantin Samouylov, Mischa Dohler, and Yevgeni Koucheryavy

Abstract—Leveraging multiple simultaneous small cell connections is an emerging and promising solution to enhance session continuity in millimeter-wave (mmWave) cellular systems that suffer from frequent link interruptions due to blockage in ultra-dense urban deployments. However, the available performance benefits of feasible multi-connectivity strategies as well as the tentative service quality gains that they promise remain an open research question. Addressing it requires the development of a novel performance evaluation methodology, which should take into account: (i) the intricacies of mmWave radio propagation in realistic urban environments; (ii) the dynamic mmWave link blockage due to human mobility; and (iii) the multi-connectivity network behavior to preserve session continuity. In this paper, we construct this much needed methodology by combining the methods from queuing theory, stochastic geometry, as well as ray-based and system-level simulations. With this integrated framework, both user- and network-centric performance indicators together with their underlying scaling laws can be quantified in representative mmWave scenarios. To ensure modeling accuracy, the components of our methodology are carefully cross-verified and calibrated against the current considerations in the standards. Building on this, a thorough comparison of alternative multi-connectivity strategies is conducted, as our study reveals that even simpler multi-connectivity schemes bring notable improvements to session-level mmWave operation in realistic environments. These findings may become an important reference point for subsequent standardization in this area.

Index Terms—5G mobile networks, millimeter-wave (mmWave) technology, multi-connectivity strategies, session continuity, link interruptions, human body blockage, dense urban deployments, integrated methodology.

I. INTRODUCTION

As soon as it became clear that the millimeter wave (mmWave) communications are feasible [1], all of the industry

V. Petrov, D. Solomitckii, A. Samuylov, M. Gapeyenko, D. Moltchanov, S. Andreev, and Y. Koucheryavy are with Tampere University of Technology, Finland. Email: firstname.lastname@tut.fi

M. A. Lema and M. Dohler are with King's College London (KCL), UK. Email: maria.lema_rosas_mischa.dohler@kcl.ac.uk

V. Naumov is with Service Innovation Research Institute, Helsinki, Finland. Email: valeriy.naumov@pfi.fi

K. Samouylov is with Peoples' Friendship University of Russia (RUDN University), Moscow, Russia and Institute of Informatics Problems, Federal Research Center "Computer Science and Control" of Russian Academy of Sciences, Moscow, Russia. Email: samuylov_ke@rudn.university

This work was supported by the project TT5G: Transmission Technologies for 5G and by Ministry of Education and Science of RF (Agreement No. 02.a03.21.0008) and by RFBF (projects No.16-07-00766, 17-07-00845). The work of S. Andreev was supported in part by a Postdoctoral Researcher grant from the Academy of Finland and in part by a Jorma Ollila grant from Nokia Foundation. The work of V. Petrov was supported by Nokia Foundation.

and academia started to invest considerable efforts into completing the fifth generation (5G) of mobile wireless technology, where the new mmWave radio is the key enabling element. In parallel, the mmWave spectrum has rapidly become a 'goldmine', and various standards developing organizations are expecting to benefit from its abundance by ratifying new specifications. In particular, cellular mmWave technology is aggressively pushed forward by exploiting first 28 GHz and then higher-frequency bands [2].

The unprecedented capacity boost promised by the ultra-dense deployments of small cells operating at mmWave frequencies, with massive available bandwidths, will facilitate the provisioning of exceptionally demanding mission-critical and resource-hungry applications that are envisaged to utilize the 5G communications infrastructure [3]. However, there is a number of unique challenges, which need to be addressed and resolved for mmWave cellular to take off rapidly, such as blockage by smaller objects due to shorter wavelength, higher path loss, etc.

Hence, countless research campaigns are underway aiming to understand these and other intricacies of mmWave and satisfy the stringent performance requirements of emerging 5G services. As a result, many of the immediate technology-related challenges will be comprehensively addressed as part of the 3GPP specification work and finalized within the Phase 1, which is expected to complete with a 5G trial by the end of 2018 in Seoul, South Korea [4].

While the current research is carefully investigating every relevant component of mmWave technology, as it is rapidly taking shape in the standards, there still remains uncertainty on how the actual 5G systems will operate in practical urban deployments (see Fig. 1), where numerous realistic factors – such as the individual parameters and dynamics of the operational environment – will determine the overall system performance.

A. State-of-the-art in mmWave research

With its attractive benefits, such as the very large available bandwidths, mmWave communications technology also poses formidable challenges. First and foremost, there is a need for completely new – different from microwave – channel models and the entire research community, including the 3GPP organization, made a focused effort in order to offer those [2], [5]–[8]. In [9], a path loss model for urban street canyon is proposed, where several existing models, such as ITU-R

M.2135 urban microcellular (UMi) line-of-sight (LoS) and Manhattan-grid non-LoS (nLoS), are parametrized based on the channel sounding campaigns.

Further, a comprehensive investigation on the accuracy of different models proposed for 5G has been completed in [10] by relying on real measurements. In addition, [11] conducts novel blockage probability analysis mindful of the specific features of the mmWave new radio by arguing that short wavelengths make smaller objects like cars, humans, and street furniture become obstacles for the LoS propagation.

More recently, to mitigate the inherently high mmWave path loss, beamforming techniques have been considered when implementing the mmWave systems [3], which in turn demanded the corresponding interference models [12]–[14]. In particular, the work in [15] contributes a fast and robust beamformer solution based on iterative fast Fourier transform methods.

Since massive MIMO is expected to become an important technique to deliver higher data rates in future mmWave systems [16], multiple research threads are progressing in this direction [17]. In [18], an interference cancellation based hybrid precoding for mmWave MIMO is proposed that demonstrates near-optimal performance. Further, the work in [19] outlines an analytical approach to characterizing the spectral efficiency of two-tier heterogeneous networks with MIMO macro base stations overlaid by small cells. In [20], a beamforming design in multi-cell multi-user systems is considered that caters for a better balance between spectral and energy efficiency.

New theoretical analysis of mmWave cellular networks employing the formulations from stochastic geometry is attempted in [21]. That work develops mathematical models for signal-to-interference-plus-noise ratio (SINR) and rate coverage in both uplink and downlink channels by assuming the field of uniformly distributed base stations and taking into account the main features of mmWave communications, including blockage by smaller objects and highly directional antennas. Targeting to lower the outage probability and boost the achievable data rate, two-timeslot full-duplex relaying scheme is designed for 5G wireless networks [22].

Past research on mmWave communications reiterates a crucial fact that due to shorter wavelengths the received signal strength is extremely susceptible to blockage by smaller objects, thus making the mmWave links highly opportunistic and potentially unreliable [23], [24]. Along these lines, densification of cellular infrastructure with static mmWave small cells may be augmented by adding mobile access infrastructure and thus improving the overall system reliability [25].

On the way to ultra-reliable communications, dual- and multi-connectivity techniques (see Fig. 1) emerge, where a user is simultaneously connected to several serving base stations [26]–[28]. In [29], the multi-connectivity aspects in a cloud radio access network are studied to improve on the performance of cell-edge users. To this effect, system-level simulations are conducted and the respective results confirm a decrease in the number of failures caused by mobility.

Following the envisioned 5G requirements [30], highly reliable mmWave communications are an essential ingredient for the next generation of wireless networks [31]. Even though there has been significant research coverage on characteri-

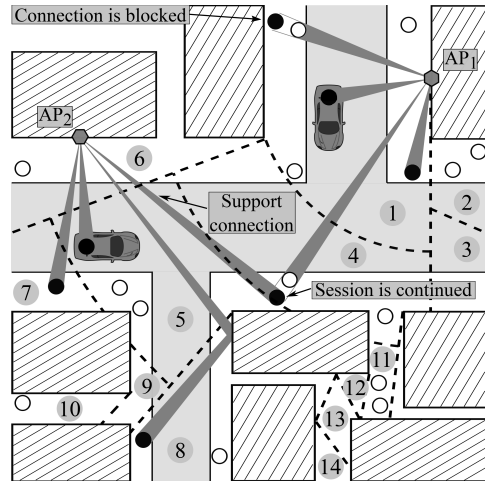


Fig. 1. Example use of mmWave multi-connectivity in urban scenarios.

zation and improvement of individual mmWave features, an integrated methodology to holistically assess the system-level performance, when dynamic multi-connectivity is employed to mitigate the very opportunistic nature of mmWave connections, is not yet available in the current literature.

B. Our contribution

Concerned by the lack of comprehensive frameworks that capture the realistic behavior of urban mmWave networks as well as quantify the potential performance improvements made available with dynamic multi-connectivity techniques, we propose a novel integrated methodology. It comprises both unique emerging methods developed exclusively for the purposes of this research and well-established tools based on our extensive past studies. We therefore combine the use of a new ray-based modeler (an emerging tool) and a mature system-level simulator (an established tool) as well as glue them together with our powerful analytical methodology.

The contributions of this work are summarized as follows.

- *Novel analytical methodology*: An elaborate mathematical framework is developed that takes into account the performance dynamics of mmWave cellular networks together with their unique features, such as dramatic signal quality degradation due to human body blockage and mobility. The proposed model targets to characterize the benefits promised by dynamic multi-connectivity techniques for mmWave systems and has been carefully validated with the system-level simulation results.
- *In-depth practical study*: A thorough investigation of the mmWave system operation in a realistic deployment is proposed that recreates every relevant detail of a real-world urban environment. Our setup captures the important mmWave-specific effects, such as reflections and diffuse scattering not only from buildings, but also from the street furniture, vehicles, and other small-scale

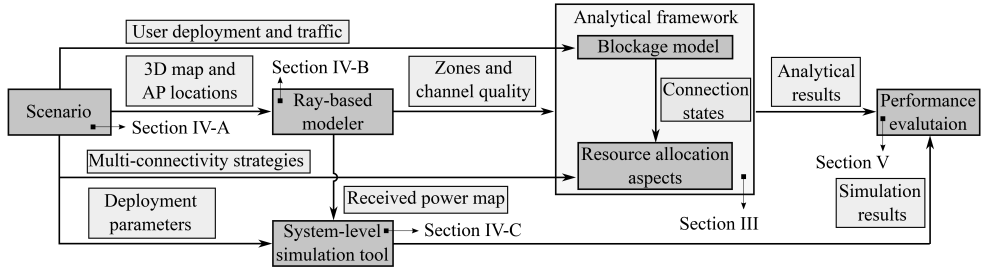


Fig. 2. Overview of our proposed methodology.

objects. The mmWave channel quality is evaluated in both LoS and nLoS conditions, while the baseline model has been calibrated with the 3GPP methodology.

- *Assessment of multi-connectivity benefits:* A comparative analysis of feasible multi-connectivity strategies within our mathematical framework built over ray-based modeling results is conducted in realistic conditions. These range from present-day cellular dual-connectivity solutions adopted for mmWave to significantly more complex but powerful multi-connectivity mechanisms. The realistic performance gains for each of the strategies are reported across both user- and network-centric metrics of interest, especially at higher traffic loads.

We detail our proposed methodology in what follows.

II. OVERVIEW AND PURPOSE OF OUR METHODOLOGY

A. Our methodology at a glance

Realistic modeling of dynamic mmWave cellular systems in urban deployments constitutes an extremely challenging task, where numerous intricate effects need to be taken into account. This is due to more complex mmWave propagation in the presence of buildings, vehicles, and humans. To evaluate the performance of mmWave systems in realistic conditions, an integrated analytical–simulation methodology is proposed in this paper (see Fig. 2).

Our performance evaluation begins with constructing a precise 3D map of the deployment area that captures all of the relevant objects with their physical dimensions of above several centimeters. The mmWave access points (APs) are then deployed and characterized in terms of transmit power, frequency, band, and other important parameters. Further, the potential user equipment (UE) locations are considered.

At the end of the first stage, the produced 3D setup is simulated within our in-house ray-based modeler that is tailor-made specifically for mmWave frequencies. It remains scalable in realistic city-size layouts and is calibrated with both the commonly accepted channel measurements from [1] as well as the recent 3GPP channel models in [2]. This tool is employed to mimic the fine-grained effects pertaining to practical mmWave deployments, such as path loss, reflections, and diffuse scattering from various objects for any relative locations of APs and the UE. The simulations are run separately for each of the AP locations.

At the next step, the ray-based modeling results are first converted into the signal-to-noise ratio (SNR), which is then translated into the scaling coefficient in Hz/bits/s that the UEs have, depending on the channel conditions (see details in Section IV-B). Thus produced scaling coefficients determine a lower bound on the expected overhead that the UE has to take into account when converting the application-layer traffic requirements into the physical-layer data rate. Based on this scaling coefficient, the entire area of interest is divided into a certain number of clusters, named “zones”. The description of the calculated zones together with the UE deployment and the traffic characteristics as well as the candidate multi-connectivity strategies serve as the input to our analytical framework.

The analytical framework comprises two main components. The first one is a novel 3D stochastic blockage model, which is introduced to capture the situations when a certain signal component is blocked by an obstacle. This model brings into our system one of the key dynamic effects, when a particular mmWave connection becomes blocked/unblocked over time realistically. The model is used to estimate the state of the individual mmWave connections in each zone at a certain moment of time.

The second component of our analytical framework is a sophisticated queuing system based formulation, which connects the results produced by the previous modeling blocks, as it embraces specific user traffic patterns, resource allocation algorithms on mmWave APs, and multi-connectivity strategies to evaluate user- and network-centric performance indicators. The output characteristics utilized in this paper are denial of service probability, session drop probability, and mean number of active sessions. A detailed definition of these metrics is given in Section V-A.

Finally, to ensure the accuracy of the produced numerical results that build on the ray-based modeling data, a supportive simulation study is conducted with the use of our system-level simulator (SLS). The latter models the mmWave system behavior at a higher level of details than the analytical framework does (see the description of the SLS in Section IV-C). Our performance evaluation concludes in Section V-C, where the numerical output of both approaches is compared and any discrepancies between the results are explained. The following subsection outlines the more specific features and the underlying assumptions of our proposed integrated methodology.

B. Key modeling considerations

To mathematically characterize the urban mmWave performance dynamics, we here discuss the key considerations related to the envisioned system functionality.

1) *User deployment*: The area of interest is divided into a number of zones of finite size, each of which is characterized by their specific mmWave channel conditions. Within every such zone, the users are deployed randomly, whereas the actual density of users in a certain zone can be set appropriately to represent non-homogeneous deployments (e.g., cluster deployments centered around certain attractors). In practice, additional ‘virtual’ zones with their respective user deployment densities can be created to model non-uniform deployments.

2) *Network deployment*: The mmWave APs in our scenario can in principle be deployed at arbitrary locations on a given map. These are assumed to be static throughout the entire observation time, but mobile APs (e.g., deployed on vehicles or drones) can also be assessed if they remain stationary for reasonable durations when serving their users.

3) *User traffic demands*: A number of user session types can be modeled, each having unique random traffic demands and service times. For a given session type, user demands in terms of the application-layer throughput are determined for the entire duration of the current session. Generally, the distribution of the target data rate can be made arbitrary, but once the user begins service, its application-layer service quality is assumed to remain unchanged.

4) *Mobility of users and blockers*: In our model, the users and potential blockers are fully mobile, but for the sake of exposition clarity the target user is assumed to remain static throughout its active session. Other users may move around in relation to the active user according to their specific patterns, thus transferring between zones dynamically. In particular, random direction mobility is assumed here for the purposes of a first-order dynamic analysis.

5) *Blockage modeling*: Human bodies are considered to be blockers for mmWave radio propagation. They are modeled as cylinders with a certain mean height and diameter. The LoS link between the AP and the UE is blocked if the line between these points intersects any cylinder (i.e., one human body). In this case, the signal strength degrades and its quality is reduced, which translates into the lower modulation and coding schemes (as modeled with our ray-based tool).

6) *Connection reliability*: While the mmWave system attempts to maintain reliable connections, the latter request different amounts of radio resources (e.g., in terms of bandwidth) depending on LoS or nLoS conditions to support the same data rate. This work does not concentrate specifically on the matters related to PHY- and MAC-layer mmWave operation (there are many ongoing studies on it [32]), by assuming that the lower layers are already equipped with the required functionality. However, we calibrate this abstraction with our system-level simulator to ensure that our key modeling choices and the corresponding parameters remain adequate.

7) *Resource allocation*: We assume that our mmWave system performs typical session management, where new requests from the users are only accepted if there are resources to serve them. To this end, a session can be initiated if and only if the

system currently has sufficient radio resources to satisfy the requested service requirements of an arriving session (e.g., in terms of its demanded bandwidth). New sessions do not cause the drops of already active sessions. The model can be further extended to support various types of resource constraints (e.g., beam steering and beam tracking limitations).

Based on the above considerations, we develop the analytical component of our proposed methodology in the sequel.

III. PROPOSED ANALYTICAL FRAMEWORK

In this section, we detail the analytical component of our proposed methodology. First, we briefly describe the modeling principles. Then, we formalize a resource sharing model based on the framework of queuing systems with multiple arrival processes, multiple serving entities with shared resources, and service interruptions caused by the LoS blockage processes. We then develop a numerical algorithm for estimating the mmWave-specific performance metrics of interest. The notation used throughout this section is summarized in Table I.

A. Capturing radio resource allocation

To characterize the resource allocation dynamics at the mmWave APs, we introduce a novel queuing system framework with multiple arrival processes that models different session types, multiple service entities each associated with a shared set of resources representing the bandwidth available at the APs, and service interruptions characterizing the process of LoS blockage. Below, we formulate our framework for a general case of K APs, L types of sessions, multiple types of resources, and a finite number of servers available at each AP.

This general model is then reduced to the considered practical mmWave scenario by assuming a smaller number of nodes that represent the APs located within the area of interest. The reduced model assumes an infinite number of servers at each node (relaxing the limit on the number of concurrent sessions), as well as considers only one type of resources, that is, the available bandwidth. The former assumption implies that new or ‘rerouted’ (due to the loss of LoS) sessions can only be lost due to the insufficient amount of resources available at the AP, while the latter means that the only resource requested by a user is the mmWave spectrum bandwidth.

We assume multiple types of service, which correspond to the set of possible modulation and coding schemes (MCSs) in the considered mmWave system that are derived by using the results of Section IV. Consequently, a user residing in the nLoS conditions may still receive data, i.e., in our model the users will explicitly request different amounts of radio resources as determined by their position within the area of interest. A newly arrived user requests service of a certain type, which is based on its location and the associated mmWave AP. Then, this user may change its association point subject to possible interruptions that correspond to losing LoS and thus having to ‘reroute’ to another AP; or staying connected to the same AP but then consuming a much higher amount of radio resources due to nLoS conditions.

TABLE I
NOTATION AND MAIN PARAMETERS: QUEUING MODEL

Notation	Description
Input parameters	
K	Number of network nodes
N_i	Maximum number of servers at node i
L	Number of possible session types
M_i	Number of different resources available for node i
\bar{R}_i	Maximum amount of resources available for node i
$F_{ij}^v(\bar{x})$	CDF of the amount of resources \bar{x} requested by a session of type j and level v at node i
λ_i	Initial arrival intensity of sessions at node i
θ_{ij}	Probability for a new session arriving at node i to request service of type j
α_{ij}	Interruption intensity of sessions of type j at node i
$p_{ij,kl}^v$	Probability for a session of type j and level v at node i to choose service type l at node k after interruption
$B_{ij}^v(x)$	CDF of session service time of type j , level v at node i
Auxiliary variables	
$X(t)$	Stochastic process denoting system state at time instant t
$\xi_{ij}^v(t)$	Number of sessions of type j at level v served at node i at time instant t
$\Psi_{ij}^v(t)$	Vector of resources occupied by sessions of type j and level v served at node i at time instant t
$\beta_{ij}^v(s)$	Laplace-Stieltjes transform of CDF $B_{ij}^v(x)$
p_{ij}^v	Probability for a session of type j and level v at node i to be dropped after interruption
$H_{ij}^v(x)$	CDF of time a session of type j and level v occupies a server associated with node i
h_{ij}^v	Mean time a session of type j and level v occupies a server associated with node i
\mathcal{T}_{ij}^v	Aggregate intensity of sessions of type j and level v at node v , including initial arrivals and 'reroutes'
ρ_{ij}^v	Traffic load of type j and level v at node v
$F_i(\bar{x})$	Weighted distribution of the amount of resources required by an arbitrary session arriving at node i
$G_i(\bar{x})$	Load distribution of the amount of resources required by a session arriving at node i , weighted by traffic
$P_m(\bar{x})$	Joint CDF of the number of sessions at node i and the amount of resources occupied by them
$\Phi_{ij,kl}^v$	Probability for a session, originally of type j and arriving at node i , to be interrupted exactly v times and be 'routed' to node k to request service of type l
$q_{rs,kl}^v$	Probability that service of a session of type s and level v at node r is interrupted and then 'routed' to node k requesting service of type l
$\pi_{ij}^v, \bar{\pi}_i$	Probability for a session of type j and level v at node v to be lost
$M_{ij,kl}^v$	Mean time spent in the system by a session that initially arrived at node i and requested service of type j , conditioned on the event that its service is successfully completed at node k and level $v+1$ while requesting service type l
Performance metrics	
n_{ij}^v	Average number of sessions of type j and level v , served by node i
n_{ij}^v, m_i, n	Mean number of sessions of type j and level v at node i
$Z_{ij}(x)$	CDF of the resource amount of type j occupied at node i
\bar{m}_{ij}	Mean amount of resources of type j occupied at node i
$\bar{\pi}_i, \bar{\pi}$	Probability for a session to be lost upon initial arrival at node i
$\bar{\pi}_{ij}, \bar{\pi}_i, \bar{\pi}$	Probability for a session, initially arriving at node i and requesting service of type j , to be lost eventually
$\sigma_{ij}, \sigma_i, \sigma$	Probability for a session, initially arriving at node i and requesting service of type j , to be served successfully
M_{ij}	Mean time spent in the system by a session that initially arrived at node i and requested service of type j

B. Queuing network formalism

Consider a queuing network that consists of K nodes as illustrated in Fig. 3. Each node i is a multi-server queue comprising N_i servers, where no waiting positions are assumed. Each arriving user session can be served as one of L session types, which differ based on their resource requirements (as calculated in Section IV) and service time distributions. The arrival process of new sessions at node i is Poisson with the intensity of λ_i . A session arriving at node i requests the service of type j with the probability θ_{ij} , $i = 1, 2, \dots, L$. Hence, the combination of λ_i and θ_{ij} characterizes the intensity of new sessions that arrive at a given AP with various radio resource requirements (be it due to user location or its desired data rate).

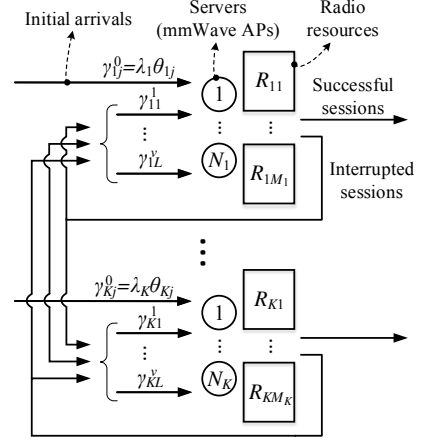


Fig. 3. An illustration of the proposed queuing network model.

Later on, we consider the initial mmWave connectivity strategies for the newly arriving sessions (detailed in Section V).

The service of active sessions of type j at node i can be interrupted at time instants that organize an external Poisson process with intensity α_{ij} , which are obtained by utilizing the LoS blockage model in Appendix A. While a session is being served, it can be interrupted multiple times. The number of session interruptions by a certain arbitrary time instant t is termed the *level* of a session. The newly arriving sessions are by definition placed onto the level 0. In addition to the limited number of servers N_i , node i is associated with a limited pool of resources of size M_i . The overall volume of resources that node i has is represented by vector $\bar{R}_i = (R_{i1}, R_{i2}, \dots, R_{iM_i})$, where R_{im} is the amount of resources of type m . The amount of resources requested by sessions of type j on level v at node i has a multivariate cumulative distribution function (CDF) $F_{ij}^v(\bar{x})$.

Let $B_{ij}^v(x)$ be the CDF of the service time for a session of type j and level v at node i , and let $\beta_{ij}^v(s)$ be its Laplace-Stieltjes transform (LST). A session of level v , whose service of type j at node i is interrupted, is 'routed' to node k according to a certain multi-connectivity strategy as specified in Section V-B, where it may change its service type to the type l with probability $p_{ij,kl}^v$. If there are sufficient resources at node k and at least one server is available, the service continues. With the complementary probability,

$$p_{ij}^v = 1 - \sum_{k=1}^K \sum_{l=1}^L p_{ij,kl}^v, \quad v = 0, 1, \dots, \quad (1)$$

the session is dropped due to insufficient resources or when all of the servers are occupied. At the 'rerouting' moments, the level of the session is increased to $v+1$. When the service time expires, the session leaves the network by receiving successful service.

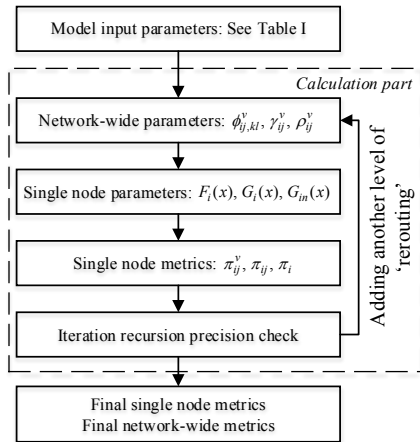


Fig. 4. Steps of our proposed calculation algorithm.

The time evolution of the queuing model is described as

$$X(t) = (X_1(t), X_2(t), \dots, X_K(t)), \quad (2)$$

where the individual components

$$X_i(t) = (\xi_{ij}^v(t), \tilde{\Psi}_{ij}^v(t)), j = 1, 2, \dots, L, v = 0, 1, \dots, \quad (3)$$

describe the state of the node i at time t , $\xi_{ij}^v(t)$ is the number of type- j sessions on level v that are currently being served at node i , and $\tilde{\Psi}_{ij}^v(t)$ is the corresponding vector of the occupied resources. The system state changes at time instants t_i , (i) when one of the sessions is interrupted, (ii) when it is served successfully and leaves the system, or (iii) when a new session arrives (be it a new or a ‘rerouted’ session). An interrupted session is immediately ‘rerouted’ to another node according to a certain strategy. If there are sufficient resources at the target node to serve this session, the service process continues. If not, the session leaves the system.

C. Numerical solution procedure

In what follows, we introduce an iterative solution algorithm to obtain the performance metrics of interest. The general structure of the algorithm is sketched in Fig. 4. The core parameters are mapped from the analytical blockage model as well as the data received from the ray-based modeling. Based on this, the algorithm iteratively calculates the metrics of interest by adding another level of rerouted sessions with its every iteration.

The proposed algorithm operates as follows. First, we calculate the network-wide parameters, which characterize the relationships between different network nodes while taking into account various levels of ‘rerouted’ sessions. These parameters will be discussed in detail in what follows. This enables us to isolate and analyze every node independently first by calculating the aggregate traffic load and its characteristics, such as the distributions of resource requirements, and then

based on the intermediate parameters to derive the probabilities of a session loss for each node.

Thus acquired metrics are then used to evaluate the session flow at higher ‘reroute’ levels. For convenience of numerical calculation, computations can be seized after any iteration subject to the desired precision, e.g., when the number of ‘rerouted’ sessions reaches zero. As the final step, the network-wide metrics are produced. In what follows, we formulate the analysis process for a single mmWave AP (termed here a node) as if it was isolated. Then, we extend it to take into account multiple nodes, as well as provide an iterative solution to establish the metrics of interest for the entire mmWave system.

1) *Performance of an isolated node*: Let us first concentrate on the operation of the session service process at an arbitrarily chosen node i . Recalling that the service of a session of type j could be interrupted at Poisson time instants, the time that a session spends at this node is the minimum of two random variables (RVs): the residual time of a session and the time until the next interruption. Let $H_{ij}^v(x)$, $x \geq 0$, be the CDF of time that a session of type j on level v occupies the server associated with node i . Recalling that the time spent in LoS state of type- j session at node i follows the exponential distribution with parameter α_{ij} and using the general expression for the minimum of RVs, we have [33]

$$H_{ij}^v(x) = 1 - e^{-\alpha_{ij}x} (1 - B_{ij}^v(x)). \quad (4)$$

Therefore, the mean time that a server at node i is occupied with the session of type j on level v , h_{ij}^v , can be obtained by using the LST of the service time distribution $b_{ij}^v(x)$ as follows

$$h_{ij}^v = \int_0^\infty 1 - e^{-\alpha_{ij}x} (1 - B_{ij}^v(x)) dx = \frac{1 - \beta_{ij}^v(\alpha_{ij})}{\alpha_{ij}}, \quad (5)$$

where $\beta_{ij}^v(\alpha_{ij})$ is the probability that the service of the session of type j on level v at node i is not interrupted, $1/\alpha_{ij}$ is the mean time until the session of type j is interrupted at node i .

Now, let γ_{ij}^v be the aggregate intensity of sessions of type j on level v arriving at the node i , including both new and ‘rerouted’ sessions, as well as denote the offered traffic load of type j sessions on level v at node i as $\rho_{ij}^v = \gamma_{ij}^v h_{ij}^v$. Let

$$\gamma_i = \sum_{v=0}^\infty \sum_{j=1}^L \gamma_{ij}^v, \quad \rho_i = \sum_{v=0}^\infty \sum_{j=1}^L \rho_{ij}^v, \quad (6)$$

and also define the following functions

$$\begin{aligned} F_i(\vec{x}) &= \frac{1}{\gamma_i} \sum_{v=0}^\infty \sum_{j=1}^L \gamma_{ij}^v F_{ij}^v(\vec{x}), \\ G_i(\vec{x}) &= \frac{1}{\rho_i} \sum_{v=0}^\infty \sum_{j=1}^L \rho_{ij}^v G_{ij}^v(\vec{x}), \\ G_{i,n}(\vec{x}) &= \sum_{k=0}^n G_i^{(k)}(\vec{x}) \frac{\rho_i^k}{k!}, i = 1, 2, \dots, K, \end{aligned} \quad (7)$$

where $G_i^{(k)}(\vec{x})$ is the k -fold convolution of $G_i(\vec{x})$, and $G_i^{(0)}(\vec{x})$ is the CDF of the zero vector $\vec{0}$. Here, $F_i(\vec{x})$ is a weighted distribution of the amount of resources required by an arbitrary session of any type or on any level that arrives at node i . $G_i(\vec{x})$ specifies the distribution of the amount of resources weighted

according to the server utilization and imposed by an arbitrary session at node i . $G_{i,n}(\vec{x})$ stands for an auxiliary function used in the subsequent derivations. Note that $G_{i,n}(\vec{x})$ can be recursively evaluated with the algorithm proposed in [34]

$$G_{i,n}(\vec{x}) = G_{i,n-1}(\vec{x}) + H_{i,n}(\vec{x}), n = 1, 2, \dots, \quad (8)$$

where

$$\begin{aligned} H_{i,1}(\vec{x}) &= \rho_i G_i(\vec{x}), \\ H_{i,2}(\vec{x}) &= \frac{\rho_i}{2} (G_i \star H_{i,1})(\vec{x}), \\ &\dots \\ H_{i,n}(\vec{x}) &= \frac{\rho_i}{n} (G_i \star H_{i,n-1})(\vec{x}), \end{aligned} \quad (9)$$

where \star denotes the convolution operation. Further, one can numerically calculate various performance metrics of interest. Particularly, the joint CDF of the number of sessions at node i and the amount of resources occupied by them is given by

$$\begin{aligned} P_{i,n}(\vec{x}) &= \frac{1}{G_{i,N_i}(\vec{R}_i)} G_{i,n}(\vec{x}) \frac{\rho_i^n}{n!}, \\ n &= 0, 1, \dots, N_i, \vec{0} \leq \vec{x} \leq \vec{R}_i, \end{aligned} \quad (10)$$

which can be used further to determine the marginal distributions as well as the means of the number of sessions and the amount of occupied resources at each node.

The conditional and unconditional probabilities of the loss of a session of type j on level v at node i , respectively, are

$$\begin{aligned} \pi_{ij}^v &= 1 - \frac{(G_{i,N_i-1} \star F_{ij}^v)(\vec{R}_i)}{G_{i,N_i}(\vec{R}_i)}, \\ \pi_i &= 1 - \frac{(G_{i,N_i-1} \star F_i)(\vec{R}_i)}{G_{i,N_i}(\vec{R}_i)}. \end{aligned} \quad (11)$$

These probabilities, in turn, allow us to calculate the probability for a session to be lost upon its initial arrival at node i and the same probability for an arbitrary session (i.e., denial of service probability) as

$$\bar{\pi}_i = \sum_{j=1}^L \theta_{ij} \pi_{ij}^0, \quad \bar{\pi} = \frac{1}{\sum_{i=1}^K \lambda_i} \sum_{i=1}^K \lambda_i \sum_{j=1}^L \theta_{ij} \pi_{ij}^0. \quad (12)$$

The average number n_{ij}^v of sessions of type j and level v served by node i is calculated as

$$n_{ij}^v = \rho_{ij}^v (1 - \pi_{ij}^v). \quad (13)$$

Then, the average number of active sessions at node i , n_i , (irrespectively of the session types and levels) and the average number of active sessions in the system, respectively, are:

$$n_i = \rho_i (1 - \pi_i), \quad n = \sum_{i=1}^K n_i. \quad (14)$$

2) *Network performance modeling*: Let us denote by γ_{kl}^v the intensity of session arrivals on level v requesting service of type l at node k . Further, let $\phi_{ij,kl}^v$ be the probability that the service of a session that originally arrives at node i and requests service of type j is interrupted exactly v times, and it is then 'routed' to node k where it requests service of type

l . It is easy to see that the intensities of arriving flows γ_{kl}^v are related to the probabilities $\phi_{ij,kl}^v$ as

$$\gamma_{kl}^v = \sum_{i=1}^K \lambda_i \sum_{j=1}^L \theta_{ij} \phi_{ij,kl}^v, v = 0, 1, \dots \quad (15)$$

Notice that for $v = 0$ we have

$$\phi_{ij,kl}^0 = \delta_{ik} \delta_{jl}, \quad (16)$$

where δ_{xy} is the Kronecker delta function.

For $v \geq 1$, the probabilities $\phi_{ij,kl}^v$ are established as

$$\phi_{ij,kl}^{v+1} = \sum_{r=1}^K \sum_{s=1}^L \phi_{ij,rs}^v q_{rs,kl}^v, v = 0, 1, \dots, \quad (17)$$

where

$$q_{rs,kl}^v = (1 - \pi_{rs}^v)(1 - \beta_{rs}^v) p_{rs,kl}^v, \quad (18)$$

where π_{rs}^v is the loss probability for a session on level v at node r requesting the service of type s and $\beta_{rs}^v = \beta_{rs}^v(\alpha_{rs})$ is the probability that this session is not interrupted. Hence, $q_{rs,kl}^v$ is the probability that the service of a session on level v arriving at node r and requesting the service of type s is interrupted, and it is then 'routed' to node k requesting the service of type l .

Assume that the arriving flows of sessions are Poisson. In this case, the performance parameters of the session service process are determined based on the intensities of the session arrivals (15). The required probabilities $\phi_{ij,kl}^v$ in (15) can be established with an iterative approximation method. Accordingly, $\phi_{ij,kl}^v$ is estimated recursively, where at each step r , $r = 0, 1, \dots$, we disregard all of the flows having the level of greater than r . The following conditions need to be satisfied

$$\begin{aligned} \phi_{ij,kl}^0(n) &= \begin{cases} \delta_{ik} \delta_{jl}, & v = 0, \\ 0, & v > 0, \end{cases} \\ \phi_{ij,kl}^v(n) &= 0, v > n, n = 1, 2, \dots \end{aligned} \quad (19)$$

The rest of the values of $\phi_{ij,kl}^{v+1}$ are approximated as

$$\phi_{ij,kl}^{v+1}(n+1) = \sum_{r=1}^K \sum_{s=1}^L \phi_{ij,rs}^v(n) (1 - \pi_{rs}^v(n)) (1 - \beta_{rs}^v) p_{rs,kl}^v, \quad (20)$$

where $\pi_{rs}^v(n)$ is the loss probability for a session on level v arriving at node r and requesting the service of type s , which corresponds to the arrival flows with the following intensities

$$\gamma_{kl}^v(n) = \begin{cases} \sum_{i=1}^K \lambda_i \sum_{j=1}^L \theta_{ij} \phi_{ij,kl}^v(n), & v = 0, 1, \dots, n \\ 0, & v > n, \end{cases} \quad (21)$$

which implies that $\pi_{rs}^v(n)$ and the corresponding intensities γ_{kl}^v are calculated iteratively: starting with the initial arrival flows (and calculating the loss probabilities $\pi_{rs}^v(n)$ under the assumption of having only the initial flows), then adding the first level of interrupted flows (and calculating the updated loss probabilities), accounting for two levels of arrival flows, etc. The process continues until the desired accuracy is achieved.

Employing the probabilities $\phi_{ij,kl}^v$, one can estimate various performance metrics of interest. In particular, the probability

that a session, initially arriving at node i and requesting the service of type j , is served successfully (irrespective of the number of service interruptions) is

$$\sigma_{ij} = \sum_{v=0}^{\infty} \sum_{k=1}^K \sum_{l=1}^L \Phi_{ij,kl}^v (1 - \pi_{kl}^v) \beta_{kl}^v. \quad (22)$$

Unconditioning the probability σ_{ij} , we obtain the probabilities for the sessions initially arriving at node i and an arbitrary session, respectively, to be served successfully as

$$\sigma_i = \sum_{j=1}^L \theta_{ij} \sigma_{ij}, \quad \sigma = \frac{1}{\sum_{k=1}^K \lambda_i} \sum_{i=1}^K \sum_{j=1}^L \lambda_i \theta_{ij} \sigma_{ij}. \quad (23)$$

Further, the probability that a session initially arriving at node i and requesting the service of type j is eventually lost due to insufficient resources at one of the nodes immediately after a service interruption at the previous node becomes

$$\tilde{\pi}_{ij} = \sum_{v=0}^{\infty} \sum_{k=1}^K \sum_{l=1}^L \Phi_{ij,kl}^v \pi_{kl}^v, \quad (24)$$

thus yielding straightaway the conditional session loss probability for the sessions of type j , i.e., the probability that an initially accepted session is lost. Similarly to the probability σ_{ij} , we have the probability for a session initially arriving at node i and an arbitrary session to be lost

$$\tilde{\pi}_i = \sum_{j=1}^L \theta_{ij} \pi_{ij}, \quad \tilde{\pi} = \frac{1}{\sum_{k=1}^K \lambda_i} \sum_{i=1}^K \sum_{j=1}^L \lambda_i \theta_{ij} \pi_{ij}. \quad (25)$$

IV. CHARACTERIZING REAL mmWAVE SCENARIOS

To demonstrate the full potential of our powerful methodology detailed in the previous sections as well as to assess the performance of a multi-connectivity mmWave system in realistic conditions, this section first outlines a representative urban deployment and then parametrizes the constructed analytical framework with the accurate mmWave channel state information based on our ray-based modeling.

A. Description of target scenario

We select the Times Square, New York City (NYC), USA as a reference urban environment for the purposes of our study. The rationale is that it has been one of the most visited places in NYC and hence multiple users with their mobile devices can request service therein. In particular, the square in question (i) has a large pedestrian area in the middle, which offers an opportunity to study the impact of human mobility on the mmWave system operation, as well as (ii) is surrounded by multiple high-rise buildings with intricate shapes, whereas adjacent streets and avenues house numerous vehicles, all of which may potentially contribute to a complex reflection/scattering picture within the realistic Manhattan-type deployment.

Since the ray-based site-specific tools are known to be very sensitive to the accuracy of the input data, a comprehensive map of the target area was acquired from the Open Street Map (OSM) online resource. Employing our developed tools, including the translator of the object coordinates from the

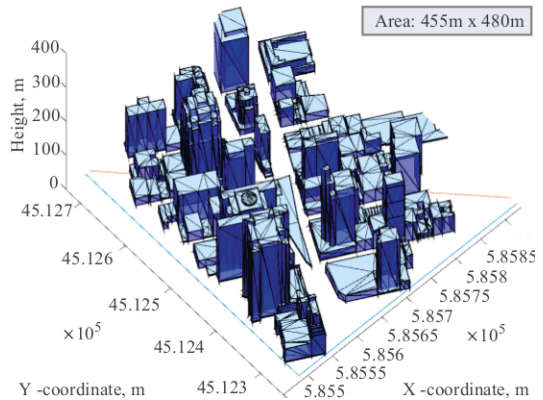


Fig. 5. Our detailed 3D model of the Times Square, NYC, USA.

geodetic to the Cartesian coordinate system (as required for more precise simulations), the OSM data were reworked into a detailed 3D map of the environment. To capture all of the relevant urban effects, this input was further coupled with the traffic densities according to the Department of Transportation, New York State [35], as well as the scene and street infrastructure locations/shape taken from 3D snapshots in Google Street View.

The constructed 3D model of the environment was then described in a manner consistent with the conventional 3D engines, including faces, vertices, bounding boxes, etc. (see Fig. 5). Building on this practical layout, we considered realistic mmWave AP and UE placement options. In the absence of existing information on the deployment of mmWave APs around the Times Square, we assessed several feasible combinations of the AP locations. To this end, twelve possible AP positions were selected (red triangles in Fig. 6, left), which can generally be divided into 2 distinct groups: corner locations and near-wall locations. Our study established that other intermediate positions do not produce significant difference compared to the two considered groups.

As human users can potentially request mmWave service at any location within the square, the alternative UE positions were modeled as a grid with the equidistant step of 1 m across the entire pedestrian area (purple points in Fig. 6, left). Altogether, 12×6031 AP-UE combinations were considered, which results in over than *seventy-two thousand* of candidate mmWave channels. The key details on the deployment- and technology-related parameters are collected in Table II.

B. Ray-based study of the Times Square

1) *Description of ray-based modeler*: To parametrize our analytical methodology with the realistic data on the mmWave radio signal propagation within the target urban environment, we employ our in-house ray-based modeler [36] that has been utilized extensively to support 3GPP standardization contributions on cellular mmWave systems. The reason for preferring a custom-built framework despite the availability of several

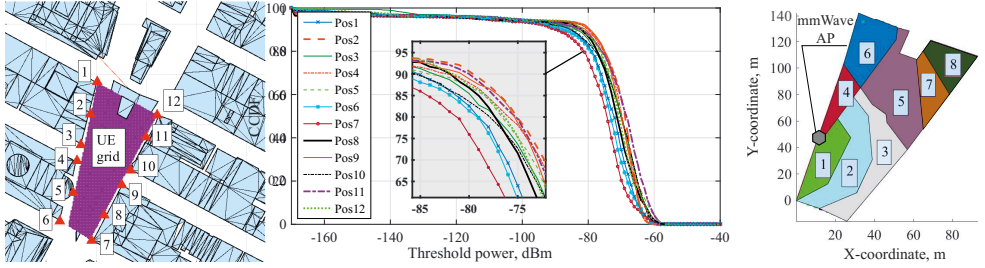


Fig. 6. Candidate deployment of APs (left); received power CCDF (center); example of observed MCS clusters for AP no. 5 when UE is in nLoS (right).

commercial tools is in the desired high level of flexibility in terms of the considered scenarios. This includes incorporation of additional entities, such as humans and vehicles, as well as the possibility to collect all of the intermediate results to calibrate the said framework against the recent measurement and simulation data for the mmWave channels.

The implemented tool comprises two major components: a physical engine and a geometrical engine. While the former module is responsible for the accurate characterization of the key physical effects, such as reflection, diffraction, and diffuse scattering, the role of the latter is to establish the feasible paths between the target transmit (Tx) and receive (Rx) antennas. The main output data of our ray-based modeler for a given mmWave AP-UE link is the channel impulse response (CIR). This parameter is further post-processed to estimate the power delay profile (PDP), the total received power, the SNR, and other important characteristics. The necessary calibration of our modeler to ensure the accuracy of the achieved results is briefly summarized in Appendix B.

Notably, the ray-based modeler does not take into account the MAC-layer features by default, but rather simulates the propagation of multi-path components in the physical domain. To reduce the impact of MAC-layer parameters on the beam management process as well as to focus more on the radio propagation studies, we assumed that the main Tx and Rx lobes are perfectly aligned to each other in case of LoS, while they are directed toward the most significant departure/arrival

path in case of nLoS.

2) *Results of our ray-based study:* We begin our ray-based study by selecting realistic AP locations across the urban deployment, see Fig. 6 (left). For this purpose, we first evaluate the distribution of the received power on the UE grid for all the candidate AP positions. As can be observed in Fig. 6 (center) that represents the complementary CDF (CCDF) of the received power, the considered potential locations provide up to 10 dB difference, wherein positions 2–5 and 9–11 offer the best performance. Coupling these results with an expectation that the real-life cellular mmWave deployments will have the maximum possible inter-AP separation, we aim to produce the minimal feasible set for the subsequent assessment of the multi-connectivity strategies. To this effect, we select the AP locations no. 2, 5, and 11 for our further study.

For each of thus preferred AP positions, we prepare a detailed map of the received power both in the LoS conditions (simulation of the unobstructed scenario) and in the nLoS conditions (simulation of the LoS path blocked by a human body 0.5 m away from the UE). The obtained values of the received power are then converted into the SNR figures by assuming the -84 dBm noise power for the considered 1 GHz channel. Finally, our produced SNR data are mapped onto the realistic MCSs with respect to the actual link conditions. For the sake of clarity, the well-studied OFDM-based MCSs (MCS13 to MCS24) from 60 GHz IEEE 802.11ad technology were adopted here.

As a result of these calculations, for each of the six regimes (three mmWave APs in two conditions: LoS/nLoS) the entire UE grid was clustered – subject to the realistic MCSs to be employed for transferring data traffic on a particular AP-UE link. Hence, Fig. 6 (right) offers an example of such clusters for AP no. 5 in nLoS conditions (to ease the presentation, these results are filtered to avoid the clusters of less than 5 m^2). The obtained MCS indexes were further recalculated into the amount of Hz per bit/s required by each of the constructed “zones”, which were finally used as the input to our above analytical framework. The session-level metrics produced by this hybrid methodology are discussed in Section V.

C. Validation of adopted modeling assumptions

To comprehensively validate the assumptions of our developed analytical framework, we utilized an elaborate system-level simulator that integrates all of the necessary proce-

TABLE II
DEPLOYMENT AND TECHNOLOGY PARAMETERS FOR RAY-BASED STUDY

Parameter	Value
<i>Deployment</i>	
Reference deployment area	Times Square, NYC, USA
Location (lat., long.)	40.758896, -73.985130
Area dimensions	530 m × 440 m
Wall materials	Concrete, glass
Number of faces	1031
Number of considered AP locations	12
Number of considered UE locations	6031
Height of the AP	10 m
Height of the UE	1.5 m
Inter-vehicle distance in the streets	5 m
Vehicle model for ray-based sims.	Two parallelepipeds, total 4 m × 1.8 m × 1.4 m
<i>Technology</i>	
Antenna polarization	Vertical
Radiated power	25 dBm
Carrier frequency	28 GHz
Bandwidth	1 GHz

dures considered by this study. The developed tool was designed by carefully following the corresponding 3GPP guidelines, as well as was calibrated with the 3GPP performance curves from [37] for microwave transmissions. To successfully integrate the mmWave radio access technology, the next-generation physical layer numerology considered by the 3GPP RAN 1 working group in [38] was employed.

Our SLS tool captures the following key procedures: user arrival process, admission control, channel state information (CSI) reporting (with the use of the channel quality indicator, CQI), guaranteed bit rate (GBR) aware scheduling, link adaptation and hybrid automatic repeat request (HARQ) mechanisms, etc. The specific system-level methods as well as the overall SLS information flow are depicted in Fig. 7. The SLS in question ran sequential dynamic simulations on the considered urban scenario. To match the capabilities of our analytical framework, the following assumptions were additionally made:

- The mmWave APs have limited capacity to serve users, meaning that new sessions are only accepted as long as there is spare capacity to satisfy their service requirements (as indicated by the GBR). Users that access the system communicate throughout their *service time*, and the scheduling process meets the demands set by the GBR.
- While the UE carries out an active session, the environment may change from LoS to nLoS conditions due to the mobility of proximate human blockers.

The entire SLS was developed in C# with a highly modular structure, which offers a reasonable balance between the flexibility to modify its modules and the computational performance. With regards to constructing our specific simulation scenario, all of the information on the layout and processing of mmWave signals (coming from the antennas) is fed into the SLS from our ray-based modeler, which has been calibrated separately with the 3GPP data (see Appendix B).

The resulting SLS is a flexible instrument that is capable of supporting multiple mmWave scenarios (with both realistic and synthetic layouts), antenna configurations (across different frequencies and radiation patterns), channel characteristics (including the latest mmWave channel data from [2]), and lower-layer 3GPP procedures (primarily PHY and MAC layers). Therefore, our simplifying considerations on the mmWave PHY layer – as incorporated by the proposed analytical framework – are relaxed in the SLS implementation and verified systematically by matching the final analytical results with those produced by the SLS. Our obtained results together with the actual performance comparison are summarized in the following section.

V. NUMERICAL RESULTS AND DISCUSSION

A. Scenario parametrization and metrics of interest

Assessing the performance of our considered mmWave system in realistic urban conditions, we here parametrize the Times Square scenario detailed in Section IV-A. First, following the images from Google Street view, we estimate the “relative” human (blocker) density to be from 2 down to 0.3, as we move from the center of the square in front of the

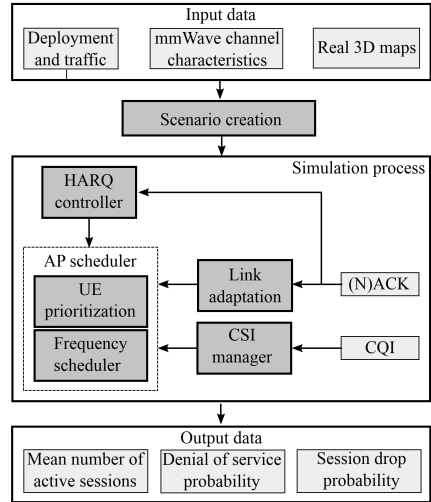


Fig. 7. High-level structure of our system-level simulator.

scene to the sides of the pedestrian area. Hence, we assume the average density of blockers, $\lambda_B = 0.5$, as we set $\lambda_{iB} = 3$ for the zone in front of the scene and $\lambda_{iB} = 0.2$ for the zones that are adjacent to the streets.

To mimic the coexistence of different traffic types, two options for user demands are modeled: 50 Mbit/s (representing the 4K video streaming) and 10 Mbit/s (corresponding to the high-definition video call). The proportion between these two traffic types is set to 1:4, so that each new session requests 50 Mbit/s with the probability of 0.2 and 10 Mbit/s with the probability of 0.8. The average duration of both session types is set to 60 s. Any new arrival is initially handled by the AP with the currently highest received signal strength.

We focus on the following session-level metrics:

- *Denial of service probability.* Probability that a new UE session is rejected by the AP upon its arrival (the session is not served at all).
- *Session drop probability.* Probability that the UE session is accepted by an AP and runs for some time, but then is dropped before its successful completion either at the current AP or at another AP, whereat this session was ‘rerouted’ by one of the multi-connectivity strategies.
- *Mean number of active sessions.* The mean number of running UE sessions, which are carried out by all of the APs in the mmWave system simultaneously.

We evaluate the first two probabilities separately, as the drop of an active session (e.g., a video call) directly translates into worse Quality of Experience (QoE). Here, the second parameter may be even more crucial for the human users, as when a session is accepted for service they would expect it to complete successfully. The discussed performance indicators were derived in Section III, equations (12), (25), and (14). Further, the actual multi-connectivity mmWave strategies, which are compared in terms of these metrics, are introduced in the

following subsection.

B. Considered multi-connectivity strategies

We first note that link blockage is a random event that for an active traffic session (e.g., an ongoing multimedia call) requires near-immediate reaction in order to preserve session continuity. This case is therefore different from the well-studied fallback to lower frequencies, which has been considered in past works on heterogeneous networks. In this study, we focus exclusively on UE-centric strategies, where the session ‘routing’ decision is made by the UE based on the potentially available network-assistance information. Therefore, here we do not address significantly more complex (and potentially non-real-time) network-centric strategies that control the reconnection behavior across the entire system.

In the next subsection, we show that even simple UE-driven multi-connectivity strategies may bring along notable performance gains across both user- and network-centric criteria. These findings advocate for the need of the corresponding support mechanisms, which can become an important consideration in future 3GPP efforts. The following multi-connectivity mmWave strategies are considered in our study (in the order of increasing implementation complexity):

0) *No reconnection (Baseline, NORECON)*: This is the simplest reference (baseline) strategy. It does not assume multi-connectivity operation, since the UE is only connected to a single AP. As a result, the session is dropped, if the AP cannot provision enough radio resources.

1) *Dual-connectivity (DCON)*: This strategy aims to lower the chances that the UE stays associated with the currently blocked mmWave AP (and builds upon 3GPP’s dual-connectivity mechanisms for microwave systems [27]). In case of LoS-to-nLoS transition for its serving AP, the UE reconnects to another (backup) AP having a lower probability of blockage for the zone wherein this UE currently resides. Hence, DCON indirectly reduces the probability of session drop due to poor (nLoS) channel conditions. This strategy requires the knowledge of which AP is the “most visible” for each of the zones (obtained by our framework in Section III).

2) *Multi-connectivity, blockage (MCON, bkg)*: This strategy is an extension of the previous case, which alleviates the following limitation of DCON strategy: multiple UEs in a particular zone are often ‘rerouted’ to the same AP, which may eventually lead to its overload. In contrast, the MCON, bkg strategy ‘reroutes’ the blocked users to other APs in a randomized manner, proportionally to the LoS blockage probabilities to those APs. The amount of required information for this strategy is higher, since the probability of blockage for all the APs has to be known.

3) *Multi-connectivity, throughput (MCON, tpt)*: This strategy makes one step further in that it takes into account the fact that user sessions are not necessarily dropped in case of blockage. Indeed, a session may continue to be served by the same AP, but at a less efficient MCS. A more intelligent behavior is thus not to avoid the blockage itself, but rather to maximize the current MCS index hence directly reducing the session drop probability. With this proposed strategy, in case

the connection to its serving mmWave AP is blocked, the UE compares its current MCS offered by this AP in the nLoS conditions against the average MCSs promised by other APs. Then the UE selects a link with the maximal MCS index and attempts to continue its session there. This strategy requires additional knowledge to be made available to the user, as not only the LoS blockage probabilities but also the average MCS indexes for all the APs are needed.

4) *Multi-connectivity, both blockage and throughput (MCON, bkg+tpt)*: This strategy is an evolved version of the previous one, where a user experiencing blockage first explicitly checks for the received signal strength on the links to all the alternative mmWave APs and then selects the connection with the highest *current* MCS value. Compared to the previous case, this strategy effectively decreases the level of randomness, as the best link in terms of the average throughput may have very low MCS index in case of nLoS and might also be blocked momentarily. At the same time, the resulting scheme is more complex in terms of its implementation at the UE, since not only knowledge of the current mmWave system state needs to be made available, but also additional connection-probe procedures have to be performed at every reconnection.

We study the relative performance of these strategies in our “Times Square” scenario.

C. Understanding performance results

In this subsection, the obtained analytical findings are explained and compared with the corresponding results by our SLS tool.

We begin by studying the denial of service probability as a function of traffic arrival intensity in a dense environment ($\lambda_B = 0.5$), see Fig. 8. Considering NORECON baseline strategy, we observe three distinct regions. The first one spans from $\lambda_I = 0$ to $\lambda_I \approx 2.27$, where the probability in question remains small as the system is underloaded (i.e., still able to handle new sessions), regardless of the actual channel conditions. Then, from $\lambda_I \approx 2.27$ to $\lambda_I \approx 5.92$ NORECON performance degrades rapidly, as the system becomes increasingly occupied with running sessions, which reduce the amount of resources left available for the newly arriving sessions. Finally, the third region starts from $\lambda_I \approx 5.92$, where most of the resources are occupied. In this region, the denial of service probability tends to 1 as $\lambda_I \rightarrow \infty$.

Continuing with the multi-connectivity strategies, we note that they demonstrate similar performance trends, but provide with gains in terms of feasible traffic loading regions from $\approx 25\%$ for the simplest DCON to $\approx 55\%$ for the more complex MCON, bkg+tpt (for the maximum tolerable level of the denial of service probability set to 0.1). Further, there is an important region after $\lambda_I \approx 7.02$, where DCON results in higher initial drop probability than the baseline NORECON. This is because DCON that aims to improve the session continuity on average, actually carries out more active sessions for the same traffic arrival intensity. Therefore, mmWave APs have reduced resources for the new sessions and might thus drop more of them.

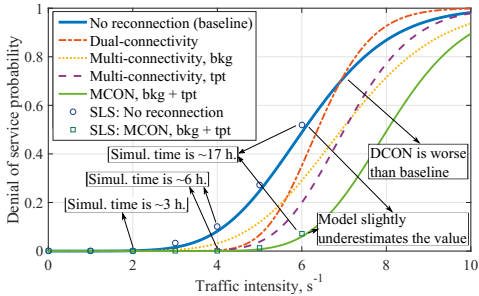


Fig. 8. Denial of service probability vs. traffic intensity.

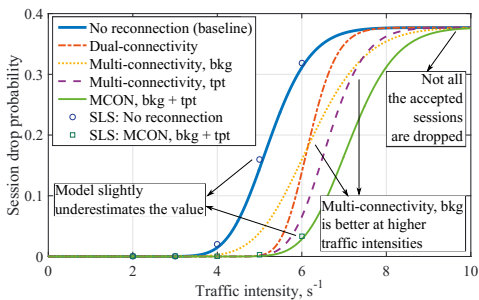


Fig. 9. Session drop probability vs. traffic intensity.

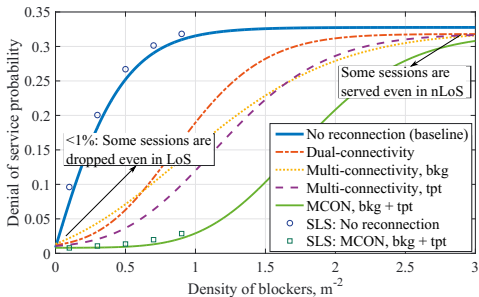


Fig. 10. Denial of service probability vs. density of blockers.

Our analytical performance observations are further confirmed by thorough SLS results for the two different strategies (as an example): baseline NORECON and the most advanced MCON, bkg+tpt. Due to rapidly increasing runtimes to produce reliable results, we have to limit the maximum traffic arrival intensity to $\lambda_I = 6$ and the maximum average density of blockers to $\lambda_B = 0.9$. Within these limitations, the SLS findings verify the analytical results, while the latter can be obtained for a broader range of input parameters. Comparing simulation and analytical data, we observe a reasonable match with under 10% of difference (caused by the fact that the mathematical model simplifies PHY and MAC operation). Owing to this convergence, in the rest of the figures we focus primarily on

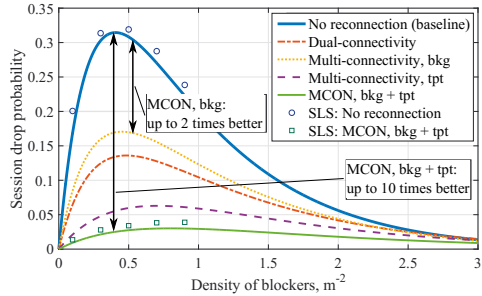


Fig. 11. Session drop probability vs. density of blockers.

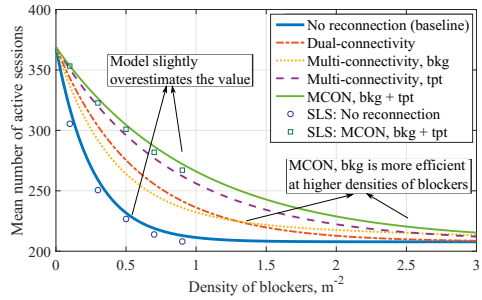


Fig. 12. Mean number of active sessions vs. density of blockers.

the analytical results when illustrating the mmWave system dynamics. We provide additional simulation results mostly for the purposes of verification.

Further, Fig. 9 reports on the session drop probability as a function of traffic arrival intensity for a dense environment ($\lambda_B = 0.5$). While the shape of the curves is similar to that for the denial of service probability, the values are notably lower due to the fact that the considered system is “conservative”: as the traffic intensity grows, our system first refrains from accepting new sessions, and only drops the already accepted ones if they request prohibitive resources due to blockage. Also, the session drop probability generally plateaus at less than 1. The value of the plateau is determined by the density of blockers, the traffic characteristics, and the amount of resources in the system. Once accepted for service, a session can only be dropped in case a blockage occurs. Comparing the impact of different multi-connectivity strategies on this parameter, we learn that there are gains from $\approx 15\%$ for MCON, bkg to $\approx 40\%$ for MCON, bkg+tpt in terms of the feasible levels of traffic intensity.

We continue by assessing the mmWave system performance as a function of the blocker density. To this end, the denial of service probability across all zones, λ_B , is shown in Fig. 10 for $\lambda_I = 5$. Here, we notice that multi-connectivity strategies have a profound effect on the denial of service probability. Particularly, up to $\approx 70\%$ gain for $\lambda_B \in [0.5, 1]$ (i.e., in the dense scenario) is observed. This gain however vanishes to zero for higher values of the density of blockers, where most

of the connections are constantly in nLoS. Fortunately, the densities of over 3 persons per m^2 are hardly possible in typical urban environments. Then, the maximum denial of service probability is lower than 1 and depends on the value of λ_I as well as the fraction of resources that are utilized on average (our considered $\lambda_I = 5$ corresponds to around 90% of occupied resources). Finally, we note that MCON, bkg is more sustainable not only at higher traffic intensities but also at larger densities of blockers.

Proceeding with our assessment, we investigate the session drop probability as a function of the density of blockers in Fig. 11. Here, a slightly higher value of the traffic arrival intensity is considered ($\lambda_I = 6$) to quantify the system performance when over 95% of its resources are occupied. First, we note that for $\lambda_B = 0$ the session drop probability is zero, as expected. Then, the parameter in question grows until when it reaches its maximum at $\lambda_B \approx 0.5$, where many sessions initially accepted in LoS conditions are dropped due to blockage as the system resources deplete in nLoS. After this point, the system tends to accept more sessions in nLoS, as the chances that a new session in LoS appears exactly at the moment when the system has completed serving a user – and thus releases some resources – decrease with the growing density of blockers (and become negligibly small after $\lambda_B \approx 2.8$).

At these values of λ_B , almost all of the accepted sessions are already in nLoS and typically do not go back to LoS throughout the session duration, since the blockage is very frequent. Again, we note approximately 50% of gain between NORECON and simple multi-connectivity strategies, DCON and MCON, bkg, while more advanced schemes, MCON, tpt and MCON, bkg+tpt, are up to 7 and 10 times better than the baseline, when $\lambda_B \approx 0.5$. With this observation, we may conclude that the multi-connectivity strategies are especially beneficial when the mmWave system is highly loaded – and the density of blockers remains average – which results in frequent interruptions of active sessions by multiple LoS-to-nLoS transitions. Since active sessions without multi-connectivity features have higher chances to be dropped already after their first transition from LoS to nLoS, the proposed multi-connectivity strategies (especially, MCON, tpt and MCON, bkg+tpt) offer them “a second chance” to continue their service in LoS, thus significantly improving session continuity.

Finally, after studying the user-centric metrics, we consider the network-centric performance by characterizing the mean number of active sessions as a function of the density of blockers in Fig. 12 for $\lambda_I = 6$. Following the NORECON curve, we observe a more than 35% degradation in the mean number of active sessions for $\lambda_B = 0.5$. For the same value of λ_B , the reduction in the number of active sessions for the more advanced multi-connectivity strategy, MCON, bkg+tpt, is only around 18%. Analyzing the entire range of λ_B , we notice that the basic strategy DCON provides up to 50 additional served sessions as compared to the baseline, while the most intelligent MCON, bkg+tpt scheme brings, on average, 70 sessions more on top of the latter.

VI. MAIN CONCLUSIONS

Both industrial and academic sectors are currently investing significant efforts into integrating the mmWave communications technology as part of the future 5G mobile networks, where multi-connectivity is expected to play an important role to improve session continuity. While rapidly defining the key elements of the next-generation mmWave cellular systems and understanding the intricate specifics of mmWave radio propagation, the community has a prompt need for an integrated evaluation methodology to assess the session-level dynamics of typical mmWave deployments. In this work, we addressed this pressing demand by proposing a powerful integrated methodology that can evaluate both user- and network-centric performance indicators. Tailored to mmWave operation in realistic urban environments, our framework takes into account the relevant properties of mmWave communications, including the detailed structure of mmWave channels, dynamic blockage of LoS by humans at mmWave, and cross-cell mmWave resource allocation. As an example, we considered a real-world Manhattan layout at 28 GHz and performed a detailed assessment of feasible multi-connectivity strategies.

Overall, the main conclusions of this work can be summarized as follows:

- 1) Multi-connectivity in dynamic mmWave systems non-incrementally improves both user- and network-centric performance. Particularly, at the density of one blocker per two square meters ($\lambda_B = 0.5$), multi-connectivity offers up to 7 times lower denial of service probability, up to 10 times lower session drop probability, and up to 25% greater number of sessions.
- 2) The average gains made available by preferring advanced over simpler multi-connectivity strategies are more modest than those, which e.g., dual-connectivity strategy DCON offers on top of the baseline performance. For instance, when the density of blockers is less than one blocker per 3 m^2 ($\lambda_B < 0.33$), the denial of service probability with the DCON strategy is around 5–6 times lower than the one in the baseline case, while the difference between the DCON and the MCON, bkg+tpt is less than 3 times. This implies that even the simplest multi-connectivity schemes notably improve the mmWave system performance.
- 3) At the same time, the use of more advanced strategies requires intelligent balancing between the available performance gains and the corresponding overheads in terms of the additional information to be collected and delivered over the dedicated signaling. The integrated methodology presented in this work may be further extended to quantify this practical trade-off, while comprehensively assessing the actual need for advanced multi-connectivity strategies in a particular urban mmWave deployment.

APPENDIX A

DYNAMICS OF LOS BLOCKAGE PROCESS

To complete the parametrization of our queuing model, we need to capture the process of LoS blockage at each mmWave AP according to [39]. The notation used throughout this

TABLE III
NOTATION AND MAJOR PARAMETERS: LOS BLOCKAGE MODEL

Notation	Description
Static blockage	
λ_i	Intensity of users in zone i
λ_{iB}	Intensity of blockers in zone i
w_P	Diameter of a blocker
h_P	Height of a blocker
$h_{P,T}$	Height of the transmitter associated with a user
h_T	Height of the AP transmitter
r	Distance between the user and the AP
d	Length of the zone where blockers may occlude the LoS between the user and the AP
S_B	Area of the LoS blockage zone
p_L	Probability of having LoS
Dynamic blockage	
λ_{iT}	Intensity of blockers entering the LoS blockage zone i
V	Speed of moving blockers
ξ	Average inter-meeting time for two moving users
$E[V]$	Relative speed of two users
$f(x,y)$	Stationary distribution of the mobility model
S_{U_i}	Area of zone i
$1/\lambda_{iT}$	Mean time between when two consecutive blockers enter the blockage zone
$F_T(x), f_T(x)$	CDF and pdf of the residence time in blockage zone
$F_B(x), f_B(x)$	CDF and pdf of nLoS interval
L	Distance traveled by a blocker inside the blockage zone
$F_L(x), f_L(x)$	Travel distance CDF inside the blockage zone

appendix is summarized in Table III. Consider an arbitrarily chosen zone U_i and let P_i be its geometric center. Recall that the intensity of users in this zone is λ_i , while the intensity of blockers is λ_{iB} .

Let us first fix a randomly chosen time instant t . A graphical illustration of the LoS blockage between the user at P_i and the mmWave AP located at the distance r from the user is illustrated in Fig. 13. The LoS to this user could be occluded by the blockers (human bodies) that are located within the so-called *LoS blockage zone* [39]. The length of this zone is

$$d = \frac{r(h_P - h_{P,T})}{h_T - h_{P,T}} + w_P/2, \quad (26)$$

where h_P is the height of the blockers, $h_{P,T}$ is the height of the Tx associated with a user, h_T is the height of the Tx associated with the mmWave AP, and r is the distance between the AP and the user.

Notice that for the realistic distances between the users and the AP, the area of the LoS blockage zone can be approximated by a rectangle. The area of the LoS blockage zone is thus

$$S_B = w_P \left(\frac{r(h_P - h_{P,T})}{h_T - h_{P,T}} + w_P/2 \right), \quad (27)$$

where w_P is the diameter of a blocker.

Further, to introduce the blockage dynamics, we first need to determine the temporal intensity of the blockers that enter the LoS blockage zone in the zone U_i , λ_{iT} . To approximate λ_{iT} , assume that the blockers and the users are moving within U_i according to the random direction model (RDM, [40]) with the constant speed of V . It has been demonstrated in [41], that the inter-meeting time between two users that move according to the RDM with random velocities of V_1 and V_2 in a square area with the side of L (and having circular coverage areas

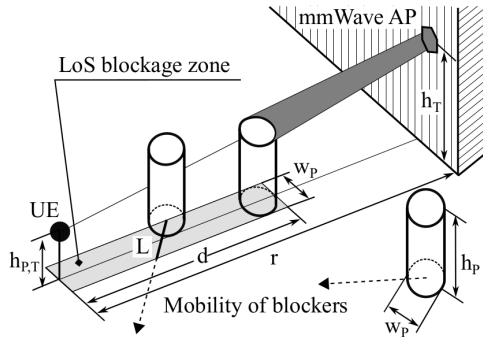


Fig. 13. An illustration of the dynamic LoS blockage process.

with the radius of R) approximately follows an exponential distribution with the parameter

$$\zeta = 2RE[V] \int_0^L \int_0^L f^2(x,y) dx dy, \quad (28)$$

where $E[V]$ is the relative speed of the users and $f(x,y)$ is the stationary distribution of the RDM model, which is known to be uniform, $f(x,y) = 1/L^2$ [41].

Considering an arbitrarily shaped zone U_i and recalling that the user is assumed to remain stationary while the blockers may move around, we can approximate the inter-meeting time of a moving blocker within the LoS blockage zone as

$$\zeta = \left(2w_P V + w_P \left(\frac{r(h_P - h_{P,T})}{h_T - h_{P,T}} + w_P \right) \right) \iint_{S_{U_i}} f^2(s) ds, \quad (29)$$

where V is the constant speed of a moving blocker and $f(s)$ is the stationary distribution of the RDM, $1/S_{U_i}$.

Based on [39] the alternating renewal process where the blocked and unblocked periods interchange is utilized. Let B and A be the RVs denoting the blocked and unblocked periods, respectively. Since the blockers enter the zone according to a Poisson process with the intensity of λ_{iT} , the time spent in the unblocked part, A , follows an exponential distribution with the parameter λ_{iT} , $F_A(x) = 1 - e^{-\lambda_{iT}x}$, having the mean $E[A] = 1/\lambda_{iT}$.

Consider now the distribution of the nLoS interval. First, observe that it may consist of a number of overlapping intervals created by individual blockers. We name an interval T created by an individual blocker the LoS blockage zone residence time. Let $F_T(x)$ and $F_B(x)$ be the CDF of the LoS blockage zone residence time and the entire nLoS interval, respectively. The CDF of the nLoS interval, $F_B(x)$, is the same as the distribution of the busy period in $M/GI/\infty$ queuing system. The CDF of the busy period is [42], see (30), which can be calculated numerically for any CDF of the LoS blockage zone residence time, $F_T(x)$

The only unknown left is the CDF of the LoS blockage zone residence time, $F_T(x)$. We first determine the CDF of the distance traversed by a blocker in the LoS blockage zone and then scale it with the constant velocity of V . The CDF of distance L traveled by a single blocker within the LoS

$$F_B(x) = 1 - \left([1 - F_T(x)](1 - \int_0^x (1 - F_B(x-z)) \exp(-\lambda_{iT} F_T(z)) \lambda_{iT} dz) + \int_0^x (1 - F_B(x-z)) |de^{-\lambda_{iT} F_T(z)}| \right), x > 0. \quad (30)$$

blockage zone can be obtained by using the RV transformation techniques as

$$F_L(x) = \begin{cases} 0, & x \leq 0, \\ w_1 F_{L_1^*}(x) + w_2 F_{L_2^*}(x), & 0 < x \leq \sqrt{d^2 + w_p^2}, \\ 1, & x > \sqrt{d^2 + w_p^2}, \end{cases} \quad (31)$$

where the weights w_1 and w_2 denote (i) the probability for a blocker to start its path from the side of length d and end it at the side of length w_p (or vice versa), and (ii) the probability for a blocker to start its path from the side of length d and end it on the other side of length d , respectively. These probabilities are given by

$$w_1 = \frac{d^2 + 3dw_p}{d^2 + 3dw_p + 2w_p^2}, \quad w_2 = \frac{2w_p^2}{d^2 + 3dw_p + 2w_p^2}. \quad (32)$$

The distribution of the blockage time can now be obtained by the linear transformation L/V , where V is the constant speed of blockers. Recall that the density of the linear transformation $Y = a + bX$ is given by

$$f_Y(y) = f_X[g^{-1}(y)] \left| \frac{dx}{dy} \right| = f_X \left(\frac{y-a}{b} \right) \frac{1}{|b|}. \quad (33)$$

The CDFs corresponding to (32) are

$$F_{L_1^*}(x) = \begin{cases} 0, & x \leq 0; \\ \frac{\pi x^2}{4w_p d}, & 0 < x \leq \min(w_p, d); \\ \frac{1}{2w_p d} (\min(w_p, d) \sqrt{x^2 - \min(w_p, d)^2} + x^2 \arcsin(\frac{\min(w_p, d)}{x})), & \min(w_p, d) < x \leq \max(w_p, d); \\ \frac{1}{2w_p d} (\min(w_p, d) \sqrt{\max(w_p, d)^2 - \min(w_p, d)^2} + d(\sqrt{x^2 - d^2} - \sqrt{\max(w_p, d)^2 - d^2}) + w_p(\sqrt{x^2 - w_p^2} - \sqrt{\max(w_p, d)^2 - w_p^2}) + \max(w_p, d)^2 (\arccos(\frac{w_p}{\max(w_p, d)}) + \arcsin(\frac{\min(w_p, d)}{\max(w_p, d)}) - \arcsin(\frac{d}{\max(w_p, d)})) + x^2 (\arcsin(\frac{d}{x}) - \arccos(\frac{w_p}{x})), & \max(w_p, d) < x \leq \sqrt{d^2 + w_p^2}; \\ 1, & x > \sqrt{d^2 + w_p^2}, \end{cases}$$

$$F_{L_2^*}(x) = \begin{cases} 0, & x \leq d; \\ \frac{d^2 - x^2 + 2w_p \sqrt{x^2 - d^2}}{w_p^2}, & d < x \leq \sqrt{d^2 + w_p^2}; \\ 1, & x > \sqrt{d^2 + w_p^2}. \end{cases} \quad (34)$$

Therefore, we obtain the probability density function (pdf) of $T = L/V$ as

$$f_T(x) = f_L(Vx)V, \quad (35)$$

where $f_L(x) = F_L'(x)$.

As one may observe, the LoS blockage process for a user located at the geometric center of U_i is a renewal process with the unblocked periods having an exponential distribution and the blocked periods following a general distribution. To apply this within the proposed dynamic queuing framework for mmWave resource allocation, we adopt the following additional assumptions: (i) all of the users in U_i have identical characteristics of the blockage process and (ii) the distribution of the blocked interval is obtained by (30). Under these assumptions, the arrival process of sessions to an arbitrary mmWave AP is Poisson. The intensity of interruptions of sessions of type j at node i is computed as

$$\alpha_{ij} = \begin{cases} 1/\lambda_{iT}, & 1 \leq j \leq L/2; \\ \frac{1}{\int_0^{\infty} x f_{B,ij}(x) dx}, & L/2 + 1 \leq j \leq L, \end{cases} \quad (36)$$

where $f_{B,ij}(x)$ is the pdf of blocked interval and L is the number of available session types. Note that $f_{B,ij}$ is independent of the session type, that is, $f_{B,ij}(x) = f_{B,ik}(x)$, $i = k$.

It is also important to note that the LoS blockage processes to different mmWave APs may be approximately independent of each other, as the dependence appears only due to an overlap of the LoS blockage zones across various APs. For realistic deployments, these areas are relatively small compared to the LoS blockage zones themselves.

APPENDIX B

CALIBRATION OF RAY-BASED MODELER WITH 3GPP DATA

This appendix reports on the calibration results for our ray-based modeler against the 3GPP data in the reference scenario. The typical deployment corresponding to our study is an idealized Manhattan grid [2]. It was therefore selected for calibration. The topology in question is standard to model urban deployments and was extensively utilized in past initiatives, such as WINNER or COST, as well as in the METIS-2020 project. In particular, the path loss results obtained by the modeler in the Manhattan grid scenario are compared with the UMi street-canyon models defined in 3GPP TR 38.900, Table 7.4.1-1: Path loss models [2]. The key simulation parameters are summarized in Table IV, while the results of the conducted calibration are offered in Fig. 14.

Our performed calibration ensures the accuracy of the constructed ray-based modeler (the average values in Fig. 14 match tightly). It also accentuates the need for utilization of the ray-based modeler in our study, since the ratified 3GPP models do not fully capture the notable channel variations at increased distance, which are caused by the multi-path interference. As a result, these accurate data are of high importance for our study to better mimic the behavior of practical mmWave systems in realistic urban conditions.

TABLE IV
CALIBRATION SCENARIO: PARAMETERS

Parameter	Value
Considered topology	3GPP Manhattan grid [2]
Material of walls	Concrete ($\epsilon_r = 5.31$, $\sigma_r = 0.484$) [43]
Number of faces	242
Number of Rx positions	1000
Antenna type	Isotropic radiator
Antenna polarization	Vertical
Number of Tx positions	5
Radiated power	0 dBm
Radiated signal shape	Sinusoidal
Carrier frequency	28 GHz

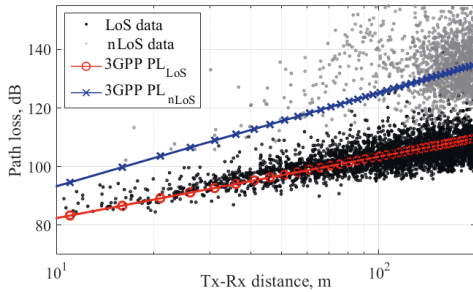


Fig. 14. Calibration results for path loss in the Manhattan grid scenario [2].

REFERENCES

- [1] T. S. Rappaport, S. Sun, R. Mayzus, H. Zhao, Y. Azar, K. Wang, G. N. Wong, J. K. Schulz, M. Samimi, and F. Gutierrez, "Millimeter wave mobile communications for 5G cellular: It will work!," *IEEE Access*, vol. 1, pp. 335–349, May 2013.
- [2] 3GPP, "Channel model for frequency spectrum above 6 GHz (Release 14)," 3GPP TR 38.900 V2.0.0, 2016.
- [3] 3GPP, "Study on scenarios and requirements for next generation access technologies," 3GPP TR 38.913 V0.3.0, 2016.
- [4] 3GPP, "RAN workshop on 5G: Summary," available at <http://www.3gpp.org/news-events/3gpp-news/1734-ran5g/>, 2015.
- [5] METIS, "Initial channel models based on measurements," METIS deliverable D1.2, April 2014.
- [6] COST IC1004, "Channel measurements and modeling for 5G networks in the frequency bands above 6 GHz," white paper, April 2016.
- [7] K. Haneda *et al.*, "5G 3GPP-like channel models for outdoor urban microcellular and macrocellular environments," in *Proc. of the 83rd IEEE Vehicular Technology Conference (VTC 2016-Spring)*, May 2016.
- [8] N. A. Muhammad, P. Wang, Y. Li, and B. Vucetic, "Analytical model for outdoor millimeter wave channels using geometry-based stochastic approach," *IEEE Transactions on Vehicular Technology*, vol. 66, pp. 912–926, February 2017.
- [9] K. Haneda, N. Omaki, T. Imai, L. Raschkowski, M. Peter, and A. Roivainen, "Frequency-agile pathloss models for urban street canyons," *IEEE Transactions on Antennas and Propagation*, vol. 64, pp. 1941–1951, May 2016.
- [10] S. Sun, T. S. Rappaport, T. A. Thomas, A. Ghosh, H. C. Nguyen, I. Z. Kovacs, I. Rodriguez, O. Koymen, and A. Partyka, "Investigation of prediction accuracy, sensitivity, and parameter stability of large-scale propagation path loss models for 5G wireless communications," *IEEE Transactions on Vehicular Technology*, vol. 65, pp. 2843–2860, May 2016.
- [11] S. Sun, T. A. Thomas, T. S. Rappaport, H. Nguyen, I. Z. Kovacs, and I. Rodriguez, "Path loss, shadow fading, and line-of-sight probability models for 5G urban macro-cellular scenarios," in *Proc. of IEEE GLOBECOM*, December 2015.
- [12] V. Petrov, D. Moltchanov, P. Kustarev, J. M. Jornet, and Y. Koucheryav, "On the use of integral geometry for interference modeling and analysis in wireless networks," *IEEE Communications Letters*, vol. 20, pp. 2530–2533, December 2016.
- [13] K. Venugopal, M. C. Valenti, and R. W. Heath, "Device-to-device millimeter wave communications: Interference, coverage, rate, and finite topologies," *IEEE Transactions on Wireless Communications*, vol. 15, pp. 6175–6188, September 2016.
- [14] V. Petrov, M. Komarov, D. Moltchanov, J. M. Jornet, and Y. Koucheryav, "Interference and SINR in millimeter wave and terahertz communication systems with blocking and directional antennas," *IEEE Transactions on Wireless Communications*, vol. 16, pp. 1791–1808, March 2017.
- [15] K. Yang, Z. Zhao, J. Liu, and Q. H. Liu, "Robust adaptive beamforming using an iterative FFT algorithm," *Signal Processing*, vol. 96, pp. 253–260, March 2014.
- [16] S. Mumtaz, J. Rodriguez, and D. Linglong, *mmWave Massive MIMO: A Paradigm for 5G*. Academic Press, 2016.
- [17] E. Björnson, E. G. Larsson, and T. L. Marzetta, "Massive MIMO: ten myths and one critical question," *IEEE Communications Magazine*, vol. 54, pp. 114–123, February 2016.
- [18] X. Gao, L. Dai, S. Han, C. I, and R. W. Heath Jr., "Energy-efficient hybrid analog and digital precoding for mmWave MIMO systems with large antenna arrays," *IEEE Journal on Selected Areas in Communications*, vol. 34, pp. 998–1009, April 2016.
- [19] W. Liu, S. Jin, C.-K. Wen, M. Matthaiou, and X. You, "A tractable approach to uplink spectral efficiency of two-tier massive MIMO cellular HetNets," *IEEE Communications Letters*, vol. 20, pp. 348–351, February 2016.
- [20] S. He, Y. Huang, Y. Lu, C. Qi, and L. Yang, "Resource efficiency: A new beamforming design for multicell multiuser systems," *IEEE Transactions on Vehicular Technology*, vol. 65, pp. 6063–6074, August 2016.
- [21] J. G. Andrews, T. Bai, M. Kulkarni, A. Alkhateeb, A. Gupta, and R. W. Heath Jr., "Modeling and analyzing millimeter wave cellular systems," *IEEE Transactions on Communications*, vol. 65, no. 1, pp. 403–430, 2017.
- [22] Z. Zhang, Z. Ma, M. Xiao, G. K. Karagiannidis, Z. Ding, and P. Fan, "Two-timeslot two-way full-duplex relaying for 5G wireless communication networks," *IEEE Transactions on Communications*, vol. 64, pp. 2873–2887, July 2016.
- [23] P. Wang, Y. Li, L. Song, and B. Vucetic, "Multi-gigabit millimeter wave wireless communications for 5G: from fixed access to cellular networks," *IEEE Communications Magazine*, vol. 53, pp. 168–178, January 2015.
- [24] A. Samuylov, M. Gapeyenko, D. Moltchanov, M. Gerasimenko, S. Singh, N. Himayat, S. Andreev, and Y. Koucheryav, "Characterizing Spatial Correlation of Blockage Statistics in Urban mmWave Systems," in *Proc. of the IEEE Globecom Workshops (GC Wkshps)*, December 2016.
- [25] A. R. Radwan, K. Huq, S. M. Mumtaz, K. Fung-Tsang, and J. Rodriguez, "Low-cost on-demand C-RAN based mobile small-cells," *IEEE Access*, pp. 1–8, May 2016.
- [26] M. Giordani, M. Mezzavilla, S. Rangan, and M. Zorzi, "Multi-connectivity in 5G mmwave cellular networks," in *Proc. of the 15th Annual Mediterranean Ad Hoc networking workshop*, 2016.
- [27] M. Lema A., E. Pardo, O. Galinina, S. Andreev, and M. Dohler, "Flexible dual-connectivity spectrum aggregation for decoupled uplink and downlink access in 5G heterogeneous systems," *IEEE Journal on Selected Areas in Communications*, vol. 34, October 2016.
- [28] M. Giordani, M. Mezzavilla, and M. Zorzi, "Initial access in 5g mmwave cellular networks," *IEEE Communications Magazine*, vol. 54, pp. 40–47, November 2016.
- [29] F. B. Tesema, A. Awada, I. Viering, M. Simsek, and G. P. Fettweis, "Mobility modeling and performance evaluation of multi-connectivity in 5G intra-frequency networks," in *Proc. of IEEE Globecom Workshops (GC Wkshps)*, December 2015.
- [30] ITU-R, "IMT vision – framework and overall objectives of the future development of IMT for 2020 and beyond," Recommendation ITU-R M.2083-0, 2015.
- [31] R. Ford, M. Zhang, M. Mezzavilla, S. Dutta, S. Rangan, and M. Zorzi, "Achieving ultra-low latency in 5G millimeter wave cellular networks," *IEEE Communications Magazine*, vol. 55, pp. 196–203, March 2017.
- [32] H. Shokri-Ghadikolaei, C. Fischione, G. Fodor, P. Popovski, and M. Zorzi, "Millimeter wave cellular networks: A MAC layer perspective," *IEEE Transactions on Communications*, vol. 63, pp. 3437–3458, October 2016.
- [33] S. Ross, *Introduction to probability models*. Academic Press, 2010.
- [34] J. P. Buzen, "Computational algorithms for closed queueing networks with exponential servers," *Communications of the ACM*, vol. 16, pp. 527–531, September 1973.
- [35] New York State Department of Transportation, "Annual average daily traffic in New York city," available at <https://www.dot.ny.gov/tdiv>, 2015.

- [36] D. Solomitckii, Q. C. Li, T. Balercia, C. R. C. M. da Silva, S. Talwar, S. Andreev, and Y. Koucheryavy, "Characterizing the impact of diffuse scattering in urban millimeter-wave deployments," *IEEE Wireless Communications Letters*, vol. 5, pp. 432–435, August 2016.
- [37] 3GPP, "Evolved universal terrestrial radio access (E-UTRA); further advancements for E-UTRA physical layer aspects (Release 9)," 3GPP TR 36.814 version 9.0.0, March 2010.
- [38] 3GPP, "Study on new radio access technology physical layer aspects," 3GPP TR 38.802 version 0.3.1, 2016.
- [39] M. Gapeyenko, A. Samuylov, M. Gerasimenko, D. Moltchanov, S. Singh, M. R. Akdeniz, E. Aryafar, N. Himayat, S. Andreev, and Y. Koucheryavy, "On the temporal effects of mobile blockers in urban millimeter-wave cellular scenarios," in *//arXiv preprint, arXiv:1705.08037v1*, 2017.
- [40] P. Nain, D. Towsley, B. Liu, and Z. Liu, "Properties of random direction models," in *Proc. of the IEEE 24th Annual Joint Conference of the IEEE Computer and Communications Societies (INFOCOM)*, March 2005.
- [41] R. Groenevelt, "Stochastic models for mobile ad hoc networks," PhD thesis, INRIA Sophia-Antipolis, 2005.
- [42] D. J. Daley, "The busy period of the $M/GI/\infty$ queue," *Queueing Systems*, vol. 38, pp. 195–204, June 2001.
- [43] ITU, "Effects of building materials and structures on radiowave propagation above 100 MHz," *ITU-R P.2040-1*, July 2015.

PUBLICATION

IV

Analysis of Intelligent Vehicular Relaying in Urban 5G+ Millimeter-Wave Cellular Deployments

V. Petrov, D. Moltchanov, S. Andreev and R. W. Heath

Proc. of IEEE Global Communications Conference (IEEE GLOBECOM)2019, 1–6

Publication reprinted with the permission of the copyright holders

Analysis of Intelligent Vehicular Relaying in Urban 5G+ Millimeter-Wave Cellular Deployments

Vitaly Petrov^{*,1}, Dmitri Moltchanov^{*}, Sergey Andreev^{*}, and Robert W. Heath Jr.[†]

^{*}Unit of Electrical Engineering, Tampere University, Finland

[†]Department of Electrical and Computer Engineering, The University of Texas at Austin, USA

{vitaly.petrov, dmitri.moltchanov, sergey.andreev}@tuni.fi, rheath@utexas.edu

Abstract—The capability of smarter networked devices to dynamically select appropriate radio connectivity options is especially important in the emerging millimeter-wave (mmWave) systems to mitigate abrupt link blockage in complex environments. To enrich the levels of diversity, mobile mmWave relays can be employed for improved connection reliability. These are considered by 3GPP for on-demand densification on top of the static mmWave infrastructure. However, performance dynamics of mobile mmWave relaying is not nearly well explored, especially in realistic conditions, such as urban vehicular scenarios. In this paper, we develop a mathematical framework for the performance evaluation of mmWave vehicular relaying in a typical street deployment. We analyze and compare alternative connectivity strategies by quantifying the performance gains made available to smart devices in the presence of mmWave relays. We identify situations where the use of mmWave vehicular relaying is particularly beneficial. Our methodology and results can support further standardization and deployment of mmWave relaying in more intelligent 5G+ “all-mmWave” cellular networks.

I. INTRODUCTION

Millimeter-wave (mmWave) communications is one of the key solutions introduced by the fifth-generation (5G) wireless networks. Adopted by 3GPP for New Radio (NR) technology, mmWave communications enable transmissions with the data rates considerably higher than those offered by 4G microwave solutions [1]. In contrast, the coverage range of a mmWave access point (AP) is expected to be smaller than that offered by sub-6 GHz cellular systems and will remain within a few hundred meters [2]. The highly directional mmWave transmissions are also susceptible to blockage – occlusion of the signal path by buildings, vehicles, and even human bodies [3]. Dense deployments of mmWave APs are a natural solution, but may incur capital and operating expenditures [4].

Millimeter-wave relays are an alternative to backhauled APs. Static mmWave relays can densify the network at lower costs than full-fledged APs without compromising its performance [5], [6]. The use of static mmWave relays has been ratified by 3GPP as part of 5G NR Rel. 15 [7]. Currently, 3GPP continues to investigate this area by targeting a possible adoption of mobile mmWave relays mounted on vehicles and drones as part of NR Rel. 17 and beyond [8]. That work is currently at an early stage focused primarily on identifying the target setups, where the deployment of mobile mmWave relays is especially beneficial. For this purpose, a holistic

methodology is required, which accounts for a realistic city deployment, features of vehicular and drone-carried relay operation, and complex propagation of mmWave signal.

In this paper, we develop a mathematical framework for the performance evaluation of a cellular network with mmWave APs, intelligent mmWave users, and mmWave vehicular relays. Our framework accounts for the specifics of a realistic urban (street) deployment, 3GPP-compatible mmWave signal propagation model with blockage caused by humans and vehicles, and alternative relaying strategies. We apply our framework to quantifying the realistic performance gains that mmWave vehicular relays may bring to an average user. We highlight the conditions where the use of mmWave vehicular relays leads to a more than two-fold increase in the spectral efficiency. Our methodology and numerical results can be used to justify the system design choices for the mmWave vehicular relaying in complex and dynamic mmWave-based networks.

II. SYSTEM MODEL

A. Scenario and Deployment

We consider a straight segment of a street with four traffic lanes and two sidewalks (see Fig. 1). The lane width is w_L and the width of the sidewalk is w_S . Static mmWave APs are deployed on the lampposts between the central lanes at a height h_A . The separation distance between the APs is d_i . On each sidewalk, there are two human paths representing a typical bidirectional flow. A human body is modeled as a cylinder with a radius r_p and a height h_p . The pedestrians on the same path are separated by a random distance ℓ , where L is a generally-distributed random variable (RV) with the cumulative distribution function (CDF) $F_L(x)$. Each pedestrian carries a mmWave user equipment (UE) at a height of h_U .

Two types of vehicles are deployed in our scenario: (i) regular vehicles termed *cars* and modeled as parallelepipeds with the dimensions of $\ell_C \times w_C \times h_C$, and (ii) large vehicles representing city buses and trucks termed *buses* and modeled as parallelepipeds with the dimensions of $\ell_T \times w_T \times h_T$. Buses and cars are deployed randomly along the centers of all the traffic lanes with a random distance d between their bumpers, where D is a generally-distributed RV with the mean $E[D]$. Each vehicle is a bus with probability p_T independently of other vehicles. A fraction of cars, p_R , are also equipped with mmWave relaying capabilities and can act as “cells on wheels” (COWs). The COW coverage range is R .

¹A part of this work has been completed during the research visit of Vitaly Petrov to The University of Texas at Austin, USA in Fall 2018.

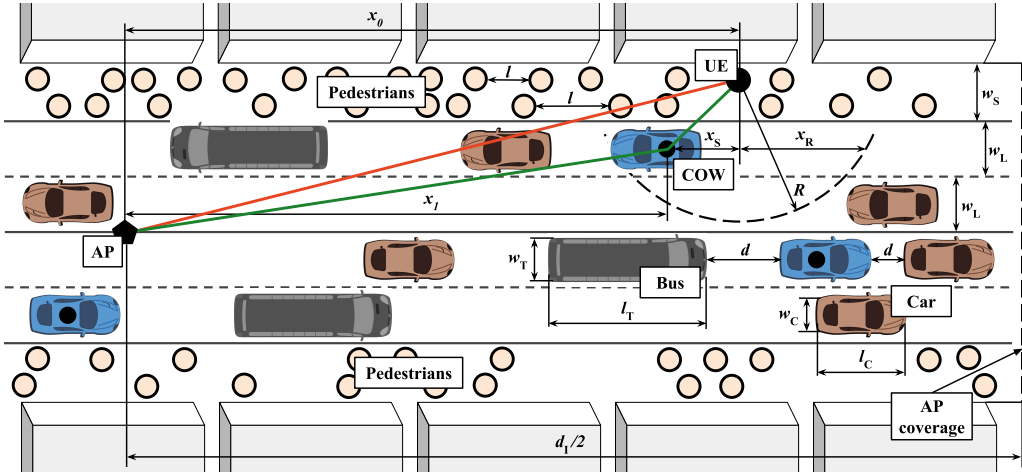


Fig. 1. Our considered urban street deployment for mmWave vehicular relaying with the regular placement of static mmWave APs, random locations of pedestrians, cars, and buses. A fraction p_R of cars are also equipped with mmWave relaying capabilities and can forward traffic between UEs and mmWave APs.

B. Propagation Model

The mmWave signal propagation is modeled following the recent 3GPP considerations [9] and accounts for both human- and vehicle-body blockage. In case where the line-of-sight (LoS) path between the communicating nodes is occluded by either a human or a vehicle body, the nodes use an alternative non-line-of-sight (nLoS) path by utilizing one of the reflected or scattered mmWave signal components [10].

Following [9], the pathloss, T , is given by

$$T = \begin{cases} 32.4 + 21.0 \log_{10}(d_{3D}) + 20 \log_{10} f_c, & \text{LoS,} \\ 32.4 + 31.9 \log_{10}(d_{3D}) + 20 \log_{10} f_c, & \text{nLoS,} \end{cases} \quad (1)$$

where f_c is the carrier frequency and d_{3D} is the 3D separation distance between the nodes.

The communicating entities in our model (APs, UEs, and COWs) set their transmit powers as P_A , P_U , and P_C , respectively. All the nodes also utilize directional antenna radiation patterns with the corresponding gains of G_A , G_U , and G_C : $G_U \leq G_C \leq G_A$. For simplicity, we assume perfect beam alignment between the communicating entities.

C. Connectivity Models

We analyze and compare three UE connectivity strategies:

- *Baseline.* All the UEs always utilize the infrastructure link to the nearest static mmWave AP. No relays are used.
- *Conservative Relay.* COWs can assist UEs within their coverage. The radio resources occupied by UE-COW connections **do not overlap** with those utilized for UE-AP and COW-AP links. This strategy primarily reflects the implementation of mobile relays in 3G and 4G systems by providing a pessimistic estimate for the performance gains of mmWave vehicular relays in our scenario.
- *Aggressive Relay.* COWs can assist UEs within their coverage. The radio resources occupied by UE-COW

connections **may overlap** with those utilized for UE-AP and COW-AP links, thus exploiting better spatial diversity of narrow-beam 5G mmWave communications [11]. This strategy offers an optimistic estimate for the performance gains of mmWave vehicular relays in our scenario.

For both relay-aided strategies, each of the UEs continuously selects the path currently characterized by the highest signal-to-noise ratio (SNR) out of those provided by the static APs and COWs. UE is assumed to instantaneously switch to the best available link via multi-connectivity mechanisms [12].

In the following sections, we develop a mathematical framework for evaluating the introduced connectivity strategies. We particularly focus on a dense deployment of mmWave APs that do not permit outages. Therefore, the UE mean spectral efficiency (SE) is selected as a primary performance indicator.

III. ANALYSIS OF BASELINE MODEL

A. Human-Body Blockage Modeling

In this subsection, we derive the probability that the link between UE and AP is blocked by a pedestrian, where the UE is separated from the AP by a fixed distance of x_0 . Following [13], the link is considered blocked if there is at least a single pedestrian center in the “blockage zone”, see Fig. 2. The width of this rectangle is $2r_p$, while its length, ℓ_B , can be derived as $\ell_B = r_p + d_{2D}(h_p - h_U)/(h_A - h_U)$, where $d_{2D} = \sqrt{(3w_S/4 + 2w_L)^2 + x_0^2}$ is the AP-UE distance.

Observe that the link can be blocked by the pedestrians on both paths. From the scenario geometry, the blockage probability for the pedestrians on the same path, p_{B,H_1} , equals the probability that at least a single cylinder base center is within the interval of length $z = r_p/\sin(\alpha)$. Hence, we have

$$p_{B,H_1} = \Pr\{\ell \leq z\} = F_L(r_p/\sin \alpha), \quad (3)$$

$$p_B = \begin{cases} F_L(z) + \frac{1-F_L(z)}{E[L]} \left(2z - \int_0^{2z} F_L(x) dx \right), & h_T < h_T^* \cap w_S \leq 2r_P + \frac{(h_P-h_U)(8w_L+3w_S)}{2(h_A-h_U)}, \\ F_L(z), & h_T < h_T^* \cap w_S > 2r_P + \frac{(h_P-h_U)(8w_L+3w_S)}{2(h_A-h_U)}, \\ 1 - \frac{(\ell_C - p_T \ell_C + E[D])(1-F_L(z) - \frac{1-F_L(z)}{E[L]}(2z - \int_0^{2z} F_L(x) dx))}{p_T \ell_T + (1-p_T) \ell_C + E[D]}, & h_T \geq h_T^* \cap w_S \leq 2r_P + \frac{(h_P-h_U)(8w_L+3w_S)}{2(h_A-h_U)}, \\ 1 - \frac{(\ell_C - p_T \ell_C + E[D])(1-F_L(z))}{p_T \ell_T + (1-p_T) \ell_C + E[D]}, & h_T \geq h_T^* \cap w_S > 2r_P + \frac{(h_P-h_U)(8w_L+3w_S)}{2(h_A-h_U)}. \end{cases} \quad (2)$$

where $F_L(x)$ is the CDF of the RV characterizing the distance between the neighboring humans on the same path.

The link can also be blocked by the pedestrians on the other path when the following two conditions apply simultaneously. First, ℓ_B has to be large enough so that this path crosses the blockage zone rectangle. Second, there should be at least one cylinder base center within the $2z$ -long segment of the path crossing the blockage zone rectangle (see Fig. 2).

The first condition can be written as $w_S/2 \leq s_B$, where $w_H = 2w_L + 3w_S/4$. For the second condition, we apply the result from [14]. Finally, the sought blockage probability is

$$p_{B,H} = \begin{cases} \frac{2z - \int_0^{2z} F_L(x) dx}{E[L]}, & w_S \leq 2r_P + 2w_H \frac{h_P - h_U}{h_A - h_U}, \\ 0, & w_S > 2r_P + 2w_H \frac{h_P - h_U}{h_A - h_U}. \end{cases} \quad (4)$$

Finally, because the events of blockage for the two paths are independent of each other, we arrive at the following expression for the human-body blockage probability

$$p_{B,H} = \begin{cases} F_L(z) + \frac{(1-F_L(z))(2z - \int_0^{2z} F_L(x) dx)}{E[L]}, & w_S \leq w_U, \\ F_L(z), & w_S > w_U, \end{cases} \quad (5)$$

where $z = r_P \sqrt{(8w_L + 3w_S)^2 + 16x_0^2} / (8w_L + 3w_S)$ and $w_U = 2r_P + w_H (h_P - h_U) / (h_A - h_U)$.

B. Vehicle-Body Blockage Modeling

In the considered scenario, a link between UE and AP can also be occluded by large vehicles, termed buses. Based on the scenario geometry in Fig. 3, the following holds for the minimal bus height that results in blockage, h_T^*

$$\frac{h_T^* - h_U}{h_A - h_U} = \frac{\sqrt{x_B^2 + w^2}}{\sqrt{x_0^2 + w_H^2}}, \quad (8)$$

where x_B is the shift of the blocking vehicle from the UE, $x_B = x_0 w / w_H$. Substituting x_B into (8), we make an important observation that h_T^* does not depend on x_0 , i.e.,

$$h_T^* = h_U + \frac{3w_S + 2w_L - 2w_T}{8w_L + 3w_S} (h_A - h_U). \quad (9)$$

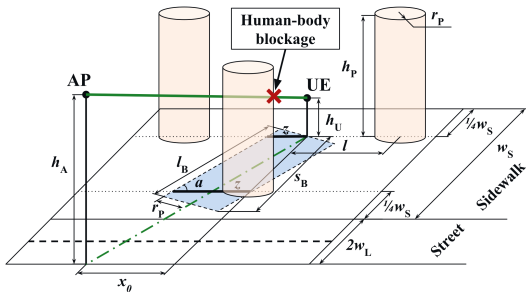


Fig. 2. Human-body blockage modeling.

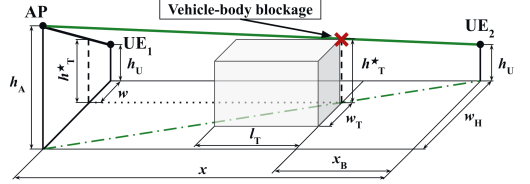


Fig. 3. Minimal height of a bus resulting in vehicle-body blockage.

We now estimate the fraction of time when the UE-AP link is blocked by a bus. Since the number of cars between the two buses on the same lane follows the geometrical distribution with parameter p_T , the mean number of cars between the two buses, $E[N_C]$, can be estimated as $E[N_C] = (1 - p_T) / p_T$. This implies that the random distance between the two buses, d_B , comprises of N_C cars and $N_C + 1$ inter-vehicle intervals:

$$E[D_B] = E[N_C \ell_C + (N_C + 1)d] = \frac{E[D] + \ell_C(1 - p_T)}{p_T}. \quad (10)$$

Recalling that the deployment of vehicles follows the renewal process with generally distributed intervals, the vehicle-body blockage probability, $p_{B,V}$, can be established as [15]

$$p_{B,V} = \begin{cases} 0, & h_T < h_T^*, \\ \frac{\ell_T}{\ell_T + E[D_B]}, & h_T \geq h_T^*. \end{cases} \quad (11)$$

C. Mean Spectral Efficiency

We now estimate the mean SE of the link between the UE and the AP. First, since the blockage events caused by humans and those caused by vehicles are independent, we derive the total blockage probability for the UE-AP link, p_B , as in (2). Further, we determine the conditional SNR values in case of LoS (non-blocked) and nLoS (blocked) signal path between the UE and the AP, S_L and S_N , respectively. Following (1),

$$S_L = 10^{\frac{F_U + G_A + G_U - N_0(B) - 32.4 - 20 \log_{10} f_c - 21.0 \log_{10}(K_U)}{10}}, \\ S_N = 10^{\frac{F_U + G_A + G_U - N_0(B) - 32.4 - 20 \log_{10} f_c - 31.9 \log_{10}(K_U)}{10}}, \quad (12)$$

where $K_U = \sqrt{x_0^2 + [2w_L + 3w_S/4]^2 + (h_A - h_U)^2}$.

We obtain the mean SE for the UE located at a separation distance of x_0 from the AP, $C(x_0)$, as

$$C(x_0) = p_B \log_2(1 + S_N) + (1 - p_B) \log_2(1 + S_L). \quad (13)$$

Finally, the mean SE for an arbitrary UE, $E[C]$, is derived as

$$E[C] = \frac{2}{d_I} \int_0^{d_I/2} C(x_0) dx_0. \quad (14)$$

$$p_B^* = \begin{cases} F_{D_B}(\ell_{B,C} - \frac{\ell_C}{2}), & h_T < h_T^*, \\ 1 - (1 - \frac{p_T \ell_T}{p_T \ell_T + (1-p_T)\ell_C + E[D]})(1 - F_{D_B}(\ell_{B,C} - \frac{\ell_C}{2})), & h_T \geq h_T^*, \end{cases} \quad (6)$$

$$C_2^\dagger(x_0, x_S) = \frac{1}{1/C^*(x_S) + 1/C^*(x_1)} = p_C \left(\frac{p_B^* p_B^*}{1/\log_2(1 + S_N^*) + 1/\log_2(1 + S_N^*)} + \frac{(1 - p_B^*) p_B^*}{1/\log_2(1 + S_L^*) + 1/\log_2(1 + S_N^*)} \right. \\ \left. + \frac{p_B^*(1 - p_B^*)}{1/\log_2(1 + S_N^*) + 1/\log_2(1 + S_L^*)} + \frac{(1 - p_B^*)(1 - p_B^*)}{1/\log_2(1 + S_L^*) + 1/\log_2(1 + S_L^*)} \right). \quad (7)$$

IV. ANALYSIS OF RELAYING MODELS

A. UE-COW Link Analysis

We now derive the mean SE for the relay link between the UE and the COW vehicle. We start by calculating the probability p_C that there is at least a single COW within the interval $[x_0 - x_R, x_0 + x_R]$, where $x_R = \sqrt{R^2 - (3w_S/4 + w_L/2)^2}$ is the maximum separation between the UE and the COW, so that the UE is under the COW coverage, R .

Recalling that only p_R of cars act as COWs, we produce the mean distance between the neighboring COWs as $E[L_R] = [\ell_C(1 - p_T) + E[D] + p_T \ell_T] / [p_R(1 - p_T)]$.

Applying the approach from subsection III-B, we obtain

$$p_C = \left(2x_R - \int_0^{2x_R} F_{L_R}(x) dx \right) / E[L_R]. \quad (15)$$

Since we consider only the COWs deployed on the side lanes, the UE-COW link is not affected by vehicle-body blockage. Further, as the antenna array at the COW is assumed to be deployed on the rooftop of a car, the height of the COW, h_C , is considered to be lower than that of the UE, h_U . Therefore, the blockage zone rectangle (see subsection III-A and Fig. 2) is always crossed by both human paths. Consequently, if there is a COW vehicle within the range of R around the UE, the blockage probability for the UE-COW link, p_B^* , can be directly obtained from (5) as

$$p_B^* = F_L(z_1) + \frac{1 - F_L(z_1)}{E[L]} \left(2z_1 - \int_0^{2z_1} F_L(x) dx \right), \quad (16)$$

where $z_1 = r_p \sqrt{(2w_L + 3w_S)^2 + 16x_S^2} / (2w_L + 3w_S)$, x_S is a random separation distance between the COW and the UE (see Fig. 1): $x_S \in [-x_R, x_R]$.

Finally, the mean SE of the UE-COW link, $C^*(x_S)$ – if there is at least a single COW in range and the UE selects a random COW out of those available – can be computed as

$$C^*(x_S) = p_B^* \log_2(1 + S_N^*) + (1 - p_B^*) \log_2(1 + S_L^*), \quad (17)$$

where the values S_L^* and S_N^* are obtained similarly to (12).

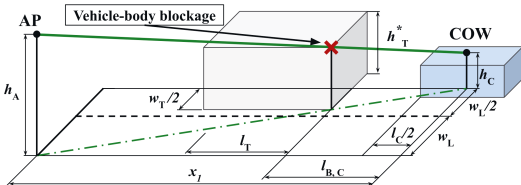


Fig. 4. Minimal height of a bus leading to blockage of COW-AP link.

B. COW-AP Link Analysis

Here, we obtain the mean SE of the link between the AP and the COW separated by x_1 from the AP. This link is only affected by vehicle-body blockage from two sources: (i) buses on the same lane and (ii) buses on the central lane.

For the latter case, the analysis is similar to that in subsection III-B. Particularly, the blockage probability for the buses on the neighboring lane, $p_{B,N}^*$, can be written as

$$p_{B,N}^* = \begin{cases} 0, & h_T < h_T^*, \\ \frac{\ell_T}{\ell_T + E[D_B]}, & h_T \geq h_T^*, \end{cases} \quad (18)$$

where $h_T^* = h_C + (2w_L - w_T)(h_A - h_C)/3w_L$ is the minimal height of a bus on the central lane yielding blockage.

Blockage of the COW-AP link by a bus on the same lane may occur if there is at least a single bus in the blockage zone of length $\ell_{B,C}$, see Fig. 4. For the given bus height and width, the blockage zone length, $\ell_{B,C}$, has to be small enough to result in a blockage situation in both horizontal and vertical planes: $\ell_{B,C} = x_1 \min \{ (h_T - h_C) / (h_A - h_C), w_T/3w_L \}$, where $x_1 = x_0 + x_S$.

The distance from an arbitrary COW vehicle to the nearest bus on the same lane is given by $d_B = N_C \ell_C + \sum_{i=1}^{N_C+1} d_i$, where N_C is a geometrically-distributed RV characterizing the number of cars between the COW and the nearest bus. The blockage probability by a bus on the same lane, $p_{B,S}^*$, is equal to the probability that d_B does not exceed $\ell_{B,C} - \ell_C/2$

$$p_{B,S}^* = Pr\{d_B \leq \ell_{B,C} - \ell_C/2\} = F_{D_B}(\ell_{B,C} - \ell_C/2), \quad (19)$$

where F_{D_B} is the CDF of the RV D_B that can be computed numerically using non-linear RV transformation techniques [16].

Observing that blockages by buses on the same and the neighboring lanes are independent events, joint blockage probability for the COW-AP link, p_B^* , is given in (6) as a combination of (18) and (19). Finally, the mean SE for the COW-AP link where COW is separated from the AP by x_1 is

$$C^*(x_1) = p_B^* \log_2(1 + S_N^*) + (1 - p_B^*) \log_2(1 + S_L^*). \quad (20)$$

The corresponding SNR values for the COW-AP link in LoS and nLoS cases, S_L^* and S_N^* , are calculated similarly to (12).

C. Joint UE-COW-AP Connection Analysis

In this subsection, we derive the mean SE for the relay-aided UE-COW-AP connection for both relaying strategies considered by our study as detailed in subsection II-C.

According to the *Aggressive* strategy, the performance of the joint UE-COW-AP connection is limited exclusively by the mean SE of the COW-AP link. Therefore, the mean SE

of the joint UE-COW-AP connection, $C_1^\dagger(x_0, x_s)$, is equal to $C^*(x_1)$. Its probability mass function (pmf), $f_{C_1^\dagger}(x)$, is thus

$$f_{C_1^\dagger}(x) = \begin{cases} p_C p_B^*, & x = \log_2(1 + S_N^*), \\ p_C(1 - p_B^*), & x = \log_2(1 + S_L^*), \\ 1 - p_C, & x = 0. \end{cases} \quad (21)$$

With the *Conservative* strategy, the radio resources allocated for UE-COW links do not overlap with those available for COW-AP and UE-AP links. Therefore, if the relay link UE-COW exists, the mean SE for the UE-COW-AP connection, $C_2^\dagger(x_0, x_s)$, is obtained as in (7).

We now derive the mean SE when a smart UE selects the best available connection out of UE-AP and opportunistic UE-COW-AP. For this purpose, we first produce the pmf for the SE of the infrastructure UE-AP link (*Baseline* strategy) where the UE is separated from the AP by x_0 , $f_C(x)$. Recalling (13),

$$f_C(x) = \begin{cases} 1 - p_B, & x = \log_2(1 + S_L), \\ p_B, & x = \log_2(1 + S_N). \end{cases} \quad (22)$$

Finally, we calculate the mean SE for the best connection with *Aggressive* and *Conservative* strategies ($C_1(x_0, x_s)$ and $C_2(x_0, x_s)$, respectively) as the maximum of two RVs representing the SE of infrastructure UE-AP and relay UE-COW-AP connections. Accordingly, the mean SE for an arbitrary UE is derived by numerical integration as

$$\begin{aligned} E[C_1] &= \frac{1}{d_1 x_R} \int_0^{d_1/2} \int_{x_0 - x_R}^{x_0 + x_R} (C_1(x_0, x_s) dx_s) dx_0, \\ E[C_2] &= \frac{1}{d_1 x_R} \int_0^{d_1/2} \int_{x_0 - x_R}^{x_0 + x_R} (C_2(x_0, x_s) dx_s) dx_0. \end{aligned} \quad (23)$$

V. NUMERICAL RESULTS

In this section, the obtained results are elaborated numerically. We model a street segment with mmWave APs operating at 28 GHz with 1 GHz of bandwidth and deployed 300 m apart from each other. Following the 3GPP considerations, the heights of APs and UEs are set to 10 m and 1.5 m, respectively [9]. The UE transmit power is 23 dBm and the antenna gains are given as $G_A = 27$ dB and $G_U = 15$ dB [17]. The radius of a human body is set to 0.3 m, while its height is 1.75 m. We assume 5% of large vehicles, i.e., $p_T = 0.05$ [18].

1) *The effect of human density*: We start with Fig. 5 introducing the mean UE SE as a function of the density of human-body blockers on the sidewalks. We first observe that the mean SE decreases with the growing density of human-body blockers. For the Baseline strategy, the mean SE decreases from 12 bits/s/Hz for 0.1 humans/m² to 8 bits/s/Hz for 1.0 humans/m². Then, we notice that the gain of the considered relaying strategies grows for a higher density of blockers. In other words, more “challenging” environments unlock better gains. The SE with Aggressive strategy is notably higher than that in Conservative case, especially at higher densities of blockers: 17 bits/s/Hz vs. 9 bits/s/Hz for 1.0 human/m².

In Fig. 5, we also assess the accuracy of our derivations and the assumptions made by the system model. For this purpose,

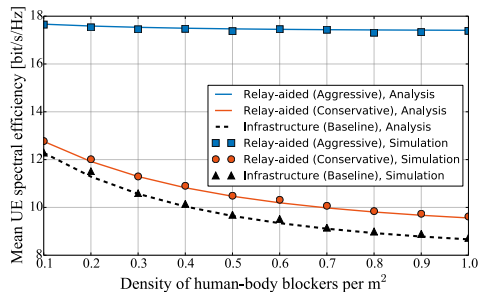


Fig. 5. Mean SE decreases with the growing density of human-body blockers. A close match between the analytical and simulation-based results is observed.

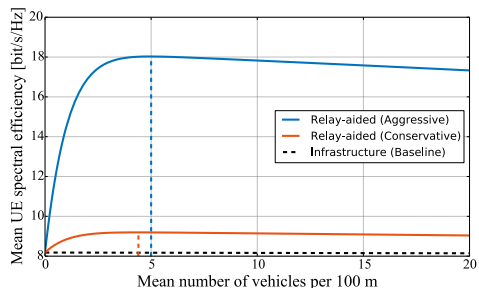


Fig. 6. High density of vehicles has a negative impact on the SE with Baseline strategy and a complex effect on the performance of relay-aided strategies.

we relax three major analytical assumptions in our simulation framework: (i) the pedestrians are not placed on the paths, but rather are uniformly distributed over the sidewalks; (ii) vehicles are not centered on their lanes, but are randomly shifted within a lane, which models realistic city traffic; and (iii) any of the vehicle’s sides can block the mmWave signal, not only the one facing the communicating node. Fig. 5 demonstrates a close match between the analytical and simulation-based results, even when the listed assumptions are relaxed. Similar correspondence between analysis and simulations is observed for other input parameters. Therefore, we rely solely on our analytical results in subsequent figures.

2) *The effect of vehicle density*: We proceed with Fig. 6 that evaluates the mean UE SE as a function of the density of vehicles in the street. In this figure, we first note that only the Baseline scheme is always negatively affected by the growing density of vehicles. In contrast, the dependency is non-monotonic for relay-aided strategies. Particularly, the mean SE decreases at high vehicle densities as a result of vehicle-body blockage. The decrease in the mean SE at lower densities of vehicles is caused by the absence of vehicular relays. We can conclude that the highest gain of relaying is observed in deployments with the medium density of vehicles: over 9 bits/s/Hz with Conservative strategy and 18 bits/s/Hz with Aggressive strategy for 3–5 vehicles per 100 m.

3) *The effect of COW coverage range*: We then analyze the impact of the COW coverage range on the mean UE SE in

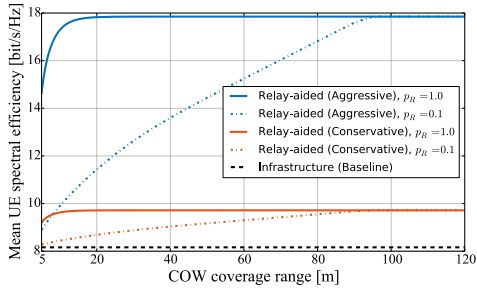


Fig. 7. Mean SE increases with COW coverage range and ceases to grow when the range becomes large enough so that $p_C \rightarrow 1$.

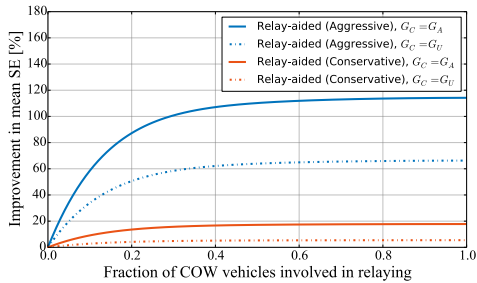


Fig. 8. Mean SE increases by 8%–120% as p_R grows. Even small fractions of COWs lead to notable performance gains with Aggressive strategy.

Fig. 7. Here, we first observe that the mean SE increases with the growing relay coverage range. Second, we notice that the SE ceases to grow when the range becomes large enough to almost guarantee a COW in the UE proximity. The value of COW range after which the mean SE stagnates heavily depends on the fraction of vehicles involved in relaying. Finally, we conclude that the Aggressive strategy notably outperforms the Conservative scheme: the mean SE for the former with only 10% of COW vehicles is higher than the corresponding value for the latter when all 100% of vehicles act as COWs.

4) *The effect of COW fraction:* Finally, we assess the overall increase in UE SE brought by COW relays in Fig. 8. Accordingly, the relative increase in the SE with respect to the Baseline strategy is presented as a function of the fraction of COW vehicles involved in relaying. Based on the obtained results, Conservative relays offer from 8% (0.1 vehicles act as COWs) to 12% (all vehicles act as COWs) increase in the mean UE SE. In the same conditions, Aggressive relays offer from 70% to 120% improvement. The gains with both strategies increase rapidly until 20% of vehicles are involved in relaying, whereas they cease growing after 40% of COW vehicles in the street. Therefore, there is no benefit in engaging more than 40% of vehicles in relaying. In contrast, the use of small fractions of COWs leads to notable performance gains.

VI. CONCLUSIONS

In this paper, we proposed a performance analysis framework for the mmWave vehicular relaying in urban street

layouts. We demonstrated that the performance gains brought by smart mmWave-based relaying are the most significant in vehicular deployments featured by dense human crowds on sidewalks and moderately-dense vehicular traffic. We also showed that even a small density of mmWave vehicular relays can lead to notable performance improvements provided that intelligent UEs can continuously select the best connectivity options out of those offered by static mmWave APs and mmWave vehicular relays.

The developed framework and the presented results can further aid in identifying the setups where the use of mmWave vehicular relaying is especially beneficial, towards the adoption of mmWave-based mobile relays as part of 5G+ networks and their standardization in NR Rel. 17 and beyond.

ACKNOWLEDGEMENT

This work was supported by the Academy of Finland (projects WiFiUS, PRISMA, and RADIANT). R. Heath was funded in part by the National Science Foundation under Grant No. ECCS-1711702 and by Honda R&D Americas.

REFERENCES

- [1] T. Bai and R. W. Heath, "Coverage and rate analysis for millimeter-wave cellular networks," *IEEE Trans. on Wireless Commun.*, vol. 14, no. 2, pp. 1100–1114, Feb 2015.
- [2] M. R. Akdeniz *et al.*, "Millimeter wave channel modeling and cellular capacity evaluation," *IEEE J. on Sel. Areas in Commun.*, vol. 32, no. 6, pp. 1164–1179, June 2014.
- [3] K. Haneda *et al.*, "5G 3GPP-like channel models for outdoor urban microcellular and macrocellular environments," in *Proc. of IEEE VTC-Spring*, May 2016.
- [4] T. Bai and R. W. Heath, "Coverage in dense millimeter wave cellular networks," in *Proc. of Asilomar Conference on Signals, Systems and Computers*, November 2013.
- [5] S. Biswas, S. Vuppala, J. Xue, and T. Ratnarajah, "On the performance of relay aided millimeter wave networks," *IEEE J. of Sel. Topics in Signal Proc.*, vol. 10, no. 3, pp. 576–588, April 2016.
- [6] H. Ding, D. B. da Costa, J. Coon, and Y. Chen, "Relay when blocked: A hop-by-hop mmWave cooperative transmission protocol," *IEEE Communications Letters*, vol. 22, no. 9, pp. 1894–1897, September 2018.
- [7] 3GPP, "Study on integrated access and backhaul (Release 15)," 3GPP TR 38.874 V16.0.0, January 2019.
- [8] 3GPP, "List of work items," <https://www.3gpp.org/DynaReport/WI-List.htm>, July 2019, [Online: Accessed 16-August-2019].
- [9] 3GPP, "Study on channel model for frequencies from 0.5 to 100 GHz (Release 14)," 3GPP TR 38.901 V15.0.0, June 2018.
- [10] M. Gapeyenko *et al.*, "An analytical representation of the 3GPP 3D channel model parameters for mmWave bands," in *Proc. of the 2nd ACM Workshop on Millimeter Wave Networks and Sensing Systems (mmNets'18) in conjunction with ACM MobiCom*, October 2018.
- [11] V. Petrov *et al.*, "Interference and SINR in millimeter wave and terahertz communication systems with blocking and directional antennas," *IEEE Trans. on Wireless Commun.*, vol. 16, no. 3, pp. 791–808, March 2017.
- [12] M. Giordani, M. Mezzavilla, S. Rangan, and M. Zorzi, "An efficient uplink multi-connectivity scheme for 5G millimeter-wave control plane applications," *IEEE Trans. on Wireless Commun.*, vol. 17, no. 10, pp. 6806–6821, October 2018.
- [13] V. Petrov *et al.*, "Dynamic multi-connectivity performance in ultra-dense urban mmWave deployments," *IEEE J. on Sel. Areas in Commun.*, vol. 35, no. 9, pp. 2038–2055, September 2017.
- [14] D. R. Cox, *Renewal theory*. Methuen and Co Ltd., 1970.
- [15] J. F. C. Kingman, *Poisson processes*. Wiley Online Library, 1993.
- [16] S. M. Ross, *Introduction to probability models*. Academic press, 2014.
- [17] Y. Huo, X. Dong, and W. Xu, "5G cellular User Equipment: From theory to practical hardware design," *IEEE Access*, vol. 5, July 2017.
- [18] M. Hallenbeck and B. Smith, "Vehicle volume distributions by classification," Washington State Transportation Center Report, July 1997.

PUBLICATION

V

Flexible and Reliable UAV-Assisted Backhaul Operation in 5G mmWave Cellular Networks

M. Gapeyenko, V. Petrov, D. Moltchanov, S. Andreev, N. Himayat and
Y. Koucheryavy

IEEE Journal on Selected Areas in Communications 36.11 (2018), 2486–2496

Publication reprinted with the permission of the copyright holders

Flexible and Reliable UAV-Assisted Backhaul Operation in 5G mmWave Cellular Networks

Margarita Gapeyenko, Vitaly Petrov, Dmitri Moltchanov,
Sergey Andreev, Nageen Himayat, and Yevgeni Koucheryavy

Abstract—To satisfy the stringent capacity and scalability requirements in the fifth generation (5G) mobile networks, both wireless access and backhaul links are envisioned to exploit millimeter wave (mmWave) spectrum. Here, similar to the design of access links, mmWave backhaul connections must also address many challenges such as multipath propagation and dynamic link blockage, which calls for advanced solutions to improve their reliability. To address these challenges, 3GPP New Radio (NR) technology is considering a *flexible and reconfigurable* backhaul architecture, which includes dynamic link rerouting to alternative paths. In this paper, we investigate the use of aerial relay nodes carried by e.g., *unmanned aerial vehicles* (UAVs) to allow for such dynamic routing, while mitigating the impact of occlusions on the terrestrial links. This novel concept requires an understanding of mmWave backhaul dynamics that accounts for: (i) realistic 3D multipath mmWave propagation; (ii) dynamic blockage of mmWave backhaul links; and (iii) heterogeneous mobility of blockers and UAV-based assisting relays. We contribute the required mathematical framework that captures these phenomena to analyze the mmWave backhaul operation in characteristic urban environments. We also utilize this framework for a new assessment of mmWave backhaul performance by studying its spatial and temporal characteristics. We finally quantify the benefits of utilizing UAV assistance for more reliable mmWave backhaul. The numerical results are confirmed with 3GPP-calibrated simulations, while the framework itself can aid in the design of robust UAV-assisted backhaul infrastructures in future 5G mmWave cellular.

Index Terms—5G New Radio; millimeter wave; multipath 3D channel model; UAV communications; integrated access and backhaul; dynamic human body blockage; moving cells.

I. INTRODUCTION

Over the past years, the work on fifth-generation (5G) networks has achieved impressive results [1], [2]. 3GPP has recently ratified non-standalone 5G New Radio (NR) technology to augment further LTE evolution. Currently, the standardization has completed the standalone 5G NR specifications to allow for independent NR-based deployments [3]. Catering for high-rate and reliable wireless connectivity, the 5G cellular paradigm aims to densify the network with terrestrial base stations [4] by additionally employing moving (e.g., car-mounted) small cells for on-demand capacity boost as well as harnessing more abundant millimeter-wave (mmWave) spectrum for both access and backhaul radio links [5], [6].

Manuscript received April 16, 2018; revised September 15, 2018; accepted September 28, 2018. This work was supported by Intel Corporation, and the Academy of Finland (projects WiFius and PRISMA). The work of M. Gapeyenko was supported by Nokia Foundation. V. Petrov acknowledges the support of HPY Research Foundation funded by Elisa. (*Corresponding author: Margarita Gapeyenko.*)

M. Gapeyenko, V. Petrov, D. Moltchanov, S. Andreev, and Y. Koucheryavy are with Tampere University of Technology, Tampere, Finland (e-mail: {firstname.lastname, evgeni.koucheryavy}@tut.fi).

N. Himayat is with Intel Corporation, Santa Clara, CA, USA (e-mail: nageen.himayat@intel.com).

Despite the notable benefits of the mmWave band, it also poses new challenges due to highly directional mmWave links subject to complex multipath propagation, which is susceptible to link blockage phenomena because of a wide range of obstacles [7]–[9]. There has been a surge in research work on reliability analysis of mmWave access to outline techniques for mitigating the inherent limitations of mmWave-based communication [10]–[14].

As that work matures, provisioning of high-rate backhaul capabilities for 5G has attracted recent attention, as mmWave backhaul links remain vulnerable to similar blockage issues [15]. Aiming to assess and improve reliability of mmWave backhaul operation in 5G NR systems, 3GPP has initiated a new study on integrated access and backhaul, which specifies the respective challenges and requirements. The planned specifications target to construct a flexible and reconfigurable system architecture with dynamic backhaul connections. In this context, the capability to reroute backhaul links in case of their blockage by moving humans and car bodies becomes essential [16]. Extending the 3GPP studies on the matter, the utilization of unmanned aerial vehicles (UAVs) equipped with radio capabilities and acting as mobile relay nodes may be considered to further improve flexibility and reliability of backhaul operation.

The recent acceleration in user traffic fluctuations calls for more flexible and reliable backhaul solutions in 5G mmWave cellular, which may require dynamic rerouting. Therefore, the integration of both terrestrial and aerial network components to achieve this goal is essential. The corresponding performance assessment requires an appropriate evaluation methodology that may capture the dynamics of backhaul links, mmWave radio propagation properties, and blockage phenomena caused by moving objects. Different from mmWave access, the research literature on 5G mmWave backhaul is scarce. In [17], the authors propose an analytical model for coexistence of access and backhaul links, while in [18] the capacity evaluation of cellular networks with in-band wireless backhaul was proposed. In [19], a performance evaluation of mmWave backhaul links is conducted.

To the best of our knowledge, an integrated methodology for flexible mmWave backhaul operation with dynamic links that reroute subject to the channel conditions has not been available as of yet. Addressing that gap, this work offers a new methodology that can assess complex scenarios with multiple terrestrial and aerial base stations. These are equipped with mmWave backhaul capabilities and can reroute their links to maintain uninterrupted connectivity over unreliable blockage-prone channels, while leveraging UAV-based relay assistance as illustrated in Fig. 1.

Our considered scenario captures three important compo-

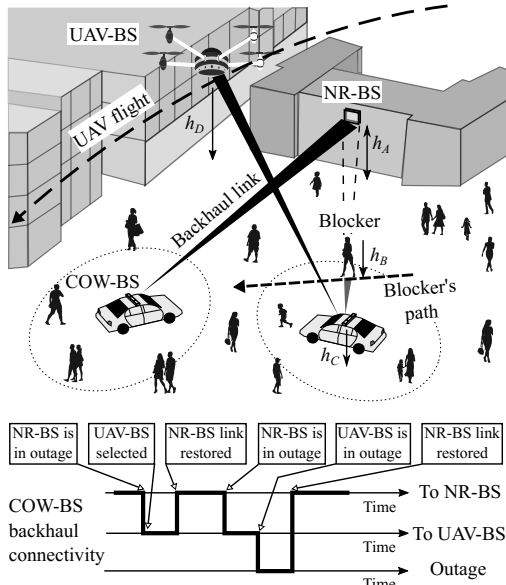


Fig. 1. Scenario of interest with UAV-BS assistance.

nents of future 5G mmWave backhaul solutions: (i) dynamic blockage of mmWave links; (ii) complex multipath propagation in urban environments; and (iii) flexible mobility of assisting UAV relays. A range of simpler scenarios can also be assessed by applying the relevant components of our developed framework with opportunistic UAV mobility model (e.g., those with static deployment of UAV-based relays [20]–[22]). The contributions of this work are therefore as follows.

- A novel mathematical framework that captures the essential features of mmWave backhaul operation under dynamic blockage by moving humans as well as possible link rerouting to UAV-based relay nodes in realistic scenarios under 3D multipath propagation. This analytical framework is further verified with detailed system-level simulations (SLS) that explicitly model the 3GPP 3D multipath propagation channel.
- A performance assessment of flexible mmWave backhaul operation in crowded urban deployments that includes both time-averaged and time-dependent metrics of interest, such as outage probability and spectral efficiency together with outage and non-outage duration distributions. A highlight of our methodology is characterization of uninterrupted connectivity duration, which accounts for tolerable outage time subject to application-specific requirements.
- An understanding of benefits made available with UAV relay assistance to mmWave backhaul reliability in realistic city scenarios. We demonstrate that under certain speed, intensity, and service capacity, the use of UAV-based relays enables significant gains for the system performance. In particular, outage probability and outage duration in the considered scenario become notably reduced, while spectral efficiency increases substantially.

The rest of this text is organized as follows. In Section II,

our system model of the target urban scenario is introduced. The analytical framework for time-averaged performance evaluation of mmWave backhaul operation is outlined in Section III. Further, an analytical model to assess temporal metrics of interest in mmWave backhaul is contributed by Section IV. The corresponding numerical results that explore the spatial and temporal characteristics of flexible mmWave backhaul by leveraging assistance of UAV relay nodes are offered in Section V. Conclusions are drawn in the last section.

II. SYSTEM MODEL

A. Network deployment and COW-BSs

We consider a circular area with the radius of R , where several “Cell on Wheels” base stations (COW-BSs) are distributed uniformly according to a Poisson Point Process (PPP) with the density of λ_C . These COW-BSs provide connectivity to the human users in their vicinity and are equipped with mmWave backhaul links to the terrestrial New Radio base stations (NR-BSs) as well as aerial UAV-carried base stations (UAV-BSs) as illustrated in Fig. 2. In the scenarios where over-provisioning leads to increased operator expenses (e.g., temporary and unexpected events), on-demand network densification with COW-BSs might become a viable option. The height of a COW-BS is h_C . A terrestrial NR-BS is located at the circumference of the circle area at the height of h_A . Since the height of a consumer vehicle is generally lower than that of a pedestrian, the latter may act as a potential blocker to the mmWave signal [23]. We assume that walking pedestrians form a PPP with the density of λ_B and the height of h_B , where $h_A > h_B > h_C$.

The human blockers in our scenario are *dynamic* and their travel patterns are assumed to follow the Random Direction Mobility (RDM) model. The angle of movement in this formulation is chosen uniformly within $[0, 2\pi)$, while the time of travel until the subsequent turn is distributed exponentially. The UAV-BSs may fly through the center of the circle by entering and leaving it at random points that are distributed uniformly across its circumference [24]. This work considers

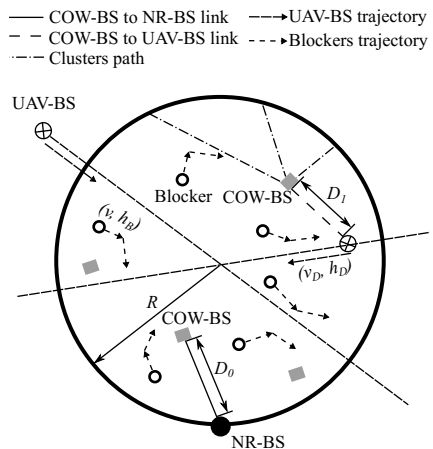


Fig. 2. Geometrical 2D illustration of target setup.

mobility of the UAV-BS as it becomes a distinguishing feature for this new type of BSs. In [25], the authors demonstrate the benefits of dynamic over static UAV deployments. Therefore, mobility modeling is important to assess system-level performance in the scenarios where several types of BSs may coexist. The speed of the UAV-BSs is v_D and their altitude is h_D . The process of entering the circle by the UAV-BSs is assumed to be Poisson in time with the intensity of λ_D . The remaining important notation is summarized in Table I.

B. 3D channel model and dynamic blockage of backhaul links

In order to model the mmWave backhaul links, we employ the current 3GPP 3D multipath channel model [11] by taking into account all of the key features of mmWave communication. The model assumes that there are multiple alternative paths (named *clusters*) between the Tx and the Rx (see Fig. 3), each featured by its own delay, pathloss, and zenith of arrival/departure angles. Each of these paths can be blocked or non-blocked by the moving human blockers using the analytical model from [8].

The COW-BSs utilize beamsteering mechanisms to always use the *best* path, which is currently non-blocked and has the strongest signal. Beamsteering employed at all the communicating nodes also minimizes the level of interference between the backhaul links, thus making the considered mmWave regime noise-limited [26]. Signal blockage by buildings is not modeled, as none occlude the backhaul links between the COW-BSs and the NR-BSs/UAV-BSs in the target scenario.

While the employed 3GPP model is sufficiently detailed and accurate [27], the complexity of the used algorithms [11] challenges its analytical tractability. Therefore, in our mathematical study, we utilize a statistical approximation of the key modeling parameters [28], such as power of every cluster transmitted by the NR-BS and the UAV-BS, $P_{A,i}$ and $P_{D,i}$, and zenith angle of arrival (ZOA) for every cluster, $\theta_{A,i}$ and $\theta_{D,i}$, where $i = 1, 2, \dots, N$ is the cluster number.

C. mmWave backhaul connectivity model

The radio channel conditions of the backhaul links are dynamic in nature due to temporal variations of the propagation environment. These are captured by the utilized propagation model [28], while the mobility of human blockers surrounding the COW-BSs is modeled explicitly in our work. The NR-BS is assumed as the primary option for the backhaul links of COW-BSs (see Fig. 1). When COW-BS is currently in outage

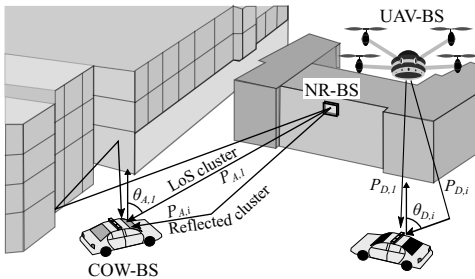


Fig. 3. 3GPP-driven 3D multipath channel model.

TABLE I
SUMMARY OF NOTATION AND PARAMETERS

Notation	Description
<i>Deployment</i>	
h_A, h_C, h_D	Heights of NR-BS, COW-BS, UAV-BS
λ_C, λ_B	Density of COW-BSs and blockers per unit area
r_B, v, h_B	Radius, speed, and height of a blocker
R	Radius of the service area
λ_D	Temporal intensity of UAV-BSs entering the service area
T_D, v_D	Time and speed of UAV-BSs traversing the service area
K_D	UAV-BS service capacity
<i>Technology</i>	
N	Number of 3D multipath propagation clusters
$\theta_{A,i}$ and $\theta_{D,i}$	ZOA of i -th cluster from NR-BS and UAV-BS
$f_{\theta_{A,i}}$ and $f_{\theta_{D,i}}$	Pdf of ZOA of i -th cluster from NR-BS and UAV-BS
C and $E[C]$	Spectral efficiency and its mean value
p_O	Outage probability
Δ_O	Tolerable outage duration
T_U and $E[T_U]$	Uninterrupted connectivity time and its mean value
<i>Mathematical framework</i>	
$P_{D,av}$	Probability of UAV-BS availability
P_A and P_D	Received power at NR-BS to COW-BS and UAV-BS to COW-BS links
f_{P_A} and f_{P_D}	Pdf of received power at NR-BS to COW-BS and UAV-BS to COW-BS links
$f_{P_{A,i}}$ and $f_{P_{D,i}}$	Pdf of power of i -th cluster arriving from NR-BS and UAV-BS
u_n	Pmf of number of UAV-BSs available for COW-BS
$p_{A,i}$ and $p_{D,i}$	Blockage probability of i -th cluster arriving from NR-BS and UAV-BS
$\lambda_{B,T}$	Temporal intensity of blockers crossing the blockage zone
T_B and L_B	Time and distance walked inside the blockage zone by a single blocker
f_η, f_ω	Pdf of blocked and unblocked intervals
f_O and f_G	Pdf of outage and non-outage duration

with respect to NR-BS (i.e., the signal received from NR-BS is too weak), COW-BS may temporarily reroute its backhaul traffic to UAV-BS traversing the area. Once the radio link to NR-BS recovers, COW-BS reconnects to the terrestrial NR-BS and reroutes its backhaul traffic back to it. Hence, the UAV-BSs are employed in unfavorable conditions to improve the continuity of backhaul links.

We measure the capacity of UAV-BS in terms of the maximum number of simultaneously supported backhaul links, which we denote as K_D . This consideration reflects the potential limitations of the mmWave radio equipment carried by the UAV-BS as well as the specifics of the employed network architecture and connectivity protocols. In its turn, the connection between the UAV-BS and the core network is inherently characterized by unobstructed line-of-sight propagation without obstacles [29]. Therefore, this link is modeled as always reliable.

D. Illustrative metrics of interest

To assess the performance quality of the mmWave backhaul links in the described scenario, we concentrate on two types of metrics, namely, time-averaged and time-dependent. In the former case, we address (i) outage probability, p_O , and (ii) spectral efficiency, C . In the latter, we assume that the system may tolerate a certain fixed outage duration Δ_O and thus derive (iii) the mean uninterrupted connectivity time, $E[T_U]$. As intermediate parameters, we also obtain (iv) the outage and non-outage duration distributions, f_O and f_G , respectively.

III. TIME AVERAGED ANALYSIS

In this section, we address the time-averaged system metrics, including outage probability and spectral efficiency.

A. Outage Probability

The outage probability p_O for a randomly chosen COW-BS in the area of interest is obtained as follows. Observe that the COW-BS is always associated with the NR-BS when the latter is in non-outage conditions. Otherwise, the COW-BS is connected to a randomly chosen UAV-BS that is available, provided that there is at least one UAV-BS in non-outage conditions having fewer than K_D COW-BSs connected to it. Hence, the outage probability is produced as

$$p_O = p_{A,O}(u_0 + (1 - u_0)(u_{0,n} + (1 - u_{0,n})p_{D,nav})), \quad (1)$$

where u_0 is the probability of having no UAV-BS traversing the area at the moment, $u_{0,n}$ is the probability of having no UAV-BS in non-outage conditions, $p_{A,O}$ and $p_{D,nav}$ are the outage probability on the COW-BS to NR-BS link and the probability that the UAV-BS is currently unavailable, respectively. In what follows, we derive these unknown terms.

1) *Outage probability on COW-BS to NR-BS and COW-BS to UAV-BS links:* Consider a randomly chosen COW-BS. Let $p_{A,i}$ be the probability that i -th cluster between the NR-BS and the COW-BS is blocked and first consider blockage of the LoS path, $p_{A,1}$. Fixing the distance x between NR-BS and COW-BS, we observe that there is always a so-called *blockage zone* as shown in Fig. 4. At any given instant of time t , the number of blockers moving according to the RDM model within the service zone follows a Poisson distribution [30]. Hence, the probability that the LoS path is blocked is given by

$$p_{A,1}(x) = 1 - e^{(-2\lambda_B r_B [x \frac{h_B - h_C}{h_A - h_C} + r_B])}. \quad (2)$$

Let D_0 be a random variable (RV) denoting the 2D distance between the NR-BS and a randomly chosen COW-BS, and let $f_{D_0}(x)$ be its probability density function (pdf). Noticing that the COW-BSs are uniformly distributed within a service area circle, the sought distance is [31]

$$f_{D_0}(x) = \frac{2x}{\pi R^2} \cos^{-1} \left(\frac{x}{2R} \right), \quad 0 < x < 2R. \quad (3)$$

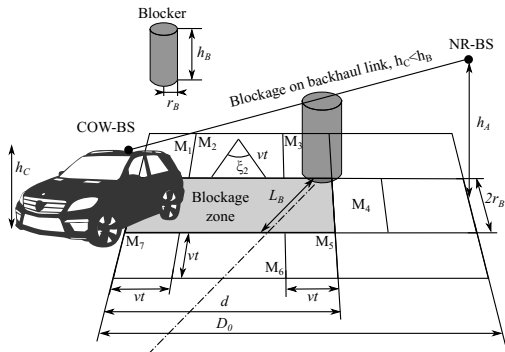


Fig. 4. Illustration of dynamic blockage process.

The LoS path blockage probability is then

$$p_{A,1} = \int_0^{2R} f_{D_0}(x) p_{A,1}(x) dx. \quad (4)$$

Consider now the blockage probability for i -th cluster, $i = 2, 3, \dots, N$. As opposed to the LoS path, the 3GPP model does not explicitly specify where the reflected cluster comes from. Instead, it provides the ZOA, $\theta_{A,i}$ and $\theta_{D,i}$, $i = 2, 3, \dots, N$. In [28], it was shown that the ZOA for all clusters follows a Laplace distribution and we denote it as the pdf $f_{\theta_{A,i}}(y; x)$.

The blockage probability $p_{A,i}(x)$ of every cluster is then

$$p_{A,i} = \int_{-\pi}^{\pi} \int_0^{2R} f_{\theta_{A,i}}(y; x) p_{A,i}(y) dx dy, \quad (5)$$

where $p_{A,i}(y)$ is the blockage probability as a function of the ZOA, derived as

$$p_{A,i}(y) = 1 - e^{[-2\lambda_B r_B (\tan y (h_B - h_C) + r_B)]}. \quad (6)$$

Substituting (6) and pdf of ZOA from [28], we obtain

$$p_{A,i} = \int_{-\pi}^{\pi} \int_0^{2R} \frac{1 - e^{-2\lambda_B r_B (\tan y (h_B - h_C) + r_B)}}{2b_z e^{\frac{y - a_z(x)}{b_z}}} dx dy, \quad (7)$$

where $a_z(x) = \frac{\pi}{2} - \arctan \left(\frac{h_A - h_C}{x} \right)$ and b_z , $z = 2, 3, \dots, N$, are the parameters estimated from the statistical data (see [28] for details) and b_z is given as

$$b_1 = 0, b_2 = 0.3146, b_3 = 0.3529, b_4 = 0.4056, b_5 = 0.4897. \quad (8)$$

After characterizing the blockage probabilities of individual clusters on the COW-BS to NR-BS link, we derive an expression for the received power. As shown in [28], the fraction of power of i -th cluster between the NR-BS and the COW-BS separated by the distance of x follows a Log-normal distribution with the pdf $f_{P_{A,i}}(y; x)$.

Once the fraction of power distributions is obtained, the received power from every cluster is calculated as

$$P_{A,z} = P_{s,z} 10^{(P_T - 30 - L)/10}, \quad z = 1, 2, \dots, \quad (9)$$

where P_T is the transmit power in dBm and L is the path loss in dB . Then, $P_{A,z}$ is given as

$$P_{A,z} = P_{s,z} 10^{(A_p - 21.0 \log_{10}(D_{3,0}))/10}, \quad (10)$$

where $A_p = P_T - 30 - 32.4 - 20 \log_{10} f_c$.

As one may observe, $P_{A,z}$ is a function of two RVs, $P_{s,z}$ and $D_{3,0}$, and $f_{D_{3,0}}(x)$ is the pdf of the 3D distance between the NR-BS and the COW-BS in the form

$$f_{D_{3,0}} = \frac{2x}{\pi R^2} \cos^{-1} \left(\frac{\sqrt{x^2 - (h_A - h_C)^2}}{2R} \right), \quad (11)$$

where $x \in (h_A - h_C, \sqrt{4R^2 + (h_A - h_C)^2})$.

Since $D_{3,0}$ and $P_{s,z}$ are independent, their joint pdf is

$$f_{P_{s,z}, D_{3,0}}(x_1, x_2) = \frac{1}{x_1 d_z \sqrt{2\pi}} e^{\left(-\frac{(\ln x_1 - \mu_z)^2}{2d_z^2} \right)} \times \frac{2x_2}{\pi R^2} \cos^{-1} \left(\frac{\sqrt{x_2^2 - (h_A - h_C)^2}}{2R} \right), \quad (12)$$

where c_z and d_z , $z = 2, 3, \dots$, are the parameters derived from the statistical data (see [28] for details) and given as

$$c_1 = -2.88, c_2 = -3.55, c_3 = -4.1, c_4 = -4.98, c_5 = -6.2, \\ d_1 = 1.2, d_2 = 1.1, d_3 = 1.3, d_4 = 1.8, d_5 = 2.51. \quad (13)$$

Finally, the pdf of $P_{A,z}$ is

$$f_{P_{A,z}}(y) = \int_{x_{2,\min}}^{x_{2,\max}} f_{P_{s,z},D_{3,0}} \left(\frac{y}{10^{(A_p - 21.0 \log_{10}(x_2))/10}}, x_2 \right) \times \\ \frac{1}{10^{(A_p - 21.0 \log_{10}(x_2))/10}} dx_2, \quad (14)$$

where $x_{2,\min} = h_A - h_C$ and $x_{2,\max} = \sqrt{4R^2 + (h_A - h_C)^2}$.

Assuming mutual independence in the cluster blockage, the pdf of the received power is produced as

$$f_{P_A}(y) = \sum_{k=1}^N \left[(1 - p_{A,k}) \prod_{j=1}^{k-1} p_{A,j} \right] f_{P_{A,k}}(y), \quad (15)$$

where the weights are the probabilities of choosing cluster i .

Finally, the outage probability with the NR-BS is

$$p_{A,O} = Pr\{P_A(y) \leq N_0 T_S\} = \int_0^{N_0 T_S} f_{P_A}(y) dy, \quad (16)$$

where N_0 is the Johnson-Nyquist noise at the receiver and T_S is the SNR threshold. Note that due to the complex structure of the conditional received power $f_{P_A}(y)$, the outage probability $p_{A,O}$ can only be produced with numerical integration.

The LoS path and i -th cluster blockage probability on a link between the UAV-BS and the COW-BS are obtained similarly except for the 2D distance between UAV-BS and COW-BS, D_1 , with the pdf given as

$$f_{D_1}(x) = \frac{4x}{\pi R^2} \left[\cos^{-1} \left(\frac{x}{2R} \right) - \frac{x}{2R} \sqrt{1 - \frac{x^2}{4R^2}} \right], \quad (17)$$

where $x \in (0, 2R)$. Using this result, the corresponding 3D distance between the UAV-BS and the COW-BS constitutes

$$f_{D_{3,1}} = \frac{4x}{\pi R^2} \left[\cos^{-1} \left(\frac{\sqrt{x^2 - (h_D - h_C)^2}}{2R} \right) - \right. \\ \left. - \frac{\sqrt{x^2 - (h_D - h_C)^2}}{2R} \sqrt{1 - \frac{x^2 - (h_D - h_C)^2}{4R^2}} \right], \quad (18)$$

where $x \in (h_D - h_C < x < \sqrt{4R^2 + (h_D - h_C)^2})$.

2) *Availability probability of UAV-BS*: To complete the derivation of p_O , we find the probability that at least one UAV-BS in non-outage conditions is available for service, $p_{D,av}$.

The time spent by each UAV-BS within the service area is constant and equals $T_D = 2Rv_D$, where v_D is the speed of UAV-BS. Hence, the number of UAV-BSs that are available in the service zone is captured by the $M/G/\infty$ queuing system with a constant service time. It is known that the number of customers in $M/G/\infty$ queue coincides with the number of customers in $M/M/\infty$ queue and follows a Poisson distribution with the parameter $\lambda_D T_D$ [32]¹.

¹To ensure a certain number of UAV-BSs above the area one may directly use a mean number of UAV-BSs.

Note that the availability of UAV-BSs is not sufficient for the COW-BS to be able to associate with them. In addition, there should be at least one UAV-BS in non-outage conditions. The intensity of such UAV-BSs is $\lambda_D T_D (1 - p_{D,O})$, where $p_{D,O}$ is the probability that a randomly selected UAV-BS resides in the outage conditions. Therefore, the number of UAV-BSs that are available for the COW-BS U follows a Poisson distribution with the probability mass function (pmf) of

$$u_n = \frac{[\lambda_D T_D (1 - p_{D,O})]^n}{n!} e^{-\lambda_D T_D (1 - p_{D,O})}, \quad (19)$$

where $n = 0, 1, \dots$.

Let W denote the number of COW-BSs in the outage conditions. The number of COW-BSs in the service area follows a Poisson distribution with the density of λ_C . Hence, the number of COW-BSs in the outage conditions also follows a Poisson distribution with the parameter of $\lambda_C p_{A,O} \pi R^2$. The probability that the UAV-BS remains available for service is

$$p_{D,av} = Pr\{K_D U - W > 0\} = \sum_{i=1}^{\infty} Pr\{Z = i\}, \quad (20)$$

where $Z = K_D U - W$.

Observe that $K_D U$ is a scaled Poisson RV in (21), which implies that $p_{D,av}$ can be evaluated numerically for any value of K_D . The pmf of Z is then established as

$$Pr\{Z = z\} = \sum_{x=0}^{\infty} \frac{|K_D x - 1| [\lambda_C p_{A,O} \pi R^2]^{(K_D x - z)}}{K_D (K_D x - z)!} \times \\ e^{(-\lambda_C p_{A,O} \pi R^2 - \lambda_D T_D (1 - p_{D,O}))} \frac{[\lambda_D T_D (1 - p_{D,O})]^{x/K_D}}{(x/K_D)!}. \quad (21)$$

B. Spectral efficiency

Consider now spectral efficiency of an arbitrarily chosen COW-BS. Observe that this COW-BS spends a fraction of time, p_A , connected to the NR-BS and a fraction of time, p_D , connected to the UAV-BS. The rest of the time, p_O , this COW-BS resides in outage. Hence, the spectral efficiency is

$$C = p_A \log_2 \left[1 + \frac{P_A}{N_0} \right] + p_D \log_2 \left[1 + \frac{P_D}{N_0} \right], \quad (22)$$

where P_A and P_D are the received powers whenever associated with NR-BS and UAV-BS.

Observe that $p_{A,O} = 1 - p_A$ is the outage probability when only NR-BS is available. Recalling that UAV-BS are only employed when the NR-BS to COW-BS link experiences outage conditions, the fraction of time that the COW-BS is associated with the UAV-BS is $p_D = p_{A,O} p_{D,av}$. Therefore, the mean spectral efficiency is provided by

$$E[C] = (1 - p_{A,O}) \int_0^{\infty} f_{P_A}(x) \log_2 \left[1 + \frac{P_A}{N_0} \right] dx + \\ + p_{A,O} p_{D,av} \int_0^{\infty} f_{P_D}(x) \log_2 \left[1 + \frac{P_D}{N_0} \right] dx, \quad (23)$$

which can be evaluated numerically.

In addition to the mean value, the form of (22) enables us to determine the distribution of the spectral efficiency. Observe that the spectral efficiencies associated with the UAV-BS to

COW-BS and the NR-BS to COW-BS links are independent RVs. The resulting pdf takes the following form

$$f_C(x) = \begin{cases} \int_0^\infty \frac{(2^{f_{PA}(y)} - 1)(2^{f_{PA}(x-y)} - 1)}{(N_0^4 2^x \log^2 2)^{-1}} dy, & x > 0, \\ p_O, & x = 0, \end{cases} \quad (24)$$

where the convolution integral can be evaluated numerically.

IV. TIME DEPENDENT ANALYSIS

In this section, we continue by quantifying uninterrupted connectivity performance, including the outage and non-outage duration distributions as well as the uninterrupted connectivity duration.

A. Dynamics of cluster blockage process

To capture the temporal dynamics of the blockage process for a single cluster, we need to track the blockers that are crossing the blockage zone, see Fig. 4. We begin by considering the dynamics of the LoS blockage process and concentrate on the temporal properties of the process when the blockers are entering the blockage zone and occluding the LoS.

We specify the area around the blockage zone as shown in Fig. 4, where the moving blockers may cross the blockage zone by occluding the LoS between the COW-BS and the NR-BS. To specify these conditions, the area around the blockage zone is further divided into i , $i = 1, 2, \dots, 7$, zones. The intensity of blockers crossing the blockage zone of the COW-BS located at the distance of x from the NR-BS is approximated as

$$\lambda_{B,T}(z) = \sum_{i=1}^7 \iint_{M_i} \frac{g_i(x, y) Pr\{A_B\} Pr\{T_B > t\}}{(\lambda_B M_i)^{-1}} dx dy, \quad (25)$$

where the event A_B is when a blocker moves towards the blockage zone (see Fig. 4), M_i is the area of zone i , $g_i(x, y)$ is the pdf of the blocker locations in zone i . Here, $g_i(x, y) = 1/M_i$ as the blockers move according to the RDM model and at every instant of time their coordinates are distributed uniformly within the area [30], while $Pr\{T_B > t\} = e^{-1/E[\tau]}$ is the probability that such movement is longer than t seconds.

Observe that the probability for a blocker to move towards CDEF is $Pr\{A_B\} = \xi_i(x, y)/2\pi$, where $\xi_i(x, y)$ is a range of movement angles within zone i that lead to crossing the blockage zone. We thus simplify (25) as

$$\lambda_{B,T}(z) = \frac{\lambda_B e^{-1/E[\tau]}}{2\pi} \sum_{i=1}^7 \iint_{M_i} \xi_i(x, y) dx dy, \quad (26)$$

where $\xi_i(x, y)$ are calculated as

$$\begin{aligned} \xi_1(x, y) &= \xi_3(x, y) = \xi_5(x, y) = \xi_7(x, y) = \cos^{-1}\left(\frac{x}{vt}\right) + \tan^{-1}\left(\frac{y}{x}\right), \\ \xi_2(x, y) &= \xi_6(x, y) = 2 \cos^{-1}(x/vt), \\ \xi_4(x, y) &= 2 \tan^{-1}(x/y), \end{aligned} \quad (27)$$

and $M_1 = M_3 = M_5 = M_7$ with x -coordinate within the range of $(0, vt)$ and y -coordinate within the range of $(0, vt/2)$, $M_2 = M_6$ with x -coordinate within the range of $(0, vt)$ and y -coordinate within the range of $(0, d - 2vt)$, M_4 with x -coordinate within the range of $(0, 2r_B)$ and y -coordinate within the range of $(0, vt)$, where $2r_B < vt$.

It has been shown in [33] that the process of meetings between a stationary node and a node moving inside a bounded area according to the RDM is approximately Poisson. We build on this result to approximate the nature of the process of blockers meeting the blockage zone. Due to the properties of the RDM model, the entry point is distributed uniformly over the three sides of the blockage zone [30].

Let η and ω be the RVs denoting the blocked and non-blocked periods, respectively. Since blockers enter the zone in question according to a Poisson process with the intensity of $\lambda_{B,T}(x)$, the time spent in the unblocked part, ω , follows an exponential distribution with the parameter of $\lambda_{B,T}(x)$, $F_\omega(t; x) = 1 - e^{-\lambda_{B,T}(x)t}$, as demonstrated in [8]. The pdf of η , $f_\eta(t; x)$, is the same as the distribution of the busy period in the $M/GI/\infty$ queuing system [34] given by (28), where F_{T_B} is the CDF of time that one blocker spends in the blockage zone, which is provided in [8].

The pdfs of the blocked and non-blocked intervals, $f_\eta(t; x)$ and $f_\omega(t; x)$, are conditioned on the distance between COW-BS and NR-BS. Deconditioning with (3), we obtain the pdfs of the blocked and non-blocked intervals when associated with the NR-BS as

$$\begin{aligned} f_\eta(t) &= \int_0^{2R} f_\eta(t; x) f_{D_0}(x; R) dx, \\ f_\omega(t) &= \int_0^{2R} f_\omega(t; x) f_{D_0}(x; R) dx, \end{aligned} \quad (29)$$

which can be calculated numerically.

To capture the dynamics of the cluster blockage process, we can represent it by using a continuous-time Markov chain (CTMC) process with two states, which is defined by the infinitesimal generator in the following form

$$\Lambda_{1,A} = \begin{bmatrix} -\alpha_{1,A} & \alpha_{1,A} \\ \beta_{1,A} & -\beta_{1,A} \end{bmatrix}, \quad (30)$$

where the subscript $(1, A)$ shows that the model is built for the LoS cluster of the NR-BS to COW-BS link, while $\alpha_{1,A} = 1/E[\eta]$ and $\beta_{1,A} = 1/E[\omega]$ are the means of blocked and non-blocked intervals of the LoS cluster given in (29).

The process of blockage for other clusters on the NR-BS to COW-BS link is analyzed similarly. The key difference is that the blockage zone is specified by the ZOA instead of the heights of NR-BS and COW-BS as well as the distance between them. Let us denote the generators of all clusters associated with the NR-BS to COW-BS link by $\Lambda_{i,A}$, $i = 1, 2, \dots, N$. Assuming independence between the cluster blockage processes, the associated CTMC model, $\{S_A(t), t > 0\}$, $S_A(t) \in \{1, 2, \dots, 2^N\}$, is a superposition of the individual blockage processes. The infinitesimal generator of $\{S_A(t), t > 0\}$ is then given by the Kronecker product of $\Lambda_{i,A}$, $i = 1, 2, \dots, N$.

The blockage dynamics of the UAV-BS to COW-BS link is represented similarly by leading to the Markov process approximation $\{S_D(t), t > 0\}$, $S_D(t) \in \{1, 2, \dots, 2^N\}$. Finally, the aggregate blockage model of both links is represented by a superposition of the blockage processes that characterize the NR-BS to COW-BS and the UAV-BS to COW-BS links. The resulting infinitesimal generator is $\Lambda = \Lambda_A \otimes \Lambda_D$.

$$F_\eta(x) = 1 - \left[[1 - F_{T_B}(x)] \left[1 - \int_0^x (1 - F_\eta(x-z)) \exp(-\lambda_{B,T} F_{T_B}(z)) \lambda_{B,T} dz \right] + \int_0^x (1 - F_\eta(x-z)) |de^{-\lambda_{B,T} F_{T_B}(z)}| \right]. \quad (28)$$

B. Performance measures of interest

1) *Outage and non-outage duration distribution:* Having the CTMC representation of the outage process, we can now calculate time-dependent performance metrics of interest, including the distributions of consecutive intervals spent in outage and non-outage conditions, the corresponding distributions of residual time, as well as the distribution and the mean duration of uninterrupted connectivity.

Let RVs G and O denote the non-outage and outage time durations, respectively. The distribution of time spent in outage, $f_O(x)$, $x > 0$, is directly given by the sojourn time in the state where all clusters are blocked. For our model, it is always state 1. The distribution of time spent in the non-outage state can be found by modifying the CTMC to have an absorption state in outage. Then, the sought distribution is the first-passage time (FPT) to the outage state that can be established by using [35]. Particularly, let $f_G(t)$ be the pdf of the FPT from the set of non-blockage states, $\{2, 3, \dots, 2 \times 2^N\}$, to the blockage state.

It is easy to see that the sought distribution is of the phase-type nature [36] with the representation $(\vec{\alpha}, S)$, where $\vec{\alpha}$ is the initial state distribution defined over $\{2, 3, \dots, 2 \times 2^N\}$ and S is obtained from the infinitesimal generator Λ by excluding the first row and column. The pdf is then given by [37] as

$$f_G(t) = \vec{\alpha} e^{St} \vec{s}_0, \quad t > 0, \quad (31)$$

where $\vec{s}_0 = -S\vec{1}$, $\vec{1}$ is the vector of ones with size $2^N - 1$, while e^{St} is the matrix exponential defined as $e^{St} = \sum_{k=0}^{\infty} \frac{1}{k!} (St)^k$.

The initial state distribution, $\vec{\alpha}$, is determined by the normalized rates out of the outage state e.g.,

$$\alpha_i = \begin{cases} 0, & i = 1, \\ \pi_i / \sum_{j=2}^{2^N} \pi_j, & i = 2, 3, \dots, 2^N. \end{cases} \quad (32)$$

2) *Uninterrupted connectivity time:* Consider now an application that may tolerate at most Δ_O in the outage conditions, which implies that all of the outages whose durations are less than Δ_O do not cause connectivity interruptions. The probability that a session is interrupted is

$$p_I = \int_0^{\Delta_O} x f_O(x) dx. \quad (33)$$

As one may observe, the duration of uninterrupted connectivity is produced by a geometrical distribution with the parameter p_I , which is scaled with the aggregate durations of non-outage and outage intervals conditioned on the event that it is smaller than Δ_O . Hence, we have

$$E[T_U] = \frac{1}{p_I} (E[G] + E[O|O \leq \Delta_O]), \quad (34)$$

where the means are readily given by

$$E[G] = \int_0^{\infty} x f_G(x) dx, \quad E[O|O \leq \Delta_O] = \int_0^{\Delta_O} x \frac{f_O(x)}{1 - p_I} dx. \quad (35)$$

V. NUMERICAL RESULTS

In this section, the obtained analytical findings are illustrated, explained, and compared with the results produced with our SLS framework. Below is an illustrative example to demonstrate the capabilities of our proposed framework, which is applicable for a range of comprehensive and realistic deployment models currently under investigation.

We address a typical crowded urban deployment, where a pedestrian plaza (e.g., St. Peter's Square, Vatican City) is modeled. The area of interest is assumed to be of circular shape with the radius of 50 m. The terrestrial NR-BS is located at a side of the square on the wall of one of the buildings at the height of 10 m. Pedestrians move around the square by following their travel patterns as described in Section II with the fixed speed of 3 km/h. UAV-BSs are assumed to traverse the pedestrian plaza at the height of 20 m with the fixed speed that varies from 5 km/h to 40 km/h. The remaining modeling parameters are summarized in Table II. Our simulation parameters partially follow the guidelines in [24] with respect to the height and the speed of the UAV-BS, as well as refer to [11] for modeling the radio part.

To validate the assumptions of our developed analytical framework, we utilize an in-house SLS tool that incorporates all of the relevant procedures considered by our study. The mmWave-specific physical layer was designed by following the corresponding 3GPP guidelines; particularly, the 3GPP's 3D multipath channel model outlined in [11] was employed. This simulation tool captures the following key procedures: session arrival process, UAV-BS arrival and departure processes, UAV-BS and pedestrian mobility, and dynamic backhaul link rerouting between the UAV-BS and the NR-BS enhanced with multi-connectivity operation [38].

The tool operates in a time-driven manner with the step of 0.01 s. To match the capabilities of our analytical framework, idealistic and reliable signaling at all the connections has been assumed: if the current connection is interrupted, the COW-BS immediately attempts to reconnect via a UAV-BS and does not spend any additional resources for this migration. For the sake of better accuracy in the output results, all of the

TABLE II
DEPLOYMENT AND TECHNOLOGY PARAMETERS

Parameter	Value
<i>Deployment</i>	
Area radius, R	50 m
Height of NR-BS, h_A	10 m
Height of UAV-BS, h_D	20 m
Height of COW-BS, h_C	1.5 m
Height of blocker, h_B	1.7 m
Radius of blocker, r_B	0.2 m
Speed of blocker, v	1 m/s
<i>Technology</i>	
NR-BS transmit power	35 dBm
UAV-BS transmit power	23 dBm
Target SNR for non-outage conditions	3 dB
COW-BS antenna gain	5 dB
UAV-BS antenna gain	7 dB
NR-BS antenna gain	10 dB
Carrier frequency	28 GHz

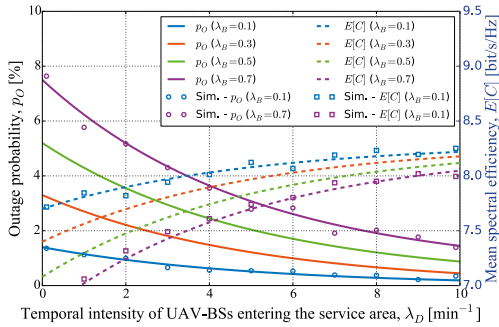


Fig. 5. Outage probability and mean spectral efficiency. Effect of crowd density and intensity of UAV-BS flights.

collected intermediate data are averaged over 100 replications, each starting with a re-deployment of the layout. Each of such replications corresponds to 10 min of real-time operation. Hence, approximately 17 hours of real-time system operation have been modeled.

1) *Effect of UAV-BS flight intensity*: The UAV-BSs are assumed to move at a moderate speed of 10 km/h. The point 0 on the OX axis represents the baseline scenario with no UAV-BS assistance. Analyzing Fig. 5, we notice that both the outage probability and the spectral efficiency are improved with the growth in the intensity of UAV-BS traversals. Specifically, for $\lambda_B = 0.7$ the outage probability decreases from 7.5% for the baseline scenario to 1.5% for 10 UAV-BSs per minute. Meanwhile, the corresponding increase in the spectral efficiency is from 6.5 bit/s/Hz to 8 bit/s/Hz, which is around 25%.

Going further, we observe that the benefits of UAV-BS assistance for performance are more visible in challenging conditions (high density of humans, such as 0.7) rather than at low blocker densities (such as 0.1 or 0.3). Moreover, Fig. 5 clearly indicates that two UAV-BSs traversing the area of interest per minute with $\lambda_B = 0.7$ reduce the outage probability down to 5.3%, which is close to 5.2% observed with $\lambda_B = 0.5$ in the baseline scenario (no UAV-BSs, $\lambda_D = 0$).

We finally note that the results of our mathematical analysis match well with those obtained via the simulation tool, which confirms the accuracy of the analytical findings. A slight difference between them is due to several simplifying assumptions introduced by the mathematical framework for

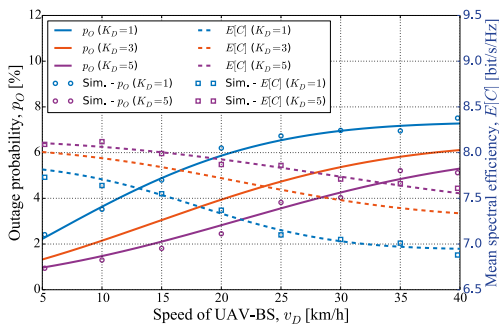


Fig. 6. Outage probability and mean spectral efficiency. Effect of UAV-BS speed and its capabilities.

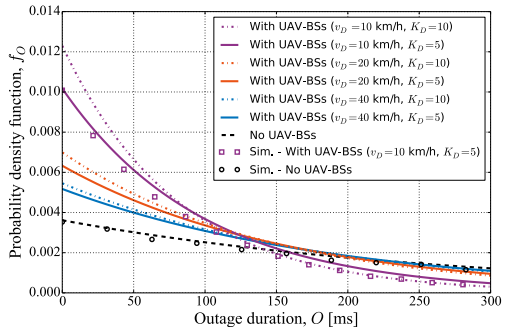


Fig. 7. Distribution of outage duration. Effect of UAV-BS speed and its capabilities.

the sake of analytical tractability: e.g., an approximation of the 3GPP's multipath propagation model as detailed in Section III and [28].

2) *Effect of UAV-BS flight speed*: The intensity of UAV-BSs traversing the area, λ_D , is fixed and set to 10 UAV-BSs per min. We model a crowded scenario with $\lambda_B = 0.7$, while the maximum number of simultaneous backhaul connections per UAV-BS, K_D , varies from 1 to 5. We observe that a decrease in the UAV-BS speeds has a notable positive effect on performance. As an example, lowering UAV-BS speeds from 40 km/h down to 10 km/h for $K_D = 1$ results in reduced outage probability from 7.1% to 3.5%, which is over 2 times. The corresponding gain in the mean spectral efficiency, $E[C]$, is smaller but still visible: from 6.9 bit/s/Hz to 7.7 bit/s/Hz.

We continue by evaluating the effect of the UAV-BS speeds in Fig. 7, which presents the pdf of the outage duration for certain values of v_D and K_D . The UAV-BS intensity, λ_D , is set to 10 per min, while the density of humans in the area, λ_B , equals 0.7. There is a notable decrease in the mean outage duration, $E[O]$, when UAV-BSs are utilized. Particularly, the said parameter decreases from 276 ms for the baseline deployment down to as low as 88 ms for ($v_D = 10$ km/h, $K_D = 10$) case. Finally, we notice that increasing the UAV-BS capacity, K_D , by two times (from 5 to 10 simultaneous connections) brings a notable decrease in the mean outage duration.

3) *Effect of service capacity of UAV-BSs, K_D* : To this aim, we analyze the primary backhaul session continuity related parameter – the average duration of the uninterrupted connectivity subject to a certain tolerable outage duration. In other words, a connection is assumed to be interrupted if and only if the outage duration is longer than a certain value, Δ_O . We illustrate these results in Fig. 8 for two UAV-BS intensities ($\lambda_D = 1$ and 10 UAV-BSs per min).

Studying Fig. 8, we notice that for 100 ms of tolerable outage, the average duration of uninterrupted connectivity grows from 7 s for the baseline scenario to 46 s for 10 UAV-BSs per min, $K_D = 10$. We then observe that the impact of an increased UAV-BS capacity, K_D , is notable but weaker than that of the intensity of UAV-BS traversals: the curve for (10 UAV-BSs per min, $K_D = 1$) is much higher than the one for (1 UAV-BS per min, $K_D = 10$). This is mainly due to the fact that at least one out of 10 UAV-BSs is much more likely to reside in non-outage conditions with respect to the COW-BS than a single UAV-BS, regardless of the capacity.

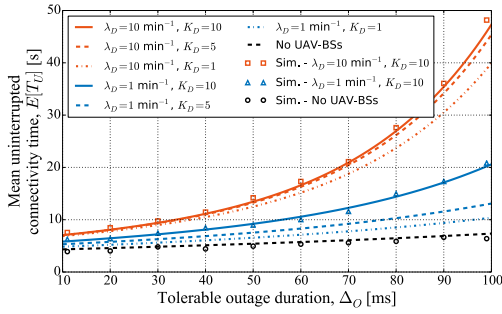


Fig. 8. Mean uninterrupted connectivity time. Effect of UAV-BS traversal intensity and its capabilities.

Finally, we observe that the relative impact of K_D on the said parameter depends on the intensity of UAV-BS flights across the area. Particularly, the improvement brought by $K_D = 5$ and $K_D = 10$ vs. $K_D = 1$ is significant for 1 UAV-BS per min and marginal for 10 UAV-BSS per min. In summary, for high intensity of UAV-BS traversals, there is no need for higher capacity of the UAV-BSSs. Meanwhile, if the intensity of UAV-BS flights is lower than required from the connectivity perspective, there is a driver to invest resources into advanced radio units on the UAV-BSSs.

VI. CONCLUSION

Dynamic and reconfigurable system architectures aiming to support backhaul operation in mmWave bands are one of the recent focus items in the ongoing 3GPP standardization. They can be further augmented by an emerging element in the 5G landscape – UAVs with flexible mobility and capability to carry radio equipment. These may become efficient backhaul connectivity providers in 5G and beyond networks, especially in case of highly dynamic traffic fluctuations to avoid excessive over-provisioning of network resources.

To this aim, we contribute a new analytical framework that incorporates 3GPP’s multipath channel model, heterogeneous mobility of UAVs and humans, as well as human body blockage effects, which are identified by 3GPP as one of the main sources of performance degradation for the prospective NR operation. Our methodology allows to produce both time-averaged and continuous-time metrics in dependence on UAV-BS speed and traversal intensity, heights of the communicating entities within the scenario (NR-BS, UAV-BS, COW-BS, and human blockers), as well as blocker dimensions and speeds.

We demonstrate that UAV-BS assistance can offer significant benefits to mmWave backhaul under certain system parameters. For instance, the intensity of UAV-BS flights equal to 10 reduces the outage probability on a COW-BS backhaul link by 6 times. Moreover, by lowering the UAV-BS speed above the service area from 40 km/h down to 10 km/h, the said outage probability drops by 2 times. Further, one may derive the target intensity of UAV-BS traversals that is required to support the key performance indicators as a function of the blocker density. The contributed framework can be applied to a wide range of practical scenarios, such as conventional layouts with the near-static deployment of UAV-BSSs by e.g., adjusting the speed parameter.

REFERENCES

- [1] M. Shafi, A. F. Molisch, P. J. Smith, T. Haustein, P. Zhu, P. D. Silva, F. Tufvesson, A. Benjebbour, and G. Wunder, “5G: A Tutorial Overview of Standards, Trials, Challenges, Deployment, and Practice,” *IEEE Journal on Selected Areas in Communications*, vol. 35, no. 6, pp. 1201–1221, June 2017.
- [2] 5GPPP, “View on 5G Architecture,” White paper v2.0, December 2017.
- [3] 3GPP, “Report of 3GPP TSG RAN meeting #78,” 3GPP RP-180516, December 2017.
- [4] J. Sachs, G. Wikstrom, T. Dudda, R. Baldemair, and K. Kittichokechai, “5G Radio Network Design for Ultra-Reliable Low-Latency Communication,” *IEEE Network*, vol. 32, no. 2, pp. 24–31, March 2018.
- [5] U. Siddique, H. Tabassum, E. Hossain, and D. I. Kim, “Wireless backhauling of 5G small cells: Challenges and solution approaches,” *IEEE Wireless Communications*, vol. 22, no. 5, pp. 22–31, October 2015.
- [6] C. Dehos, J. L. Gonzalez, A. D. Domenico, D. Ktenas, and L. Dussault, “Millimeter-wave access and backhauling: The solution to the exponential data traffic increase in 5G mobile communications systems?” *IEEE Communications Magazine*, vol. 52, no. 9, pp. 88–95, September 2014.
- [7] T. Bai, R. Vaze, and R. W. Heath, “Analysis of blockage effects on urban cellular networks,” *IEEE Transactions on Wireless Communications*, vol. 13, no. 9, pp. 5070–5083, September 2014.
- [8] M. Gapeyenko *et al.*, “On the temporal effects of mobile blockers in urban millimeter-wave cellular scenarios,” *IEEE Transactions on Vehicular Technology*, vol. 66, no. 11, pp. 10 124–10 138, November 2017.
- [9] V. Petrov, M. Komarov, D. Moltchanov, J. M. Jornet, and Y. Koucheryavy, “Interference and SINR in Millimeter Wave and Terahertz Communication Systems With Blocking and Directional Antennas,” *IEEE Transactions on Wireless Communications*, vol. 16, no. 3, pp. 1791–1808, March 2017.
- [10] V. Petrov, M. A. Lema, M. Gapeyenko, K. Antonakoglou, D. Moltchanov, F. Sardin, A. Samuylov, S. Andreev, Y. Koucheryavy, and M. Dohler, “Achieving End-to-End Reliability of Mission-Critical Traffic in Softwarized 5G Networks,” *IEEE Journal on Selected Areas in Communications*, vol. 36, no. 3, pp. 485–501, March 2018.
- [11] 3GPP, “Study on channel model for frequencies from 0.5 to 100 GHz (Release 15),” 3GPP TR 38.901 V15.0.0, June 2018.
- [12] F. B. Tesema, A. Awada, I. Viering, M. Simsek, and G. Fettweis, “Evaluation of context-aware mobility robustness optimization and multi-connectivity in intra-frequency 5G ultra dense networks,” *IEEE Wireless Communications Letters*, vol. 5, no. 6, pp. 608–611, December 2016.
- [13] O. E. Ayach, S. Subramanian, J. E. Smee, A. Sampath, and J. Li, “Method and apparatus for connection point discovery and association in a directional wireless network,” October 2016, US9474013B2. [Online]. Available: <https://patents.google.com/patent/US9474013B2/en>
- [14] M. Mousaei and B. Smida, “Optimizing pilot overhead for ultra-reliable short-packet transmission,” in *IEEE International Conference on Communications*, May 2017.
- [15] NGMN, “Small cell backhaul requirements,” White paper, June 2012.
- [16] 3GPP, “Study on integrated access and backhaul (Release 15),” 3GPP TR 38.874 V0.4.0, August 2018.
- [17] C. Saha, M. Afshang, and H. S. Dhillon, “Integrated mmWave Access and Backhaul in 5G: Bandwidth partitioning and downlink analysis,” Available: <https://arxiv.org/pdf/1710.06255.pdf>, 2018.
- [18] K. Balachandran, J. Kang, K. Karakayali, and J. Singh, “Capacity benefits of relays with in-band backhauling in cellular networks,” in *IEEE International Conference on Communications*, May 2008.
- [19] M. Jaber, F. J. Lopez-Martinez, M. A. Imran, A. Sutton, A. Tukmanov, and R. Tafazolli, “Wireless backhaul: Performance modelling and impact on user association for 5G,” *IEEE Transactions on Wireless Communications*, pp. 1–1, 2018.
- [20] I. Bor-Yaliniz, A. El-Keyi, and H. Yanikomeroglu, “Efficient 3-D placement of an aerial base station in next generation cellular networks,” in *IEEE International Conference on Communications*, May 2016.
- [21] E. Kalantari, M. Z. Shaker, H. Yanikomeroglu, and A. Yongacoglu, “Backhaul-aware robust 3D drone placement in 5G+ wireless networks,” in *IEEE International Conference on Communications Workshops (ICC Wkshps)*, May 2017, pp. 1–6.
- [22] M. Mozaffari, W. Saad, M. Bennis, and M. Debbah, “Efficient deployment of multiple unmanned aerial vehicles for optimal wireless coverage,” *IEEE Communications Letters*, vol. 20, no. 8, pp. 1647–1650, August 2016.
- [23] K. Haneda *et al.*, “5G 3GPP-like channel models for outdoor urban microcellular and macrocellular environments,” in *IEEE 83rd Vehicular Technology Conference (VTC Spring)*, May 2016.

- [24] 3GPP, "Study on enhanced LTE support for aerial vehicles, (Release 15)," TR 36.777 V15.0.0, January 2018.
- [25] A. Fotouhi, M. Ding, and M. Hassan, "Dynamic base station repositioning to improve performance of drone small cells," in *2016 IEEE Globecom Workshops (GC Wkshps)*, December 2016, pp. 1–6.
- [26] J. G. Andrews, T. Bai, M. Kulkarni, A. Alkhateeb, A. Gupta, and R. W. Heath, "Modeling and analyzing millimeter wave cellular systems," *IEEE Transactions on Communications*, vol. 65, no. 1, pp. 403–430, January 2016.
- [27] M. Zhang, M. Polese, M. Mezzavilla, S. Rangan, and M. Zorzi, "Ns-3 Implementation of the 3GPP MIMO Channel Model for Frequency Spectrum above 6 GHz," in *Workshop on ns-3*, June 2017.
- [28] M. Gapeyenko, V. Petrov, D. Moltchanov, S. Andreev, Y. Koucheryavy, M. Valkama, M. R. Akdeniz, and N. Himayat, "An Analytical Representation of the 3GPP 3D Channel Parameters for mmWave Bands," in *2nd ACM Workshop on Millimeter-Wave Networks and Sensing Systems*, October 2018, pp. 1–6.
- [29] Y. Zeng, R. Zhang, and T. J. Lim, "Wireless communications with unmanned aerial vehicles: Opportunities and challenges," *IEEE Communications Magazine*, vol. 54, no. 5, pp. 36–42, May 2016.
- [30] P. Nain, D. Towsley, B. Liu, and Z. Liu, "Properties of random direction models," in *IEEE INFOCOM*, vol. 3, March 2005.
- [31] A. M. Mathai, *An introduction to geometrical probability: Distributional aspects with applications*. CRC Press, 1999, vol. 1.
- [32] G. Newell, "The $M/G/\infty$ queue," *SIAM Journal on Applied Mathematics*, vol. 14, no. 1, pp. 86–88, 1966.
- [33] R. Groenevelt, "Stochastic models for mobile ad hoc networks," INRIA Sophia-Antipolis, PhD thesis, 2005.
- [34] D. J. Daley, "The busy period of the $M/G/\infty$ queue," *Queueing Systems: Theory and Applications*, vol. 38, no. 2, pp. 195–204, 2001.
- [35] J. G. Kemeny, J. L. Snell *et al.*, *Finite Markov chains*. van Nostrand Princeton, NJ, 1960, vol. 356.
- [36] T. Altiok, "On the phase-type approximations of general distributions," *IIE Transactions*, vol. 17, no. 2, pp. 110–116, 1985.
- [37] M. F. Neuts, *Matrix-geometric solutions in stochastic models: an algorithmic approach*. Courier Corporation, 1981.
- [38] V. Petrov *et al.*, "Dynamic multi-connectivity performance in ultra-dense urban mmWave deployments," *IEEE Journal on Selected Areas in Communications*, vol. 35, no. 9, pp. 2038–2055, September 2017.



Margarita Gapeyenko (margarita.gapeyenko@tut.fi) is a Ph.D. candidate at the Laboratory of Electronics and Communications Engineering at Tampere University of Technology, Finland. She earned her M.Sc. degree in Telecommunication Engineering from University of Vaasa, Finland, in 2014, and B.Sc. degree in Radio-Engineering, Electronics, and Telecommunications from Karaganda State Technical University, Kazakhstan, in 2012. Her research interests include mathematical analysis, performance evaluation, and

optimization methods for mmWave networks, UAV communications, and (beyond-)5G heterogeneous systems.



Vitaly Petrov (vitaly.petrov@tut.fi) received the M.Sc. degree in information systems security from the Saint Petersburg State University of Aerospace Instrumentation, St Petersburg, Russia, in 2011, and the M.Sc. degree in communications engineering from the Tampere University of Technology, Tampere, Finland, in 2014, where he is currently pursuing the Ph.D. degree. He was a Visiting Scholar with the Georgia Institute of Technology, Atlanta, USA, in 2014 and a Strategic Intern with the Nokia Research Center, Helsinki, Finland, in 2012. He is

the recipient of Best Student Paper Award at IEEE VTC-Fall'15 and Best Student Poster Award at IEEE WCNC'17. His current research interests are in Internet-of-Things, mmWave/THz band communications, nanonetworks, cryptology, and network security.



Dmitri Moltchanov (dmitri.moltchanov@tut.fi) is a Senior Research Scientist in the Laboratory of Electronics and Communications Engineering, Tampere University of Technology, Finland. He received his M.Sc. and Cand.Sc. degrees from Saint-Petersburg State University of Telecommunications, Russia, in 2000 and 2002, respectively, and Ph.D. degree from Tampere University of Technology in 2006. His research interests include performance evaluation and optimization issues of wired and wireless IP networks, Internet traffic dynamics, quality of user experience of real-time applications, and traffic localization P2P networks. Dmitri Moltchanov serves as TPC member in a number of international conferences. He authored more than 50 publications.



Sergey Andreev (sergey.andreev@tut.fi) received the Specialist and Cand.Sc. degrees from St. Petersburg State University of Aerospace Instrumentation, St. Petersburg, Russia, in 2006 and 2009, respectively, and the Ph.D. degree from Tampere University of Technology, Finland, in 2012. Since 2018, he has been a Visiting Senior Research Fellow with the Centre for Telecommunications Research, King's College London, U.K. He is currently a Senior Research Scientist with the Laboratory of Electronics and Communications Engineering, Tampere University of Technology. He has authored or co-authored over 150 published research works on wireless communications, energy efficiency, heterogeneous networking, cooperative communications, and machine-to-machine applications.



Nageen Himayat is a Principal Engineer with Intel Labs, where she leads a team conducting research on several aspects of next generation (5G/5G+) of mobile broadband systems. Her research contributions span areas such as multi-radio heterogeneous networks, mm-wave communication, energy-efficient designs, cross layer radio resource management, multi-antenna, and non-linear signal processing techniques. She has authored over 250 technical publications, contributing to several IEEE peer-reviewed publications, 3GPP/IEEE standards, as well as holds numerous patents. Prior to Intel, Dr. Himayat was with Lucent Technologies and General Instrument Corp, where she developed standards and systems for both wireless and wire-line broadband access networks. Dr. Himayat obtained her B.S.E.E degree from Rice University, and her Ph.D. degree from the University of Pennsylvania. She also holds an MBA degree from the Haas School of Business at University of California, Berkeley.



Yevgeni Koucheryavy (evgeni.koucheryavy@tut.fi) received the Ph.D. degree from the Tampere University of Technology, in 2004. He is a Professor with the Laboratory of Electronics and Communications Engineering, Tampere University of Technology, Finland. He is the author of numerous publications in the field of advanced wired and wireless networking and communications. His current research interests include various aspects in heterogeneous wireless communication networks and systems, the Internet of Things and its standardization, and nanocommunications. He is an Associate Technical Editor of the IEEE Communications Magazine and Editor of the IEEE Communications Surveys and Tutorials.

PUBLICATION

VI

Comparison of Airborne and Landed Deployments for On-Demand UAV-based mmWave Access Points

V. Petrov, M. Gapeyenko, D. Moltchanov, S. Andreev and R. W. Heath

IEEE Wireless Communications Letters (2020), 1–5. Submitted publication

Publication reprinted with the permission of the copyright holders

PUBLICATION

VII

On Unified Vehicular Communications and Radar Sensing in Millimeter-Wave and Low Terahertz Bands

V. Petrov, G. Fodor, J. Kokkoniemi, D. Moltchanov, J. Lehtomaki, S. Andreev,
Y. Koucheryavy, M. Juntti and M. Valkama

IEEE Wireless Communications 26.3 (2019), 146–153

Publication reprinted with the permission of the copyright holders

On Unified Vehicular Communications and Radar Sensing in Millimeter-Wave and Low Terahertz Bands

Vitaly Petrov*, Gabor Fodor, Joonas Kokkonen, Dmitri Moltchanov, Janne Lehtomäki, Sergey Andreev, Yevgeni Koucheryavy, Markku Juntti, and Mikko Valkama

Abstract—Future smart vehicles will incorporate high-data-rate communications and high-resolution radar sensing capabilities operating in the millimeter-wave and higher frequencies. These two systems are preparing to share and reuse a lot of common functionalities, such as steerable millimeter-wave antenna arrays. Motivated by this growing overlap, and advanced further by the space and cost constraints, the vehicular community is pursuing a vision of unified vehicular communications and radar sensing, which represents a major paradigm shift for next-generation connected and self-driving cars. This article outlines a path to materialize this decisive transformation. We begin by reviewing the latest developments in hybrid vehicular communications and radar systems, and then propose a concept of unified channel access over millimeter-wave and higher frequencies. Our supporting system-level performance characterization relies upon real-life measurements and extensive ray-based modeling to confirm the significant improvements brought by our proposal to mitigating the interference and deafness effects. Since our results aim to open the door to unified vehicular communications and radar sensing, we conclude by outlining the potential research directions in this rapidly developing field.

I. TODAY'S VEHICULAR COMMUNICATIONS AND RADARS

Over the last decade, vehicular communications have experienced a fundamental transformation by absorbing the impact of several waves of research and development trends in this field. *The first wave* came in the mid-2000s, with the IEEE 802.11p initiative that enabled data exchange between vehicles over the unlicensed frequency band around 5.9 GHz. The subsequent IEEE 802.11p-2010 standard amendment supported ad-hoc vehicular communications with data rates of up to 27 Mbit/s over 10 MHz-wide channels and was later superseded by conventional Wi-Fi IEEE 802.11-2012 specification. In parallel, vehicle-centric operations have been facilitated by additional standards that regulated the higher layers of a vehicular network (e.g., IEEE 1609.32 Standard for Wireless Access in Vehicular Environments, WAVE) [1]. This formed a consistent set of specifications for microwave-based vehicular communications, referred to as cooperative, connected, and automated mobility (CCAM) in Europe and dedicated short-range communications (DSRC) in the United States.

By design, the 802.11p-family of technologies is dedicated to direct vehicle-to-vehicle (V2V) interactions. Hence, these

*A part of this work has been completed during the research visits of Vitaly Petrov to Ericsson Research, Sweden.

G. Fodor is with Ericsson Research and the School of Electrical Engineering and Computer Science of KTH Royal Institute of Technology, Sweden.

V. Petrov, D. Moltchanov, S. Andreev, Y. Koucheryavy, and M. Valkama are with Tampere University of Technology, Tampere, Finland.

J. Kokkonen, J. Lehtomäki, and M. Juntti are with the Centre for Wireless Communications, University of Oulu, Oulu, Finland.

This work was supported by the Academy of Finland 6Genesis Flagship (grant 318927) as well as projects PRISMA and WiFiUS. The work was also funded by Business Finland under the project RF CONVERGENCE. V. Petrov acknowledges the support of HPY Research Foundation funded by Elisa.

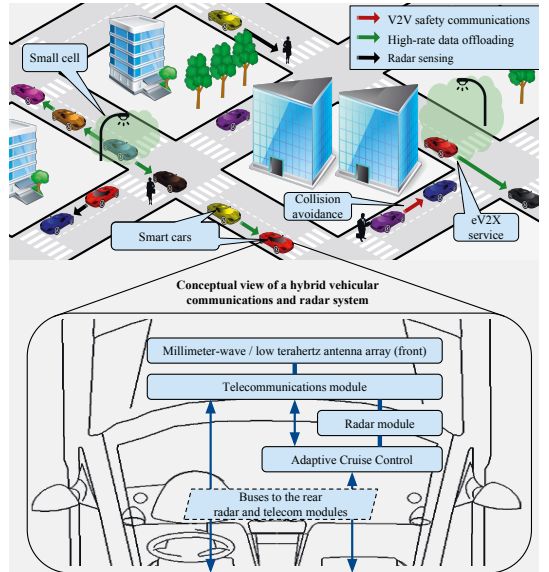


Fig. 1. Joint V2V communications and automotive radar applications.

are not intended to be used for vehicle-to-pedestrian (V2P) or vehicle-to-infrastructure (V2I) data exchange. In response to this gap, *the second wave* of standardization activities has been dedicated to vehicular-to-everything (V2X) communications over 3GPP LTE technology, where uplink, downlink (for V2P and V2I), and sidelink (for V2V) operations were ratified [2]. Early work was initiated in 2014, while the key requirements and use cases were identified by the 3GPP's Technical Specification Group on Service and System Aspects (TSG-SA) in 2016. The corresponding enablers to support mission-critical V2X communications were presented in 2017 as part of LTE Release 14. V2X over LTE enables reliable connectivity within hundreds of meters at around 100 ms end-to-end latencies (from the source to the destination application).

A. Emerging mmWave V2X Communications and Radar

Within LTE Release 15 and beyond, 3GPP explores the feasibility of next-generation (5G-grade), enhanced V2X (eV2X) use cases, which range from platooning to remote driving [3]. Many of these scenarios require extremely high data rate and reliability levels, as well as low latencies [4]. For example, “bird’s eye view” and “see-through vision” demand up to 50 Mbit/s at 50 ms delay, while “automated overtake” requires 10 ms latency with 10^{-5} reliability. These stringent requirements engage the community to initiate *the third wave* of

V2X communications research, by targeting the New Radio (NR) technology that will complement LTE [5]. It is expected to primarily operate in millimeter-wave (mmWave) spectrum; that is, 30–300 GHz. NR-V2X will augment LTE V2X in massive deployments of connected vehicles and its standardization has started recently. The academic groups are advancing this vision by exploring mmWave-based V2X communications over 60 GHz, 79 GHz, and even low terahertz frequencies at 300 GHz and beyond [6].

Today’s automotive radar sensing systems also occupy the mmWave band and, particularly, the frequencies of 76–81 GHz. The existing solutions can generally be classified into three categories: (i) long-range radars (up to 100 m) that typically sense the forward direction for the adaptive cruise control applications; (ii) middle-range radars (tens of meters) dedicated to cross-traffic alerts or blind-spot detection; and (iii) short-range radars (several meters), which are exploited by parking assistance and pre-crash services. Solutions operating in the 77 and 79 GHz bands are already in commercial use, while the total number of mmWave radars can easily reach 10 for a modern high-class vehicle.

B. From Trial Deployments to Massive mmWave V2X

While the *feasibility* of mmWave V2X communications and radar sensing has already been confirmed, the focus of recent research efforts has shifted towards enabling *scalable* operation in massive (semi-)autonomous driving with smart interconnected vehicles (see Fig. 1) [7]. The major scalability concerns are – jointly for data transmission and radar sensing – related to massive interference from neighboring vehicles, which challenges the reliability, latency, and achievable data rate of NR-V2V communications [6]. Further, there may be dangerous sensing inaccuracies that lead to the emergence of “ghost” obstacles. The level of interference in such systems *must* be kept under control to make collective autonomous driving safe and efficient.

In this article, we tackle the aforementioned challenges by advancing the paradigm of *hybrid vehicular communications and radar sensing* over the mmWave band and beyond. We systematically review and classify the contemporary approaches in this field as well as propose a conceptual joint channel access framework that aims to reduce the levels of interference in both communications and radar operations. We evaluate this concept in a realistic urban scenario by relying on: (i) real-life measurements and (ii) our in-house ray-based modeling framework to quantify the potential gains of unifying mmWave-based vehicular communications and radar sensing. Our proposal can be integrated into future releases of 3GPP NR and IEEE 802.11. We conclude by outlining the research perspectives in this area that are meant to open a discussion on the future mmWave and beyond vehicular networking.

II. REVIEW OF JOINT TELECOM & RADAR FOR V2V

The concept of joint communications and radar applications has been evolving continuously over several decades. More recently, utilization of mmWave frequencies in this context became particularly beneficial, since much of the communications and radar systems functionality partially overlaps in these

bands. In this section, we review the contemporary approaches to hybrid vehicular communications and radar sensing, which typically follow either of the *three* options:

A. Time-Domain Duplex (TDD)

The first approach assumes independent operation of telecom and radar subsystems, while the utilization of antenna hardware may be shared between them in a time-based manner [8]. There is a switching process between the two time intervals: (i) when the antenna system (e.g., a single antenna or an antenna array) is used for data communications and (ii) when the antenna system is exploited to transmit and receive radar sequences. The corresponding modulated waveform can be generated with a direct digital synthesizer (DDS) [8].

TDD class of solutions features lower implementation complexity. At the same time, the resultant system scalability may be rather limited, since fast switching between data and radar modes cannot be synchronized effectively among all of the communicating vehicles. Hence, when one of the cars is transmitting its data, the destination node may reside in the radar mode, not being able to receive it. In addition, since perfect time synchronization is difficult to achieve, the data and radar transmissions can interfere with each other.

B. Telecom Messages over Radar Transmissions (ToR)

The second approach suggests modulating the data messages on top of the radar transmissions. This category typically employs Pulse Position Modulation (PPM) for the data transmissions. The corresponding systems are featured by relatively high radar resolution and accuracy since no stringent constraints on the choice of the radar sequences are imposed, while each transmission serves the purposes of sensing.

The scalability of these solutions is higher as compared to the TDD schemes since data transmissions do not impede the sensing process of the radar module. However, spectrum utilization remains inherently low, since the choice of applicable modulation and coding schemes is limited to a set of basic options. As a result, the achievable data rate is low even at the mmWave band: about 200 Mbps over 3 GHz bandwidth [9].

C. Radar Sensing over Telecom Transmissions (RoT)

The solutions in this group are more recent and specific to mmWave frequencies. Their feasibility is maintained by the specialized properties of the preambles used in mmWave radio communications standards (e.g., IEEE 802.11ad/ay or 3GPP NR). This approach suggests reusing the same preamble detection mechanisms in order to provide distance and velocity estimation for the nearby driving vehicles.

It has recently been validated experimentally and shown to be beneficial from both the data rate and the sensing accuracy perspectives [10]. At the same time, the sensing capabilities of the developed prototype are still inferior to those offered by the commercially-available dedicated radar systems as well as remain vulnerable to uncontrolled interference from other cars initiating their data transmissions nearby. Further, RoT approaches require tight agreement between many stakeholders as they embrace the know-how of radars from vehicular vendors – all the relevant signaling has to be standardized

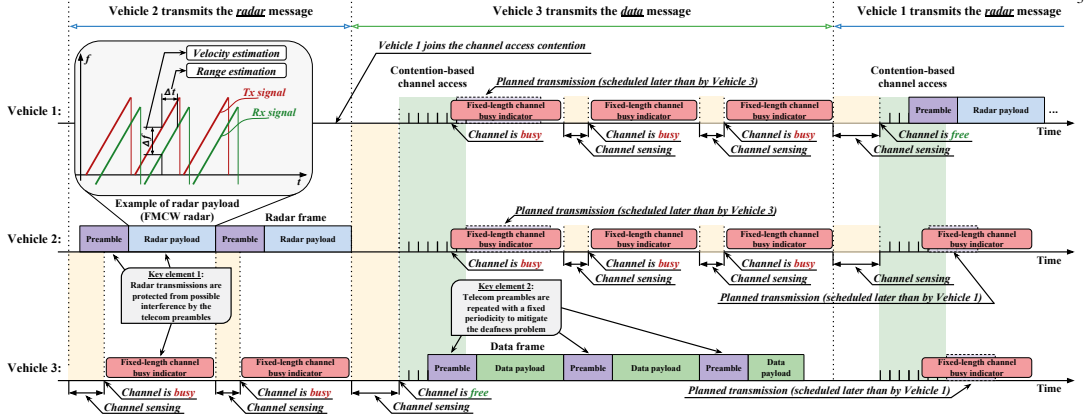


Fig. 2. Proposed integration of V2V communications and radar.

publicly. Hence, while this class of systems has technical advantages as compared to the previous two, the business perspectives of the corresponding solutions remain unclear.

III. HARMONIZED V2V TELECOM & RADAR FRAMEWORK

Summarizing our above review of existing approaches for joint radar and communications in V2V, current functionality of telecom and radar subsystems is mostly separated, as the associated modules operate *independently* and only occasionally share common equipment in the transceiver to access the radio channel. Addressing the gap, we seek to explore the synergy of the involved subsystems rather than aim at their straightforward blending within a single physical device.

A. Turning Competitors into Allies

Instead of constructing a communications system on top of the radar functionality or achieving the radar goals over a communications module, we envisage a possibility to *intelligently combine the communications and radar subsystems* in a way that they perform harmonized operations, while both benefiting from the capabilities of the mmWave band. Particularly, we conceptualize a TDD-inspired solution (see subsection II-A) where synchronization between vehicular communications and radar operations is conducted not within a single car but rather propagates across the entire collision domain of the neighboring vehicles.¹ The communications and radar functionalities need to be either placed into a unified module or be located as separate but interconnected devices, still employing a certain level of hardware reuse, as well as synchronization to share the common wireless channel in the time domain [8]. The solution reduces the probability that the radar sensing performed by one of the vehicles interferes with the transmissions coming from another vehicle and vice versa.

Our proposal offers the much needed scalability and reliability as well as flexibility for vendors to develop their own radar waveforms without losing the integrity within the employed communications protocol. Moreover, with this approach, the

¹Here, “collision domain” refers to the set of vehicles potentially affecting each others’ transmissions: the generated interference is higher than the noise level.

accuracy of the radar subsystem can also be improved by integrating the results of the communications preamble detection and the actual radar waveform operation [10]. We thus advocate for a harmonized framework over a multi-tenancy multiple access channel, where the same preambles are used to indicate radar as well as data transmissions. Hence, the radar messages avoid interference by following well-established random-access communications mechanisms, whereas the notorious deafness problem is resolved by periodic transmissions of additional preambles (see Fig. 2). The resulting Radar-Aware Carrier-Sense Multiple Access (RA-CSMA) scheme comprises two major components: (i) a unified frame structure for transmitted communications and radar messaging and (ii) a radar-aware preamble detection based channel-access protocol for directional V2V communications.

B. Unified Frame Structure

In the proposed system design, the communications and radar module controls the shared antenna system. The vehicle performing the radar sensing first utilizes a telecom module to participate in contention-based channel access and, as a result of this procedure, transmits a preamble to “reserve” the channel for the duration of a frame (see Fig. 2). Then, the vehicle changes its operating mode from communications to radar to initiate the actual sensing. The sensing period may consist of a single or multiple transmissions/receptions of the radar sequences, as illustrated in Fig. 2 (top left). Finally, once the “reserved” time is over, the vehicle switches its operating mode back to communications and either “reserves” the channel again by transmitting another preamble or switches to the Rx mode and continues transmitting/receiving other data by following the CSMA-based access procedure.

In order to implement the intended operation, an additional fixed-length field to indicate the frame category has to be introduced. It needs to be located in the header to enable fast decoding of the frame category at the hardware level. All of the frames coming from other vehicles and marked as “radar” are immediately dropped at the receiver. The described operation allows for utilizing a unified collision avoidance mechanism for both the communications and radar subsystems, hence reducing the time-to-market and manufacturing costs. More-

over, it offers robust protection of the radar sequences, since radar frame transmissions enjoy “collision-free” environment: following the described procedure, no other vehicles in the same collision domain can initiate a transmission as long as the medium is reserved. The latter is crucial for developing safety solutions as it reduces interference and thus enables more accurate distance and obstacle velocity estimation [11].

C. Radar-Aware Channel Access with Preamble Repetition

The deafness problem in V2V communications may affect the transmission of both the data and the radar messages. The conventional mechanisms based on energy detection or frame header decoding are not sufficiently robust to rely upon when detecting transmissions of the neighboring vehicles, especially across the reflected paths. To address this challenge, we propose the use of additional preambles by injecting them into the channel with a fixed periodicity and minimal interframe spacing as illustrated in Fig. 2. It has been demonstrated that preamble-based detection is much more reliable even in extremely low-SNR regimes [10].

Design of a particular preamble sequence to accommodate the described concept remains an open research issue. It is, however, worthwhile to note that the discussed preamble detection over reflected/scattered signals is technically feasible since this procedure is already a part of the basic communications and radar functionality. In the described channel access scheme, the vehicle that is about to transmit first listens on the channel for one inter-preamble interval. If a preamble is detected, the channel busy indicator is set for another interval. Otherwise, the channel is considered idle and the vehicle initiates its channel access procedure. With the proposed approach, the rest of the radio technology signaling can be applied to the envisioned operation with minimal changes.

The outlined channel access procedure introduces an additional delay in the radar sensing operation. However, accounting for $5\mu\text{s}$ -long slots (as in IEEE 802.11ay) and the maximum backoff counter of 1024, the total delay value does not exceed 5.12 ms. Furthermore, since the size of the collision domain in realistic deployments is around 2–3 vehicles, the said counter does not typically exceed 16. This keeps the channel access delay under a few milliseconds, which is in-line with the requirements for beyond-5G mission-critical communications [4]. Importantly, a vehicle can travel not more than a few centimeters during such ms-scale intervals. Hence, the extra delay caused by channel access does not affect the radar operations significantly.

In the following section, we comprehensively study the implications of the proposed RA-CSMA scheme on the performance of mmWave-based V2V applications.

IV. PERFORMANCE EXPECTATIONS IN MMWAVE V2V

Our proposed RA-CSMA scheme relies upon the ability of the vehicle that initiates a transmission to sense active transmissions by other vehicles in the same collision domain even in cases where only reflected or scattered paths are available at its transceiver. In order to evaluate the proposed concept, we first have to carefully characterize the specifics

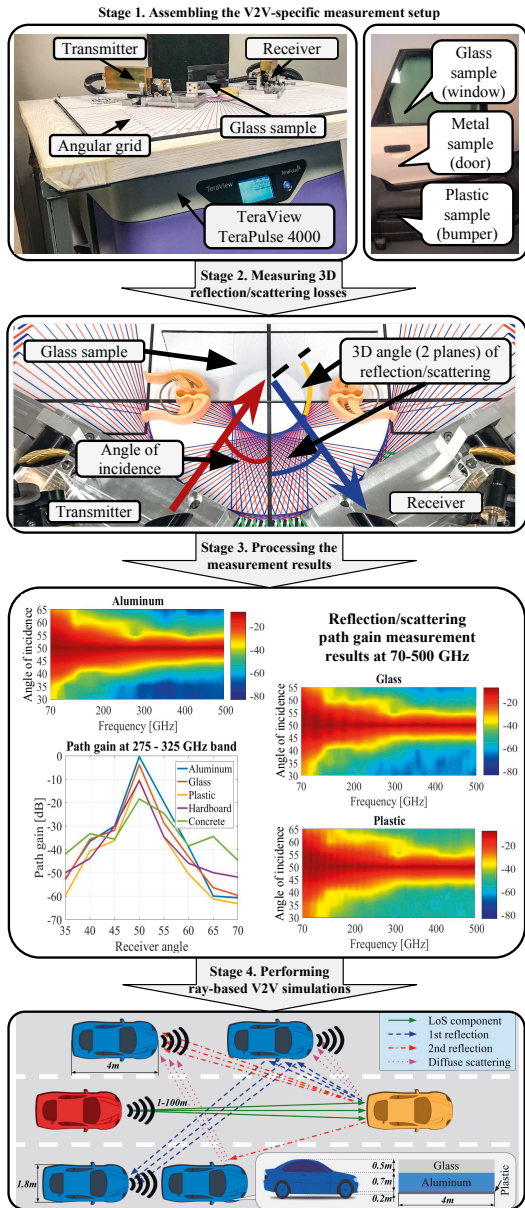


Fig. 3. Our compound measurement-simulation based evaluation methodology for the performance assessment of hybrid V2V systems.

of mmWave propagation in vehicular environments, with the main focus on the effects related to the mmWave signal reflection and scattering from the bodies of vehicles. For this purpose, an integrated measurement-simulation campaign has been conducted (see Fig. 3).

A. Specifics of mmWave Propagation in V2V Scenarios

To characterize mmWave signal propagation in realistic V2V environments, we first conduct a measurement campaign that aims to analyze and report on the properties of reflection and scattering at the frequencies of up to 500 GHz from the materials typical for the vehicle bodies, including aluminum, glass, and hard plastic (see Fig. 3, Stage 1). The measurements were performed at the University of Oulu by using TeraView TeraPulse 4000, which is capable of mmWave and terahertz band transmission/reception from 60 GHz to 4 THz. The signal attenuation has been measured as a function of the selected material and three 2D angles: the angle of incidence and the angles of reflection/scattering in two planes.

To this end, Fig. 3, Stage 3 displays an example of the measurement results for 50° angle of arrival. Aluminum is the best reflector out of the considered materials with the reflection loss being on the order of 0–5 dB. In contrast, other materials (glass and, especially, plastic) are characterized by much higher scattering losses, which are particularly visible at the frequencies of above 100 GHz. Similar measurements have been carried out for other angles of arrival with the step of 5° and stored in a way that the ray-based framework can calculate the corresponding path gain as a function of the angle of incidence and 3D angle of reflection/scattering.

The obtained measurement results are then applied to evaluate the performance of mmWave V2V communications with different channel access schemes (including the proposed RA-CSMA) in a typical urban deployment. Particularly, a wide city avenue with a randomized deployment of vehicles has been considered (see Fig. 3, Stage 4). The utilized parameters

TABLE I
PARAMETERS OF OUR RAY-BASED STUDY.

Deployment	Area of interest: Segment of a street, 200 m long, 3 lanes in each direction (6 lanes in total) Lane width: 2.75 m Sidewalk width: 3 m Total street width: 22.5 m Propagation: Urban canyon, street is surrounded by concrete buildings of 30 m height
Radio part	Environment: Air, $T = 296$ K and 1.8% of water vapor Frequency: 300 GHz Bandwidth: 10 GHz Tx power: 0 dBm Tx antenna gain: 30 dB Rx antenna gain: 30 dB Antennas: In front and rear bumpers (0.2 m altitude). Perfect beam alignment between Tx and Rx is assumed
Vehicles	Model: Parallelepiped $4\text{ m} \times 1.8\text{ m} \times 1.4\text{ m}$ Material: Glass (top 0.5 m); steel (middle 0.7 m); plastic (bottom 0.2 m) Reflection/scattering properties: Defined by the measurement results in subsection IV-A Inter-vehicle distance: Setup 1: Random (exponentially distributed); Setup 2: Constant for all the vehicles Speed: Setup 1: Normally distributed with the mean of 30 km/h; Setup 2: Constant for all the vehicles, 5 km/h
Channel access	Idealistic: Perfect TDMA, ideal time synchronization, thus no inter-vehicle interference (upper bound) RA-CSMA: Proposed scheme, CSMA with preamble repetition (see Section III for details) Uncoordinated: Uncoordinated random access Adaptive access: Uncoordinated random access with binary exponential backoff operation (from 8 to 1024)

are summarized in Table I.

To characterize the introduced scenario and collect first-order performance results, an in-house ray-based modeling framework was employed [12]. It is mainly implemented in Python, operates in a time-driven manner, and adopts the measurement data from TeraView test environment as input for the reflection/scattering properties of the incorporated materials. Our framework utilizes a ray-tracing approach with surface tessellation, where the signal propagation in the air is modeled as proposed in [13]. For the sake of better accuracy in the output results, all of the acquired intermediate data have been averaged over 1,000 replications.

B. Scalability of Channel Access Schemes for mmWave V2V

First, Fig. 4 reports on the spectral efficiency of a V2V communications link in case the distance between two connected vehicles varies from 1 to 100 m, while all other vehicles are deployed randomly with the average distance of 10 m between each other. The inter-vehicle distance is distributed exponentially, as in Setup 1 (see details in Table I). The utilization of the envisioned RA-CSMA channel access scheme improves both the link spectral efficiency and the achievable communications range where data transmissions remain sufficiently reliable ($SINR \geq 10$ dB). It is also observed that with our proposed solution the realistic communications range can reach up to a hundred of meters even with 10 GHz of bandwidth and over 300 GHz carrier frequency, thus enabling a number of attractive rate-hungry applications currently envisioned for e.g., NR-V2V. Similar RA-CSMA performance is observed for 79 GHz and 150 GHz mmWave frequencies.

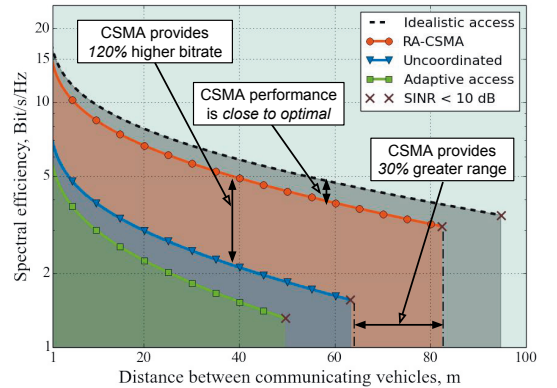


Fig. 4. Spectral efficiency of mmWave V2V system with RA-CSMA.

Further, Fig. 5 illustrates the impact of correct preamble detection on the reliability of mmWave-band V2V communications and radar sensing. This figure demonstrates the average SINR at the receiver as a function of the mean distance between the vehicles in our scenario of interest. Here, the distance between the source and the destination vehicles (red and yellow, respectively, in Fig. 3, Stage 4) is modeled similarly to the distances between other neighboring

vehicles. It follows one of the two setups that correspond to different deployment scenarios. The first one characterizes a freeway scenario, where the distances between the vehicles are modeled as independent and exponentially distributed random variables. In the second setup, the distances between all of the vehicles are kept constant, thus capturing dense urban traffic.

C. Interference- vs. Noise-Limited Operation of mmWave V2V

Analyzing Fig. 5, we emphasize three distinct regimes for mmWave V2V communications and radar sensing, which are generally agnostic to the selected channel access scheme as well as the assumed distribution of inter-vehicle distances:

1) *The ultra-dense regime*: corresponds to < 1 m of inter-vehicle separation and is characterized by the highest level of SINR. Radio signal attenuation in this case is low, while the impact of interference is marginal due to substantial blockage by car bumpers and wings.

2) *The dense regime*: is characterized by the inter-vehicle distance from ≈ 1 m to 10–20 m. The role of interference becomes of primary importance, since the useful signal is not as strong, whereas there are many other vehicles nearby.

3) *The sparse regime*: has the average inter-vehicle distance of greater than 10–20 m. It is mostly affected by the noise level; the useful signal becomes notably attenuated, while the population of interfering vehicles remains low.

A minor improvement in the SINR when switching from Setup 1 to Setup 2 is explained by the fact that the first setup allows for situations where the distance between the communicating vehicles is long, while the distances between the vehicles on the neighboring lanes are short, so there are multiple vehicles to interfere with an active transmission.

D. Reliability Aspects of Radar Sensing

Applying the results from Fig. 5 to the radar sensing operation, we note that a connection between the estimated SINR values and the effective range of the radar sensing is complex, since the probability of successful obstacle detection at a particular distance is related not only to the SINR value but also to the specific obstacle shapes and material, the surrounding environment, and, importantly, the details of the radar implementation (type of the utilized radar, sampling frequency, filtering, and many more). Nevertheless, the improved SINR values – as confirmed with Fig. 5 – contribute to the reliability of radar sensing, since higher SINR leads to better range and accuracy of the distance and velocity estimation [11].

Summarizing, the proposed channel access method offers decisive performance improvements in terms of communications range, data rates, and SINR in dense scenarios, thus contributing to better scalability of mmWave vehicular communications and radar sensing in massive deployments. In the following section, we discuss the current and prospective research directions related to V2X over mmWave and beyond.

V. TOWARDS MASSIVE AND SCALABLE V2X

A. Present and Future of V2X over mmWave and Beyond

The contemporary V2X roadmap outlined by the 5G Public Private Partnership (5G-PPP) imposes gradually increasing

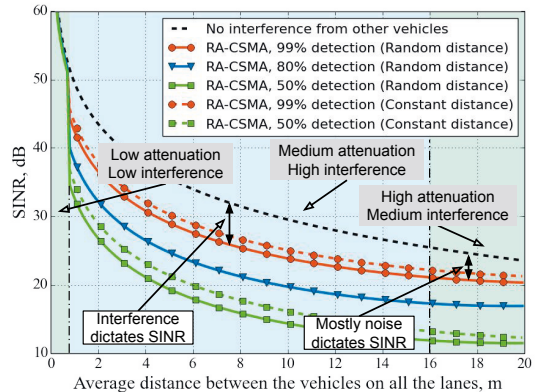


Fig. 5. Impact of successful preamble detection on SINR performance.

requirements on the supporting communications technology in terms of its reliability, latency, and offered data rates. The envisioned 5G-PPP scenarios are grouped into phases that range from awareness driving, through cooperative driving, to, ultimately, synchronized driving, wherein vehicles are autonomously driven in a wide range of situations [3].

Following the outlined use cases, novel approaches are required to achieve the desired tradeoff between the implementation complexity and the spectral efficiency. Specifically, for direct V2V communications, hybrid automatic repeat request (HARQ) operation over the 3GPP sidelink requires support of point-to-point communications at both PHY and MAC layers. In addition, the choice of the most beneficial locations and characteristics of the antenna arrays for hybrid V2X communications and radar sensing are currently under consideration.

B. Harnessing Even Higher Frequencies

Motivated by the continuously growing demands imposed by the amounts of data traffic to be transmitted over vehicular networks (up to 1Tbit/hour per connected vehicle according to some predictions [6]), the research community begins to contemplate the carrier frequencies beyond 100 GHz as a valuable asset for future V2X systems. Several radio communications stakeholders are already exploring the use of frequencies available in the high-mmWave/low-THz bands. The data rates of up to 10Gbit/s over up to 850 m have been demonstrated at 120 GHz [14]. An attractive potential of beyond-100 GHz band has recently been recognized by IEEE: its IEEE 802.15.3d Task Group identified the 275–325 GHz band as the one feasible for extremely high access rates of up to 100 Gbit/s. Alongside with this trend, automotive radars are also moving higher up in frequency to improve their latencies and resolution of the obtained images. Recently, an automotive imaging radar solution at 150 GHz has been demonstrated [15].

The path beyond 300 GHz requires the development of novel transceivers, which are capable of operating at these extreme frequencies. Such transceivers are required to be featured by adequately high power and sensitivity, while at the same time

reach low noise figures – all to overcome the inherently high pathloss at these frequencies. Additional band-specific difficulties emerge related to generating high-power signals at (low-)THz frequencies, the so-called *THz gap*, as well as increased attenuation of the radio waves due to *molecular absorption*. In addition, the future high-mmWave/low-THz technology needs to manage the antenna systems with ultra-narrow beamwidth (few degrees at the maximum), thus challenging the current beamsteering and beamtracking implementations.

Higher power consumption caused by immaturity of the discussed technology is another factor that limits commercial deployments of vehicular systems operating beyond 300 GHz. Researchers are now working on different technologies to tackle this problem, ranging from the state-of-the-art complementary metal-oxide-semiconductor (CMOS), through alternative semiconductor materials (e.g., III-V compound semiconductor), as well as novel materials, such as graphene. In addition, widely-employed orthogonal frequency division multiplexing (OFDM) features high peak-to-average power ratio (PAPR), which becomes an issue for terahertz-band channels. Hence, the community is exploring the applicability of novel waveforms to effectively harness this promising band.

C. Cellular-Assisted Network Management

The further evolution of mmWave V2X requires their tighter integration into the emerging 5G architecture, where cellular systems may be employed to control the mmWave-based direct V2V and radar sensing more efficiently than any decentralized solution with only partial knowledge of the radio environment can do. The latter leads to the concept of cellular-assisted V2X (C-V2X). One of the main advantages of C-V2X is that it can address the V2X applications in an end-to-end manner within the same technology, which constitutes a scalable and future-proof solution. Also, as part of the 3GPP standards suite, C-V2X offers an evolution path from LTE to (beyond-)5G systems. Built-in mmWave radars can also exploit the benefits of cellular assistance as they may share the data between multiple cars and road infrastructure nodes to perform radio sensing in a distributed albeit more effective manner.

However, C-V2X functionality calls for new network management solutions to effectively orchestrate all of the available communications, data storage (caching), and computing capabilities. Particularly, the optimized balance levels of data pre-processing have to be determined between (i) exchanging all the sensed raw data among the interconnected vehicles, as one extreme, and a more conservative approach (ii) conducting the required sensing locally and only sharing the relevant post-processed knowledge, as another extreme. Design of these novel solutions mediates between vehicular, communications, and mobile computing communities, thus calling for their concerted effort to materialize the scalable, reliable, and high-rate vehicular communications of tomorrow.

VI. CONCLUSIONS

The impending proliferation of interconnected autonomous vehicles will dramatically increase the intensity and depth of

vehicular communications and radar sensing integration. The envisioned utilization of mmWave and even higher frequency bands will (i) provide abundant radio resources for high-resolution imaging, which is essential for accurate recognition of the road surface, cars, and other surrounding objects, as well as (ii) facilitate high-rate data exchange between connected and self-driving cars. At the same time, the adoption of wider spectrum and directional antenna systems alone will not automatically lead to a successful implementation of scalable vehicular systems, since the underlying interference and deafness issues challenge the reliability and performance of both communications and radar operations.

Along these lines, an emerging concept of unified vehicular communications and radar sensing developed in this article becomes a promising candidate to make the two “pairs of eyes” of a vehicle harmonized with each other, thus paving the way to unprecedentedly massive deployments of interconnected smart cars. By going further and integrating other intelligent entities on and along the road (radio access infrastructures, networked road signs, connected pedestrians, video surveillance systems, etc.) via next-generation 3GPP NR, LTE, and IEEE technologies, the rapidly maturing automotive environment may ultimately evolve into a hyper-intelligent transportation system, by providing a more convenient, safe, and efficient driving experience.

REFERENCES

- [1] Y. L. Morgan, “Notes on DSRC & WAVE standards suite: Its architecture, design, and characteristics,” *IEEE Commun. Surveys & Tuts.*, vol. 12, no. 4, pp. 504–518, Fourth Quarter 2010.
- [2] H. Seo *et al.*, “LTE evolution for Vehicle-to-Everything services,” *IEEE Commun. Mag.*, vol. 54, no. 6, pp. 22–28, June 2016.
- [3] Volkswagen AG *et al.*, “5G automotive vision,” 5G Infrastructure Public Private Partnership (5G PPP), White paper, Oct. 2015.
- [4] V. Petrov *et al.*, “Achieving end-to-end reliability of mission-critical traffic in software-defined 5G networks,” *IEEE J. on Sel. Areas in Commun.*, vol. 36, no. 3, pp. 485–501, March 2018.
- [5] S. Chen *et al.*, “Vehicle-to-Everything (V2X) services supported by LTE-based Systems and 5G,” *IEEE Commun. Stand. Mag.*, vol. 1, no. 2, pp. 70–76, July 2017.
- [6] J. Choi *et al.*, “Millimeter-wave vehicular communication to support massive automotive sensing,” *IEEE Commun. Mag.*, vol. 54, no. 12, pp. 160–167, Dec. 2016.
- [7] X. Ge, Z. Li, and S. Li, “5G software defined vehicular networks,” *IEEE Commun. Mag.*, vol. 55, no. 7, pp. 87–93, July 2017.
- [8] L. Han and K. Wu, “Radar and radio data fusion platform for future intelligent transportation system,” in *Proc. of EuRAD*, Sept. 2010.
- [9] M. Bocquet *et al.*, “A multifunctional 60-GHz system for automotive applications with communication and positioning abilities based on time reversal,” in *Proc. of EuRAD*, Sept. 2010.
- [10] P. Kumari *et al.*, “IEEE 802.11ad-based radar: An approach to joint vehicular communication-radar system,” *IEEE Trans. on Veh. Tech.*, vol. 67, no. 4, pp. 3012–3027, Apr. 2018.
- [11] A. Gameiro *et al.*, “Research challenges, trends and applications for future joint radar communications systems,” *Wireless Pers. Commun.*, vol. 100, no. 1, pp. 81–96, May 2018.
- [12] V. Petrov *et al.*, “Last meter indoor terahertz wireless access: Performance insights and implementation roadmap,” *IEEE Commun. Mag.*, vol. 56, no. 6, pp. 158–165, June 2018.
- [13] J. M. Jornet and I. F. Akyildiz, “Channel modeling and capacity analysis for electromagnetic wireless nanonetworks in the terahertz band,” *IEEE Trans. on Wireless Commun.*, vol. 10, no. 10, pp. 3211–3221, Oct. 2011.
- [14] I. Kallfass *et al.*, “64 Gbit/s transmission over 850 m fixed wireless link at 240 GHz carrier frequency,” *J. of Infrared, Millim., and Ter. Waves*, vol. 36, no. 2, pp. 221–233, Feb. 2015.
- [15] D. Jasteh *et al.*, “Low-THz imaging radar for outdoor applications,” in *Proc. of IRS*, June 2015.

AUTHORS' BIOGRAPHIES

Vitaly Petrov (vitaly.petrov@tut.fi) is a PhD candidate at the Laboratory of Electronics and Communications Engineering at Tampere University of Technology, Finland. He received the Specialist degree (2011) from SUAI University, St. Petersburg, Russia, as well as the M.Sc. degree (2014) from Tampere University of Technology. He is the recipient of Best Student Paper Award at IEEE VTC-Fall, Boston, USA, 2015 and Best Student Poster Award at IEEE WCNC, San Francisco, USA, 2017. Vitaly (co-)authored more than 30 published research works on terahertz band/mmWave communications, Internet-of-Things, nanonetworks, cryptography, and network security.

Gabor Fodor (gabor.fodor@ericsson.com) received the M.Sc. and Ph.D. degrees in electrical engineering from the Budapest University of Technology and Economics in 1988 and 1998 respectively. He is currently a master researcher at Ericsson Research and an adjunct professor at the KTH Royal Institute of Technology, Stockholm, Sweden. He was a co-recipient of the IEEE Communications Society Stephen O. Rice prize in 2018. He is serving as an Editor of the IEEE Transactions on Wireless Communications.

Joonas Kokkonen (joonas.kokkonen@oulu.fi) is a Postdoctoral Research Fellow with the Centre for Wireless Communications, University of Oulu. He received the B.Sc. (2011), M.Sc. (2012), and Dr.Sc. (2017) degrees from University of Oulu, Oulu, Finland. He was a Visiting Researcher with Tokyo University of Agriculture and Technology, Japan (2013) and a Visiting Researcher with State University of New York at Buffalo, USA (2017). Joonas's research interests include THz band and mmWave channel modeling and communication systems.

Dmitri Moltchanov (dmitri.moltchanov@tut.fi) received the M.Sc. and Cand.Sc. degrees from the St. Petersburg State University of Telecommunications, Russia, in 2000 and 2003, respectively, and the Ph.D. degree from the Tampere University of Technology in 2006. Currently he is University Lecturer with the Laboratory of Electronics and Communications Engineering, Tampere University of Technology, Finland. He has (co-)authored over 150 publications. His current research interests include 5G/5G+ systems, ultra-reliable low-latency service, industrial IoT applications, mission-critical V2V/V2X systems, and blockchain technologies.

Janne Lehtomäki (janne.lehtomaki@oulu.fi) is an Adjunct Professor with the Centre for Wireless Communications, Uni-

versity of Oulu. He received the M.Sc. (1999) and the Ph.D. (2005) in telecommunications from University of Oulu. His research interests are in terahertz wireless communication, channel modeling, IoT, and spectrum sharing. Janne co-authored the winner of the Best Paper Award at IEEE WCNC 2012. He is an Editorial Board Member of Elsevier Physical Communication.

Sergey Andreev (sergey.andreev@tut.fi) is an Assistant Professor in the Laboratory of Electronics and Communications Engineering at Tampere University of Technology, Finland. He received the Specialist degree (2006) and the Cand.Sc. degree (2009) both from St. Petersburg State University of Aerospace Instrumentation, St. Petersburg, Russia, as well as the Ph.D. degree (2012) from Tampere University of Technology. Sergey (co-)authored more than 150 published research works on wireless communications, energy efficiency, and heterogeneous networking.

Yevgeni Koucheryavy (yevgeni.koucheryavy@tut.fi) is a Full Professor in the Laboratory of Electronics and Communications Engineering, Tampere University of Technology, Finland. He received his Ph.D. degree (2004) from Tampere University of Technology. He is the author of numerous publications in the field of advanced wired and wireless networking and communications. He is Associate Technical Editor of IEEE Communications Magazine and Editor of IEEE Communications Surveys and Tutorials.

Markku Juntti (markku.juntti@oulu.fi) received a Dr.Sc. (Tech.) degree in electrical engineering from the University of Oulu, Finland, in 1997. He has been with the University of Oulu since 1992. In 1994–1995 he visited Rice University, Houston, Texas. He has been a professor of telecommunications at the University of Oulu since 2000. His research interests include communication and information theory, signal processing for wireless communication systems, and their application in wireless communication system design.

Mikko Valkama (mikko.valkama@tut.fi) received his M.Sc. and D.Sc. degrees (both with honors) from Tampere University of Technology, Finland, in 2000 and 2001, respectively. In 2003, he worked as a visiting research fellow at San Diego State University, California. Currently, he is a Full Professor and Head of the Laboratory of Electronics and Communications Engineering at Tampere University of Technology, Finland. His research interests include radio communications, radio systems and signal processing, with specific emphasis on 5G and beyond mobile networks.

PUBLICATION

VIII

Exploiting Multipath Terahertz Communications for Physical Layer Security in Beyond 5G Networks

V. Petrov, D. Moltchanov, J. M. Jornet and Y. Koucheryavy

*Proc. of IEEE Conference on Computer Communications Workshops (IEEE INFOCOM
WKSHPS)2019, 1–8*

Publication reprinted with the permission of the copyright holders

Exploiting Multipath Terahertz Communications for Physical Layer Security in Beyond 5G Networks

Vitaly Petrov*, Dmitri Moltchanov*, Josep Miquel Jornet[†], Yevgeni Koucheryavy*

*Tampere University, Finland

[†]University at Buffalo, The State University of New York, USA,

Email: *{vitaly.petrov, dmitri.moltchanov, evgeny.koucheryavy}@tuni.fi, [†]jmjornet@buffalo.edu

Abstract—Terahertz (THz) band communications, capable of achieving the theoretical capacity of up to several terabits-per-second, are one of the attractive enablers for beyond 5G wireless networks. THz systems will use extremely directional narrow beams, allowing not only to extend the communication range but also to partially secure the data already at the physical layer. The reason is that, in most cases, the Attacker has to be located within the transmitter beam in order to eavesdrop the message. However, even the use of very narrow beams results in the considerably large area around the receiver, where the Attacker can capture all the data. In this paper, we study how to decrease the message eavesdropping probability by leveraging the inherent multi-path nature of the THz communications. We particularly propose sharing the data transmission over multiple THz propagation paths currently available between the communicating entities. We show that, at a cost of the slightly reduced link capacity, the message eavesdropping probability in the described scheme decreases significantly even when several Attackers operate in a cooperative manner. The proposed solution can be utilized for the transmission of the sensitive data, as well as to secure the key exchange in THz band networks beyond 5G.

I. INTRODUCTION

Terahertz band (0.3–10 THz) communication is the next frontier of wireless networks, allowing for data exchange at rates of up to several terabits-per-second [1]. The two major advances brought by the use of THz band on top of the fifth-generation (5G)-grade millimeter wave (mmWave) radio are: (i) active harnessing of wide frequency bands above 300 GHz [2]; and (ii) utilization of ultra-massive multiple input multiple output (MIMO) systems with theoretically up to several thousands of antenna elements [3]. These enhanced beyond 5G systems may not only improve the performance in existing use-cases, but also enable novel haptic services, such as data kiosk [4], massive augmented and virtual reality (AR/VR) [5], and tactile Internet [6], among others.

One of the first standards for the communications over the THz band has been released by IEEE in 2017 [7], with several others currently in development [8]. The research community is also making significant progress in designing the miniaturized hardware modules for the prospective THz band radio [9], channel and capacity modeling [10], [11], novel link-layer techniques [12], and enhanced system-level solutions [13], [14]. These efforts promise that commercial THz communications systems will appear in the near future [15].

To alleviate the effects of severe propagation losses, THz band systems are expected to rely upon extremely directional

antenna radiation patterns providing noticeable gains at both transmit and receive sides [3]. Furthermore, the THz frequencies are naturally prone to blockage by both stationary and mobile objects in the channel, including building walls, vehicles, furniture, and even human bodies [14], [16]. This leads to complex dynamic multi-path propagation environment between the access point (AP) and the user equipment (UE) with a single line-of-sight (LoS) component and multiple non-line-of-sight (nLoS) reflected and scattered paths [11], [17]. To enable uninterrupted data transmission, the beamsteering mechanism has to be used to continuously select the path, currently characterized by the best signal-to-noise (SNR) ratio.

The use of extremely directional narrow beams brings inherent benefits to the physical layer security of mmWave and THz band communications [18]. The reason is that the Attacker has to physically be within the transmitting beam in order to decode any notable portion of data [19]. It has been particularly shown in [20] and [21] that the use of narrow beams together with the physical layer security-specific encoding allows to substantially decrease the probability of data to be eavesdropped in both LoS and nLoS conditions. Nevertheless, the perfect secrecy can still not be achieved, as the “*eavesdropping zone*” – the area, where the Attacker can successfully eavesdrop the data, is still relatively large [22].

There have been some techniques recently proposed to overcome this issue and reduce the size of the eavesdropping zone by sharing the secret communications with UE among several APs or several distant antenna arrays at a single AP [23]. Particularly, the envisioned distance between several antenna arrays at the THz band radio is shown to be insufficient for a significant spatial diversity of beams [24]. On its turn, as the channel conditions change rapidly [16], [25], the data sharing among several APs notably increases the system complexity by requiring real-time synchronization among several THz APs.

To overcome the abovementioned issues, we propose and analyze an enhanced method to build a secure THz communications system by utilizing multiple propagation paths between a given AP and UE. We particularly focus on the multi-path approach, where the node consequently transmits the different shares of the sensitive data over different propagation paths currently available towards the receiver (see Fig. 1). The data are encoded in a way that the receiver can decode the message only if it successfully receives *all* the shares. We show that although this scheme slightly reduces the link capacity versus

the baseline *single-path* scheme (as the nLoS paths are also used even when the better LoS path is available), the message eavesdropping probability drastically decreases, even when attackers operate in a cooperative manner. To the best of authors' knowledge, this is one of the first studies addressing the security of the THz communications at the physical layer.

The contributions of this work are summarized as follows.

- A *mathematical framework* capable to characterize the message eavesdropping probability, the link capacity, and the secrecy rate of THz communications in typical outdoor urban deployments. The framework is flexible to account for the different number of THz multi-path components used for the data exchange, as well as for various crowd and attackers densities around UE.
- A *comparative analysis* of baseline *single-path* and proposed *multi-path* strategies for secure THz communications within our mathematical framework. The trade-offs between the performance-centric and security-centric metrics of interest are reported for a wide range of system and environment parameters.

The rest of the paper is organized as follows. The system model for our study is introduced in Sec. II. The mathematical framework to characterize the secrecy rate in our system and the trade-off between link capacity and eavesdropping probability is developed in Sec. III. The numerical results illustrating the introduced trade-offs between the secrecy level and the performance are discussed in Sec. IV. The conclusions are outlined in the last section.

II. SYSTEM MODEL

In this section, we specify the system model by introducing its individual components. We start describing the deployment of interest, then proceed with the radio part describing propagation, blockage, antenna, and eavesdropping assumptions. Finally, we define the metrics of interest. The main notation used in the paper is summarized in the Table I.

1) *Scenario and Deployment*: We model a single communication link between a THz band AP at a height h_A (e.g., at the lamp post or on the wall) and a THz band UE at a height h_U , located d meters apart from the AP. There are two types of objects surrounding the UE: (i) humans, acting as blockers for THz propagation paths and (ii) attackers, eavesdropping all the data that passes through their location (see Fig. 1).

The humans are assumed to follow Poisson point process (PPP) in \mathcal{R}^2 with the density of μ units per square meter. Humans are modeled by cylinders with height h_B and base radius r_B . The attackers are also deployed according to PPP in \mathcal{R}^2 around the UE with the density λ . Both blockers and attackers are modeled to remain stationary during the entire data transmission, which is a realistic assumption, as the THz data frame duration is expected to be very short [2].

2) *Propagation Model*: The link between the AP and the UE involve N alternative paths that can be used to transmit the data (see Fig. 1). Each of the paths is characterized by its attenuation, zenith of arrival/departure (ZOA/ZOD) and azimuth of arrival/departure (AOA/AOD).

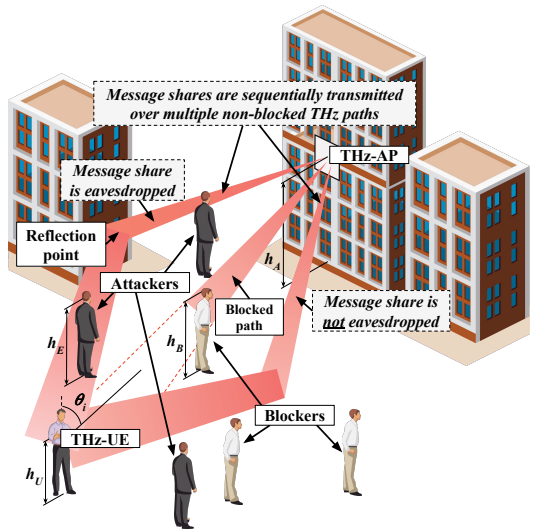


Fig. 1. Secure THz band communications in urban deployments.

The received power $P(x)$ is calculated following the THz band-specific model proposed in [26], while the individual attenuations of the multi-path components and ZOA follow the approximations from [27]¹. Each of the paths suffers from random blockages by humans surrounding the UE. As the THz signal gets significantly attenuated by the human body [15], the data transmission cannot be performed over the path if it is occluded. Thus, at a given time instant, only the currently non-blocked paths are assumed available for the data transmission.

3) *Antenna Model*: We assume planar antenna arrays at both AP and UE sides with the corresponding antenna gains G_A and G_U . For simplicity, we model the single-lobe cone-shape antenna radiation patterns following [28].

A viable approximation for the angular beam width α of a planar array is provided by $102^\circ/L$, where L is the number of antenna elements in the appropriate plane [29]. Similarly, the linear gain can be approximated as [29]

$$G = \frac{1}{\theta^+ - \theta^-} \int_{\theta^-}^{\theta^+} \frac{\sin(L\pi \cos(\theta)/2)}{\sin(\pi \cos(\theta)/2)} d\theta, \quad (1)$$

where θ^\pm are the beam angular points.

4) *Security and Attackers Model*: In this work, we analyze and compare two solutions for secure data transmission over the THz band. In the first solution, termed as *single-path*, the sensitive data gets transmitted as a single message over a single “best” path – the path currently associated with the greatest SNR. We compare the baseline single-path approach with the alternative solution, termed as *multi-path*, where

¹Out of many available multi-path propagation models for mmWave and THz frequencies (e.g., [11], [17], [24], among others), the model from [27] provides the simplest, analytically-tractable expressions for ZOA and received power share in a random urban outdoor deployment, needed for our analysis.

TABLE I
NOTATION USED IN THE PAPER.

Parameter	Interpretation
h_A, h_U	THz-AP and THz-UE heights
λ	Spatial density of eavesdroppers
μ	Spatial density of blockers
h_B, r_B	Blockers height and radius
h_E	Eavesdroppers height
L_A, L_U	Number of THz-AP and THz-UE antenna elements
G_A, G_U	THz-AP and THz-UE gains
α	Beamwidth of the THz-AP antenna radiation pattern
K	Attenuation caused by reflection
N	Total number of paths available at the UE
M	Number of paths used in <i>Multi-path</i> scheme, $M \leq N$
x	2D distance between THz-AP and THz-UE
d	3D distance between THz-AP and THz-UE
θ_i	Zenith of arrival angle of cluster i
$P_{S,i}$	Received power share of cluster i
P_i	Received power of cluster i
N_0	Johnson-Nyquist noise
$C(x)$	Shannon rate at distance x
$C_S(x)$	Secrecy rate at distance x
$l_{E,i}, w_{E,i}$	Length and width of eavesdropping zone of cluster i
$l_{B,i}, w_{B,i}$	Length and width of blockage zone of cluster i
$P_{B,i}$	Blockage probability of cluster i
$P_{E,i}$	Eavesdropping probability of cluster i
$q_{N,i}$	Probability of having i out of N clusters blocked
$v_{N,i}$	Eavesdropping probability with i out of N clusters blocked
P_E	Eavesdropping probability

the message containing the sensitive data gets split over M , $M \leq N$, strongest paths. The secure encoding is used so that the message can be decoded only if all the shares are received [20].

The role of attackers is to compromise the secrecy of the THz band communications. In this work, we assume passive attackers, who eavesdrop all the messages passing around them but do not block the signal or modify any data. We also assume that all the attackers operate in a cooperative manner, that is, the message share is assumed eavesdropped if it is captured by at least a single attacker. The attackers successfully eavesdrop the message if they capture all of the message shares.

5) *Metric of Interest*: We concentrate on characterizing the trade-off between eavesdropping probability, P_E , and link capacity at the air interface, $C(x)$ between AP and UE located at two-dimensional (2D) distance x . The former is defined as the probability that a field of attackers are capable of overhearing the ongoing transmission.

For the single-path scheme, the link capacity is assumed to equal the Shannon rate of the path with the greatest SNR out of all currently available non-blocked paths. For the multi-path scheme, the link capacity is defined as a Shannon rate over M currently non-blocked paths used for the data exchange, i.e.,

$$C(x) = \frac{B}{M} \sum_{i=1}^M \log_2(1 + S_i(x)), \quad (2)$$

where S_i , $i = 1, 2, \dots, M$ are the SNR values at the distance x over the path i . Finally, we also characterize the secrecy rate, $C_S(x)$, defined as the rate of data not eavesdropped by the attackers.

III. SECRECY AND PERFORMANCE ANALYSIS

In this section, we develop a model for assessing the trade-off between eavesdropping probability and achieved data rate. We first characterize blockage and eavesdropping probabilities for individual paths and then proceed with metrics of interest.

A. Eavesdropping Zones for THz Multipath Propagation

In order to eavesdrop the message, the attacker has to be physically located within the transmitting beam. Therefore, the size of the eavesdropping zone – the ground-level 2D zone around the UE, where the attacker has to stay in order to still be within the transmitting beam – can be calculated from the deployment parameters, as detailed in this subsection. For the first-order analysis, we approximate the eavesdropping zone for the path i with a rectangle $l_{E,i} \times w_{E,i}$, where $w_{E,i}$ is determined by the actual width (in meters) of the AP beam around UE, while $l_{E,i}$ is defined by the AP beam elevation around UE and the eavesdroppers height, see Fig. 2.

For the antenna model, discussed in Section II, the width of the eavesdropping zone for the LoS path, $w_{E,1}$, can be estimated as follows, see Fig. 2(a),

$$w_{E,1} = d \tan(\alpha/2), \quad (3)$$

where d is the three-dimensional (3D) distance between the AP and UE and α is the AP beamwidth.

Then, the length of the eavesdropping zone for the LoS case, $l_{E,1}$ is derived from the scenario geometry as

$$l_{E,1} = x - (h_A - h_E) \tan(\theta_1 - \alpha/2), \quad (4)$$

where x is 2D distance between the AP and the UE nodes, h_A is the AP height, h_E is the eavesdropper height, and θ_1 is the line-of-sight zenith angle of arrival.

The model in [27] does not provide the exact number of reflections and scatterings for a given path. We construct an approximation assuming one reflection and no scattering for the nLoS path. This approximation upper bounds the size of the eavesdropping zone. *In practice, the zone can be smaller as there can be more than one reflection on the nLoS path.*

The spatial density of the received power from the nLoS path is inversely proportional to the width of the beam going over this path. Therefore, the eavesdropping zone width for nLoS path can be calculated as

$$w_{E,i} = d \tan(\alpha/2) \sqrt{P_{S,1}/(P_{S,i}K)}, \quad (5)$$

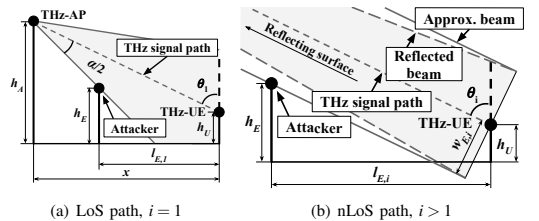


Fig. 2. Projections of the eavesdropping zones for LoS and nLoS cases.

where $P_{S,1}$ is the LoS power share, $P_{S,i}$ is the random variable (RV) representing the power share of the i -s nLoS path. Here, K is the additional attenuation caused by the reflection from the object. K is at least 10 dB for the typical materials [14].

Consequently, the approximate length of the eavesdropping zone, $l_{E,i}$ can be derived as follows, see Fig. 2(b),

$$l_{E,i} = (h_E - h_U) \tan(\theta_i) + w_{E,i} / \cos(\theta_i), \quad (6)$$

where h_U is the UE height and θ_i is an RV representing the current ZOA for the selected path.

For the PPP field of attackers, we derive the eavesdropping probability for the path i , $p_{E,i}$, as the probability that at least a single attacker is located in the corresponding zone as, i.e.,

$$p_{E,i} = 1 - e^{-\lambda w_{E,i} l_{E,i}}, i = 1, 2, \dots, N. \quad (7)$$

B. Blockage Zones for THz Multipath Propagation

Let $p_{B,i}$ be the probability that the i -th communication path between AP and UE is blocked and consider blockage of LoS path, $p_{B,1}$, first. For a certain 2D distance x between AP and UE, we observe that there is always the so-called *LoS blockage zone* as shown in Fig. 3. Using geometric arguments, the width and length of the LoS blockage zone are

$$w_{B,1} = 2r_B, l_{B,1} = \left(x \frac{h_B - h_U}{h_A - h_U} + r_B \right), \quad (8)$$

where r_B is the radius of the human blocker.

Using the void probability for the PPP of blockers, we have

$$p_{B,1} = 1 - e^{-2\mu_B \left[x \frac{h_B - h_U}{h_A - h_U} + r_B \right]}. \quad (9)$$

Let $\theta_i(x)$, $i = 2, 3, \dots, N$, be the RVs denoting ZOA. Consider now the blockage probability for the i -th path, $p_{B,i}$, $i = 2, 3, \dots$. As shown in [27], ZOA of the path i can be approximated by Laplace distribution with the probability density function (pdf)

$$f_{\theta_i}(y;x) = \frac{1}{2b_i(x)} e^{-\frac{|y-d_i(x)|}{b_i(x)}}, y \in [0;\pi], i = 2, 3, \dots, \quad (10)$$

where y is the corresponding ZOA value and $a^{(i)}(x)$, $b^{(i)}(x)$, $i = 2, 3, \dots, N$, are the parameters.

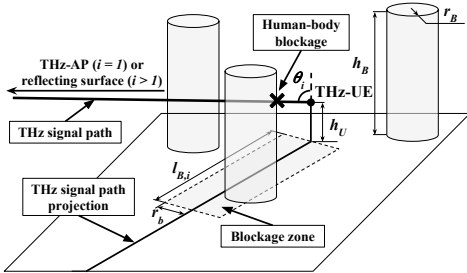


Fig. 3. Blockage zone geometry for LoS and nLoS cases.

Following [27], $a_i(x)$ is independent of the path number i and depends on the separation distance x only: $a_i(x) = a_j(x)$, $\forall i, j = 2, 3, \dots, N$. Furthermore, the mean of ZOA for all the paths coincides with the ZOA of the LoS path. In the contrary, $b_i(x)$ is independent of the distance and depends on the path index i only.

Similarly to the LoS path, for any given ZOA value y_i of the path i , $i = 2, 3, \dots, N$, we define *path i blockage zone*. Using geometric arguments, see Fig. 3, for path i we have [30].

$$p_{B,i}(y;x) = 1 - e^{-2\lambda_B r_B (\tan y_i (h_B - h_U) + r_B)}. \quad (11)$$

Accounting for pdf of θ_i we get

$$p_{B,i}(x) = \int_0^\pi f_{\theta_i}(y;x) p_{B,i}(y;x) dy, \quad (12)$$

that can be evaluated numerically.

C. Clusters Capacity

Having characterized the blockage probabilities of individual clusters of AP to UE link, we now proceed deriving the capacity of individual clusters. Below, we first characterize the received power and then provide the sought capacity.

The fraction of power from the cluster over the i -th path, $P_{S,i}$, $i = 1, 2, \dots$, follows Log-normal distribution with pdf

$$f_{P_{S,i}}(y;x) = \frac{1}{y d_i \sqrt{2\pi}} e^{-\frac{(\ln y - c_i)^2}{2d_i^2}}, i = 1, 2, \dots, N, \quad (13)$$

where c_i , d_i , $i = 2, 3, \dots$, are parameters. Both c_i and d_i are independent of x and depend on the path index i only [27].

The received power from every cluster is calculated as

$$P_i(x) = P_{S,i} 10^{(P_T + G_A + G_U - T(x))/10}, i = 1, 2, \dots, N, \quad (14)$$

where P_T is transmit power and T is the path loss, G_A and G_U are the AP transmit and UE receive antenna array gains. Substituting the path loss at low THz frequencies we have

$$P_i(x) = P_{S,i} 10^{\frac{P_T + G_A + G_U - 20 \log_{10} f_c - 20 \log_{10} x - 10kx / \ln(10) - 147.55}{10}}, \quad (15)$$

where f_c is the frequency, and k is the absorption coefficient.

Accounting for (13) the received power over a path i is

$$f_{P_i}(y;x) = f_{P_{S,i}}(y/A(x);x), \quad (16)$$

where $A(x) = 10^{\frac{P_T + G_A + G_U - 20 \log_{10} f_c - 20 \log_{10} x - 10kx / \ln(10) - 147.55}{10}}$.

Having obtained the received power over the path i , the Shannon rate for the path i can be written as

$$C_i(x) = B \log_2(1 + P_i(x)/N_0), i = 1, 2, \dots, N, \quad (17)$$

where N_0 is the Johnson-Nyquist noise over the bandwidth B .

Note that $C_i(x)$ are all non-linear functions of RVs P_i , $i = 1, 2, \dots, N$. Following [31], pdf of a RV Y , $w(y)$, expressed as function $y = \phi(x)$ of another RV X with pdf $f(x)$ is

$$w(y) = \sum_j f(\psi_j(y)) |\psi_j'(y)|, \quad (18)$$

where $x = \psi_j(y) = \phi^{-1}(x)$ is the inverse functions.

$$C(x) = \prod_{j=1}^3 (1 - p_{B,j}) \frac{1}{3} [C_1(x) + C_2(x) + C_3(x)] + p_{B,3} \prod_{j=1}^2 (1 - p_{B,j}) \frac{1}{2} [C_1(x) + C_2(x)] + p_{B,1} \prod_{j=2}^3 (1 - p_{B,j}) \frac{1}{2} [C_2(x) + C_3(x)] \\ + p_{B,2} \prod_{j=1,3} (1 - p_{B,j}) \frac{1}{2} [C_1(x) + C_3(x)] + (1 - p_{B,1}) \prod_{j=2}^3 p_{B,j} C_1(x) + (1 - p_{B,3}) \prod_{j=1}^2 p_{B,j} C_3(x) + (1 - p_{B,2}) \prod_{j=1,3} p_{B,j} C_2(x). \quad (24)$$

The inverse branch of interest of the Shannon rate function and its derivative are given by

$$\Psi(y) = N_0(2^{y/B} - 1), \quad \Psi'(y) = N_0 \log(2) 2^{y/B} / B, \quad (19)$$

leading to rate pdf in the following form

$$f_{C_i}(y; x) = \frac{A(x) \log(2) 2^{\frac{y}{B}}}{B(2^{\frac{y}{B}} - 1) d_i \sqrt{2\pi}} e^{-\frac{(\ln \frac{N_0(2^{y/B} - 1)}{A(x)} - c_i)^2}{2d_i^2}}, \quad i = 1, 2, \dots \quad (20)$$

D. Capacity and Eavesdropping Probability

We now proceed deriving the capacity and eavesdropping probabilities of THz communications for both single-path and multi-path transmission schemes.

1) *Shannon capacity*: Recall that in the single-path transmission scheme AP and UE always operate using the path having the highest received power. Sorting the paths in descending order of their means, we get the following approximation for Shannon capacity of the single-path scheme

$$C(x) = \sum_{i=1}^M \left[\prod_{j=1}^{i-1} p_{B,j} \right] (1 - p_{B,i}) C_i(x). \quad (21)$$

Observe that in (21) the rate is expressed as a sum of weighted components. To obtain the pdf of $C(x)$ one may use the convolution of individual components $C_i(x)$ directly in RV domain or, alternatively, using Laplace transform. However, recalling the property of the mean value, we have

$$E[C(x)] = \sum_{i=1}^M \left[\prod_{j=1}^{i-1} p_{B,j} \right] (1 - p_{B,i}) \int_0^{\infty} f_{C_i}(y; x) y dy, \quad (22)$$

that can be evaluated numerically.

Estimating capacity for the multi-path scheme, where a number of paths are simultaneously used for communications, is a more involved process. Considering the case of $M = 2$ and concentrate on estimating the capacity, we have

$$C(x) = (1 - p_{B,1})(1 - p_{B,2}) \frac{1}{2} [C_1(x) + C_2(x)] + (1 - p_{B,1}) p_{B,2} C_1(x) + p_{B,1} (1 - p_{B,2}) C_2(x). \quad (23)$$

For $M = 3$, we have (24). One may obtain similar expressions for any $M > 3$. However, for large values of M , e.g., $M = 20$, the calculations become unmanageable. In this case, we propose to rely upon the following approximation. Recall, that $M \leq N$ and the mean ZOA of path i , $i = 2, 3, \dots, N$ coincides with the LoS ZOA. This implies that $p_{B,i} \approx p_{B,j} = p_B, \forall i, j = 1, 2, \dots, N$. Although we still need to distinguish between the paths, the probability of choosing any combination of paths is independent of their indexes. Thus,

the probability of having i out of M paths non-blocked, $q_{M,i}$, follows a Binomial probability mass function

$$q_{M,i} = \binom{M}{i} (1 - p_B)^i p_B^{M-i}, \quad i = 1, 2, \dots, M. \quad (25)$$

Using this approximation, we have for $M = 2$

$$C(x) = q_{2,1} \frac{C_1(x)}{2} + q_{2,1} \frac{C_2(x)}{2} + q_{2,2} \left(\frac{C_1(x)}{2} + \frac{C_2(x)}{2} \right). \quad (26)$$

Similarly, for $M = 3$ we arrive at

$$C(x) = \frac{1}{3} q_{3,1} \sum_{i=1}^3 C_i(x) + \frac{1}{3} q_{3,2} \left[\frac{1}{2} (C_1(x) + C_2(x)) + \frac{1}{2} (C_2(x) + C_3(x)) + \frac{1}{2} (C_1(x) + C_3(x)) \right] + \frac{1}{3} q_{3,3} \sum_{i=1}^3 C_i(x). \quad (27)$$

Now, consider the contribution of an arbitrarily chosen path i to the achieved capacity. Observe that when j paths are non-blocked and LoS path is one of them, the share of time it is used for transmission is $1/j$. The overall number of combinations how to choose j out of M paths is $\binom{M}{j}$, while the number of times path i appears in these combinations is $\binom{M-1}{j-1}$. Summing up over all possible numbers of non-blocked paths with corresponding Binomial probabilities, we get the following expression for the capacity of the multi-path scheme

$$C(x) = \sum_{i=1}^M \sum_{j=1}^M q_{M,j} \frac{\binom{M-1}{j-1}}{\binom{M}{j}} \frac{1}{j} C_i(x) = \frac{1 - p_B^M}{M} \sum_{i=1}^M C_i(x). \quad (28)$$

Similarly to the single-path model, the capacity expression takes the form of weighted sum of rates. The mean value of the rate at the distance x is thus immediately given by

$$E[C(x)] = \frac{1 - p_B^M}{M} \sum_{i=1}^M \int_0^{\infty} f_{C_i}(y; x) y dy. \quad (29)$$

2) *Eavesdropping Probability*: To estimate the eavesdropping probability we need to take into account the eavesdropping zone for LoS path is different from the rest of the paths. Furthermore, recall that we are interested in eavesdropping probability conditioned on at least one path non-blocked at UE. The latter probability is given by $1 - \prod_{i=1}^M p_{B,i}$.

Observe that the probability that the path i is currently in use is $(1 - p_{B,i}) \prod_{j=1}^{i-1} p_{B,j}$. Thus, the probability that path i is currently in use and eavesdropped is $(1 - p_{B,i}) p_{E,i} \prod_{j=1}^{i-1} p_{B,j}$. Summing over non-blocked paths we get

$$p_E = \frac{\sum_{i=1}^M \left((1 - p_{B,i}) p_{E,i} \prod_{j=1}^{i-1} p_{B,j} \right)}{1 - \prod_{i=1}^M p_{B,i}}, \quad (30)$$

where $p_{E,i}$ is eavesdropping probability for the path i .

Similarly to the capacity calculations, the eavesdropping probability for the described multi-path scheme can be estimated differentiating between the blockage probabilities for different paths, $p_{B,i}$, $i = 1, 2, \dots, M$. Let $v_{M,i}$ be the probability that i paths are currently non-blocked, and there is at least one eavesdropper in all the zones for all the paths in use. Let $v_{M,0}$ be the probability that there are no non-blocked paths. Then

$$\begin{aligned} v_{1,0} &= p_{B,1}, v_{1,1} = (1 - p_{B,1})p_{E,1}, \\ v_{2,0} &= p_{B,1}p_{B,2}, v_{2,1} = v_{1,1}p_{B,2} + v_{1,0}(1 - p_{B,2})p_{E,2}, \\ &\dots, \end{aligned} \quad (31)$$

leading to the following recursion

$$v_{M,i} = v_{M-1,i-1}(1 - p_{B,M})p_{E,M} + v_{M-1,i}p_{B,M}. \quad (32)$$

Finally, the eavesdropping probability is derived as

$$p_E = \frac{\sum_{i=1}^M v_{M,i}}{1 - \prod_{i=1}^M p_{B,i}}, \quad (33)$$

while the secrecy rate $C_S(x)$ is given by $C_S(x) = (1 - p_E)C(x)$.

Observe that differentiating between cluster blockage probabilities, only recurrent expression can be provided. Assuming that $p_{B,i} \approx p_{B,j} = p_B$, $\forall i, j = 1, 2, \dots, N$, and differentiating between eavesdropping probability of LoS cluster and other clusters, $p_{E,1} = p_{E,L}$, $p_{E,i} = p_{E,nL}$, $i = 2, 3, \dots, N$, a simple approximation can be provided. Particularly, in this case the probability that i out of M clusters are currently non-blocked is provided in (25). For any i non-blocked clusters, the probability that LoS cluster blocked is $\frac{M-1}{M} \frac{M-2}{M-1} \times \dots \times \frac{M-i}{M-i+1} = \frac{M-i}{M}$. Alternatively, LoS cluster is non-blocked is just i/M . Combining these results one arrives at the following approximation

$$p_E = \frac{\sum_{i=1}^M q_{M,i} \left(\frac{M-i}{M} p_{E,nL}^i + \frac{i}{M} p_{E,L} p_{E,nL}^{i-1} \right)}{1 - \prod_{i=1}^M p_{B,i}}. \quad (34)$$

IV. NUMERICAL ASSESSMENT

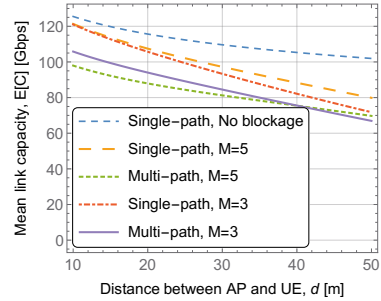
In this section, we characterize the trade-off between the achieved capacity and eavesdropping probability for the single-path and multi-path schemes as a function of system parameters. The system parameters are summarized in Table II.

1) *The link capacity:* We start characterizing the link capacity (Shannon rate) for both single-path and multi-path schemes as a function of system parameters illustrated in Fig. 4. Particularly, Fig. 4(a) shows the link capacity as a function of the distance between AP and UE for both schemes and the different number of paths maintained at UE, $M = 3$ and $M = 5$. An upper capacity bound for the baseline single-path scheme without blockers, i.e., $\mu = 0$, is also highlighted. Expectedly, in the presence of blockers, the capacity of both schemes get severely compromised. Furthermore, as one may observe, the difference between the single-path and the multi-path schemes is only noticeable up to approximately 40–50 m of the separation distance between AP and UE. For $d > 50$ m, the LoS path is characterized by high blockage probability, so the dominating effect of this path becomes less profound.

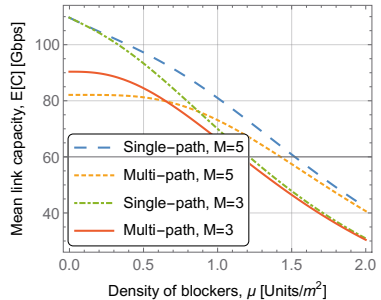
TABLE II
DEFAULT SYSTEM PARAMETERS.

Parameter	Value
Carrier frequency, f_c	300 GHz
Bandwidth, B	5 GHz
Transmit power, P_T	0 dBm
AP height, h_A	5 m
UE height, h_U	1.5 m
Blockers height, h_B	1.7 m
Blockers radius, r_B	0.3 m
Eavesdroppers height, h_E	1.7 m
Default spatial blockers density, μ	0.5 bl./m ²
Default spatial eavesdroppers density, λ	0.01 cav./m ²
AOA, ZOA, power share	Parameterized following [27]
AP antenna array elements, L_A	{512, 1024, 2048}
UE antenna array	128 × 128 elements ($L_U = 128$)

The inherent multi-path diversity of terahertz communications plays a critical role in achieved link capacity. Particularly, as evident from Fig. 4(a), allowing UE to use more paths result in better performance for the single-path scheme for all the considered values of d . Furthermore, the difference increases with the distance as the probability of using LoS path decreases due to the blockage. This behavior is also valid for the multi-path scheme and for large distances between AP and UE, i.e., starting from $d \approx 40$ m. For smaller values of



(a) $L_A = 1024$, $\mu = 0.5$



(b) $L_A = 1024$, $d = 30$ m

Fig. 4. THz communications capacity for *Single-path* and *Multi-path* schemes.

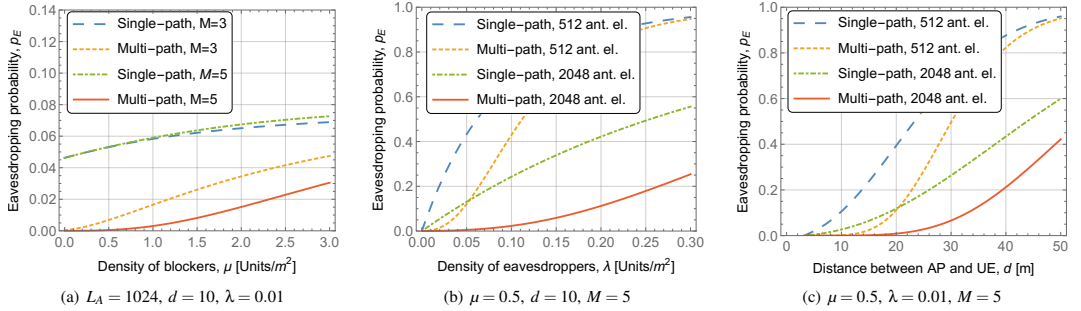


Fig. 5. THz communications eavesdropping probability for *Single-path* and *Multi-path* schemes.

d the effect is reversed. The main reason here is again the dependence of the paths blockage zones sizes on d . When d is small, the probability that all the paths are non-blocked is high for both $M = 3$ and $M = 5$ implying that the contribution of the LoS path to the overall capacity is higher for $M = 3$. As d increases, blockage probability for the LoS path increases, thus, reducing the role of this path for the link capacity.

Consider now the effect of spatial blockers density, μ , on the Shannon rate illustrated in Fig. 4(b). Logically, for the small values of μ , the link capacity of baseline schemes coincide, as the LoS path is used almost all the time. For larger values of μ , the rate starts to deviate drastically, as the probability of simultaneously blocking 3 paths becomes much smaller than the corresponding probability for $M = 5$. Furthermore, the difference between the link capacities for the considered schemes decreases with the growth of the blockers density and the values almost coincide for $\mu = 1.5$ units/m². Similarly to Fig. 4(a), we observe that for the small values of μ , the multi-path scheme with $M = 3$ outperforms the one with $M = 5$.

2) *The eavesdropping probability*: We now proceed with studying the eavesdropping probability for a wide range of system parameters illustrated in Fig. 5. Particularly, Fig. 5(a) shows the eavesdropping probability for both schemes as a function of the spatial density of blockers, μ . As one may observe, for a wide range of μ , the multi-path scheme provides substantial performance gains at the slight decrease in achieved system capacity, as illustrated in Fig. 4(b) for both $M = 3$ and $M = 5$. Specifically, for $\mu = 1.5$ and $M = 5$ the loss in capacity is only 2–3 Gbps, while the difference in the eavesdropping probability is over 600%: decreasing from approximately 0.06 for the single-path scheme to less than 0.01 for the multi-path scheme. It is also logical to observe that the greater number of the available paths, M , leads to the lower eavesdropping probability for both schemes.

Let us now study the behavior of both schemes as a function of the spatial density of eavesdroppers, λ , as shown in Fig. 5(b) for the two values of the number of antenna elements at the AP, $L_A = 512$ and $L_A = 2048$. One of the critical trends here is that the increase in L_A leads to better performance for both the single-path and multi-path schemes. The underlying reason is

that the system with the higher value of L_A leads to the smaller size of the eavesdropping zone and, thus, lower values of the individual eavesdropping probabilities for a given path. For $L_A = 2048$, the gains are observed across the entire range of the density of eavesdroppers, while for $L_A = 512$ both curves converge already at $\lambda \approx 0.03$ units/m². The eavesdropping probability for the single-path and the multi-path schemes is shown in Fig. 5(c) as a function of the 2D distance between the AP and the UE, d , for two values of L_A . For $L_A = 2048$ the noticeable gains are observed across the entire range of d , while for $L_A = 512$ the curves converge at $d \approx 50$ m.

3) *The secrecy rate*: Finally, we study the secrecy rate, C_S , presented in Fig. 6 as a function of the density of blockers. The secrecy rate metric here combines the previous two (C and p_E), thus, allowing to compare the two schemes within a single plot. As observed from Fig. 6, the multi-path scheme achieves considerably greater secrecy rate over a wide range of system parameters. The gain varies from approximately 4 Gbps for the low density of eavesdroppers, $\lambda = 0.03$, to more than 10 Gbps for $\lambda = 0.1$. Similar conclusions are observed for the secrecy rate as a function of other system parameters, such as distance and the number of antenna elements, L_A .

In summary, the multi-path scheme achieves notable gains over the single-path in both the eavesdropping probability and the secrecy rate at a cost of a slightly decreased link capacity.

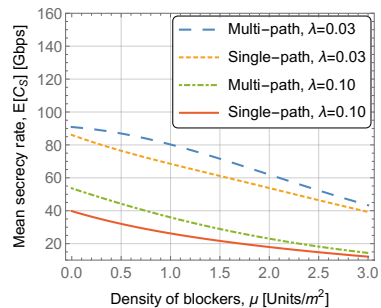


Fig. 6. Secrecy rate for *Single-path* and *Multi-path* schemes, $d = 15$ m, $M = 5$.

V. CONCLUSIONS

Secure data transmission is one of the critical requirements for the wireless systems beyond 5G. The prospective use of THz band provides additional tools for securing communications already at the physical layer. In this paper, we have investigated how the security of data transmissions can be leveraged by exploiting the multi-path propagation of THz communications. We have developed a mathematical framework capturing the inherent trade-offs between the eavesdropping probability and the capacity of a THz link in a typical urban scenario with various crowd and attackers densities, and the different number of multi-path components. With the proper parameterization, our framework can be further applied to the analysis of other THz-specific deployments, such as indoor office, house, etc.

We have also shown that sharing the message across all the currently non-blocked propagation paths between AP and UE with the proposed *multi-path* scheme drastically decreases the eavesdropping probability and increases the secrecy rate of THz communications at the expense of slightly reduced link capacity. With the slightly degraded capacity and the overheads of beam realignment procedure and additional coding, brought by the *multi-path* scheme, the proposed solution can be utilized selectively, e.g., to improve the security of sensitive communications (online banking, cryptocurrency transactions, etc.), as well as to secure the exchange of the session encryption keys. The baseline *single-path* scheme can be applied to all other non-sensitive communications. The presented study may serve as one of the building blocks towards secure and robust wireless communications over the THz band as an integral part of beyond 5G networks.

ACKNOWLEDGEMENTS

The authors would like to thank the anonymous reviewers of IEEE INFOCOM 2019 UBTCN Workshop for their helpful and constructive comments that greatly contributed to improving the final version of the paper. J. M. Jornet acknowledges the support from NSF Grant CNS-1730148.

REFERENCES

- [1] K. Huang and Z. Wang, "Terahertz terabit wireless communication," *IEEE Microwave Magazine*, vol. 12, no. 4, pp. 108–116, June 2011.
- [2] I. F. Akyildiz, J. M. Jornet, and C. Han, "Teranets: Ultra-broadband communication networks in the terahertz band," *IEEE Wireless Communications*, vol. 21, no. 4, pp. 130–135, August 2014.
- [3] I. F. Akyildiz and J. M. Jornet, "Realizing ultra-massive MIMO (1024×1024) communication in the (0.06–10) terahertz band," *Nano Communication Networks*, vol. 8, pp. 46–54, June 2016.
- [4] D. He *et al.*, "Stochastic channel modeling for kiosk applications in the terahertz band," *IEEE Transactions on Terahertz Science and Technology*, vol. 7, no. 5, pp. 502–513, September 2017.
- [5] K. Sakaguchi *et al.*, "Where, when, and how mmWave is used in 5G and beyond," *IEICE Transactions on Electronics*, vol. E100.C, no. 10, pp. 790–808, October 2017.
- [6] M. Simsek, A. Aijaz, M. Dohler, J. Sachs, and G. Fettweis, "5G-enabled tactile internet," *IEEE Journal on Selected Areas in Communications*, vol. 34, no. 3, pp. 460–473, March 2016.
- [7] "IEEE Standard for High Data Rate Wireless Multi-Media Networks – Amendment 2: 100 Gb/s Wireless Switched Point-to-Point Physical Layer," IEEE Std 802.15.3d-2017, Specification, 2017.
- [8] T. Kurner and S. Rey, "IEEE 802.15.3d and other activities related to THz communications. Where to go next?" in *Towards Terahertz Communications Workshop*, March 2018.
- [9] Q. J. Gu, "Thz interconnect: The last centimeter communication," *IEEE Communications Magazine*, vol. 53, no. 4, pp. 206–215, April 2015.
- [10] V. Petrov, M. Komarov, D. Moltchanov, J. M. Jornet, and Y. Koucheryavy, "Interference analysis of EHF/THF communications systems with blocking and directional antennas," in *Proc. of IEEE Global Communications Conference (GLOBECOM)*, December 2016.
- [11] C. Han, A. O. Bicen, and I. F. Akyildiz, "Multi-ray channel modeling and wideband characterization for wireless communications in the terahertz band," *IEEE Transactions on Wireless Communications*, vol. 14, no. 5, pp. 2402–2412, May 2015.
- [12] C. Han and I. F. Akyildiz, "Distance-aware bandwidth-adaptive resource allocation for wireless systems in the terahertz band," *IEEE Transactions on Terahertz Science and Tech.*, vol. 6, no. 4, pp. 541–553, July 2016.
- [13] V. Petrov, D. Moltchanov, and Y. Koucheryavy, "Applicability assessment of terahertz information showers for next-generation wireless networks," in *Proc. of IEEE International Conference on Communications (ICC)*, May 2016.
- [14] V. Petrov, J. Kokkonen, D. Moltchanov, J. Lehtomaki, Y. Koucheryavy, and M. Juntti, "Last meter indoor terahertz wireless access: Performance insights and implementation roadmap," *IEEE Communications Magazine*, vol. 56, no. 6, pp. 158–165, June 2018.
- [15] I. F. Akyildiz, J. M. Jornet, and C. Han, "Terahertz band: Next frontier for wireless communications," *Physical Communication*, vol. 12, pp. 16–32, September 2014.
- [16] J. Kokkonen, J. Lehtomaki, K. Umehayashi, and M. Juntti, "Frequency and time domain channel models for nanonetworks in terahertz band," *IEEE Transactions on Antennas and Propagation*, vol. 63, no. 2, pp. 678–691, February 2015.
- [17] S. Priebe, M. Jacob, and T. Kurner, "AoA, AoD and ToA characteristics of scattered multipath clusters for THz indoor channel modeling," in *Proc. of the 11th European Wireless Conference*, April 2011, pp. 1–9.
- [18] B. Li, H. Gao, and X. Jing, "Mapping millimeter wave propagation to 5G physical layer: A brief review and look forward," in *Proc. of ISCIT*, September 2016, pp. 695–699.
- [19] Y. Zhu, L. Wang, K. Wong, and R. W. Heath, "Physical layer security in large-scale millimeter wave ad hoc networks," in *Proc. of IEEE Global Communications Conference (GLOBECOM)*, December 2016.
- [20] Y. Wu *et al.*, "A survey of physical layer security techniques for 5G wireless networks and challenges ahead," *IEEE Journal on Selected Areas in Communications*, vol. 36, no. 4, pp. 679–695, April 2018.
- [21] K. Xiao, S. Zhang, and Y. He, "On the secrecy capacity of 5G new radio networks," *Wireless Communications and Mobile Computing*, May 2018.
- [22] J. Ma *et al.*, "Security and eavesdropping in terahertz wireless links," *Nature*, 2018.
- [23] M. Karmoose *et al.*, "Leveraging mm-wave communication for security," *CoRR*, vol. abs/1803.08188, March 2018.
- [24] S. Priebe *et al.*, "Channel and propagation measurements at 300 GHz," *IEEE Transactions on Antennas and Propagation*, vol. 59, no. 5, pp. 1688–1698, May 2011.
- [25] V. Petrov, M. A. Lema, M. Gapeyenko, K. Antonakoglou, D. Moltchanov, F. Sardis, A. Samuylov, S. Andreev, Y. Koucheryavy, and M. Dohler, "Achieving end-to-end reliability of mission-critical traffic in software-defined 5G networks," *IEEE Journal on Selected Areas in Communications*, vol. 36, no. 3, pp. 485–501, March 2018.
- [26] J. M. Jornet and I. F. Akyildiz, "Channel modeling and capacity analysis for electromagnetic wireless nanonetworks in the terahertz band," *IEEE Transactions on Wireless Communications*, vol. 10, no. 10, pp. 3211–3221, October 2011.
- [27] M. Gapeyenko, V. Petrov, D. Moltchanov, S. Andreev, Y. Koucheryavy, M. Valkama, M. R. Akdeniz, and N. Himayat, "An analytical representation of the 3GPP 3D channel model parameters for mmWave bands," in *Proc. of 2nd Workshop Millim.-Wave Netw. Sens. Syst., ACM MobiCom*, October 2018.
- [28] V. Petrov, M. Komarov, D. Moltchanov, J. M. Jornet, and Y. Koucheryavy, "Interference and SINR in millimeter wave and terahertz communication systems with blocking and directional antennas," *IEEE Transactions on Wireless Communications*, vol. 16, no. 3, pp. 1791–1808, March 2017.
- [29] A. B. Constantine *et al.*, "Antenna theory: analysis and design," *Microwave Antennas (third edition)*, John Wiley & Sons, 2005.
- [30] M. Gapeyenko, V. Petrov, D. Moltchanov, S. Andreev, N. Himayat, and Y. Koucheryavy, "Flexible and reliable UAV-assisted backhaul operation in 5G mmWave cellular networks," *IEEE Journal on Selected Areas in Communications*, vol. 36, no. 11, pp. 2486–2496, November 2018.
- [31] S. Ross, *Introduction to probability models*. Academic Press, 2010.

